QUANTUM LIQUIDS AND QUANTUM CRYSTALS

A discussion of the dispersion curve of energy excitations in liquid ^{4}He

I. V. Bogoyavlenskii, A. V. Puchkov,* and A. N. Skomorokhov

Research Center of the Russian Federation "Institute of Physics and Power Engineering," ul. Bondarenko 1, Obninsk 249033, Russia

L. V. Karnatsevich

National Research Center "Kharkov Institute of Physics and Technology," ul. Akademicheskaya 1, Kharkov 61108, Ukraine

(Submitted February 10, 2004)
Fiz. Nizk. Temp. **30**, 995–1008 (October 2004)

An investigation of the dispersion of excitations in a quantum liquid, superfluid ^{4}He, is carried out. An attempt is made to systematize the published experimental data that indicate a substantially different nature of excitations with wave vectors corresponding to different parts of the dispersion curve of liquid ^{4}He. Neutron spectroscopy data are analyzed in relation to a certain physical hypothesis concerning the formation of such a spectrum, and it is found that the majority of the known experimental facts can be explained in framework of that hypothesis. Particular attention is paid to a comparison of the experimental data obtained on the DIN-2PI time-of-flight spectrometer (at the IBR-2 Reactor, Dubna) with the results obtained at foreign research centers. © *2004 American Institute of Physics.* [DOI: 10.1063/1.1808151]

1. INTRODUCTION

By 2001, sixty years had passed since the publication of Landau's paper[1] in which he proposed a form for the excitation spectrum in superfluid liquid ^{4}He and constructed a theory of helium II based on that proposed form. Nevertheless, questions concerning the nature of the spectrum of energy excitations in liquid helium and in Bose systems in general have been attracting interest ever since. In his first paper on the theory of superfluidity,[1] Landau, applying the quantum hydrodynamics he had developed, proposed the existence of two types of collective excitations. One type involves the potential motion of the liquid and comprises simple sound quanta—phonons whose energy ε is a linear function of the wave vector **Q**. Landau attributed the other type of excitations to the vortical motion of the liquid, and for that reason they would come to be named ''rotons'' by Tamm. It was assumed that the energy of the rotons depends quadratically on their wave vector and has a gap Δ: $\varepsilon(Q) = \Delta + (\hbar^2 Q^2/2\mu)$, where μ is the effective mass of the roton. Thus it was assumed that there exist two independent branches of excitations. An attempt to calculate the velocity of second sound (which had been measured to high accuracy by Peshkov[2]) on the basis of the proposed picture convinced Landau in 1947 to abandon these ideas and propose the presence of a unified dispersion curve for energy excitations in liquid helium[3] in the well-known form with a linear initial segment (phonons) and a characteristic roton minimum. In another paper of 1947 Bogolyubov,[4] using a model of a weakly nonideal Bose gas in the presence of a Bose condensate in the system, obtained for the above-condensate excitations a dispersion curve of the same form—with a linear initial segment. Somewhat later, experimental papers on the scattering of neutrons on superfluid ^{4}He confirmed the form of Landau's dispersion curve. However, the physical nature of the excitations on different parts of that curve remained an open question. A commonly held view was that the superfluid ^{4}He can be described completely in terms of the concept of a gas of single-particle excitations (quasiparticles) having a unified dispersion relation. In such an interpretation, Bose systems are essentially different from Fermi systems (e.g., from liquid ^{3}He), where one considers different types of excitations (single-particle, single-pair, multipair, collective).[5] We note that such a differentiation between helium isotopes is not completely understood from a general theoretical standpoint.

By the end of the 1950s it had become possible to do experiments on inelastic neutron scattering in liquid helium. The first experiments of this kind were done at the Chalk River National Laboratory in Canada[6,7] and somewhat later in other laboratories, including in the USSR (at JINR, Dubna).[8,9] The dispersion curve extracted from those experiments for the excitations in liquid ^{4}He was indeed a single curve quantitatively similar to the form postulated by Landau (Fig. 1). The neutron-scattering experiments determined the values of the energy transfer ε corresponding to the maximum of the scattering peak at given wave vector transfers **Q**, and the dispersion curve was constructed from those points. Those data are insufficient to assess the nature of the excitations under study, since, depending on the form of the excitations, the scattering peak can have different width, intensity, and shape, and these parameters of the peak can depend differently on the external conditions. More-detailed studies of the neutron scattering peaks in liquid ^{4}He showed that the characteristics of the peaks as a function of temperature and

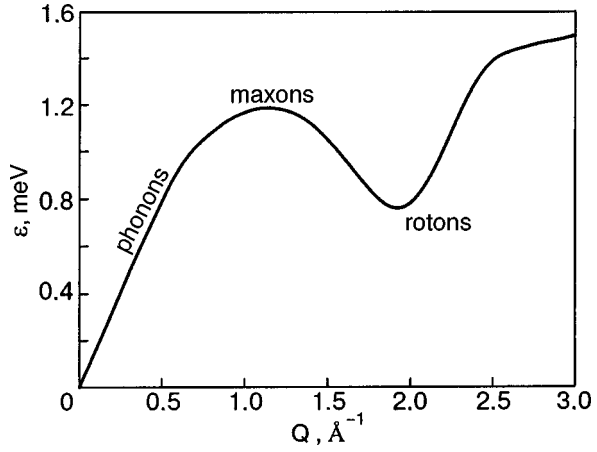

FIG. 1. Dispersion curve of excitations in superfluid ^{4}He under saturated vapor pressure at $T<1.5$ K.

pressure are substantially different for the long- and short-wavelength parts of the dispersion curve. At present the inelastic neutron scattering studies of the spectrum of excitations in helium by different groups of authors have produced a large volume of experimental data indicating that the excitations pertaining to the phonon (initial) and maxon–roton parts of the dispersion curve are of different natures. Thus it seems that it is necessary to revisit Landau's original hypothesis[1] that there are two different types of excitations, although now, as will be discussed below, the roton part is not associated with vortical motion.

At this new level the papers by Glyde and Griffin (see, e.g., Refs. 10 and 11) advanced the hypothesis of a different physical nature of the phonon and maxon–roton parts of the dispersion curve. In their opinion, the long-wavelength (phonon) part of the spectrum is determined by collective excitations of the zero-sound type, the existence of which was proposed earlier by Pines,[12] and the maxon–roton part is determined by single-particle excitations. A unified curve is formed as a result of a ''hybridization'' of these two branches of excitations. A similar but somewhat refined concept of the formation of a unified spectrum as a result of the interaction of the dispersion curves of collective and single-particle excitations was proposed in Ref. 13. In the present paper we systematize the published experimental results indicating the existence of excitations of different natures on different parts of the dispersion curve in ^{4}He and analyze them on the basis of a qualitative model of the formation of the outwardly unified dispersion curve proposed in Refs. 13 and 14.

2. EXCITATIONS IN THE PHONON REGION OF THE DISPERSION CURVE

In Ref. 1 Landau had this to say about these excitations: ''in respect to the excited levels of the potential spectrum, the potential internal motion of the liquid is none other than longitudinal, i.e., sound, waves. The corresponding 'elementary excitations' are therefore simply sound quanta, i.e., phonons.'' Sound in quantum liquids, ^{4}He in particular, can be excited by an external source. These small nonequilibrium oscillations against an equilibrium background in quantum liquids have been well studied experimentally.[15] Collective sound excitations also arise on account of the energy of the heat bath, which is held at a certain finite temperature in equilibrium with the liquid, and this contributes to the thermodynamic quantities characterizing a many-particle system. The nature of the nonequilibrium and thermal phonons is completely identical, and the only different is in their manner of excitation and, hence, their energy. At low frequencies, such that $\omega\tau\ll 1$, where τ is the time between collisions, the collective sound excitations are described by hydrodynamic equations. In the intermediate region ($\omega\tau\sim 1$) there is a substantial rise in the damping of the collective excitations. In the high-frequency region $\omega\tau\gg 1$ once again there are weakly damped waves of the zero-sound type, which must be described using kinetic equations. Such a picture is observed in liquid ^{3}He (Ref. 16); it is typical of many other liquids, including classical ones.[17] Analysis of the experiments in ^{4}He, in particular, those which are discussed below, shows that in this respect there are no essential differences between liquid ^{4}He and other liquids.

The phonon region of the dispersion curve will be understood to mean that part from $Q=0$ to $Q\approx 0.7$ Å^{-1}. The upper boundary of this region is not strictly defined, and the interval from $Q\approx 0.35$ Å^{-1} to $Q\approx 0.7$ Å^{-1} can be regarded as a transition region from the phonon to the maxon–roton part. The minimum value of the wave vector transfer that is realizable in neutron experiments is $Q_{\min}\approx 0.1$ Å^{-1}.

We recall that what is measured in experiment is not the dynamic structure factor $S(Q,\omega)$ but the doubly differential neutron scattering cross section $d^2\sigma/(d\Omega dE)$, which is related to $S(Q,\omega)$ by the well-known relation

$$\frac{d^2\sigma}{d\Omega dE}=N\frac{\sigma}{4\pi\hbar}\frac{k}{k_0}S_{\exp}(Q,\omega),$$

where $d\Omega$ is an interval of scattering solid angles, dE is the scattering energy interval, N is the number of atoms in the system, and σ is the neutron scattering cross section of a bound atom.

A neutron with wave vector $\mathbf{k}_0$ and energy E_0 acquires a wave vector $\mathbf{k}$ and energy E in a scattering event. By changing its direction of motion and gaining (or losing) energy in the scattering process, a neutron transfers to the sample a momentum $\hbar\mathbf{Q}$ and an energy $\varepsilon=\hbar\omega$:

$$\hbar\mathbf{Q}=\hbar\mathbf{k}_0-\hbar\mathbf{k},$$

$$\hbar\omega=E_0-E-\varepsilon.$$

After a preliminary processing, which takes into account various methodological corrections, one can obtain an experimental dynamic structure factor $S_{\exp}(Q,\omega)$ which is a superposition of one-phonon, multiphonon, and multiple scattering of neutrons:

$$S_{\exp}(Q,\omega)=S_1(Q,\omega)+S_{\mathrm{mph}}(Q,\omega)+S_{\mathrm{mpl}}(Q,\omega).$$

We are interested in the one-phonon component, which corresponds to the creation of a single excitation in a neutron scattering event and which carries information about the properties of that excitation. It is the component $S_1(Q,\omega)$ that will be subject to fitting below with the use of different models, followed by a detailed analysis of the model parameters. When we speak of the position or width of the ''scattering peak'' below we shall have in mind the corresponding fitting parameters of the model description of $S_1(Q,\omega)$.

Let us turn to an analysis of the experimental results of neutron experiments in this region. We consider the data on the position of the maximum of the scattering peak $\varepsilon(Q)$, its full width at half maximum (FWHM), denoted 2Γ, and the relative intensity Z of the peak and the behavior of that quantity with changing temperature, pressure, and value of the wave vector transfer. Before turning to that analysis, let us consider the form of the dynamic structure factor $S(Q,\omega)$ or the shape of the neutron scattering peaks.

Shape of the scattering peaks

For a strongly interacting many-particle system the dynamic structure factor $S(Q,\omega)$ cannot, of course, be calculated exactly. To describe the shape of the scattering peak, an expression for the dynamic structure factor is approximated by some rather simple function containing a set of adjustable parameters. The functions used for this purpose include the Gaussian and Lorentzian[18] and a ''damped harmonic oscillator'' (DHO) function (see, e.g., Refs. 19 and 20). It should be emphasized that the use of any of these functions is only a means of describing the experimentally observed peak, and one can only say that some approximation or other matches the general properties of the dynamic structure factor which follow from requirements of symmetry and other fundamental principles. In this respect the DHO function has the advantage that it takes into account scattering processes involving both losses and gains of energy, which becomes important at energies $\varepsilon < kT$ (Refs. 11, 21, and 22). According to Refs. 19, 20, and 23, in the phonon part of the dispersion curve the experimental peaks are described well enough by a single DHO fitting function. However, as Q increases, in the region of the transition to maxons at $Q > 0.37$ Å^{-1}, description by a single function becomes insufficient. For adequate description of the shape of the peak it becomes necessary to introduce a superposition of two approximating functions.[24,25] It should be noted that we have previously[26,27] attempted to describe the experimental scattering peaks with the use of the simplest model, a superposition of Gaussian functions. In doing so, we neglected a number of methodological effects. Refinement of the experimental and data-processing techniques showed that the indicated effects can substantially distort the final result. This led us to carry out a new analysis of the spectra on the basis of a description of the neutron scattering peaks in the form a DHO function and to reconsider the results. They were published in Ref. 19 together with a detailed exposition of the procedures used in processing the spectra. In addition, additional precision measurements of the spectra in the phonon–maxon transition region were carried out, the results of which are presented in detail in Ref. 20.

Let us mention one more circumstance: if two or more components (e.g., of the DHO type) can be discerned in the scattering peak, then, strictly speaking, it is necessary to analyze each of these components with respect to the parameters indicated above. However, in the region under study the second component, which can be discerned for $Q > 0.37$ Å^{-1}, is so weak that it actually has no effect on the values of the parameters of $\varepsilon(Q)$, 2Γ, and Z of the main component in comparison with the corresponding values for the total scattering peak. Therefore the accuracy of determination of the parameters of the weak component does not permit one to analyze their dependence on the external conditions. We shall discuss the behavior of this component in more detail below when we consider the maxon–roton region of the dispersion curve.

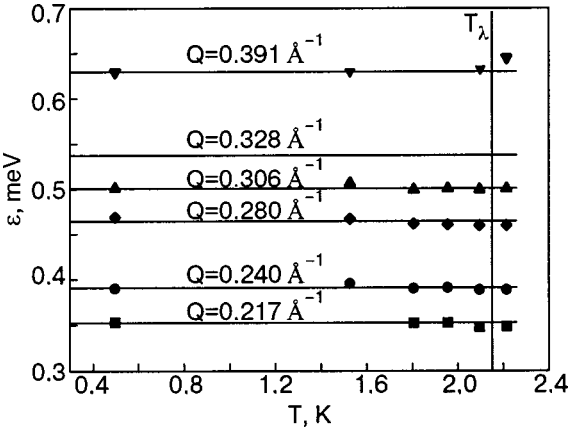

FIG. 2. Temperature dependence of the energy of excitations in liquid ^{4}He at different values of the wave vector transfer in the phonon region of the dispersion curve under saturated vapor pressure.[20]

Position of the dispersion curve $\varepsilon(Q)$

The position of the maximum of the scattering peak determines the form of the dispersion curve in the coordinates $\varepsilon - Q$, where ε is the excitation energy and Q is the wave vector transfer. Accurate neutron data as to the shape of the dispersion curve and its initial segment have been obtained by many authors over a wide range of temperatures, from 0.5 to 4.5 K, and at pressures of up to 2.5 MPa (see Refs. 7, 18–20, 23–30, etc.). Among the most recent results the most complete and precise data obtained by the authors in the phonon region are given in Refs. 20 and 31.

First of all, it should be noted that the inelastic scattering peaks at momentum transfers corresponding to the phonon part of the dispersion curve are sharp and well-defined in both the superfluid and normal phases. The most characteristic feature of the phonon part of the curve is the temperature independence of its parameters and, importantly, the insensitivity to the transition from the superfluid to the normal state (see Fig. 2). (The slight ''dip'' of the ε values in a narrow temperature region around T_λ which was observed in Ref. 7 and to a certain degree in Ref. 20, lies at the limits of experimental accuracy.) Only with growth of Q (for $Q > 0.35$ Å^{-1}, according to the data of Ref. 20) does the upward shift in energy of the dispersion curve at the transition to the normal state become noticeable. We note straightaway that such behavior of the phonon region of the dispersion curve differs sharply from the maxon–roton region, the position of which depends on temperature and changes substantially at the transition from the superfluid to the normal state. With increasing pressure the slope of the phonon part of the dispersion curve increases, but as before it remains independent of temperature and the phase state of the liquid. Thus the position of the phonon part is determined exclusively by the density of the liquid helium, which, as we know, varies weakly with temperature.

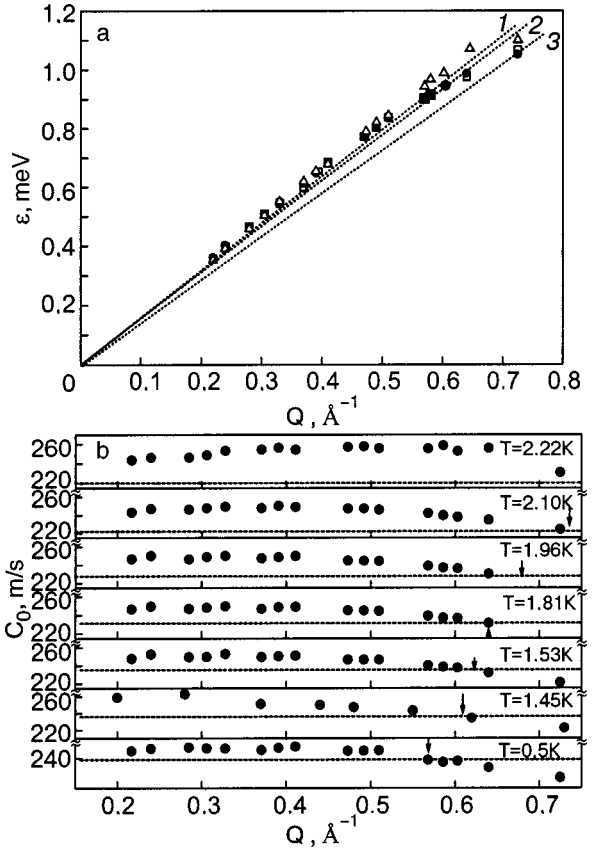

FIG. 3. Anomalous dispersion curve of excitations in the phonon region in liquid ^{4}He under saturated vapor pressure[20] at different T [K]: 0.5 (□), 1.53 (●); 2.22 (△); the dotted straight lines correspond to the following values of the first-sound velocity at T [K]: 2.22 (*1*), 1.53 (*2*), 0.5 (*3*) (a). The initial parts of the dispersion curve in the coordinates $C_0(Q)$ for a number of temperatures.[20] The horizontal lines correspond to the velocity of first sound. The arrows indicate the value of Q_c for the corresponding temperature (b).

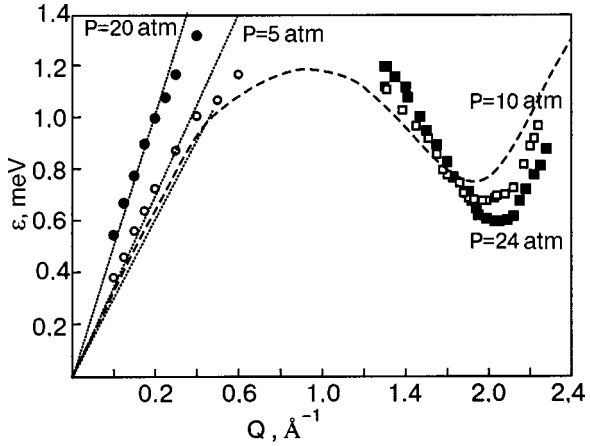

FIG. 4. Dispersion curves in liquid ^{4}He at different pressures: data of Ref. 30 for $T=1$ K (●) and (○); data of Ref. 21 for $T=1.3$ K (□) and (■). The dotted straight lines correspond to the first-sound velocities for the corresponding external conditions in terms of pressure and temperature. The dashed curve is the dispersion curve averaged over many experimental data points at temperatures $T<1.5$ K under saturated vapor pressure.

Anomalous dispersion

The velocity of sound waves ($C_0=\varepsilon/Q$) obtained from the inelastic neutron scattering experiments are usually compared with the velocity C_1 of hydrodynamic first sound, which is well known from other experiments.[15] It is clear that $C_0=C_1$ for $Q=0$. A comparison of the velocities at nonzero but small values of Q shows that $C_0>C_1$ under the same thermodynamic conditions. This phenomenon is referred to as anomalous dispersion. As is seen in Fig. 3, the values of the excitation energy obtained from neutron experiments at fixed Q lie noticeably higher than those corresponding to a linear dispersion law $\varepsilon(Q)=C_1Q$. With increasing Q the deviation from the linear dispersion law increases at first, reaches a maximum, and then begins to fall. At a certain point Q_c the experimental dispersion curve crosses the straight line $\varepsilon(Q)=C_1Q$. The wave vector Q_c corresponding to the crossing point depends on temperature, increasing from $Q_c=0.5$ Å^{-1} at $T=0.5$ K to $Q_c=0.8$ Å^{-1} at $T=2.3$ K and even to 1.1 Å^{-1} at $T=4$ K. (This is well seen in Fig. 3b, where the data are presented in the coordinates C_0 versus Q.) Figure 3 once again shows that the position of the phonon part of the dispersion curve is independent of temperature.

The explanation for the observed ''anomaly'' is perfectly obvious by virtue of the difference in the velocities of zero sound and first sound. The zero-sound velocity is independent of temperature and higher than the velocity of first sound, and the velocity of first sound should be temperature dependent, as is in fact observed. Such an ''anomaly'' is characteristic not only for ^{4}He but also for many other liquids, in particular, for ^{3}He (Ref. 16) and also for liquid Rb, Ne, and H_2 (see the bibliography of Ref. 17). This attests to a unified physical nature of the excitations observed at low Q in these liquids and of the unified nature of the ''anomaly'' in the sound dispersion law. Theoretical estimates of the value of the anomaly in ^{4}He were made in Ref. 13, and the values obtained were close to the experimental values. Remarkably, the transition from the superfluid to the normal state does not have any qualitative effect on this picture. With increasing pressure (i.e., density of the system) the described regularities of the anomalous dispersion are also preserved completely: only quantitative changes are seen, since the velocities of both first and zero sound in liquid ^{4}He increase with pressure and, hence, so does slope of the curve $\varepsilon(Q)$. Experimentally the behavior of $\varepsilon(Q)$ under pressure was first studied in detail in Ref. 30 (Fig. 4). This qualitative picture is confirmed by the data of more recent papers (e.g., Ref. 32).

Width of the scattering peaks

The experimental determination of the intrinsic width of the neutron scattering peaks is rather complicated, since it involves taking the resolution function of the spectrometer into account in an adequate way.[33,34] For this reason it should be kept in mind that there may be systematic deviations between the results of different studies. The curves of the FWHM of the scattering peak $2\Gamma(T)$ according to the data of Ref. 20 for several values of Q are presented in Fig. 5. These curves are smooth, described well by an exponential function, and up to $Q\approx0.35$ Å^{-1} their character is unchanged upon the transition of ^{4}He from the normal to the superfluid state. The dependence of 2Γ on Q at different temperatures on the phonon part of the dispersion curve has been studied, e.g., in Refs. 20 and 36 (Fig. 6). Within the

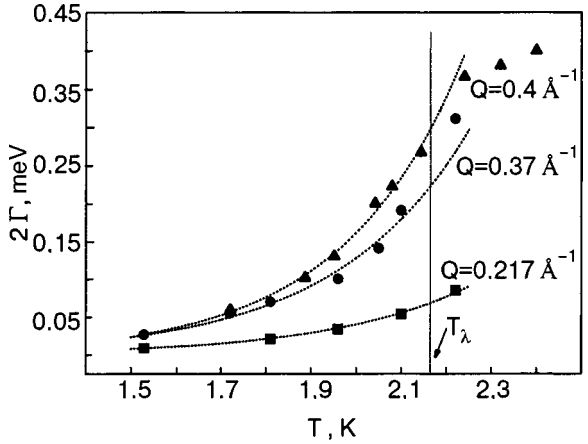

FIG. 5. Temperature dependence of the width (FWHM 2Γ) of the one-phonon neutron scattering peak at momentum transfers corresponding to the phonon region of the dispersion curve: (●) and (■)—data of Ref. 20; (▲)—data of Ref. 29. The dotted curves are approximations by exponential relations obtained from the experimental data below $T=2$ K.

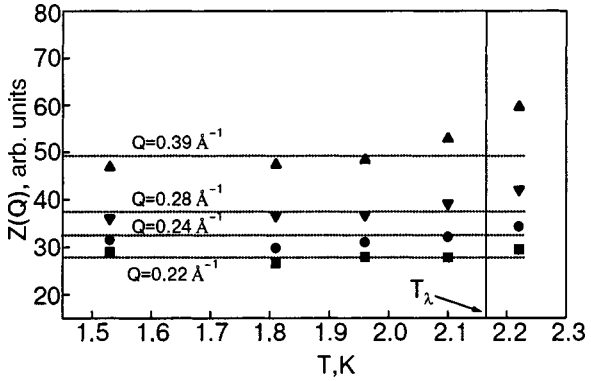

FIG. 7. Relative intensity $Z(Q)$ of the one-phonon neutron scattering in liquid ^{4}He as a function of temperature for different values of the wave vector transfer Q in the phonon region of the dispersion curve.[20] The horizontal straight lines reflect the temperature dependence of the relative intensity of the peaks.

experimental accuracy they are close to linear. However, at momentum transfers in the region of the transition from the phonon to the maxon–roton part of the dispersion curve one observes a pronounced change in the character of these curves (see Fig. 6).

Relative intensity of the scattering peaks

Figure 7 shows the temperature dependence of the intensity Z in the phonon part of the dispersion curve for several values of Q, according to the data of Ref. 20. It is seen in the figure that the intensity is practically independent of temperature and of the state of the liquid helium (normal or superfluid). Here, as in the width of the peak, the λ transition begins to be manifested only at momentum transfers $Q > 0.35$ Å^{-1}. In the phonon region the $Z(Q)$ curve is close to linear (Fig. 8),[20] but in the transition region from phonons to maxons the character of the curves changes. Characteristically in normal helium the linear region of $Z(Q)$ extends to higher values of Q (see Fig. 8).

In concluding this Section we note that the experimental study of the phonon part of the spectrum in liquid ^{4}He is of fundamental value for the theory of superfluid many-particle Bose systems, since, as we have said, there are different explanations for the nature of the linear part of the spectrum. Bogolyubov's result[4] is often interpreted as a microscopic basis for Landau's phenomenological dispersion relation. The authors do not believe that such an interpretation is justified. As may be seen from the work cited at the beginning of this Section, Landau understood "phonons" to mean longitudinal acoustic vibrations of the liquid, and there is no doubt about the presence of such collective excitations. Such excitations exist in a liquid completely independently of whether it is superfluid or normal, whether or not there is a Bose condensate in the system, and whether the liquid consists of Bose or Fermi particles. The Bogolyubov quasiparticles have a completely different nature, being single-particle (atomlike) excitations, the dispersion relation of which at large momenta asymptotically approaches that of free particles, analogous to those which Landau introduced at a phe-

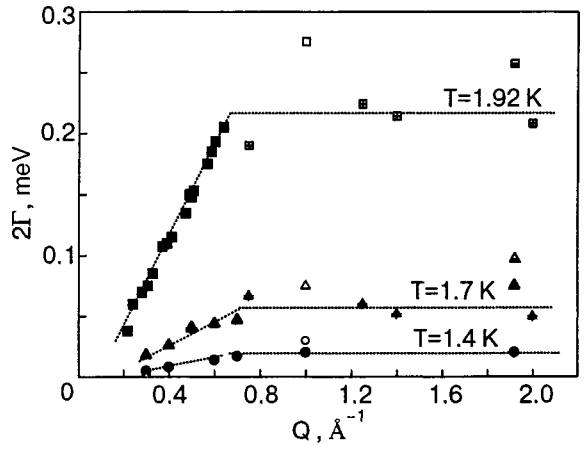

FIG. 6. Width 2Γ of the one-phonon neutron scattering peak as a function of the wave vector transfer **Q** according to the data of different papers at different temperatures. $T=1.92$ K: (■)—Ref. 20, (⬓)—Ref. 29, (□)—Ref. 32, (⊞)—Ref. 35). $T=1.7$ K: (▲)—Ref. 36, (▲)—Ref. 29, (△)—Ref. 32, (⧋)—Ref. 35. $T=1.4$ K: (●)—Ref. 36, (○)—Ref. 32. The dotted straight lines are linear approximations of the characteristic parts of the experimental curves.

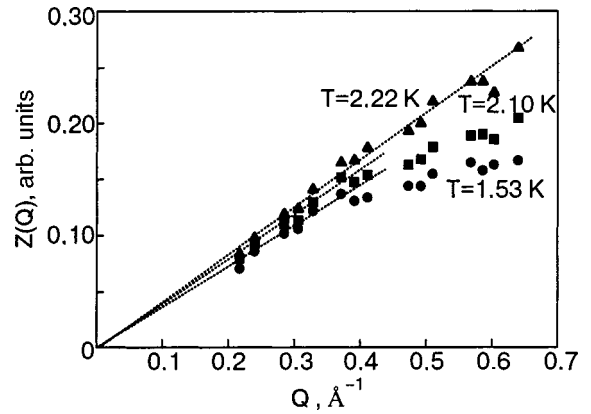

FIG. 8. Relative intensity $Z(Q)$ of the one–phonon neutron scattering as a function of the wave vector transfer Q at different temperatures in the phonon region of the dispersion curve.[20] The dotted straight lines are linear approximations.

nomenological level in his theory of the Fermi liquid.[37] These quasiparticles are actually true particles, the dispersion relation of which has been modified because of their interaction. The number of Bogolyubov quasiparticles, unlike the number of Landau quasiparticles in the theory of the normal Fermi liquid, does not coincide with the total number of particles of the liquid because of the breakdown of the phase symmetry and the presence of single-particle and pair condensates in the Bose system.

This raises the question of what type of excitations form the phonon part of the dispersion curve in ^{4}He. Are they excitations by quanta of collective coherent vibrations of the medium, or are they single-particle excitations similar to those considered by Bogolyubov?[4] The coexistence of two branches of excitations, each with its own intensity, is also possible. The set of experimental data presented above (in any case, for the main components), in particular, the temperature independence of the shape of the initial part of the curve and its insensitivity to the phase transition and the similarity of the phonon part to the picture typically seen in many other liquids, gives a definite indication that the linear part of the spectrum of ^{4}He, as Landau assumed,[1] is formed by collective acoustic vibrations, quanta of first sound in the hydrodynamic region, with a transition to zero-sound quanta with increasing energy. The possible role played by single-particle excitations analogous to Bogolyubov's is discussed below in the connection with the maxon–roton part of the dispersion curve.

3. EXCITATIONS IN THE MAXON ROTON REGION OF THE DISPERSION CURVE

Let us turn to a discussion of the maxon–roton part of the dispersion curve, which pertains to excitations with $Q > 0.7$ Å^{-1}. The properties of excitations in this part of the spectrum differ substantially from those in the phonon part.

Shape of the scattering peaks

The possibility that an additional broad component is present in the structure of the scattering peak here has been discussed in a number of papers, starting with the work of Woods and Svensson.[38] At the present time it has been established that, starting with the transition region from phonons to maxons, a single approximating function is insufficient for adequate description of the shape of the scattering peak. Experimentally this was found as a result of precise measurements of the phonon–maxon part of the dispersion curve on IN6 spectrometer in Grenoble[23] and the DIN-2PI spectrometer at Dubna.[19,20] According to those studies, at $Q > 0.37$ Å^{-1} additional intensity appears on the high-energy wing of the neutron scattering peak (see, e.g., Fig. 9), which can be interpreted as the appearance of a component due to excitations of another type. The intensity of that component is higher the closer the temperature to T_λ.

Position of the dispersion curve $\varepsilon(Q)$

As an illustration of the position of the neutron scattering peaks for the two distinguished components, the data of Ref. 20 are presented in Fig. 10. The dispersion curve of the main component is denoted by a solid line. The dispersion curve for the additional, much weaker component lies higher

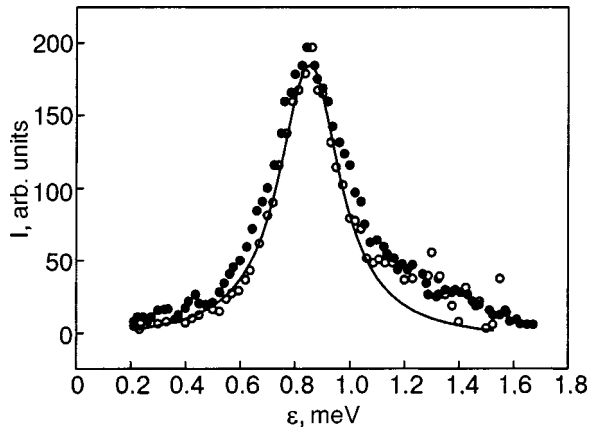

FIG. 9. Dynamic structure factor of superfluid ^{4}He near T_λ at $Q = 0.55$ Å^{-1}: (○)—data of Ref. 26, (●)—Ref. 23. The solid curve is an approximation using a "damped harmonic oscillator" function.

in energy. We note that because of the low intensity of the additional component, the parameters of the main component in respect to width, position, and intensity do not differ appreciably from those of the combined peak within the error of measurement. Therefore, for analysis of the main component below we shall simply analyze the parameters of the combined peak. Figure 11 shows the temperature dependence of the excitation energies for typical values of Q in the maxon–roton region. Unlike the phonon part, the shape and position of the maxon–roton part of the curve varies quite noticeably with temperature. With increasing temperature the excitation energy of the maxon part increases, while that of the roton part decreases, so that the maxon–roton part becomes more bendy. Figure 4 illustrates the fact that the change of the dispersion curve with increasing pressure occurs completely differently in the maxon–roton part than in the phonon part.

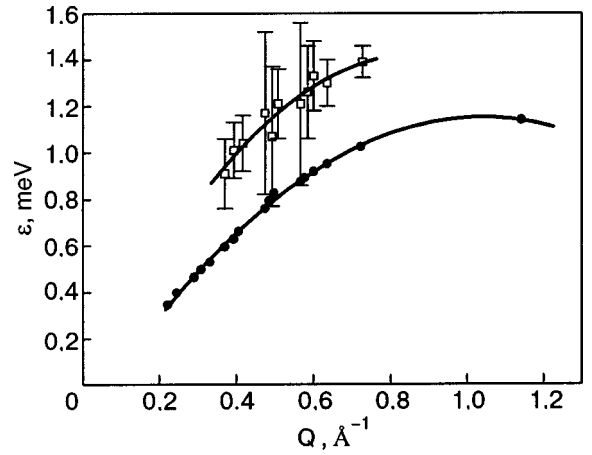

FIG. 10. Position of the dispersion curves of the main (●) and additional (□) components of the dynamic structure factor of liquid ^{4}He under saturated vapor pressure and for momentum transfers corresponding to the transition region from the phonon to the maxon parts of the dispersion curve at a temperature of 2.10 K according to the data of Ref. 20. The vertical bars on the points for the additional component correspond to the peak width 2Γ.

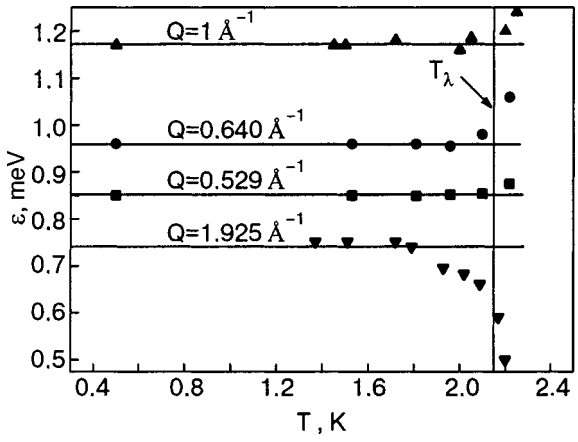

FIG. 11. Temperature dependence of the energy of excitations in liquid ^{4}He for different values of the wave vector transfer in the maxon–roton region of the dispersion curve at the saturated vapor pressure.

Width of the scattering peak

The possibility that two or more components coexist in the maxon–roton region complicates the introduction of a single intrinsic peak width. If one nevertheless considers the scattering peak to be integral and determines its FWHM formally, then one obtains the temperature curves of the peak width shown in Fig. 12. This width will to high accuracy be that of the main, narrower and more intense component. It is seen in the figure that as the temperature of the transition from the superfluid to the normal phase of liquid ^{4}He is approached, the character of the temperature dependence of the peak width in the phonon–maxon region changes and no longer corresponds to the exponential dependence obeyed at low temperature.

A very clear illustration of the different nature of the phonon and maxon–roton excitations is given by the dependence of the width of the integral peaks on the wave vector transfer (Fig. 6). This dependence is sharply different for $Q<0.7$ Å^{-1} (where 2Γ increases linearly with increasing Q) and $Q>0.7$ Å^{-1} (where 2Γ is practically independent of Q).

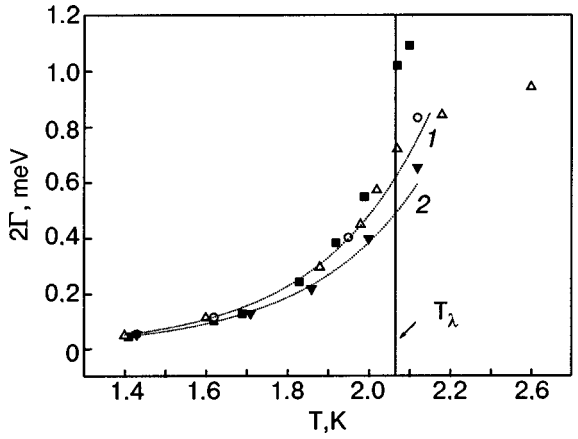

FIG. 12. Temperature dependence of the peak width (FWHM 2Γ) of the one-phonon neutron scattering in liquid ^{4}He in the maxon–roton part of the dispersion curve at the saturated vapor pressure for different values of the momentum transfer Q [Å^{-1}]: 1.925 (■—Ref. 29); 1 (○—Ref. 20), 0.6 (▼—Ref. 20), 1 (△—Ref. 23). The dotted curves are approximations by exponential relations obtained from the experimental data below $T=2$ K: $Q=1$ Å^{-1} and 1.925 Å^{-1} (*1*), $Q=0.6$ Å^{-1} (*2*).

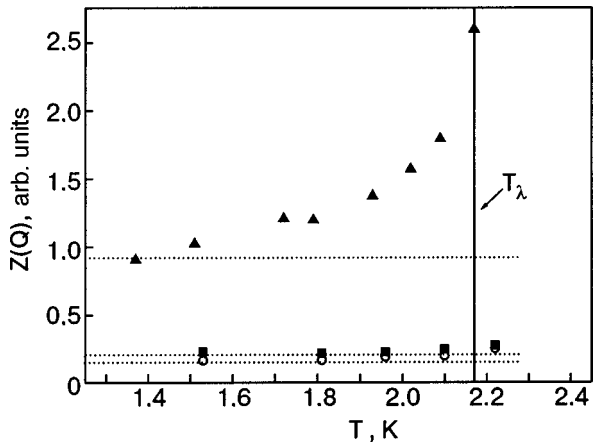

FIG. 13. Relative intensity $Z(Q)$ of the one-phonon neutron scattering of liquid ^{4}He at saturated vapor pressure as a function of temperature in the maxon–roton region of the dispersion curve for different values of the momentum transfer Q [Å^{-1}]: 0.59 (○—Ref. 20), 1.15 (■—Ref. 20), 1.925 (▲—Ref. 29).

The widths of the peaks of the weaker component are represented by the vertical bars in Fig. 10; they are much larger than the peak widths of the main component.

Relative intensity of the scattering peaks

As we have said, the intensity of the main component practically coincides with that of the central peak. The relative intensity $Z(T)$ for maxons and rotons, which varies weakly at lower temperatures, increases sharply at $T>2$ K, and the increase continues, even more rapidly, in the normal phase (Fig. 13). The $Z(Q)$ curve, as we see, differs from that in the phonon part of the spectrum (Fig. 7). The dependence of the energy of the peak on the wave vector transfer, $Z(Q)$, shown in Fig. 14, has a characteristic maximum in the roton region and is also different from $z(Q)$ for the phonon part. The intensity of the additional, broad component is much less than that of the main component (Fig. 15).

It should also be noted that the data given above on the parameters of the additional component in the maxon–roton region are taken from Ref. 20, in which the measurements

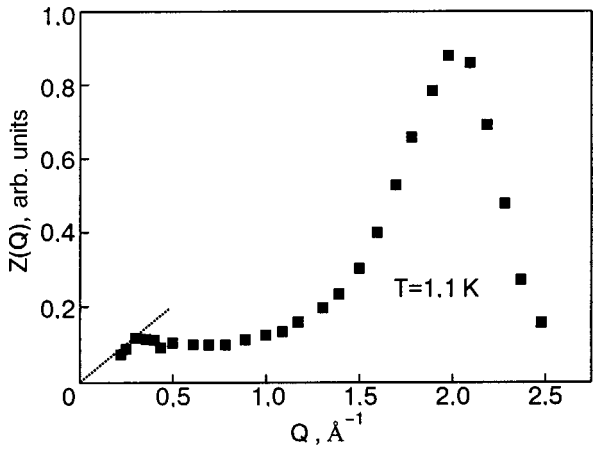

FIG. 14. Dependence of the relative intensity $Z(Q)$ of the integral neutron scattering peaks in superfluid ^{4}He at saturated vapor pressure as a function of the wave vector transfer Q (according to the data of Ref. 5). The dotted straight line is a linear interpolation of the initial part of the curve.

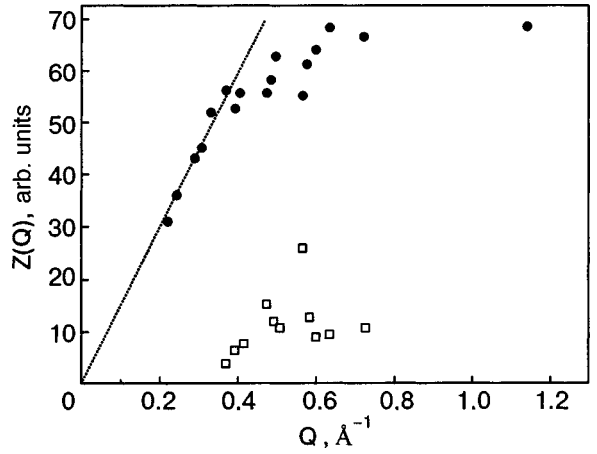

FIG. 15. Intensity $Z(Q)$ of the main (●) and additional (□) components of the one-phonon neutron scattering peak of liquid ^{4}He at saturated vapor pressure in the transition region from the phonons to maxons at a temperature of 2.1 K according to the data of Ref. 20. The dotted straight line corresponds to the linear dependence of $Z(Q)$ in the phonon part of the dispersion curve.

were made up to $Q=1$ Å^{-1}. The existence of a second component at larger values of the wave vector transfer has been noted at a qualitative level in many studies (see, e.g., Ref. 38), but it has not been reliably discriminated analytically.

4. DISCUSSION AND ANALYSIS OF THE RESULTS

Summarizing the experimental results reviewed here, we can reach the following main conclusions.

1. The whole set of data indicates the substantially different physical nature of the main component of the excitations on the phonon and maxon–roton parts of the dispersion curve of superfluid liquid ^{4}He.

2. The excitations forming the phonon part at Q from 0 to 0.37 Å^{-1} are characterized by the following features. The position of the dispersion curve $\varepsilon(Q)$ corresponds to group velocities of the excitations higher than the velocity of first sound (Fig. 3). The position of the dispersion curve is independent of temperature and is unaffected by the transition of the liquid ^{4}He from the superfluid to the normal state (Fig. 2). With increasing pressure (^{4}He density) the dispersion curve is shifted upward in excitation energy (Fig. 4). The width 2Γ of the scattering peak is a linear function of the wave vector transfer Q (Fig. 6), while the temperature dependence is described by an exponential function whose character is unchanged at the transition of the helium from the normal to the superfluid phase (Fig. 5). The intensity Z of the neutron scattering peaks depends linearly on the value of Q and is almost independent of temperature (Figs. 7 and 8). The shape of the neutron scattering peaks is described well by a single DHO function to within the accuracy of the experiments. A well-defined phonon part is characteristic not only of the superfluid phase but also exists for $T>T_\lambda$ and is also observed in many liquids, including nonquantum ones.

3. The main component of the dynamic structure factor $S(Q,\omega)$ at momentum transfers Q from 0.37 to 2.5 Å^{-1}, which pertain to the maxon–roton part of the dispersion curve, is characterized by the following properties. The position of the dispersion curve is independent of temperature at low temperatures up to 2 K, and only above 2 K does a noticeable variation of the energy position of the peaks begin (Fig. 11). In the normal phase the position of the dispersion curve differs substantially from the classical low-temperature curve (see Fig. 1). With increasing pressure the position of the dispersion curve varies in a rather complex manner: it increases in energy on the maxon part and decreases on the roton part (Fig. 4). The width 2Γ of the neutron scattering peaks is apparently independent of the wave vector transfer Q (Fig. 6). Below 2 K the temperature dependence of the width of the scattering peaks is described well by an exponential function; at higher temperatures approaching the λ transition the increase of the width with increasing temperature becomes stronger; then, after transition to the normal phase, the temperature dependence becomes much weaker (Fig. 12). The Q dependence of the intensity Z of the scattering peaks is characterized by a broad, flat minimum in the maxon region and a large maximum in the roton region (Fig. 14). The temperature dependence of the intensity is rather weak up to 2 K, but above that temperature it increases noticeably upon the transition to the normal phase (Fig. 13). The dynamic structure factor $S(Q,\omega)$ is not described by a single function of the DHO type (Fig. 9). At Q in the region from 0.37 to 0.8 Å^{-1} the authors of Ref. 20 could distinguish a second, weaker component (Figs. 10 and 15); apparently the second component exists at higher values of Q, particularly in the roton region.[38] It is important to note that the second component is reliably distinguished only at rather high temperatures (above 2 K). Sharp, well-defined neutron scattering peaks at momentum transfers corresponding to the maxon–roton part are characteristic only for the superfluid phase of ^{4}He and are not observed above the λ point nor in other liquids.

Let us analyze the experimental facts adduced above. We note that the nature of the main component of the maxon–roton excitations is essentially due to the breaking of the phase symmetry of the state and to the presence of the Bose condensate. In Ref. 10 it was conjectured that, unlike the collective phonon branch, the excitations of the maxon part have a single-particle (atomlike) nature, i.e., they are essentially individual atoms whose dispersion relations have been modified as a result of the interaction with the surrounding particles. We note that the single-particle excitations are also of a collective nature, but their ''collectivity'' differs considerably from the collective character of photon excitations, which are quanta of coherent vibrations of the many-particle system as a whole. As we have said, it was single-particle excitations that were considered by Bogolyubov in his famous paper on the theory of a slightly nonideal Bose gas.[4] The dispersion relation of Bogolyubov quasiparticles is substantially determined by the presence of a Bose condensate in the system, and it is therefore natural to identify the maxon–roton excitations with precisely these quasiparticles, which should have an analog in a strongly interacting system. The variability of the number of single-particle excitations in a superfluid Bose liquid, unlike the single-particle excitations in a normal Fermi liquid, where their number is equal to the number of particles, is due to the presence of single-particle and pair Bose condensates in the system.

If the single-particle excitations in real liquid helium are

identified with the quasiparticles considered by Bogolyubov[4] in the approximation of a slightly nonideal Bose gas, then a somewhat strange situation arises: a superposition of the linear parts of the spectra of excitations of different natures: quanta of coherent acoustic vibrations and single-particle excitations. We note that experiments have given no indication of the presence of such a superposition. It should be noted that there are no very weighty theoretical grounds for requiring that the dispersion relation of single-particle excitations have a linear acoustic character at small wave vectors. Indeed, the linear dispersion relation in Ref. 4 was obtained in the framework of a certain approximation that is a simplified version of the self-consistent field approximation. In the present paper we have taken into account the mean field produced by particles of the Bose condensate, determined as the anomalous quasi-mean $\langle a_k a_{-k}\rangle$ (a_k is the annihilation operator of a particle with momentum k), on the grounds that it is small in the case of a weak interaction. It has been shown[14] that when this particular mean field, which does not vanish for arbitrarily weak but not identically zero interaction, gives rise to a qualitatively new effect—the presence of a gap in the spectrum of single-particle excitations. This effect has a clear physical meaning—the gap determines the minimum energy that must be expended in order to tear a particle out of the Bose condensate of interacting particles and thereby create an above-condensate single-particle excitation. The value of the gap is determined by the anomalous quasi-mean $\langle a_k a_{-k}\rangle$, the particle number density n_0 of the single-particle Bose condensate, and the interatomic interaction constant U_0.

We note that the discussion of the possibility of excitations of a gap character in superfluid helium has a long history. Back in one of the early papers on the theory of the energy spectrum of the liquid, Bijl[39] came to the conclusion that an ''energy gap'' was present between the normal and all the excited states, a view that was criticized by Landau[1] on the grounds that that result would mean that low-frequency acoustic vibrations could not propagate in the liquid. We note that Landau's objection is eliminated if it is assumed that excitations with an energy gap exist together with the acoustic branch of excitations, and that is in fact what Landau had postulated in Ref. 1. In a number of papers developing upon Bogolyubov's approach[4] it was shown that, instead of a spectrum going linearly to zero, a gap appears.[40–42] Solutions with an energy gap in the self-consistent field model are discussed by Griffin[43] and were also obtained in Ref. 14. Nevertheless, in view of the apparent agreement of Bogolyubov's dispersion curve with the experimental dispersion curve in superfluid liquid helium, the ''acoustic'' character of the single-particle excitations with small momenta in Bose systems can be regarded as an established fact.[44]

Thus the arguments presented and the experimental data analyzed above suggest the following picture of the structure of the spectrum of energy excitations in liquid ^{4}He.

There are two types (modes) of elementary excitations in superfluid ^{4}He, which correspond to pronounced peaks in the dynamic structure factor for neutron scattering in different parts of the dispersion curve: a collective mode (zero sound, which goes over to first sound at very low frequencies) and a single-particle mode. The collective (zero-sound) mode, as in all liquids, is attenuated with increasing wave vector and, apparently is practically indiscernable at $Q>1$ Å^{-1}. The dispersion curve of the single-particle mode has a gap character and ''crosses'' the dispersion curve of the collective mode. At such a ''crossing'' the dispersion curves split (Fig. 16). It should be noted that a similar structure of the dispersion curve of the energy excitations in superfluid ^{4}He was discussed previously in Ref. 14 (Fig. 17). In addition, there should exist modes of pair excitations: particle–hole, two-particle, and two-hole, and modes of different multipair excitations. Those modes should be considerably weaker than the main modes in superfluid helium and may not be observed in experiment. It should be noted that the present-day level of measurement accuracy does not permit an analysis of the internal structure of the additional components of the neutron scattering. It follows from the above picture of the spectrum that two branches of excitations should exist at small values of the wave vector, i.e., in the phonon part of the dispersion curve: one with lower energy (collective) and one with higher energy (single-particle). In neutron-scattering experiments, as we have said, for $Q<0.37$ Å^{-1} only the collective, zero-sound mode is well defined. How can one account for the fact that the single-particle peak is not observed all the way to $Q=0$? We note that if at fixed Q there are several peaks corresponding to several modes of excitations, then their intensity cannot be arbitrary. In par-

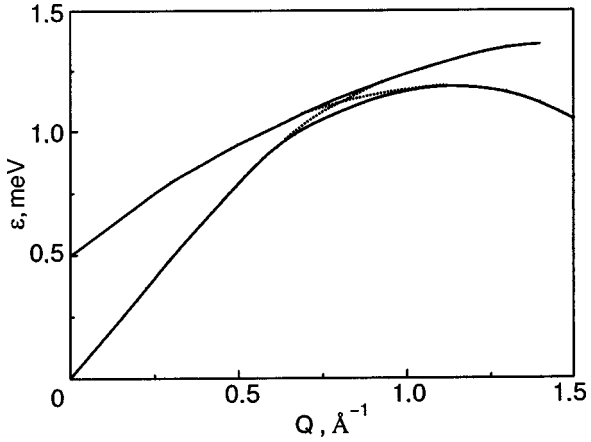

FIG. 16. Possible picture of the splitting of the dispersion curves of two modes of excitations in superfluid ^{4}He.

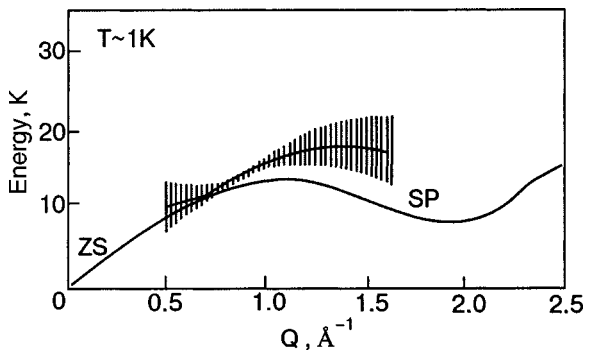

FIG. 17. Possible picture of the trend of the dispersion curves of two branches of excitations in superfluid ^{4}He (Ref. 45). The zero-sound (ZS) mode of excitations is strongly damped at $Q>1$ Å^{-1}. The single-particle (SP) mode of excitations is strongly damped for $Q<0.7$ Å^{-1}.

ticular, the intensity of any peak cannot grow while the intensity of the other peaks remains unchanged. This follows from the sum rule for the dynamic structure factor:[5]

$$\int_0^\infty d\omega\omega S(Q,\omega)=\frac{NQ^2}{2m}, \tag{1}$$

which follows from the fundamental law of conservation of the number of particles. Formula (1) shows that at fixed Q and N the area under the curve $f(\omega)=\omega S(Q,\omega)$ is constant for any many-particle systems independently of the form of the function $S(Q,\omega)$. Since the phonon peak is well defined for $Q<0.37$ Å^{-1}, it can be assumed that the main intensity is concentrated specifically in it, while the peak due to the single-particle excitations is weakly expressed and may therefore simply escape notice in experiment. Nevertheless, it is of fundamental interest to attempt to separate out the high-energy single-particle excitations in this region of the spectrum. In a certain part of the dispersion curve 0.37 Å$^{-1}<Q<0.8$ Å^{-1} the simultaneous manifestation of two modes of excitations is observed.[20] Apparently, as we have said, the additional component of the excitations is manifested experimentally also in the roton part of the dispersion curve of superfluid ^{4}He (see, e.g., Refs. 10, 29, and 38). It should be noted that the additional scattering components are reliably distinguished at relatively high temperatures of the experiment (above 2 K). This is characteristic for pair excitations created in the scattering of neutrons on preexisting thermal excitations of the system in its above-condensate part. This suggests another hypothesis: the characteristic changes in the temperature dependence of $\varepsilon(T)$, $2\Gamma(T)$, and $Z(T)$ at temperatures above 2 K near T_λ (Fig. 11–13) for the maxon–roton part of the dispersion curve may be due to the fact that the contribution of the additional scattering component was inadequately subtracted in the analysis of the parameters of the main component. This additional component distorts the parameters of the main component, and in the normal phase only it remains.

In the normal phase of liquid ^{4}He (in the absence of the Bose condensate) only excitations involving fluctuations of the density of the liquid can appear. Here evidently the zero-sound mode (the peak at $Q\leqslant 0.6$ Å^{-1}) contributes on the phonon part of the dispersion curve and pair excitations (the broad peak at $Q\geqslant 0.6$ Å^{-1}) contributes on the maxon–roton part. The single-particle excitations in the normal phase are not seen directly in neutron scattering experiments, since by virtue of conservation of particle number the creation or annihilation of an individual single-particle excitation in the normal phase is impossible.[13,14]

We have said that the well-defined mode of single-particle excitations in superfluid liquid ^{4}He in a wide region of wave vector transfers **Q** can be observed in a neutron experiment only when a macroscopic Bose condensate is present in the system. The existence of such a condensate can be regarded as reliably established experimentally. A detailed analysis of all the studies in this region, including those of the present authors, is given in a review.[46] The experiments showed that the Bose condensate appears in liquid helium immediately upon its transition to the superfluid state. With decreasing temperature the relative density of the Bose condensate increases, and at 0 K it reaches $\sim 10\%$.

In this paper we have examined the existing experimental data from the standpoint of a certain physical hypothesis concerning the formation of the spectrum of elementary energy excitations. The majority of the existing known experimental facts can be explained in the framework of that hypothesis.

The authors express their sincere gratitude to Yu. M. Poluéktov for helpful discussions of the results of this study.

This study was supported by the Government Scientific and Technical Program ''Topical problems in condensed matter physics'' in the category ''Neutron studies.''

*E-mail: puchkov@ippe.ru

[1] L. D. Landau, Zh. Eksp. Teor. Fiz. **11**, 592 (1941).
[2] V. Peshkov, J. Phys. **20**, 389 (1946).
[3] L. D. Landau, J. Phys. (Moscow) **11**, 91 (1947).
[4] N. N. Bogolyubov, Izv. Akad. Nauk SSSR Ser. Fiz. **11**, 77 (1947).
[5] D. Pines and P. Nozières, *Theory of Quantum Liquids*, Benjamin, New York (1966), Mir, Moscow (1967).
[6] H. Palevsky, K. Othes, and K. E. Larsson, Phys. Rev. **112**, 11 (1959).
[7] R. A. Cowley and A. D. B. Woods, Can. J. Phys. **49**, 177 (1971).
[8] V. G. Liforov, M. N. Nikolaev, A. G. Novikov, V. Z. Nozik, V. V. Orlov, V. A. Parfenov, V. A. Semenov, V. I. Smirnov, and V. F. Turchin, Res. Appl. Nucl. Syst., Vienna (1966), p. 196.
[9] Zh. A. Kozlov, V. A. Parfenov, and B. Sidzhimov, Preprint OIYaI R3–7519 [in Russian], JINR, Dubna (1973).
[10] H. R. Glyde and A. Griffin, Phys. Rev. Lett. **65**, 1454 (1990).
[11] H. R. Glyde, Phys. Rev. **45**, 7321 (1992).
[12] D. Pines, in *Quantum Fluids*, D. F. Brewer (ed). American Elsevier, New York (1966).
[13] Yu. M. Poluéktov and L. V. Karnatsevich, Preprint KhFTI 2001–1 [in Russian], Kharkov Institute of Physics and Technology (2001).
[14] Yu. M. Poluéktov, Fiz. Nizk. Temp. **28**, 604 (2002) [Low Temp. Phys. **28**, 429 (2002)]
[15] B. N. Esel'son, M. I. Kaganov, É. Ya. Rudavskiĭ, and I. A. Serbin, Sov. Phys. Usp. **112**, 591 (1974) [*sic*].
[16] R. Scherm, K. Gückelsberger, B. Fak, K. Skold, A. J. Dianoux, H. Godfrin, and W. G. Stirling, Phys. Rev. Lett. **59**, 217 (1987).
[17] C. Morkel, T. Bondensteiner, and H. Gemperlein, Phys. Rev. E **47**, 2575 (1993).
[18] Zh. A. Kozlov, Fiz. Élem. Chastits At. Yadra **27**, 1705 (1996) [Phys. Part. Nucl. **27**, 699 (1996)].
[19] N. M. Blagoveshchenskii, I. V. Bogoyavlenskii, L. V. Karnatsevich, A. V. Puchkov, and A. N. Skomorokhov, Fiz. Nizk. Temp. **23**, 509 (1997) [Low Temp. Phys. **23**, 374 (1997)].
[20] I. V. Bogoyavlenskii, A. V. Puchkov, and A. N. Skomorokhov, Preprint FÉI–2886 [in Russian], Institute of Physics and Power Engineering, Obninsk (2001).
[21] O. W. Dietrich, E. H. Graf, C. H. Huang, and L. Passell, Phys. Rev. A **5**, 1377 (1972).
[22] R. J. Donelly, J. A. Donelly, and R. N. Hills, J. Low Temp. Phys. **44**, 471 (1981).
[23] K. Andersen, W. G. Stirling, R. Sherm, and A. Stunault, J. Phys.: Condens. Matter **6**, 821 (1994).
[24] I. V. Bogoyavlenskii, A. V. Puchkov, and A. Skomorokhov, Physica B **284–288**, 25 (2000).
[25] N. M. Blagoveshchenskii, I. V. Bogoyavlenskii, L. V. Karnatsevich, V. G. Kolobrodov, A. V. Puchkov, and A. N. Skomorokhov, Czech. J. Phys. **46**, 253 (1996).
[26] I. V. Bogoyavlenskiĭ, L. V. Karnatsevich, Zh. A. Kozlov, V. G. Kolobrodov, V. B. Priezzhev, A. V. Puchkov, and A. N. Skomorokhov, Fiz. Nizk. Temp. **20**, 626 (1994) [Low Temp. Phys. **20**, 489 (1994)].
[27] N. M. Blagoveschenskii, I. V. Bogoyavlenskii, L. V. Karnatsevich, Zh. A. Kozlov, V. G. Kolobrodov, V. B. Priezzhev, A. N. Skomorochov, and V. S. Yarunin, Phys. Rev. B **50**, 16550 (1994).
[28] W. G. Stirling, *75th Jubilee Conference on Helium-4*, J. G. M. Armitage (ed.), World Scientific, Singapore (1983), p. 109.
[29] W. G. Stirling and H. R. Glyde, Phys. Rev. B **41**, 4224 (1990).
[30] E. C. Svensson, P. Martel, and A. D. B. Woods, Phys. Lett. A **55**, 151 (1975).

[31] I. V. Bogoyavlenskii, A. V. Puchkov, and A. Skomorokhov, Physica B **276–278**, 465 (2000).
[32] M. R. Gibbs, K. H. Andersen, W. G. Stirling, and H. Schober, J. Phys.: Condens. Matter **11**, 603 (1999).
[33] N. M. Blagoveshchenskii, I. V. Bogoyavlenskii, A. V. Puchkov, and A. N. Skomorokhov, Czech. J. Phys. **46**, 255 (1996).
[34] I. V. Bogoyavlenskii, A. V. Puchkov, A. N. Skomorokhov, and S. V. Poupko, Physica B **234–236**, 324 (1997).
[35] J. A. Tarvin and L. Passel, Phys. Rev. B **19**, 1458 (1979).
[36] F. Mezei and W. G. Stirling, *75th Jubilee Conference on Helium-4*, J. G. M. Armitage (ed.), World Scientific, Singapore (1983), p. 111.
[37] L. D. Landau, Zh. Éksp. Teor. Fiz. **30**, 1058 (1956) [Sov. Phys. JETP **3**, 920 (1956)].
[38] A. D. B. Woods and E. C. Svensson, Phys. Rev. Lett. **41**, 974 (1978).
[39] A. Bijl, Physica **7**, 869 (1940).
[40] M. Girardeau and R. Arnowitt, Phys. Rev. B **113**, 755 (1959).
[41] G. Wentzel, Phys. Rev. **120**, 1572 (1960).
[42] M. Luban, Phys. Rev. **128**, 965 (1962).
[43] A. Griffin, Phys. Rev. **53**, 9341 (1996).
[44] D. J. Thouless, *Quantum Mechanics of Many-Body Systems*, 2nd ed., Academic Press, New York (1972), Mir, Moscow (1975).
[45] E. C. Svensson and A. Griffin, Physica B **241–243**, 501 (1990).
[46] I. V. Bogoyavlenskii, L. V. Karnatsevich, Sh. A. Kozlov, and A. V. Puchkov, Fiz. Nizk. Temp. **16**, 139 (1990) [Sov. J. Low Temp. Phys. **16**, 77 (1990)].

Translated by Steve Torstveit

Impurity condensation in liquid and solid helium

E. B. Gordon*

Institute of Problems of Chemical Physics, Russian Academy of Sciences, Chernogolovka 142432, Russia
(Submitted February 23, 2004; revised April 1, 2004)
Fiz. Nizk. Temp. **30**, 1009–1018 (October 2004)

It is shown from an analysis of x-ray structural and IR spectroscopic studies that when impurity particles are introduced into liquid or solid helium, the clusters formed in the cold part of a gas jet have a pronounced spatial separation of impurities with different volatility. In particular, in the condensation of partially dissociated diatomic molecules the atoms are highly concentrated near and on the surface of the clusters. Segregation of this kind is preserved in the condensate in liquid helium, which consists of clusters stuck together into a porous structure; in solid helium clusters are isolated. The presence of high concentrations of atoms in the surface layer at the boundary with condensed helium explains the specifics of condensate behavior observed by methods of optical spectroscopy, ESR, and thermometry. An experimental strategy is developed for detecting the formation of an impurity–helium solid. [DOI: 10.1063/1.1808152]

INTRODUCTION

The unique phenomena taking place in liquid and solid helium have been observed experimentally largely owing to the unique purity of the object—the solubility of any foreign impurities in liquid helium is vanishingly small. At the same time, the interaction of a quantum liquid or quantum crystal—liquid or solid helium—with impurities that have been added is of fundamental interest. It is reasonable that such studies have been done primarily with ''natural'' impurities. For example, investigation of the behavior of the light isotope ^{3}He in liquid ^{4}He permitted H. London in 1951 to state the principle of deep cooling, which is realized in so-called dilution refrigerators, and a group of physicists from Kharkov in the 1970s to discover the quantum diffusion effect in solid helium.[1] Studying the mobility of charges in condensed helium has led to the discovery of the so-called ''bubble'' arising around an electron due to its delocalization[2] and the ''snowball,'' a concentration of helium around a heavy positive ion.[3] Recently the behavior of helium under conditions of restricted geometry has been the subject of much research interest; such conditions are realized in porous structures of the aerogel type, which can also be treated as a sort of impurity. It is of great interest to study the interaction of helium, especially ^{3}He, with surfaces, which demonstrate the structurization of the boundary layers of a quantum liquid.[4]

The diversity of phenomena observed in the interaction of condensed helium with various inclusions has stimulated attempts to introduce truly foreign microparticles into it. As a rule, the concentrations of impurities that can be introduced into helium have been extremely low, sufficient only for optical studies of allowed transitions in the atoms. An important exception is the method based on the capture of impurities into freely expanding cold helium droplets. Although the concentrations of particles that can be introduced into helium here are also small, the method of detection of the spectra, which is based on registration of the decrease in size of the droplet due to evaporation of part of the helium atoms owing to the release of the energy of the absorbed photon in it, is sufficiently sensitive for studying the spectra of molecules. At the same time, the fact that a particle trapped in a droplet cannot undergo a transition from one droplet to another prevents coalescence of the impurity and thereby ensures that the particles under study are reliably isolated. By now this method has been used to study the spectra of a large number of molecules, and interesting effects characterizing the interaction of a quantum liquid with quantum microinclusions have been observed.[5,6] The limitations of the method include the fact that the spectra are influenced by the restricted size of the droplets and, especially, the impossibility of varying the temperature and pressure.

JET METHODS OF INTRODUCING IMPURITIES INTO LIQUID HELIUM

Small concentrations of an impurity can be created in solid or liquid helium, for example, by laser ablation of a target immersed in the helium, but for the majority of the conceivable applications the impurities must be introduced into condensed helium externally, from the gas phase, and with the substance under investigation highly diluted by helium to avoid coalescence of the impurity as the gas is cooled. It should be kept in mind, however, that cooling helium, say, from 300 K to a few kelvin requires removing an energy of around 450 K per atom, while at the same time each helium atom evaporated from the liquid carries with it a maximum of 7 K. In other words, in the steady-state case the counterflow of evaporated helium must be 60 times greater than the flow directed toward the liquid helium. This means that under conditions close to uniform there cannot be any appreciable flows at all. Just such a situation existed in the first experiments, where a Dewar containing liquid nitrogen or helium was connected to a volume filled with the condensed gas;[7,8] recently the authors of Ref. 9 turned to a similar technique.[9] In such an experimental arrangement some temperature profile is established in the gas through heat conduction, and coalescence of the impurity begins at those

places where the temperature is close to the dew point. Until the clusters of impurity molecules forming there reach a certain size they are unaffected by gravity and move up and down in a nonuniform temperature field under the influence of Brownian motion and convective flows. The critical size at which the clusters begin to acquire a predominant direction of motion downward, to a region of lower temperatures, can be estimated on the basis of the Boltzmann distribution in the field of gravity:

$$N \approx \frac{kT}{mg\Delta h}, \tag{1}$$

where N is the number of molecules in the cluster, m is the mass of a molecule, and Δh is the characteristic height of the condensation region. For a substance with a molecular weight of 20 with $\Delta h = 1$ cm and a temperature $T = 200$ K we find that the number of molecules in the cluster to be $N \approx 10^6$ and the characteristic spatial dimension of the cluster to be around 30 nm. Since even after the critical size is reached the precipitation of the clusters demonstrates rather slowly, they are able to grow in size and freeze together into flakes long before reaching the region of really low temperatures, and for that reason the structure of the condensate does not depend strongly on whether the condensation takes place in liquid nitrogen or liquid helium. The rate of the gravity-controlled process of impurity precipitation in the liquid, the size of the flakes, and the density of the condensate formed all depend on the size of the precipitation region and the gas pressure but, as the experiment of Ref. 9 showed, liquid helium can be filled rather rapidly with a porous condensate similar in structure to an aerogel.

To achieve a steady gas flow toward the surface of the liquid helium, this flow and the counterflow of evaporating helium must be spatially separate. This was first realized by us in Ref. 10, where gaseous helium containing a small impurity of the particles to be studied was admitted into the cryostat through a small aperture, ensuring a high initial velocity of the jet. The existence of a directed gas jet all the way from the aperture to the superfluid helium surface located several centimeters below was proved by the presence of a rather deep, stationary dimple on the liquid surface, and the jet itself was visualized by the bright recombination radiation when an electric discharge acted on the mixture (a tip about 1 mm in diameter was brought to the surface). The temperature of the jet, measured from the structure of the rotational electronic–vibrational band of recombination radiation of molecular nitrogen, remained sufficiently high all the way to the surface of the liquid helium.[11] The formation of such a well-organized flow at extremely high gas densities was rather unexpected, and the cause of this effect should be sought in the gasdynamic features of the propagation of a ''warm'' dilute gas in cold and dense helium. Whatever the reason, this technique, the basic scheme of which is illustrated in Fig. 1a, permitted the time of the gas transport to the liquid helium surface to be shortened by many orders of magnitude. This made it possible, through the preliminary application of an rf electrical discharge to the gaseous mixture, to bring energetic labile products such as atoms, free radicals, and metastable excited particles to the surface and stabilize them in the liquid helium, i.e., it permitted the low-

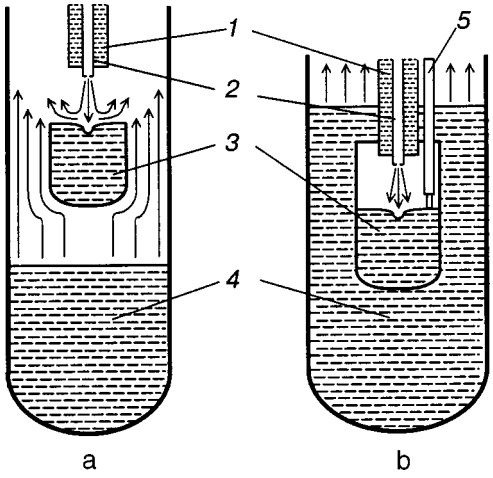

FIG. 1. Schematic diagrams of the jet techniques with open (a) and closed (b) helium cycles in the measurement cell:[13] *1*—liquid-nitrogen-cooled source with a small aperture on the bottom for forming the jet; *2*—electrodes for rf electrical discharge; *3*—cell filled with superfluid helium; *4*—main helium bath of the pumped cryostat; *5*—capillary for controlling the level of superfluid helium in the cell. The directions of the flows of gaseous helium are indicated by arrows.

temperature creation of materials with a high density of stored energy; this was the motivation for the studies mentioned. In addition, the presence of such products made it possible to employ not only visual but also other, quantitative means of investigation, such as electron spin resonance (ESR), optical spectroscopy, thermometry, etc.

It is of fundamental importance that under conditions of flow the question of the coalescence of impurity particles acquires a kinetic character—is there or is there not sufficient time for clusters of a given size to form during the flight to the surface from the place where the temperature of the particles in the flow becomes low enough for coalescence to occur. In particular, it is sufficient to take the impurity concentration so low that its molecules do not collide with each other at all during the time of flight, and the impurity reaches the helium surface in the form of individual atoms or molecules. For estimation we take the temperature and density of the helium in the jet to be such that the termolecular reaction of coalescence of impurity particles approaches its bimolecular limit, and its cross section is equal to the gaskinetic one. In that case the particles are incident on the liquid helium as isolated molecules if their concentration obeys

$$n \ll \frac{W}{\sigma v \Delta h}, \tag{2}$$

where W is the velocity of the jet, σ is the gaskinetic cross section, and v is the thermal velocity of the impurity molecules. For a jet propagating at the speed of sound, coalescence will clearly not occur at impurity concentrations much lower than 10^{15} particles/cm^3, while at lower jet velocities the admissible impurity concentrations are proportionally lower. In principle, instead of using a mixture prepared beforehand one can introduce the impurity into the helium gas jet immediately before it enters the superfluid helium, e.g., by laser ablation from a solid target, as was recently implemented in Ref. 12 in a technique analogous to that described in Ref. 10.

As we have said, the condensation of a jet in liquid helium leads to significant heat release, and in a cryostat in which the low temperature is maintained by pumping of helium vapor this requires a high-powered pump. For example, for a warm helium flow of 10^{20} atoms per second the power released in cooling it to helium temperatures (and this is the main heat release) amounts to almost 1 W, and so 0.01 mole of helium per second must be pumped out of the cryostat to maintain a steady temperature. At a temperature of 1.5 K, which corresponds to a saturated vapor pressure of helium equal to 4.7 mbar, a pumping rate of 60 liter/s is required.

Although the main counterflow of evaporating helium occurs from the main bath of the cryostat, evaporation from the superfluid-helium-filled cup is also rather intense. Therefore, the main part of the jet (approximately 60–80%) was reflected from the liquid helium surface, carried along by the ascending flow. The probability of trapping of an impurity by liquid helium is increased significantly by using a technique which we proposed recently[13] wherein the flow and counterflow of helium are physically separate (see Fig. 1b). In that case the thermal coupling of the main helium bath with the cell in which the condensation of the helium jet occurs is achieved through the thermal conductivity of the material of the walls of the cell. When electrolytic copper was used, the temperature difference of the helium bath and the superfluid helium inside the cell did not exceed 0.01 K during the condensation. The superfluid helium inside the cell served as a cryopump for the condensing jet; its level was maintained constant by removing helium through an additional capillary. Under steady-state conditions outflow through this capillary determined the flow entering the liquid helium. In this technique the ascending flow in the cell was absent altogether, and the entire jet was trapped by the liquid helium. In addition, the closed cycle for the helium used in the condensation made it possible to work with specially purified helium and even with ^{3}He. In every other way the condensation conditions were the same as for the technique with an open helium cycle.

Of course, the coalescence of an impurity can continue inside the liquid helium. The interaction of individual molecules and small clusters in a quantum liquid is one of the most interesting questions in the problem under discussion. In experiments using the jet technique extraordinarily high concentrations of stabilized atoms, a specific influence of superfluidity on the stability of the samples, and unusually long lifetimes of electronically excited metastable atoms trapped in the condensate have been observed. This has led us to the idea that a peculiar impurity–helium solid phase exists inside the helium.[14] It was assumed that it consists of individual particles or small clusters that are frozen together, each surrounded by a helium monolayer solidified owing to its localization in the van der Waals force field. Of course, such a state can only be metastable, and the calculated barrier for the process of pair coalescence of two impurity centers surrounded by a helium shell is only 28 K, which is insufficient to bring about long-term stability,[15] although in a three-dimensional lattice the barrier should be about three times as high, thus ensuring the necessary metastability. We have attempted to observe this impurity–helium phase, but, unfortunately, all of our attempts have proved futile. In particular, x-ray studies done in collaboration with co-workers at Princeton University[16] unambiguously indicated that the condensate contained impurity particle clusters having a rather regular internal structure and dimensions of around 3 nm. Recently analogous experiments were done at Cornell University using a similar method of condensation (a review of those studies was given by D. M. Lee at the Nobel Laureates Conference in 2002).[17] Those experiments reproduced many of the results which we had obtained previously, but at the same time it was found that the propagation of sound in the condensate precipitated in superfluid helium is the same as in an aerogel impregnated with liquid helium.[18]

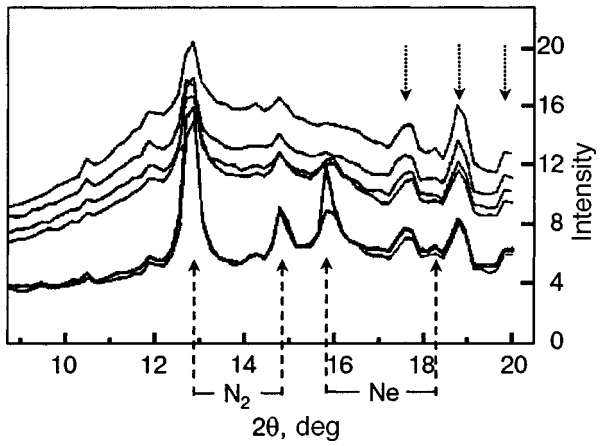

FIG. 2. Diffraction pattern of a sample obtained by condensation of an N_2:Ne:He = 1:1:200 mixture.[22] The four top curves correspond (from top to bottom) to a hold of the sample in liquid helium (4.2 K); the lower curves correspond to a dry sample at $T = 13$ K (fine line) and $T = 16$ K (heavy line). The positions of the diffraction peaks are indicated by arrows. The three arrows pointing downward indicate the positions of the peaks of the cell material beryllium. The background scattering observed is mainly due to the liquid helium.

The fact that the condensate obtained in liquid helium consists of impurity clusters was not unexpected, since the coalescence of impurity molecules could occur already in the gas phase, during their transport to the helium surface. Indeed, both in our studies and in recent investigations done by an analogous technique[16–18] the impurity concentration was at least 2–3 orders of magnitude higher than that corresponding to criterion (2). Finally, the most recent study[19] done by this same technique obtained spectroscopic proof of the formation of clusters in the lower part of the jet. And although the authors of Refs. 16–18 continued to use the term ''impurity–helium phase'' that had been introduced in Ref. 14, it is clear that we are dealing with a completely different object. It is worthwhile to clarify at the start whether impurity condensation in superfluid helium from a jet directed into it is simply a convenient way of creating an aerogel-like porous structure inside the liquid or whether the structure that is formed has specific properties. This question is one of the main topics of the present paper.

It is convenient to begin our analysis of the problem with an examination of the results obtained in the condensation of binary mixtures of impurities. Figure 2 shows the x-ray diffraction patterns of the condensate of a mixture of nitrogen and neon in helium, N_2:Ne:He = 1:1:200. This experiment was done by us in collaboration with a Princeton group at the synchrotron radiation source at Brookhaven National Labo-

ratory (USA) during the time when the work reported in Ref. 16 was being done. The spectrum of the condensate clearly shows that the two peaks of nitrogen corresponding to its cubic lattice structure are both present. Analysis of the shape of the peaks, analogous to that performed in Ref. 16, shows that under the assumption of a perfect crystal lattice they correspond to clusters containing about 10^3 molecules. In nitrogen clusters containing 0.1% neon distributed randomly such peaks should be observed for clusters consisting of 10^4 molecules, while a 1% impurity content in the clusters should suppress the diffraction altogether (at least no signs of diffraction are detected at a 10% Ne content in N_2; Ref. 20). The intensities of the peaks were close to those obtained in the condensation of pure nitrogen, which indicates that there should not be many clusters of mixed elemental composition. Thus in the condensation of mixtures containing equal amounts of nitrogen and neon, compact inclusions are formed which consist of at least 10^3 nitrogen molecules and contain less than 1% neon impurity atoms. It is hard to imagine that such a segregation by elemental composition could occur inside liquid helium, where any foreign particles stick together with a probability close to unity. Therefore, one must assume that under the conditions of our experiments either clusters of nitrogen (which is less volatile than neon) have time to grow in the gas before it reaches the temperature region where coalescence of neon begins or else a solid solution of nitrogen and neon that forms has time to decompose during cooling. In the absence of a jet, on account of repeated annealing during the Brownian motion of a cluster, phase separation is extremely probable. However, under the conditions of our experiments, since the saturated vapor pressure at which condensation begins (10 Pa) is reached at 40 and 14 K for nitrogen and neon, respectively, and the directionality of the motion of the particles inside the jet makes the kinetics of their temperature variation monotonic, this can scarcely come about. The high concentrations of stabilized atoms observed in our experiments are direct proof of phase separation during growth of the cluster—upon separation into an individual phase the atoms would undoubtedly recombine.

The x-ray scattering cross section on nitrogen molecules and neon atoms are comparable, and the total number of each in the observation zone should be equal. Nevertheless, the diffraction peaks of neon, if present at all in the spectrum of the condensate at $T=4.2$ K, are very weak. (Only on heating to $T=13-16$ K, when the mobility in neon is frozen out, do the peaks corresponding to the fcc structure of crystalline neon appear, the amplitude and width of which are close to those for nitrogen.) A natural cause of such behavior is the deposition a significant fraction of the neon on the surface of already formed nitrogen clusters during sedimentation in the gas. For equal volumes occupied by the elements, the thickness of the shell of the cluster, which determines the width of the diffraction peak from the shell material, should be (as is easily estimated) a factor of 6 smaller than the diameter of the core, which determines the width of the peak from the core material. At the same time, the formation of the first neon layers on the surface of a nitrogen cluster should begin at a higher temperature than the formation of neon clusters, since the Ne-N_2 interaction is stronger than the Ne-Ne interaction.

Similar effects were later observed[21] in the precipitation of mixtures of D_2 and N_2: in the condensate found inside liquid helium the diffraction peaks from both deuterium and nitrogen clusters were clearly observed.

Let us now analyze the consequences of the model of successive coalescence in the jet in the case when the impurity particles studied are partially dissociated diatomic molecules, such as H_2, D_2, and, primarily, N_2, as it is for their condensates that the most interesting results have been obtained, which led to the hypothesis of an impurity–helium solid. The polarizability of atoms is always much less than that of molecules made up of them, and the nitrogen atom is well modeled by a neon atom, since their polarizabilities are close. In particular, a hypothetical cluster of unrecombined N atoms should be formed approximately at the same temperatures as a cluster of Ne atoms. This means that in the condensation of nitrogen that has been partially dissociated by an rf electrical discharge, clusters consisting of molecular nitrogen form first, and then N atoms condense on their surface. The segregation effect should be just as strong as in the case of impurity neon, since the local concentration of atoms in the condensate should be determined most likely not by their content in the initial gaseous mixture but by the maximum admissible concentration in respect to the mutual recombination of stabilized atoms. This conclusion seems to us to be extremely important, and we therefore deemed it necessary to find a way of rejecting even the improbable possibility of phase segregation during the metamorphoses of the two different substances of the condensate *inside liquid helium*. For this it was necessary to suppress the motion of microparticles of the condensate in the condensed helium, i.e., to carry out the condensation in solid helium.

INTRODUCTION OF IMPURITIES IN SOLID HELIUM

In the matrix isolation technique it is standard practice to dilute the substance to be investigated with a rare gas and deposit everything as a solid on a cold substrate. However, such an approach is inapplicable for isolation in helium, simply because helium is the only substance that does not have a triple point and a region of coexistence of the gaseous and solid phases. It would seem that an even more difficult problem to overcome is that the position of the interface between the solid and liquid helium at a fixed pressure is determined by the temperature field, and nothing can be ''grown'' on it as is usually done in the growth of a sample in the common matrix isolation technique. Nevertheless, we have managed to devise a method of growing impurity-doped helium crystals.[23,24] The principle of the method is clear from Fig. 3.

A helium crystal was grown in a vertical cylindrical vessel made of sapphire which was placed in a volume of superfluid helium. The vessel is connected at the top to a high-pressure (26–30 bar) helium feed system. If helium is removed from the bottom of the vessel at a constant rate, then, since the friction of the crystal against the unwettable walls of the vessel is small compared to the forces arising even at very low pressure gradients, the crystal as a whole begins to move downward. Then on account of the helium flow into the cell from the feed system, the crystal simulta-

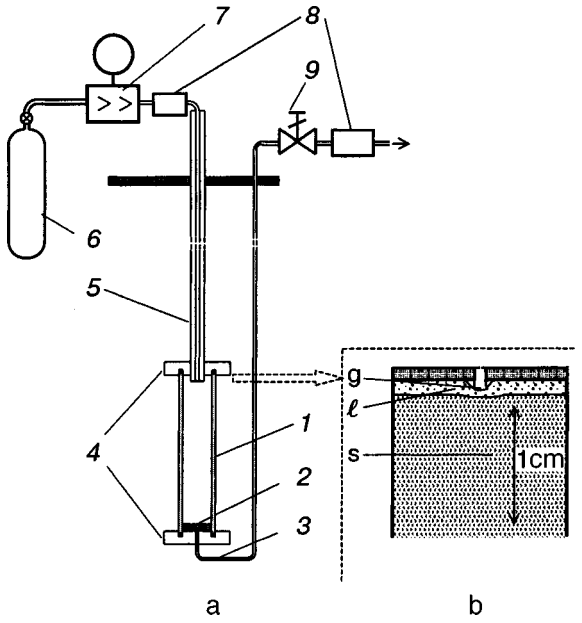

FIG. 3. Schematic diagram of the technique for introducing impurities into solid helium:[23] *1*—sapphire tube, *2*—porous filter of aluminum oxides, *3*—outlet capillary, *4*—copper flanges, *5*—inlet capillary with vacuum thermal isolation and a small aperture on the lower end, *6*—high-pressure tank, *7*—pressure regulator (reducer), *8*—flow regulators, *9*—valve. The inset b shows the typical geometry of growth of a doped helium crystal; *g* is the gas dimple, *l* is a layer of liquid (superfluid) helium, *s* is solid helium.

neously grows upward to the original position. Thus the sample remains in place, while its content is shifted downward at a rate determined by the outflow from the cell. Since the incoming flow is fed through a small aperture and a small amount of a target impurity is admixed to the helium, the high-power jet that arises rapidly conveys the impurity toward the surface of the solid.

Figure 3a shows a typical geometry of the sample growth process on an experimental apparatus created at Kyoto University in Japan.[25] By suitably choosing the experimental conditions—the pressure in the cell, the helium flow rate, and the power heating the jet-forming aperture—one can achieve stability of the position of the upper edge of the helium crystal to an accuracy of 0.2 mm for one hour. Over that amount of time a doped crystal more than 20 mm thick can be formed.

To demonstrate the segregation effect in a jet over a solid helium surface we chose conditions close to those in the experiments on impurity condensation in liquid helium. The size of the inlet aperture was such that the nominal velocity of the jet at the nozzle exit was close to the sound velocity; since the gas density was three orders of magnitude higher, the aperture diameter was chosen equal to 20 μm. While the typical degree of dilution of the impurity in the initial mixture in liquid helium experiments was 1:100, here it was 1:100000. The CO molecule was chosen as the impurity; a high-resolution FTIR spectrometer was used to register the vibrational transition ($v=0,\ J=0\rightarrow v=1,\ J=1$), which takes place in vacuum at a frequency of 2143 cm^{-1}. As we know, in solid carbon monoxide the transition in question has the form of a comparatively broad (2.5 cm^{-1}) band centered at 2140 cm^{-1}; in the case of matrix isolation of the CO molecules by neon the linewidth is around 0.1 cm^{-1}; in

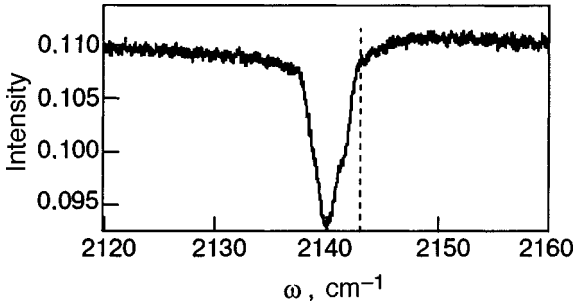

FIG. 4. Absorption spectrum of a helium crystal doped with a carbon monoxide and neon, CO:Ne=1:12.[25] The dashed line indicates the position of the most intense R_0 line in the case when CO is isolated in parahydrogen.

the case of isolation by parahydrogen the observed linewidth is less than 10^{-3} cm^{-1}, and the same width can be expected in solid helium. Figure 4 shows the spectrum of CO upon condensation in solid helium of a CO:Ne:He=1:12:80000 mixture. Since 12 Ne atoms can be placed simultaneously around the CO molecule, in the case of a random distribution of particles in the condensate a significant fraction of the CO molecules should be isolated from the other molecules by at least one layer of neon atoms. This would be sufficient to decrease the linewidth by many times in comparison with solid CO and to increase the intensity by the same factor. However, the band that was detected does not differ in any way from that registered in the condensation of a CO:He mixture and is similar in shape to the band observed in solid CO, which is known from the literature. Thus even in this case clusters of the less volatile impurity component are selectively formed during condensation. The size of the CO clusters is rather large—for the oligomers $(\mathrm{CO})_n$, $n<10$, the center of the line should be found at another frequency, and the corresponding structure should be seen on its envelope. Such an experiment, unlike the condensation of a jet in liquid helium, evidently proves that segregation by composition occurs in the clusters before the impurity enters the condensed helium.

STRUCTURE OF THE CONDENSATE

The foregoing analysis showed that the key feature of the condensate obtained in the introduction of a jet of gaseous helium containing an impurity into liquid and solid helium is the spatial separation of impurities of different natures in the clusters formed. Particularly interesting consequences are observed for a molecular impurity that is partially dissociated under the influence of an electrical discharge, for example. In that case the weakly polarizable chemically active atoms are concentrated in the peripheral regions of the cluster, and if the cluster does not consist of a very large number of molecules and if their degree of dissociation is not too high, then the atoms will be distributed near and on the surface, as is shown schematically in Fig. 5. As we have said, the concentration of atoms in that region is limited exclusively by their recombination, and that is the maximum local concentration that can be obtained by low-temperature stabilization. Indeed, the atoms are practically in direct contact with superfluid helium, and the criteria of thermal stability (against thermal and thermal-wave explosion), which were considered in Ref. 26, are always met for them.

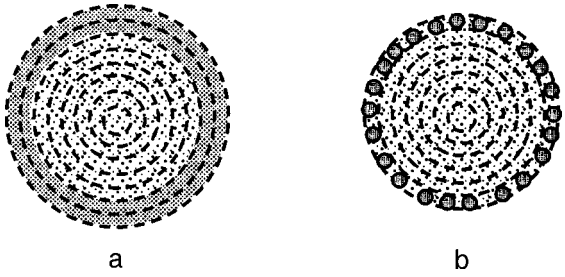

FIG. 5. Idealized structure of the clusters (grain of an impurity condensate in condensed helium) in the case of an impurity consisting of two components taken in equal amounts (a) and an impurity consisting of partially dissociated diatomic molecules (b). It is assumed that the clusters contain 1000 molecules; the layers are indicated by dashed circles.

Therefore the concentration of stabilized atoms will be determined by their thermal stability, i.e., by the lifetime with respect to recombination at a given temperature.

If in accordance with the x-ray diffraction data[16] it is assumed that clusters forming the condensate consist of 1000 molecules, then it is easy to deduce that even at a degree of dissociation of tens of percent the atoms are stabilized mainly on the surface of the cluster. They can therefore be assumed, with all the consequences of that assumption, to be physisorbed on a surface consisting of the parent molecules and immersed in superfluid helium. In particular, one should observe a specific influence of the helium environment on the optical spectra due to restructuring of the helium environment upon excitation of the atom.[27,28] It becomes clear why the spectra that we observed previously, corresponding to luminescence at the transition $^2D \rightarrow {}^4S$ of the metastable nitrogen atoms, depended on the type of heavy rare gas (Xe, Kr, Ar, and Ne) admixed in the condensate and had a shape resembling the spectra of atoms isolated in liquid and solid helium.[28] An unusually large local concentration of atoms which is independent of the degree of dissociation of the initial molecules over wide limits explains the shape of the ESR spectra of N (Ref. 30), H, and D (Ref. 31) atoms stabilized in superfluid helium. The high local concentration of nitrogen atoms realized even at high dilution of the nitrogen by heavy rare gases makes it possible for the known mechanism of thermoluminescence to appear:[7] $N+N \rightarrow N_2^*$; $N_2^* + N \rightarrow N_2 + N^*(2D)$, which we had previously rejected on the grounds of the low probability of encounter of three N atoms in the case of a random spatial distribution of atoms of different types. This can explain the superlong time of the green afterglow of the nitrogen-atom-containing condensate in liquid helium and the annealing effect.[15]

Thus despite the presence of a powerful gas jet directed toward the surface of condensed helium, the coalescence of an impurity contained in it occurs practically at dew temperature, but at the same time, as experiments show, the rate of cooling is high enough to prevent recombination of the atoms trapped in the condensate before they reach the liquid helium. The analysis carried out allows one to narrow down exactly what is the object being studied in the optical, ESR, x-ray diffraction, etc. detection of the condensate obtained in liquid and solid helium. With this key one can reinterpret the numerous data that have been accumulated over many years in studies of the condensation of impurities in superfluid helium and of the impurity–helium solids.

The question of the existence of an impurity–helium solid phase as originally understood[14] merits particular attention. Although physical arguments about the metastability of a structure consisting of frozen-together solid helium clusters arising around heavy microimpurities in helium are completely reasonable, the degree of this metastability is unclear. At the same time, none of the experiments known to us has been set up in such a way that this phase can be formed. The observation of the sticking together of two SF_6 molecules inside a cold liquid helium drop[32] does not lend optimism. However, the experimental techniques that have now been developed permit one to propose a strategy for searching for such a phase. The simplest would be to use the technique of introducing impurities into solid helium[23,24] after conditions for stabilization of individual molecules in it have been achieved. For this, one should work with impurity concentrations ensuring the absence of binary collisions of impurity molecules during their transport in the jet to the surface of the condensed helium and their subsequent motion through the layer of liquid helium to the surface of the crystal. After that it would be necessary to the melt the helium by lowering the pressure by, say, 1 bar and then raising it again to the value necessary for secondary solidification. A typical effective pressure exerted by the impurity on the first helium shell is hundreds of bar, while at the same time, for the second layer of helium atoms this pressure is only a few bar.[27] This means that if the external pressure is close to the pressure of solidification of helium, then not one but two or more layers will be found around the impurity in the solid state. The impurity–helium solid phase obtained by the method just described should have a higher stability against the pairwise sticking together of impurity particles, since they are separated by large distances in it (four or more layers of helium). We tested this procedure during completion of the work reported in Ref. 33. The main complications—the choice of an adequate method for tracking the state of the impurity molecules with a sensitivity of 10^{12} molecules/cm^3 or better as well as purification of the high-pressure helium to 1 ppb (10^{-7}%) are in principle solvable.

By the way, in Ref. 19 it was concluded, on the basis of a comparison of the kinetic energy of a particle entering the liquid helium with the work against the forces of surface tension in the creation of a bubble inside the liquid, that the embedding of individual molecules from the jet into the liquid is practically impossible. However, the nitrogen molecules and atoms considered in Ref. 19, like the majority of other particles, form structures of attraction (''snowballs'') around themselves in liquid helium; in these structures the attraction of the helium shell to the impurity is compensated by the mutual repulsion of the He atoms in the shell.[27,28] Such a character of the interaction with the environment is also indicated directly by the form of the calculated helium density profile[19] around the N atoms and clusters of molecular nitrogen, which demonstrates compressing of the helium around the impurity. Therefore, even in the framework of the crude approximation used, in the co-condensation of helium and an impurity there should be a *release* of energy rather than an *expenditure*, and, in contrast to the conclusion of the

authors of Ref. 19 there should not exist any restrictions on the velocity of the particle for its absorption inside the liquid. In general, a direct answer to the question of the existence of energy barriers to the entry of an impurity into the medium is given by the value of the chemical potential of the corresponding particle in the medium—for nitrogen atoms in liquid helium, for example, it is 300 K lower than in vacuum.[27]

The low-temperature chemical reactions in isolated clusters of reactants under conditions of their initiation by active particles trapped in clusters have a number of attractive features.[34] The fact that in the condensation of atom-containing mixtures in liquid and solid helium these atoms are stabilized on the surface of the clusters—grains of the condensate—makes this substance still more interesting for use in low-temperature chemistry.

This study was done with the support of the Russian Foundation for Basic Research, Grant No. 04-03-32684.

*E-mail: gordon@binep.ac.ru

[1] V. N. Grigor'ev, B. N. Esel'son, and V. A. Mikheev, Zh. Éksp. Teor. Fiz. **64**, 608 (1973) [Sov. Phys. JETP **37**, 309 (1973)]; Zh. Éksp. Teor. Fiz. **66**, 321 (1974) [Sov. Phys. JETP **39**, 153 (1974)]; Fiz. Nizk. Temp. **1**, 5 (1975) [Sov. J. Low Temp. Phys. **1**, 1 (1975)].
[2] J. Jortner, N. R. Kestner, M. H. Cohen, and S. A. Rice, J. Chem. Phys. **43**, 2614 (1965).
[3] M. W. Cole and R. A. Bachman, Phys. Rev. B **15**, 1388 (1977).
[4] H. Franco, R. E. Rapp, and H. Godfrin, Phys. Rev. Lett. **57**, 1161 (1986).
[5] J. P. Toennies and A. F. Vilesov, Annu. Rev. Phys. Chem. **49**, 1 (1998).
[6] S. Grebenev, J. P. Toennies, and A. F. Vilesov, Science **279**, 2083 (1998).
[7] A. M. Bass and H. P. Broida, *Formation and Trapping of Free Radicals*, Academic Press, New York (1960).
[8] P. Savich and A. Shalnikov, J. Phys. USSR **10**, 299 (1946).
[9] A. M. Kokotin and L. P. Mezhov-Deglin, Fiz. Nizk. Temp. **28**, 235 (2002) [Low Temp. Phys. **28**, 165 (2002)].
[10] E. B. Gordon, L. P. Mezhov-Deglin, and O. F. Pugachev, JETP Lett. **19**, 63 (1974).
[11] E. B. Gordon, L. P. Mezhov-Deglin, O. F. Pugachev, and V. V. Khmelenko, Chem. Phys. Lett. **54**, 282 (1978).
[12] V. Ghazarian, J. Eloranta, and V. A. Apkarian, Rev. Sci. Instrum. **73**, 3606 (2002).
[13] R. E. Boltnev, G. Frossati, E. B. Gordon, I. N. Krushinskaya, E. A. Popov, and A. Usenko J. Low Temp. Phys. **127**, 245 (2002).
[14] E. B. Gordon, V. V. Khmelenko, A. A. Pelmenev, E. A. Popov, and O. F. Pugachev, Chem. Phys. Lett. **155**, 301 (1989).
[15] E. B. Gordon, V. V. Khmelenko, A. A. Pelmenev, E. A. Popov, O. F. Pugachev, and A. F. Shestakov, Chem. Phys. **170**, 411 (1993).
[16] V. Kirykhin, B. Keimer, R. E. Boltnev, V. V. Khmelenko, and E. B. Gordon, Phys. Rev. Lett. **79**, 1774 (1997).
[17] V. V. Khmelenko, S. I. Kiselev, D. M. Lee, and C. Y. Lee, Phys. Scr. **102**, 118 (2002).
[18] S. I. Kiselev, V. V. Khmelenko, and D. M. Lee, Fiz. Nizk. Temp. **26**, 874 (2000) [Low Temp. Phys. **26**, 641 (2000)].
[19] E. A. Popov, J. Eloranta, J. Ahokas, and H. Kunttu, Fiz. Nizk. Temp. **29**, 684 (2003) [Low Temp. Phys. **29**, 510 (2003)].
[20] A. E. Curzon and M. E. Estell, J. Phys. C: Solid State Phys. **4**, 689 (1971).
[21] S. I. Kiselev, V. V. Khmelenko, D. M. Lee, V. Kiryukhin, R. E. Boltnev, E. B. Gordon, and B. Keimer, Phys. Rev. B **65**, 024517 (2002).
[22] V. Kirykhin, B. Keimer, R. E. Boltnev, V. V. Khmelenko, and E. B. Gordon, unpublished results.
[23] E. B. Gordon, A. Usenko, and G. Frossati, J. Low Temp. Phys. **130**, 15 (2003).
[24] E. B. Gordon, G. Frossati, A. Usenko, Ya. Aratono, and T. Kumada, Physica B **329–333**, 404 (2003).
[25] E. B. Gordon, T. Momose, and N. Nakashima, to be published.
[26] E. B. Gordon, L. P. Mezhov-Deglin, O. F. Pugachev, and V. V. Khmelenko, Zh. Éksp. Teor. Fiz., **73**, 952 (1977) [Sov. Phys. JETP **46**, 502 (1977)].
[27] E. B. Gordon and A. F. Shestakov, Fiz. Nizk. Temp., **26**, 5 (2000) [Low Temp. Phys. **26**, 1 (2000)].
[28] E. B. Gordon and A. F. Shestakov, Khim. Fiz. **21**, 16 (2002).
[29] R. E. Boltnev, E. B. Gordon, V. V. Khmelenko, A. A. Pelmenev, M. V. Martynenko, E. A. Popov, and A. F. Shestakov, J. Chem. Phys. **92**, 362 (1995).
[30] E. B. Gordon, A. A. Pel'menev, O. F. Pugachev, and V. V. Khmelenko, Fiz. Nizk. Temp. **8**, 691 (1982) [Sov. J. Low Temp. Phys. **8**, 299 (1982)].
[31] E. B. Gordon, A. A. Pel'menev, O. F. Pugachev, and V. V. Khmelenko, Fiz. Nizk. Temp. **11**, 563 (1985) [Sov. J. Low Temp. Phys. **11**, 307 (1985)].
[32] J. Harms, M. Hartmann, B. Sartakov, J. P. Toennies, and A. F. Vilesov, J. Chem. Phys. **110**, 5124 (1999).
[33] E. B. Gordon, T. Kumada, M. Ishiguro, and Y. Aratono, submitted to J. Chem. Phys. , (2004).
[34] E. B. Gordon, Doklady Ross. Akad. Nauk **378**, 650 (2001).

Translated by Steve Torstveit

Relaxation and dissipative processes in the phonon–impuriton system of concentrated superfluid mixtures of ^{3}He in ^{4}He

A. A. Zadorozhko,* T. V. Kal'ko, É. Ya. Rudavskiĭ, V. K. Chagovets, and G. A. Sheshin

B. Verkin Institute for Low Temperature Physics and Engineering, National Academy of Sciences of Ukraine, pr. Lenina 47, Kharkov 61103, Ukraine

K. E. Nemchenko

V. N. Karazin Kharkov National University, pl. Svobody 4, Kharkov 61022, Ukraine

(Submitted February 27, 2004)
Fiz. Nizk. Temp. **30**, 1019–1027 (October 2004)

The effective thermal conductivity of superfluid mixtures of ^{3}He in ^{4}He with an initial concentration of 9.8% ^{3}He is investigated in the temperature interval 70–500 mK. The results, together with previously available experimental data on the thermal conductivity, viscosity, and mass and spin diffusion, are analyzed in the framework of the kinetic theory of the phonon–impuriton system of superfluid mixtures. It is shown that the experimental results for all the kinetic coefficients can be described from a unified viewpoint if the corresponding impuriton–impuriton scattering times are used as adjustable parameters. The role of each relaxation process in the complex hierarchy of relaxation times is determined as a function of temperature and concentration. It is found that even in concentrated mixtures a substantial contribution to the establishment of equilibrium is made by three-phonon processes. The phonon–impuriton relaxation times are calculated by integrating over the phonon energy in the entire region where such processes are allowed.
[DOI: 10.1063/1.1808153]

1. INTRODUCTION

Kinetic processes in ^{3}He–^{4}He superfluid mixtures are governed by the interaction of elementary excitations—phonons, rotons, and ^{3}He impurity excitations (impuritons). These interactions were first considered by Khalatnikov and Zharkov,[1] who calculated the corresponding relaxation times and the main kinetic coefficients of ^{3}He–^{4}He mixtures: the thermal conductivity, diffusion, and viscosity. The appearance of experimental data on the absorption of first sound at low temperatures[2,3] stimulated further development of the theory. Baym, Saam, and Ebner used those data in constructing a detailed kinetic theory of ^{3}He–^{4}He superfluid mixtures at temperatures below 0.6 K, when the roton contribution can be neglected. The theory[4–6] gave a quantitative explanation of the acoustic experiments[2,3] done with mixtures of ^{3}He in ^{4}He with a molar concentration $x \sim 5\%$ ^{3}He. Subsequent experimental studies of the kinetic processes in more dilute mixtures of ^{3}He in ^{4}He showed a noticeable difference between experiment and theory, this difference growing with decreasing concentration of the mixtures.

Further progress in the understanding of relaxation processes in dilute ^{3}He–^{4}He superfluid mixtures was achieved following precision measurements[7] of the relative change of the velocity of first sound in dilute mixtures of ^{3}He in ^{4}He, which stimulated further development of the kinetic theory by Adamenko and Tsyganok.[8,9] It was shown that the presence of anomalous dispersion in the phonon spectrum substantially alters the phonon–impuriton relaxation in the mixtures and leads to a new two-step mechanism of phonon relaxation in the presence of ^{3}He quasiparticles.[10] The results of various kinetic experiments were analyzed from the standpoint of the understanding that had been achieved, and a complex hierarchy of relaxation times was established (see the review[11]).

In the 1980s the kinetics of the phonon–impuriton system[11] was investigated only in only dilute mixtures of ^{3}He in ^{4}He. Since the concentration of the mixture substantially determines practically all the relaxation times, one can expect noticeable changes in the kinetic behavior of the mixtures as the concentration is increased. A feature specific to concentrated mixtures is the higher Fermi degeneracy temperature of the gas of impuritons. The temperature region investigated in experiments often lies in the intermediate region between the quantum and classical limits, where there are no analytical expressions for the relaxation times. In concentrated superfluid mixtures at low temperatures a first-order phase transition—phase separation—occurs, whereupon the concentration of the dilute phase changes with changing temperature.

Recently the kinetic properties of concentrated mixtures of ^{3}He in ^{4}He have been studied experimentally with steady-state heat fluxes of different strength acting on the system.[12,13] This made it possible to obtain information about the relaxation of the temperature and concentration of the mixtures, to determine the boundary at which the thermal convective instability begins, and to measure the effective thermal conductivity. In the present study we continue our experimental research on the effective thermal conductivity, focusing our attention mainly on the interpretation of the results in the framework of the modern kinetic theory of the phonon–impuriton system of ^{3}He–^{4}He superfluid mixtures.

We analyze the temperature dependence of the other kinetic coefficients—the viscosity and mass and spin diffusion, and also the characteristic relaxation times governing the respective processes.

2. CHARACTERISTIC RELAXATION TIME IN THE PHONON–IMPURITON SYSTEM OF THE MIXTURES

Establishment of equilibrium in the impuriton subsystem of the mixtures occurs on account of the scattering of ^{3}He quasiparticles on each other. The characteristic impuriton–impuriton relaxation time for the nondegenerate region is usually written in the form (see Ref. 11)

$$\tau_{33}=\frac{A}{xT^n}, \tag{1}$$

where x is the molar concentration of ^{3}He in the mixture, the constant A is determined from the corresponding experimental data, and the exponent lies in the range $0.5\leqslant n\leqslant 1$.

For the degenerate region the impuriton relaxation time was determined in Ref. 4:

$$\tau_{33}=\frac{\alpha}{T^2}\left[1+\beta\left(\frac{T}{T_F}\right)^2\right], \tag{2}$$

where T_F is the Fermi degeneracy temperature, and the concentration-dependent parameters α and β are fit from a comparison with the acoustic data.[2,3]

We note that formulas (1) and (2) express the relaxation time in the impuriton subsystem, which determines the shear viscosity of the mixture and, as a consequence, the viscous absorption of first sound. We denote this time by $\tau_{33\eta}$; it characterizes the process of impuriton scattering on an impuriton, accompanied by momentum changing.

In the phonon subsystem the establishment of equilibrium occurs in a more complex way. Since the phonon spectrum has decay instability in the initial region at not too high a total pressure, three-phonon processes are allowed. This leads to the rapid establishment of equilibrium along a chosen direction (longitudinal relaxation).[11] In the subsystem of thermal phonons with average velocity $\overline{\varepsilon}=3k_BT$ the longitudinal relaxation time is equal to

$$\tau_{\parallel}=2.6\cdot 10^{-10}T^{-5}[\mathrm{s}]. \tag{3}$$

Total equilibrium in the phonon subsystem of pure ^{4}He is determined by the transverse phonon relaxation with a characteristic time $\tau_{\perp}$ that is always much greater than $\tau_{\parallel}$. In ^{3}He–^{4}He superfluid mixtures, the processes of interaction of phonons with impuritons play an important role in the establishment of total equilibrium. As was shown in Ref. 10, under such conditions a two-step relaxation mechanism is realized: the energetic phonons on account of Rayleigh scattering relax toward the impuritons, and all the remaining phonons, over a time $\tau_{\parallel}$, relax toward the energetic phonons. The resultant phonon–impuriton relaxation time is

$$\tau_{\mathrm{ph3}}=\frac{\int\tilde{t}(\tilde{t}+\tau_{\parallel})^{-1}n'y^4dy}{\int(\tilde{t}+\tau_{\parallel})^{-1}n'y^4dy}, \tag{4}$$

where $y=\varepsilon/k_B$ is the phonon energy in kelvin,

$$n'=\frac{d}{d\varepsilon}\left(\left[\exp\left(\frac{\varepsilon}{k_BT}\right)-1\right]^{-1}\right)$$

is the derivative of the Bose–Einstein energy distribution function for the phonons;

$$\tilde{t}=(t_{\mathrm{abs}}^{-1}+t_{\mathrm{sc}}^{-1})^{-1} \tag{5}$$

is a combination of the scattering time t_{sc} for phonons on ^{3}He quasiparticles and the absorption time t_{abs} of phonons by impuritons.

The times $(t_{\mathrm{sc}})_l$ for the scattering of phonons by impuritons were determined in Ref. 4 as a function of the phonon momentum p and the scattering angle. Here it was found that the relaxation times are proportional to p^{-4}; this corresponds to Rayleigh scattering of the long-wavelength ''light'' phonon on the ''heavy'' ^{3}He point quasiparticle:

$$(t_{\mathrm{sc}})_l=\frac{a_ln_4}{xcp^4}, \quad l=1,2,..., \tag{6}$$

where c is the velocity of first sound in ^{4}He, n_4 is the number of ^{4}He atoms per unit volume, and the values of the constants a_l are given in Ref. 11. They correspond to the lth-order terms in the expansion of the phonon-impuriton collision integral in Legendre polynomials. Here $l=1$ corresponds to the transport of a change in the density of phonons, which characterizes heat conduction, and also the transport of quasiparticles, which characterizes mass and spin diffusion. The polynomial with $l=2$ corresponds to momentum changing of the system and causes shear viscosity. The relaxation times with $l\geqslant 3$ do not correspond to any fixed dissipative coefficient in the hydrodynamic regime but are responsible for relaxation in the phonon–impuriton system in the kinetic and transition regimes.

Processes of phonon absorption and emission by impuritons are taken into account in (4) because in the integral of (6) over momenta a divergence arises at the lower limit. This is due to the rapid growth of the phonon mean free path with decreasing momentum (by a p^{-4} law). The absorption and emission of phonons by ^{3}He quasiparticles limits the mean free path of the long-wavelength phonons, and the corresponding time t_{abs} has the form

$$t_{\mathrm{abs}}=\frac{4}{3}\frac{P_3}{\rho_4}\lambda_i^2\rho^2\tau_{33\eta}\frac{1+\left(\frac{cp}{2\pi k_BT}\right)^2}{1+\left(\frac{cp}{2\pi k_BT}\right)^2+\left(\frac{cp}{\hbar}\tau_{33\eta}\right)^2}, \tag{7}$$

where P_3 is the osmotic pressure of the gas of impuritons; $\rho_4=m_4n_4$ is the ^{4}He density (m_4 is the mass of the ^{4}He atom); λ_i is a parameter of the mixture, determined by the energy and effective mass of the ^{3}He quasiparticles; $\tau_{33\eta}$ is the viscous relaxation time of the impuritons, which governs the absorption of first sound in the mixture and the shear viscosity. The hierarchy of relaxation times (1)–(7) is given in Ref. 11. Here the absorption relaxation time is the characteristic time of the net difference of absorption and emission processes.

3. EFFECTIVE THERMAL CONDUCTIVITY

3.1. Features of the technique and the experimental results

For measurement of the thermal conductivity the method of a steady heat flux emitted by a flat heater placed in the lower part of a cylindrical measurement cell is used. The layout of the measurement cell, which was 2.4 cm in diameter and 4.7 cm high and had thin stainless steel walls, is described in detail in Ref. 12. The establishment of a steady-state temperature distribution is established after the heat flux is turned on is registered by two identical resistance thermometers. The measurements were made in two series of experiments with different distances between thermometers: 10 and 27 mm. The upper part of the cell had a clamped-on thermal contact with a cold source—the platform of a dilution refrigerator, the temperature of which was measured by a ^{3}He melting curve thermometer.

A mixture with an initial concentration of 9.8% ^{3}He was investigated in the temperature region 70–500 mK. Below a temperature of 235 mK in the absence of the heat flux the mixture was separated into a lower, superfluid phase and an upper, normal phase with a concentration close to pure ^{3}He. In this case both thermometers are found in the lower, superfluid phase. In the presence of a heat flux the ^{3}He atoms move to the colder upper part of the cell, their concentration in that part grows, and, according to the phase diagram, separation sets in at a higher temperature. Measurements were made at a constant temperature of the platform of the dilution refrigerator and upper flange of the cell and at different values of the heating power. Special attention was paid to ensuring the absence of convective phenomena, i.e., it was verified that a linear dependence existed between the value of the applied heat flux density $\dot{Q}$ and the temperature gradient ∇T that appeared:

$$\dot{Q}=k_{\text{eff}}\nabla T. \tag{8}$$

The coefficient of proportionality k_{eff} in (8) is the effective thermal conductivity of the mixture. The temperature dependence of k_{eff} obtained in the experiment is presented in Fig. 1, where for comparison the results of measurements of the effective thermal conductivity made at higher temperatures (above $\sim$0.65 K)[14] are also shown. It is seen in Fig. 1 that the data of the present study are in good agreement with the results of Ref. 14.

Since in ^{3}He–^{4}He superfluid mixtures in the presence of a heat flux both a temperature gradient and a concentration arise simultaneously, heat is transported both by the diffusion of phonons and by the true heat conduction of ^{3}He quasiparticles; this, according to Ref. 1, is described by an effective thermal conductivity. The existence of an effective thermal conductivity that is determined both by the ordinary dissipative heat conduction and also by mass diffusion and thermodiffusion of impurities is a unique feature of ^{3}He–^{4}He superfluid mixtures.

3.2. Comparison with theory

The total thermal conductivity of the phonon–impuriton system of ^{3}He–^{4}He superfluid mixtures can be written in the form of a sum of the impuriton part and a part due to the diffusion of phonons:[15]

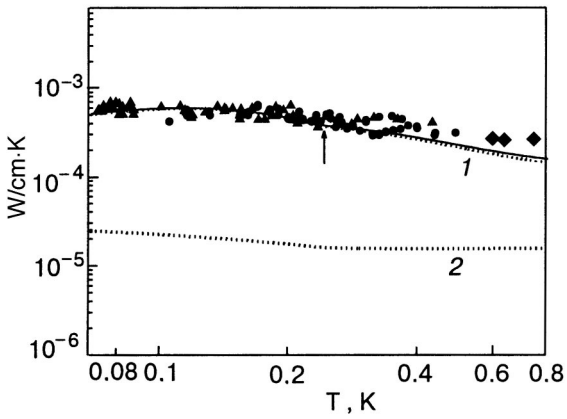

FIG. 1. Temperature dependence of the effective thermal conductivity of a ^{3}He–^{4}He mixture with an initial concentration of 9.8% ^{3}He. The arrow indicates the phase separation temperature. The data of the present study for two distances between thermometers [mm]: 10 (●) and 27 (▲); the data of Ref. 14 (♦). The solid curve is a calculation according to formulas (9)–(11). The dotted curves *1* and *2* are, respectively, the phonon and impuriton contribution to the effective thermal conductivity.

$$k_{\text{eff}}=k_3+k_D=k_3+D_m\frac{u_{2\varepsilon}^2}{u_2^2}C_V\left(1-\frac{k_T}{k_T^*}\right)^2, \tag{9}$$

where $C_V=C_3+C_4$ is the heat capacity per unit volume of the mixture, written as the sum of the heat capacities of the impuriton gas and thermal excitations, $k_T=D_m/D_T$ is the thermodiffusion ratio of the mixture, D_m and D_T, which were introduced in Ref. 1, are the coefficients of mass diffusion and thermodiffusion at constant temperature and concentration, u_2 is the speed of second sound, $u_{2\varepsilon}^2=\overline{S^2}T/C_V\rho_n$, $\overline{S}=S_3-(\partial S_3/\partial n_3)_T n_3$ is a parameter of the impuriton subsystem which depends on the entropy S_3 of the impuriton gas and the number of impuritons per unit volume n_3, $\rho_n=\rho_3+\rho_{nt}$ is the total normal density of the mixture, ρ_{nt} is the density of the normal component of the thermal excitations of the mixture;

$$k_T^*=-T\frac{\nabla x}{\nabla T}=\left(\frac{(\partial P_3/\partial T)_{xP}}{(\partial P_3/\partial x)_{TP}}\right)$$

is a parameter relating the concentration gradient and temperature gradient.

The thermal conductivity k_D due to phonon diffusion and the true thermal conductivity k_3 of the impuriton gas in formula (9) can be written in the gaskinetic approximation in the form

$$k_D=\frac{1}{3}C_{\text{ph}}c^2\tau_{\text{ph3}}, \tag{10}$$

$$k_3=\frac{1}{3}C_3v_3^2\tau_{33k}, \tag{11}$$

where $v_3=[(3/2m_3^*)(\partial P_3/\partial n_3)]^{1/2}$ is the average velocity of the impuritons[8] (m_3^* is the effective mass of the impuritons).

In this study we have calculated the effective thermal conductivity k_{eff} with the use of Eqs. (9)–(11). The relaxation time τ_{ph3} that appears in Eq. (10) was determined by formulas (4)–(7), and the time $\tau_{33\eta}$ in Eq. (7) was found from independent experimental data on the shear viscosity (see Sec. 5). We note that in contrast to Refs. 4 and 5, where

TABLE I. Dependence of the parameter a, which determines the time τ_{33k}, on the ^{3}He concentration.

x%^{3}He	1.3	5.0	9.8
a, K·s	7.2×10^{-12}	7.8×10^{-12}	9×10^{-12}

the relaxation time was calculated for thermal phonons of the average energy $\overline{\varepsilon}_{\rm ph}=3k_BT$, the time $\tau_{\rm ph3}$ was determined by integration over energies from 0 to the value 10 K at which the phonon spectrum becomes nondecaying.

Since the conditions of the experiment correspond to the intermediate region between degenerate and nondegenerate states, for which no analytical expression for τ_{33k} has been obtained, here we used the following empirical expression:

$$\tau_{33k}=\frac{a}{xT}, \tag{12}$$

where the constant a played the role of a fitting parameter and was determined from the experimental data. Analysis showed that good agreement with the experimental values of the effective thermal conductivity (Fig. 1) is achieved in the whole temperature region for $a=9\times10^{-12}$ K·s. An analogous approach has also been taken for the results of experiments[19] in which the effective thermal conductivity of weaker mixtures of ^{3}He in ^{4}He was measured. The parameter a in formula (12) depends weakly on concentration (see Table I) and is independent of temperature.

Calculations showed that the main contribution to the effective thermal conductivity of the mixture comes from the phonon part (the dotted line *1* in Fig. 1). The corresponding values of the time τ_{33k} which determine the thermal conductivity of the gas of impuritons and the other characteristic relaxation times are presented in Fig. 2. As we see from the curves, the impuriton–impuriton scattering process is the fastest process in the hierarchy shown, and that means that equilibrium is established more rapidly in the impuriton subsystem than in the phonon subsystem.

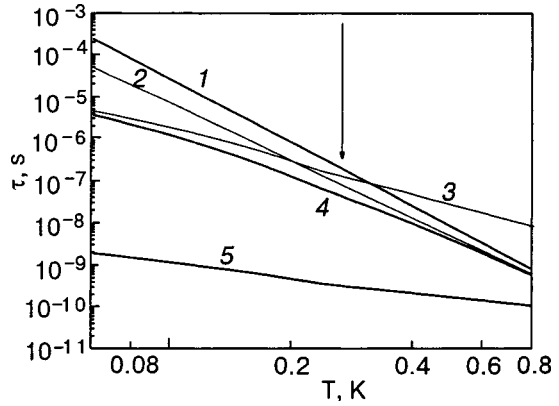

FIG. 2. Characteristic times of the different relaxation processes in the phonon–impuriton system as functions of temperature for a mixture with an initial concentration of 9.8% ^{3}He: the longitudinal phonon relaxation time $\tau_{\parallel}$ (*1*); the Rayleigh scattering time $\tau_{\rm sc}$ for phonons on impuritons (*2*); the time $\tau_{\rm abs}$ associated with the absorption (emission) of phonons by impuritons (*3*); the total phonon–impuriton relaxation time $\tau_{\rm ph3}$ (*4*); the impuriton–impuriton relaxation time τ_{33k}, which determines the effective thermal conductivity of the gas of impuritons (*5*).

Analysis of the behavior of the resultant relaxation time $\tau_{\rm ph3}$ in the phonon–impuriton system showed that at high temperatures the main process is the scattering of phonons on impuritons, with a characteristic time $\tau_{\rm sc}$. The longitudinal relaxation time $\tau_{\parallel}$ in the phonon subsystem at high temperatures is close to $\tau_{\rm sc}$, and its contribution increases with decreasing concentration. As the temperature is lowered the absorption of phonons by impuritons, with a characteristic time $\tau_{\rm abs}$, becomes the dominant process. However, in that case, as analysis of formula (7) shows that the longitudinal relaxation of phonons must be taken into account even at high concentrations of ^{3}He.

The arrow in Fig. 1 indicates the phase separation temperature of the initial mixture. Within the limits of experimental error no noticeable anomaly in the behavior of the effective thermal conductivity was observed. Here it was taken into account that at temperatures below phase separation the concentration of the mixture studied decreased with decreasing temperature in accordance with the phase diagram.

4. DIFFUSION

In ^{3}He–^{4}He superfluid mixtures the mass transport processes are very specific, since the flux of impurities here is governed by not only the concentration gradient but also the temperature gradient, and therefore the diffusion is due to heat conduction. In the general case of arbitrary temperature and concentration this process is described, as is shown in Ref. 15, by an effective diffusion coefficient having the form

$$D_{\rm eff}=D_m\frac{u_{2\varepsilon}^2}{u_2^2}\left(1-\frac{k_T}{k_T^*}\right)^2+\frac{k_3}{C_V}\frac{u_{2N}^2}{u_2^2}, \tag{13}$$

where $u_{2N}^2=n_3/\rho_n(\partial P_3/\partial n_3)_{T,n_4}$, with $u_2^2=u_{2N}^2+u_{2\varepsilon}^2$.

Analysis of formula (13) shows that the coefficient of mass diffusion D_m and the effect diffusion coefficient $D_{\rm eff}$ practically coincide ($D_{\rm eff}\approx D_m$) at high temperatures and low concentrations, when the thermal excitations give the dominant contribution to the thermodynamic property of the mixture.

In the other limiting case—low temperatures and high concentrations—the effective diffusion is determined by the thermal diffusivity χ_3 of the mixture: $D_{\rm eff}\approx k_3/C_3\equiv\chi_3$.

4.1. Mass diffusion

For the phonon–impuriton system of ^{3}He–^{4}He superfluid mixtures the coefficient of mass diffusion D_m, calculated in Refs. 9 and 16, has the form

$$D_m=\frac{2}{3}\overline{\varepsilon}_3 n_3\frac{\rho_{n\rm ph}}{\rho_n^2}\tau_{\rm ph3}, \tag{14}$$

where $\rho_{n\rm ph}$ is the phonon part of the density of the normal component; the phonon–impuriton relaxation time $\tau_{\rm ph3}$ was used in calculating the diffusion part of the effective thermal conductivity. The mean energy of the impuritons, $\overline{\varepsilon}_3$, can be expressed in the general case in terms of the osmotic pressure of the gas of ^{3}He quasiparticles:

$$\overline{\varepsilon}_3=\frac{3}{2}\left(\frac{\partial P_3}{\partial n_3}\right)_T. \tag{15}$$

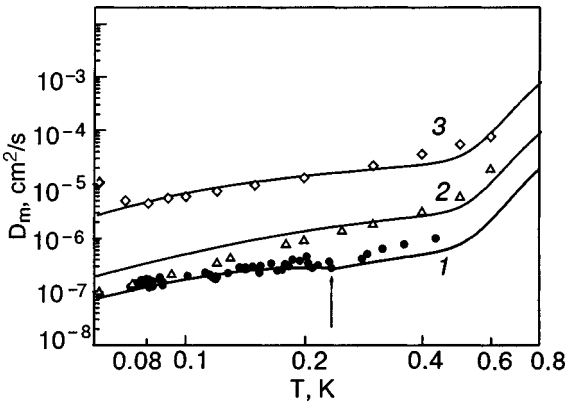

FIG. 3. Temperature dependence of the coefficient of mass diffusion calculated from the experimental data on the effective thermal conductivity: 9.8% ^{3}He (present study; *1*); 5% ^{3}He (Ref. 19; *2*), 1.32% ^{3}He (Ref. 19; *3*). The solid curves were calculated according to Eq. (13).

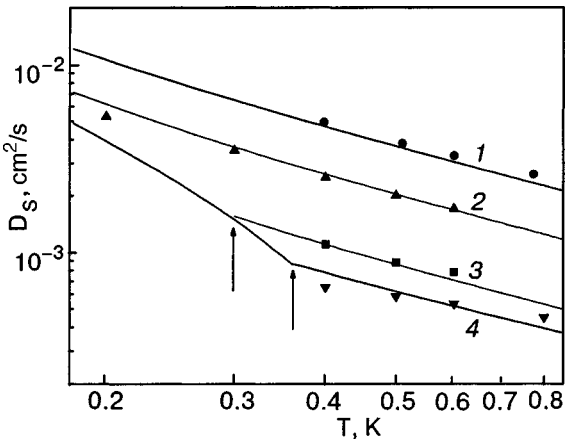

FIG. 4. Temperature dependence of the spin diffusion coefficient for different ^{3}He concentrations: 3% (Ref. 21; *1*); 5% (Ref. 20; *2*); 9.8% (interpolation; *3*); 13.4% (Ref. 22; *4*); the arrows indicate the phase separation temperature of the initial mixtures. The solid lines we calculated according to formulas (16) and (17).

We note that the definition of the mass diffusion coefficient for superfluid mixtures, written in form (14), differs somewhat from the corresponding formula for the classical case. As was shown in Ref. 15, the difference is due to the fact that in ^{3}He–^{4}He superfluid mixtures impurities diffuse in a gas of thermal excitations, which transport mass only in accordance with the coefficient of thermal expansion, which is anomalously small in liquid helium. In classical mixtures all components of the system contribute to the mass transport.

For determination of the the coefficient D_m according to Eqs. (14) and (15) the values of the osmotic pressure from Ref. 17 and the values of the effective mass m_3^* taken from Ref. 18 were used. The temperature dependence of the coefficient of mass diffusion obtained for the mixture under study is given in Fig. 3, which also shows the values of the coefficient of mass diffusion calculated in an analogous way from the experimental data on the effective thermal conductivity, which were obtained previously[19] for mixtures with concentrations of 1.32 and 5.0% ^{3}He. It is seen in the figure that the value of D_m decreases with decreasing temperature. In the limit $T\to 0$, when the contribution of thermal phonons is absent, the value of D_m should go to zero in accordance with (14), and the processes of temperature and concentration relaxation are then determined by the true thermal conductivity of the impuriton subsystem $k_{\text{eff}}=k_3$.

4.2. Spin diffusion

Information about diffusion processes in ^{3}He–^{4}He superfluid mixtures is usually obtained in NMR experiments (on the nuclei of the ^{3}He atoms, which have spin 1/2), and the values of the diffusion coefficient thus obtained are called the spin diffusion. The most detailed data on D_s over a wide interval of temperatures and concentrations were obtained in Refs. 20–22, where it was established that D_s increases in value with decreasing temperature and that D_s^{-1} depends linearly on the concentration. The analysis in Ref. 21 of the experimental data for dilute mixtures of ^{3}He in ^{4}He (less than $\sim 3\%$ ^{3}He) pertains to the high-temperature region, where the dominant contribution is given by rotons.

In the low-temperature region, where the influence of the rotons is negligible and the main kinetic processes are governed by ^{3}He–phonon and ^{3}He–^{3}He collisions such a description is inadequate. Since for concentrated mixtures the main contribution to the density of the normal component is from ^{3}He quasiparticles, the coefficient of spin diffusion, as was shown in Ref. 16, is determined solely by processes in the impuriton gas and can be expressed as follows:

$$D_s=\frac{2}{3}\frac{\overline{\varepsilon_3}}{m_3^*}\tau_{33s}. \tag{16}$$

The impuriton–impuriton relaxation time τ_{33s} was treated in Ref. 16 as a fitting parameter.

It was demonstrated in Ref. 16 that good agreement with the experimental data can be obtained if in calculations using formula (16) the relaxation time τ_{33s} is taken in the form

$$\tau_{33s}=\frac{B}{xT^2}[\text{s}], \tag{17}$$

where B is a constant independent of the temperature and concentration.

Here we have used the approach developed in Ref. 16. Figure 4 shows the temperature dependence of the coefficient of spin diffusion D_s for different ^{3}He concentrations according to the experimental data of Refs. 20–22 and also the values of D_s for the concentration (9.8% ^{3}He) investigated in the present study, obtained by interpolation of the results of Refs. 19–21. The solid curves in Fig. 4 correspond to a calculation according to formulas (16) and (17) with the constant $B=7\times 10^{-12}$. This means that the behavior of the relaxation time τ_{33s} is described by formula (16) over a wide range of concentrations and temperatures. All of the experiments represented in Fig. 4 pertain to an intermediate region between the quantum and classical regimes for impuritons.

A comparison of formulas (14) and (16) shows that in the investigated temperature and concentration range the value of D_m is several orders of magnitude smaller than D_s. This difference is explained by the following circumstance. Usually mass diffusion requires the presence of at least two different components, and in the absence of one of them (in our case phonons at $T\to 0$) the diffusion process itself in the framework of the model of Ref. 1 loses meaning. It follows

from formula (14) that $D_m \to 0$ for $T \to 0$. Under these conditions the mass transport occurs in the process of equilibration of the temperature and is described by the true thermal conductivity of the impuriton gas. However, in the general case of arbitrary temperature and concentration, as was shown in Ref. 15, the mass transport is governed by the effective diffusion coefficient. We note that in classical binary mixtures one often considers the interdiffusion coefficient, which does not vanish when the concentration of one of the components goes to zero. In such a case that coefficient determines the diffusion of an isolated impurity atom, which is directly related to its mobility.

At the same time, the coefficient of spin diffusion D_s at low temperatures tends toward the value $v_F^2 \tau_{33s}$, which is actually the coefficient of self-diffusion of impuritons. Thus as the temperature is lowered, D_m decreases while D_s increases, and therefore at low temperatures these coefficients differ strongly. However, at high enough temperatures and low enough concentrations ($x < 5\%$ ^{3}He) the coefficients D_m and D_s are practically equal:

$$D_m \approx D_s \approx \frac{2}{3} \frac{\overline{\varepsilon}_3}{m_3^*} \frac{\rho_{n3}}{\rho_{n\mathrm{ph}}} \tau_{\mathrm{ph}3}, \tag{18}$$

as is confirmed by experiment.

5. VISCOSITY

The viscosity of the phonon–impuriton system of the mixture consists of two parts: the viscosity due to the transport of momentum by phonons, η_{ph}, and the impuriton viscosity η_3, when momentum is transported by ^{3}He quasiparticles:

$$\eta = \eta_{\mathrm{ph}} + \eta_3, \tag{19}$$

where the phonon part of the viscosity has been calculated in Ref. 5:

$$\eta_{\mathrm{ph}} = \frac{2}{5} c^2 \rho_{n\mathrm{ph}} \tau_{\mathrm{ph}3}. \tag{20}$$

An expression for the impuriton part of the viscosity was obtained in Ref. 4:

$$\eta_3 = P_3(x,T)\, \tau_{33\eta}, \tag{21}$$

where the relaxation time $\tau_{33\eta}$ is one of the main parameters governing the absorption of first sound on account of the first viscosity.[18]

Estimates show that in view of the smallness of $\rho_{n\mathrm{ph}}$ in formula (19), η_{ph} makes up only 3.5% of the total viscosity, and this contribution can be neglected, i.e., $\eta \approx \eta_3$. The ^{3}He–^{3}He relaxation time $\tau_{33\eta}$ in formula (20) was determined as an adjustable parameter by fitting to experimental data on the viscosity of mixtures containing 5 and 7.0% ^{3}He.[23] Analysis showed that good agreement with experiment is obtained for

$$\tau_{33\eta} = \frac{5.5 \times 10^{-12}}{x T^{3/2}} [\mathrm{s}]. \tag{22}$$

The temperature dependence of the shear viscosity for the mixture under discussion, calculated according to formula (21) with the use of (22), is given in Fig. 5. Also shown

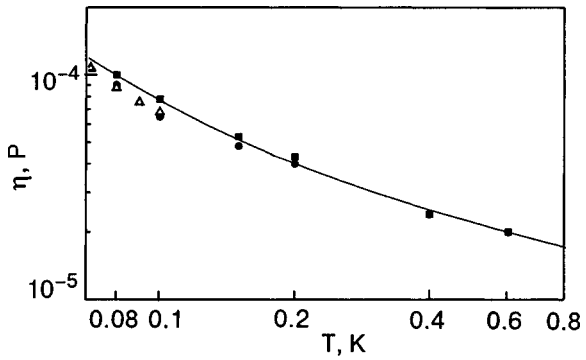

FIG. 5. Temperature dependence of the shear viscosity of ^{3}He–^{4}He superfluid mixtures with ^{3}He concentrations: 5% (Ref. 23; ●); 7% (Ref. 23; ■); 6.2% (Ref. 24; △). The solid curve was calculated according to Eq. (20) for a mixture with a concentration of 7% ^{3}He.

there are the experimental data on the viscosity obtained in Refs. 23 and 24 for concentrations of 5.5, 6.2, and 7% ^{3}He. These data, within the experimental error, are well described by a single curve in accordance with formulas (21) and (22).

6. CONCLUSION

Analysis of the experimental data (obtained in the present study and by other authors) on the effective thermal conductivity, viscosity, mass and spin diffusion in superfluid mixtures of ^{3}He in ^{4}He over a wide range of concentrations has shown that at low temperatures they can be adequately described from a unified viewpoint in the framework of the kinetic theory of the phonon–impuriton system of superfluid mixtures. The kinetic properties of the impuriton subsystem of superfluid mixtures can be described in the framework of a Fermi gas model all the way to concentrations of $\sim 10\%$ ^{3}He. As a result, the role of each of the relaxation processes in the complex hierarchy of relaxation times was determined.

In characterizing the impuriton–impuriton scattering processes we note that the different relaxation times correspond to different dissipative coefficients. The behavior of the shear viscosity in the low-temperature region is determined by the impuriton–impuriton relaxation time $\tau_{33\eta}$. This time determines both the time t_{abs} and the absorption of first sound in the mixture. The impuriton part of the effective thermal conductivity is determined by the relaxation time τ_{33k}, while the contribution due to the diffusion of phonons depends substantially on the time t_{abs} and, through it, on $\tau_{33\eta}$. The relaxation times governing the mass diffusion are practically the same as those that govern the effective thermal conductivity, which is due to diffusion of phonons. The behavior of the spin diffusion is governed by the impuriton–impuriton relaxation time τ_{33s}. Figure 6 shows the temperature dependence of these relaxation times. The fact that they are somewhat different from each other is due to the different physical nature of the kinetic coefficients under consideration and to the fact that the impuriton–impuriton scattering probability depends strongly on the momentum of the impuritons and the scattering angle.

From a physical standpoint this difference is due to the fact that the different dissipative processes are due to the transport of different physical quantities. The thermal conductivity relates to the transport of energy, the viscosity to

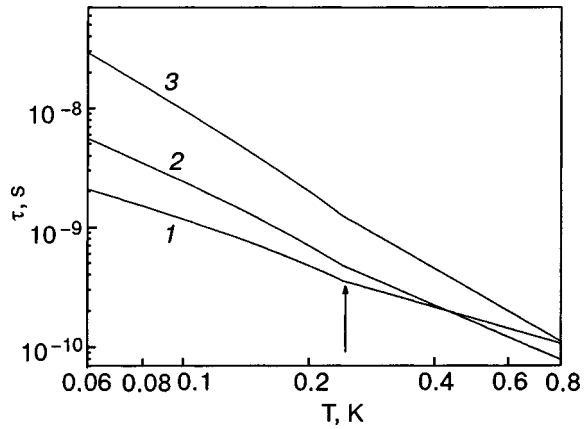

FIG. 6. Temperature dependence of the relaxation times associated with impuriton–impuriton scattering for a mixture with with an initial concentration of 9.8% ^{3}He: τ_{33k}, which governs the true thermal conductivity of the gas of impuritons (*1*); $\tau_{33\eta}$, which governs the shear viscosity (*2*); τ_{33s}, which governs the spin diffusion (*3*). The arrow corresponds to the separation temperature.

the transport of momentum, and the spin diffusion to the transport of the nuclear spin of ^{3}He. From a mathematical standpoint the corresponding scattering frequencies $\tau_{33\eta}^{-1}$, τ_{33k}^{-1}, and τ_{33s}^{-1} are different eigenvalues of the impuriton–impuriton collision integral. An exact calculation of these frequencies is difficult at present because of the lack of reliable data on the ^{3}He–^{3}He interaction potential.

We also note that in concentrated superfluid mixtures of ^{3}He in ^{4}He, especially at low temperatures, the dominant role in the establishment of equilibrium is played by processes of phonon absorption and emission. In the other limiting case, that of relatively high temperatures and low concentrations (below 1% ^{3}He), the relaxation of phonons in the presence of impuritons occurs with a substantial influence of the three-phonon interaction.[11] The analysis done in the present paper shows that the contribution of these processes must be taken into account for mixtures with high concentrations as well (up to 10% ^{3}He). This is actually the first evidence that the anomalous character of the initial part of the dispersion curve is preserved for concentrated superfluid mixtures of ^{3}He in ^{4}He.

The authors thank V. N. Grigor'ev for a helpful discussion of the results of this study.

This investigation was supported in part by the Ukrainian Government Foundation for Basic Research (Project 02.07/00391, Contract F7/286-2001).

*E-mail: zadorozhko@ilt.kharkov.ua

[1] I. M. Khalatnikov and V. A. Zharkov, Zh. Éksp. Teor. Fiz. **32**, 1108 (1957) [Sov. Phys. JETP **5**, 905 (1957)].
[2] B. M. Abraham, Y. Eckstein, J. B. Keterson, and J. H. Vignos, Phys. Rev. Lett. **17**, 1254 (1966).
[3] B. M. Abraham, Y. Eckstein, J. B. Keterson, and M. Kuchnir, Phys. Rev. Lett. **20**, 251 (1968).
[4] G. Baym and C. Ebner, Phys. Rev. **164**, 235 (1967).
[5] G. Baym and W. F. Saam, Phys. Rev. **171**, 172 (1968).
[6] G. Baym, W. F. Saam, and C. Ebner, Phys. Rev. **173**, 306 (1968).
[7] É. Ya. Rudavskiĭ and V. K. Chagovets, Fiz. Nizk. Temp. **10**, 1031 (1983) [Sov. J. Low Temp. Phys. **10**, 538 (1983)].
[8] I. N. Adamenko and V. I. Tsyganok, Zh. Éksp. Teor. Fiz. **87**, 865 (1984) [Sov. Phys. JETP **60**, 491 (1984)].
[9] I. N. Adamenko and V. I. Tsyganok, Zh. Éksp. Teor. Fiz. **88**, 1641 (1985) [Sov. Phys. JETP **61**, 978 (1985)].
[10] I. N. Adamenko, É. Ya. Rudavskiĭ, V. I. Tsyganok, and V. K. Chagovets, JETP Lett. **39**, 487 (1984).
[11] I. N. Adamenko and É. Ya. Rudavskii, Fiz. Nizk. Temp. **13**, 3 (1987) [Sov. J. Low Temp. Phys. **13**, 1 (1987)].
[12] A. A. Zadorozhko, T. V. Kal'ko, E. Ya. Rudavskiĭ, V. K. Chagovets, and G. A. Sheshin, Fiz. Nizk. Temp. **29**, 367 (2003) [Low Temp. Phys. **29**, 275 (2003)].
[13] A. A. Zadorozhko, T. V. Kal'ko, É. Ya. Rudavskiĭ, V. K. Chagovets, and G. A. Sheshin, Fiz. Nizk. Temp. **29**, 829 (2003) [Low Temp. Phys. **29**, 619 (2003)].
[14] T. S. Sullivan, V. Steinberg, and R. E. Ecke, J. Low Temp. Phys. **90**, 343 (1993).
[15] I. N. Adamenko and K. É. Nemchenko, Fiz. Nizk. Temp. **22**, 995 (1996) [Low Temp. Phys. **22**, 759 (1996)]; K. É. Nemchenko, Fiz. Nizk. Temp. **24**, 941 (1998) [Low Temp. Phys. **24**, 708 (1998)].
[16] I. N. Adamenko, K. E. Nemchenko, A. V. Zhukov, Chung-In Um, T. F. George, and L. N. Pandey, J. Low Temp. Phys. **111**, 145 (1998).
[17] J. G. M. Kuerten, C. A. H. Castelijns, A. T. A. H. de Waele, and H. M. Gijman, Cryogenics **25**, 419 (1985).
[18] A. A. Zadorozhko, T. V. Kal'ko, É. Ya. Rudavskii, I. A. Usherov-Marshak, V. K. Chagovets, and G. A. Sheshin, Fiz. Nizk. Temp. **28**, 107 (2002) [Low Temp. Phys. **28**, 73 (2002)].
[19] W. R. Abel and J. C. Wheatly, Phys. Rev. Lett. **21**, 1231 (1968).
[20] A. C. Anderson, D. O. Edwards *et al.*, Phys. Rev. Lett. **17**, 367 (1966).
[21] J. E. Opfer, K. Luszczynski, and R. E. Norberg, Phys. Rev. **172**, 192 (1968).
[22] R. B. Harrison and J. Hatton, J. Low Temp. Phys. **6**, 43 (1972).
[23] S. A. Kuenhold, D. B. Crum, and R. E. Sarwinski, Phys. Lett. A **41**, 13 (1972).
[24] R. Konig and F. Pobell, J. Low Temp. Phys. **89**, 465 (1992).

Translated by Steve Torstveit

Drag of superfluid current in bilayer Bose systems

D. V. Fil*

Institute for Single Crystals of the National Academy of Sciences of Ukraine 60 Lenin Ave., Kharkov 61001, Ukraine

S. I. Shevchenko†

B. Verkin Institute for Low Temperature Physics and Engineering of the National Academy of Sciences of Ukraine, 47 Lenin Ave., Kharkov 61103, Ukraine

(Submitted March 15, 2004)
Fiz. Nizk. Temp. **30**, 1028–1037 (October 2004)

An effect of nondissipative drag of a superfluid flow in a system of two Bose gases confined in two parallel quasi-two-dimensional traps is studied. Using an approach based on the introduction of density and phase operators, we compute the drag current at zero and finite temperatures for arbitrary ratio of particle densities in the adjacent layers. We demonstrate that in a system of two ring-shaped traps the ''drag force'' influences the drag trap in the same way as an external magnetic flux influences a superconducting ring. This allows one to use the drag effect to control persistent current states in superfluids and opens up the possibility of implementing a Bose analog of the superconducting Josephson flux qubit. © *2004 American Institute of Physics.* [DOI: 10.1063/1.1808194]

1. INTRODUCTION

The existence of nondissipative supercurrents is a common feature of superconducting and superfluid systems. Among various applications of superconductivity, considerable attention has been paid to the use of superconducting circuits as very sensitive magnetometers (superconducting quantum interferometer devices). At present there is renewed interest in such systems in view of the possibility of using superconducting circuits with weak links as elements of quantum computers (Josephson qubits). In view of the similarity between superfluids and superconductors, one can expect that the former may also be used for implementing qubits.

Supercurrent in superconductors is coupled to the vector potential of electromagnetic fields. It allows one to control persistent current states by external fields. Obviously, there is no such channel for control in uncharged superfluid Bose systems. In this paper we study another possibility based on a nondissipative drag effect.

The drag in normal systems has been investigated experimentally and theoretically by many authors (see, for instance, the reviews[1,2]). Attention was mainly focused on the study of bilayer electron systems in semiconductor heterostructures. In such systems an interlayer drag effect takes place. The effect is caused by electron–electron scattering processes and it reveals itself in the appearance of a drag voltage in one layer when a normal current flows in the adjacent layer. If the former layer is in a closed circuit, the drag voltage induces a drag current flowing through the circuit. The effect is accompanied by dissipation of energy and takes place only at finite temperatures. Roughly, the drag voltage increases by a T^2 law (the deviation from this law observed experimentally[3] is connected with a phonon contribution to the interaction between the carriers[4]).

In superfluid and superconducting systems another kind of drag may take place. This drag is nondissipative and is connected with a redistribution of supercurrent between two superfluid (superconducting) components. In contrast with the drag in a normal state, the superfluid drag has the largest value at zero temperatures and decreases with increasing temperature. The existence of nondissipative drag in superfluid systems was pointed out for the first time in the paper by Andreev and Bashkin.[5] In that paper a three-velocity hydrodynamic model of a ^{3}He–^{4}He mixture was developed. It has been shown that the superfluid behavior of such systems can be described by including a ''drag'' term in the free energy. This term is proportional to the scalar product of the superfluid velocities of the two components times the difference between the effective and bare masses of ^{3}He atoms. The nondissipative drag effect in superconductors has been studied in the paper by Duan and Yip.[6] Those authors argue[6] that the value of the drag can be obtained from the energy of zero-point fluctuations. It was shown that this energy contains a ''drag'' term analogous to that obtained in Ref. 5 in the hydrodynamic approach. The theory of nondissipative drag in a bilayer system of charged bosons was developed by Tanatar and Das[7] and by Terentjev and Shevchenko.[8]

The existence of nondissipative drag in a system of two one-dimensional wires in a persistent current state was predicted by Rojo and Mahan.[9] It was also shown by Duan[10] that nondissipative drag is responsible for the emergence of an interlayer Hall voltage in bilayer electron systems in the fractional quantum Hall regime.

On the basis of previous studies one can consider nondissipative drag as a fundamental property of systems with macroscopic quantum coherence. For a system of uncharged bosons this effect is especially important, since the ''drag force'' plays a role similar to the role of the magnetic vector potential in superconductors. It opens up new possibilities for observing the effects caused by phase coherence in such

systems. One of the goals of this paper is to point out this analogy. In particular, we show that the nondissipative drag effect allows one to realize a superposition of flux states in a superfluid ring with a Josephson weak link.

Great attention is now being paid to the study of ultracold alkali-metal vapors confined in magnetic and optical traps, where Bose–Einstein condensation of atoms has been observed.[11] Advances in technology allow one to manipulate the parameters of such systems and make ultracold atomic gases a unique object for the study of various quantum-mechanical phenomena.

In this paper we study the effect of nondissipative drag in a system of two quasi-two-dimensional atomic Bose gases confined in two parallel traps. To describe such a situation we take into account that the densities of atoms in the drive and drag layers can be unequal. In previous studies[7,8] only the case of two layers with equal densities of the particles was considered. Another important factor is the temperature. In atomic gases it is of the order of or higher than the energy of intralayer interactions. Previously, the dependence of nondissipative drag on the temperature has been treated only qualitatively.[6,8] Here we study the temperature dependence quantitatively. We also evaluate the drag for concrete mechanisms of interlayer interaction in atomic Bose gases.

2. MODEL AND APPROACH

The geometry of a Bose cloud can be modified significantly by varying the configuration of external fields forming the trap. When the confining potential is strongly anisotropic and the temperature and the chemical potential are smaller than the separation between the energy levels of spatial quantization in one direction, the Bose gas can be treated as a two-dimensional one. Recently, low-dimensional atomic gases have been realized experimentally.[12]

Bose clouds of a ring shape can be created by using toroidal traps. A configuration of two toroidal traps situated one above the other is convenient for the study of the drag effect. It follows from the discussion below that if one excites a circulating superflow in one trap it inevitably leads to a redistribution of this superflow between the two traps, and superfluid currents appear in both rings.

The main features of the drag effect can be understood from the study of a system of two uniform two-dimensional Bose gases situated in parallel layers. The Hamiltonian of the system can be presented in the form

$$H=\sum_{l=1,2}(E_l-\mu_l N_l)+\frac{1}{2}\sum_{l,l'=1,2}E_{ll'}^{\mathrm{int}}, \tag{1}$$

where

$$E_l=\int d^2r\,\frac{\hbar^2}{2m}[\nabla\hat{\Psi}_l^+(\mathbf{r})]\nabla\hat{\Psi}_l(\mathbf{r}) \tag{2}$$

is the kinetic energy,

$$E_{ll'}^{\mathrm{int}}=\int d^2r\,d^2r'\hat{\Psi}_l^+(\mathbf{r})\hat{\Psi}_{l'}^+(\mathbf{r}')V_{ll'}(\mathbf{r}-\mathbf{r}')\times\hat{\Psi}_{l'}(\mathbf{r}')\hat{\Psi}_l(\mathbf{r}) \tag{3}$$

is the energy of the intralayer ($l=l'$) and interlayer ($l\neq l'$) interaction, and $N_l=\int d^2r\hat{\Psi}_l^+(\mathbf{r})\hat{\Psi}(\mathbf{r})$. Here $\hat{\Psi}$ is the Bose field operator, l is the layer index, $\mathbf{r}$ is the two-dimensional radius vector lying in the layer, and μ_l are the chemical potentials. To be more specific, we consider the case of point interaction between the atoms: $V_{11}(\mathbf{r})=V_{22}(\mathbf{r})=\gamma\delta(\mathbf{r})$, $V_{12}(\mathbf{r})=V_{21}(\mathbf{r})=\gamma'\delta(\mathbf{r})$, with $\gamma>0$ and $|\gamma'|<\gamma$. Assuming the barrier between the two traps is quite high, we neglect the tunneling between the layers.

For further analysis it is convenient to use the density and phase operator approach (see, for instance, Refs. 13, 14). The approach is based on the following representation for the Bose field operators:

$$\hat{\Psi}_l(\mathbf{r})=\exp[i\varphi_l(\mathbf{r})+i\hat{\varphi}_l(\mathbf{r})]\sqrt{\rho_l+\hat{\rho}_l(\mathbf{r})}, \tag{4}$$

$$\hat{\Psi}_l^+(\mathbf{r})=\sqrt{\rho_l+\hat{\rho}_l(\mathbf{r})}\exp[-i\varphi_l(\mathbf{r})-i\hat{\varphi}_l(\mathbf{r})], \tag{5}$$

where $\hat{\rho}_l$ and $\hat{\varphi}_l$ are the density and phase fluctuation operators, $\rho_l=\langle\hat{\Psi}_l^+(\mathbf{r})\hat{\Psi}_l(\mathbf{r})\rangle$ is the c-number term of the density operator (one can see that it is just the density of atoms in the layer l), and $\varphi_l(\mathbf{r})$ is the c-number term of the phase operator (in the approach considered, the inclusion of this term in the phase operator allows one to describe states with nonzero average superflows).

Substituting Eqs. (4), (5) into Hamiltonian (1) and expanding it in series in powers of $\hat{\rho}_l$ and $\nabla\hat{\varphi}_l$, we arrive at the expression

$$H=H_0+H_1+H_2+\ldots. \tag{6}$$

In (6) the term

$$H_0=\int d^2r\left\{\sum_l\left[\frac{\hbar^2}{2m}\rho_l(\nabla\varphi_l(\mathbf{r}))^2+\frac{\gamma}{2}\rho_l^2-\mu_l\rho_l\right]+\gamma'\rho_1\rho_2\right\} \tag{7}$$

does not contain the operator part, the term

$$H_1=\int d^2r\left\{\sum_l\left\{\left[\frac{\hbar^2}{2m}(\nabla\varphi_l(\mathbf{r}))^2+\gamma\rho_l+\gamma'\rho_{3-l}-\mu_l\right]\times\hat{\rho}_l(\mathbf{r})+\frac{\hbar^2}{m}\rho_l[\nabla\varphi_l(\mathbf{r})]\nabla\hat{\varphi}_l(\mathbf{r})\right\}\right\} \tag{8}$$

is linear in the phase and density fluctuation operators, and the term

$$H_2=\int d^2r\left\{\sum_l\frac{\hbar^2}{2m}\left[\frac{(\nabla\hat{\rho}_l(\mathbf{r}))^2}{4\rho_l}+\rho_l(\nabla\hat{\varphi}_l(\mathbf{r}))^2+[\nabla\varphi_l(\mathbf{r})](\hat{\rho}_l(\mathbf{r})\nabla\hat{\varphi}_l(\mathbf{r})+[\nabla\hat{\varphi}_l(\mathbf{r})]\hat{\rho}_l(\mathbf{r}))+\frac{i}{2}([\nabla\hat{\rho}_l(\mathbf{r})]\nabla\hat{\varphi}_l(\mathbf{r})-[\nabla\hat{\varphi}_l(\mathbf{r})]\nabla\hat{\rho}_l(\mathbf{r}))\right]+\frac{\gamma}{2}[(\hat{\rho}_1(\mathbf{r}))^2+(\hat{\rho}_2(\mathbf{r}))^2]+\gamma'\hat{\rho}_1(\mathbf{r})\hat{\rho}_2(\mathbf{r})\right\} \tag{9}$$

is quadratic in the $\nabla\hat{\varphi}_l$ and $\hat{\rho}_l$ operators.

If the chemical potentials are fixed, the Hamiltonian H_0 is minimized under the conditions

$$\frac{\hbar^2}{2m}(\nabla\varphi_l(\mathbf{r}))^2+\gamma\rho_l+\gamma'\rho_{3-l}-\mu_l=0, \tag{10}$$

$$\nabla(\rho_l \nabla \varphi_l(\mathbf{r}))=0. \tag{11}$$

Fulfillment of Eqs. (10), (11) means that the H_1 term in the Hamiltonian (6) vanishes. One should note that, as follows from Eq. (10), the densities of the components are independent of the coordinates only when the phase gradients remain space independent as well.

The quadratic part of the Hamiltonian determines the spectrum of elementary excitations. Hereafter we will neglect the higher-order terms in the Hamiltonian (6). These terms describe the scattering of the quasiparticles, and they can be omitted if the temperature is much smaller than the critical temperature ($T_c \sim \hbar^2\rho/m$).

3. DRAG CURRENT

The current density operator

$$\hat{\mathbf{j}}_l=\frac{i\hbar}{2m}[(\nabla\hat{\Psi}_l^+)\hat{\Psi}_l-\hat{\Psi}_l^+\nabla\hat{\Psi}_l], \tag{12}$$

rewritten in terms of the phase and density operators, has the form

$$\hat{\mathbf{j}}_l=\frac{\hbar}{m}\sqrt{\rho_l+\hat{\rho}_l}[\nabla(\varphi_l+\hat{\varphi}_l)]\sqrt{\rho_l+\hat{\rho}_l}. \tag{13}$$

Expanding (13) in powers of the density and phase fluctuation operators and neglecting the terms of order higher than quadratic, we obtain the following expression for the mean value of the current density:

$$\mathbf{j}_l=\frac{\hbar}{m}\rho_l\nabla\varphi_l+\frac{\hbar}{2m}(\langle[\nabla\hat{\varphi}_l]\hat{\rho}_l\rangle+\langle\hat{\rho}_l\nabla\hat{\varphi}_l\rangle). \tag{14}$$

In deriving Eq. (14) we have taken into account that $\langle\hat{\varphi}_l\rangle=\langle\hat{\rho}_l\rangle=0$.

To compute the averages in (14) we rewrite the quadratic part of the Hamiltonian in terms of the operators of creation and annihilation of the elementary excitations. In the absence of the interlayer interaction ($\gamma'=0$) this can be done by the substitution

$$\hat{\rho}_l(\mathbf{r})=\sqrt{\frac{\rho_l}{S}}\sum_{\mathbf{k}} e^{i\mathbf{kr}}\sqrt{\frac{\epsilon_k}{E_{lk}}}[b_l(\mathbf{k})+b_l^+(-\mathbf{k})], \tag{15}$$

$$\hat{\varphi}_l(\mathbf{r})=\frac{1}{2i}\sqrt{\frac{1}{\rho_l S}}\sum_{\mathbf{k}} e^{i\mathbf{kr}}\sqrt{\frac{E_{lk}}{\epsilon_k}}[b_l(\mathbf{k})-b_l^+(-\mathbf{k})], \tag{16}$$

where the operators b_l^+, b_l satisfy the Bose commutation relations. Here S is the area of the system, $\epsilon_k=\hbar^2k^2/2m$ is the spectrum of free atoms, and $E_{lk}=\sqrt{\epsilon_k(\epsilon_k+2\gamma\rho_l)}$ is the spectrum of elementary excitations at $\gamma'=0$ and $\nabla\varphi_l=0$.

In the case considered, the substitution (15), (16) reduces the Hamiltonian (9) to the form

$$H_2=\sum_{l\mathbf{k}}\left[\mathcal{E}_l(\mathbf{k})b_l^+(\mathbf{k})b_l(\mathbf{k})+\frac{1}{2}(E_{lk}-\epsilon_k)\right] + \sum_{\mathbf{k}} g_k[b_1^+(\mathbf{k})b_2(\mathbf{k})+b_1(\mathbf{k})b_2(-\mathbf{k})+\text{h.c.}], \tag{17}$$

where

$$\mathcal{E}_l(\mathbf{k})=E_{lk}+\frac{\hbar^2}{m}\mathbf{k}\nabla\varphi_l, \tag{18}$$

$$g_k=\gamma'\epsilon_k\sqrt{\frac{\rho_1\rho_2}{E_{1k}E_{2k}}}. \tag{19}$$

The Hamiltonian (17) contains terms nondiagonal in the Bose creation and annihilation operator and can be diagonalized using the u-v transformation

$$b_l(\mathbf{k})=u_{l\alpha}(\mathbf{k})\alpha(\mathbf{k})+u_{l\beta}(\mathbf{k})\beta(\mathbf{k})+v_{l\alpha}(\mathbf{k})\alpha^+(-\mathbf{k}) + v_{l\beta}(\mathbf{k})\beta^+(-\mathbf{k}), \tag{20}$$

(see Ref. 15) which reduces the Hamiltonian (17) to the form

$$H_2=\sum_{\mathbf{k}}\left[\mathcal{E}_\alpha(\mathbf{k})\left(\alpha^+(\mathbf{k})\alpha(\mathbf{k})+\frac{1}{2}\right) + \mathcal{E}_\beta(\mathbf{k})\left(\beta^+(\mathbf{k})\beta(\mathbf{k})+\frac{1}{2}\right)-\epsilon_k\right]. \tag{21}$$

It is convenient to present the u-v coefficients and the energies of the elementary excitations as series in powers of g_k. The $u-v$ coefficients read as

$$\begin{pmatrix} u_{1\alpha}(\mathbf{k}) & u_{1\beta}(\mathbf{k}) \\ u_{2\alpha}(\mathbf{k}) & u_{2\beta}(\mathbf{k}) \end{pmatrix}=\begin{pmatrix} A_{\mathbf{k}} & -\dfrac{g_k}{\mathcal{E}_1(\mathbf{k})-\mathcal{E}_2(\mathbf{k})} \\ \dfrac{g_k}{\mathcal{E}_1(\mathbf{k})-\mathcal{E}_2(\mathbf{k})} & B_{\mathbf{k}} \end{pmatrix}+\mathcal{O}(g_k^3), \tag{22}$$

$$\begin{pmatrix} v_{1\alpha}(\mathbf{k}) & v_{1\beta}(\mathbf{k}) \\ v_{2\alpha}(\mathbf{k}) & v_{2\beta}(\mathbf{k}) \end{pmatrix} =\begin{pmatrix} -\dfrac{g_k^2[\mathcal{E}_2(\mathbf{k})+\mathcal{E}_2(-\mathbf{k})]}{[\mathcal{E}_1(\mathbf{k})+\mathcal{E}_1(-\mathbf{k})][\mathcal{E}_1(-\mathbf{k})-\mathcal{E}_2(-\mathbf{k})][\mathcal{E}_1(-\mathbf{k})+\mathcal{E}_2(\mathbf{k})]} & -\dfrac{g_k}{\mathcal{E}_1(\mathbf{k})+\mathcal{E}_2(-\mathbf{k})} \\ -\dfrac{g_k}{\mathcal{E}_1(-\mathbf{k})+\mathcal{E}_2(\mathbf{k})} & \dfrac{g_k^2[\mathcal{E}_1(\mathbf{k})+\mathcal{E}_1(-\mathbf{k})]}{[\mathcal{E}_2(\mathbf{k})+\mathcal{E}_2(-\mathbf{k})][\mathcal{E}_1(-\mathbf{k})-\mathcal{E}_2(-\mathbf{k})][\mathcal{E}_1(\mathbf{k})+\mathcal{E}_2(-\mathbf{k})]} \end{pmatrix} +\mathcal{O}(g_k^3), \tag{23}$$

where

$$A_{\mathbf{k}}=1-\frac{g_k^2}{2}\left(\frac{1}{[\mathcal{E}_1(\mathbf{k})-\mathcal{E}_2(\mathbf{k})]^2}-\frac{1}{[\mathcal{E}_1(\mathbf{k})+\mathcal{E}_2(-\mathbf{k})]^2}\right), \tag{24}$$

$$B_{\mathbf{k}}=1-\frac{g_k^2}{2}\left(\frac{1}{[\mathcal{E}_1(\mathbf{k})-\mathcal{E}_2(\mathbf{k})]^2}-\frac{1}{[\mathcal{E}_1(-\mathbf{k})+\mathcal{E}_2(\mathbf{k})]^2}\right). \tag{25}$$

The spectra of the elementary excitations are found to be

$$\mathcal{E}_\alpha(\mathbf{k})=\mathcal{E}_1(\mathbf{k})+g_k^2\left[\frac{1}{\mathcal{E}_1(\mathbf{k})-\mathcal{E}_2(\mathbf{k})}-\frac{1}{\mathcal{E}_1(\mathbf{k})+\mathcal{E}_2(-\mathbf{k})}\right]+\mathcal{O}(g_k^4), \tag{26}$$

$$\mathcal{E}_\beta(\mathbf{k})=\mathcal{E}_2(\mathbf{k})-g_k^2\left[\frac{1}{\mathcal{E}_1(\mathbf{k})-\mathcal{E}_2(\mathbf{k})}+\frac{1}{\mathcal{E}_1(-\mathbf{k})+\mathcal{E}_2(\mathbf{k})}\right]+\mathcal{O}(g_k^4). \tag{27}$$

One can see that the small parameter of the expansion is $g_k/|\mathcal{E}_1(\mathbf{k})-\mathcal{E}_2(\mathbf{k})|\ll 1$. The last inequality takes place for all k, if $\gamma' \max(\rho_1,\rho_2)\ll\gamma|\rho_1-\rho_2|$. Since in most cases of interest the interlayer interaction is much smaller than the intralayer one, for bilayer systems with different densities in the adjacent layers one can neglect the $\mathcal{O}(g_k^3)$ and higher-order terms in Eqs. (22), (23), (26), (27).

Using representation (15), (16), we obtain from (14) the following expression for the current density:

$$\mathbf{j}_l=\frac{\hbar}{m}\rho_l\nabla\varphi_l+\frac{\hbar}{mS}\sum_{\mathbf{k}}\mathbf{k}\langle b_l^+(\mathbf{k})b_l(\mathbf{k})\rangle. \tag{28}$$

Substituting Eq. (20) with coefficients (22), (23) into Eq. (28), computing the averages, and expanding the result in powers of the phase gradients, we obtain the following expression for the currents:

$$\mathbf{j}_1=\frac{\hbar}{m}[(\rho_{s1}-\rho_{\mathrm{dr}})\nabla\varphi_1+\rho_{\mathrm{dr}}\nabla\varphi_2], \tag{29}$$

$$\mathbf{j}_2=\frac{\hbar}{m}[(\rho_{s2}-\rho_{\mathrm{dr}})\nabla\varphi_2+\rho_{\mathrm{dr}}\nabla\varphi_1]. \tag{30}$$

Equations (29), (30) are given in the approximation linear in $\nabla\varphi_l$. Here the terms of higher order in the phase gradients can be neglected if the phase gradients $\nabla\varphi_l$ are much smaller than the inverse healing lengths $\xi_l^{-1}\sim\sqrt{m\gamma\rho_l}/\hbar$ (this corresponds to velocities of the superflow much smaller than the critical velocities $v_{cl}\sim\sqrt{\gamma\rho_l/m}$). In Eqs. (29), (30) the quantities ρ_{sl} and ρ_{dr} with an accuracy up to the g_k^2 are determined by the expressions

$$\rho_{sl}=\rho_l+\frac{1}{S}\sum_{\mathbf{k}}\varepsilon_k\frac{\partial N_{lk}}{\partial E_{lk}}-\frac{1}{S}\sum_{\mathbf{k}}g_k^2\epsilon_k\left[(-1)^l\left(\frac{\partial N_{1k}}{\partial E_{1k}}-\frac{\partial N_{2k}}{\partial E_{2k}}\right)\left(\frac{1}{(E_{1k}+E_{2k})^2}-\frac{1}{(E_{1k}-E_{2k})^2}\right)+\frac{\partial^2 N_{lk}}{\partial E_{lk}^2}\left(\frac{1}{E_{1k}+E_{2k}}+\frac{(-1)^l}{E_{1k}-E_{2k}}\right)\right], \tag{31}$$

$$\rho_{\mathrm{dr}}=\frac{2}{S}\sum_{\mathbf{k}}g_k^2\epsilon_k\left[\frac{1+N_{1k}+N_{2k}}{(E_{1k}+E_{2k})^3}-\frac{N_{1k}-N_{2k}}{(E_{1k}-E_{2k})^3}+\frac{1}{2}\left(\frac{\partial N_{1k}}{\partial E_{1k}}+\frac{\partial N_{2k}}{\partial E_{2k}}\right)\left(\frac{1}{(E_{1k}-E_{2k})^2}-\frac{1}{(E_{1k}+E_{2k})^2}\right)\right]. \tag{32}$$

Here $N_{lk}=[\exp(E_{lk}/T)-1]^{-1}$ is the Bose distribution function. One can see that in the absence of the interlayer interaction ($g_k=0$) the value of ρ_{dr} is equal to zero, and Eq. (31) for ρ_{sl} is reduced to the well-known expression for the density of the superfluid component at finite temperatures. If the interlayer interaction is switched on, the value of ρ_{dr} becomes nonzero. Then, even in the absence of the phase gradient in the drag layer the superfluid current in this layer emerges as a response to the phase gradient in the drive layer.

Equations (31), (32) were derived under assumption $\rho_1\neq\rho_2$ (and, consequently, $E_{1k}\neq E_{2k}$). The case $\rho_1\approx\rho_2$ requires more rigorous consideration, since in this case the mixing of the modes is strong even for a weak interlayer interaction. One can find that the expressions (31), (32) remain finite at $\rho_1\to\rho_2$:

$$\lim_{\rho_1\to\rho_2}\rho_{s1}=\lim_{\rho_1\to\rho_2}\rho_{s2}=\frac{1}{S}\sum_{\mathbf{k}}\varepsilon_k\frac{\partial N_k}{\partial E_k}-\frac{1}{2S}\sum_{\mathbf{k}}\frac{g_k^2\epsilon_k}{E_k}\left(\frac{\partial^2 N_k}{\partial E_k^2}-E_k\frac{\partial^3 N_k}{\partial E_k^3}\right), \tag{33}$$

$$\lim_{\rho_1\to\rho_2}\rho_{\mathrm{dr}}=\frac{1}{4S}\sum_{\mathbf{k}}\frac{g_k^2\epsilon_k}{E_k^3}\left(1+2N_k-2E_k\frac{\partial N_k}{\partial E_k}+\frac{2}{3}E_k^3\frac{\partial^3 N_k}{\partial E_k^3}\right), \tag{34}$$

where E_k is the energy of the elementary excitations at $\rho_1=\rho_2$ and $\gamma'=0$. Using the exact expressions for the spectra and the $u-v$ coefficients, we find for the case of two layers with equal densities and in the weak interlayer interaction limit $\gamma'\ll\gamma$ that the quantities ρ_{sl} and ρ_{dr} are determined just by Eqs. (33), (34). This allows us to conclude that Eqs. (31), (32) are valid for an arbitrary ratio between the densities.

Let us first consider the case of zero temperature. We define the drag current as the current in the drag layer (e.g., layer 1) in the absence of the phase gradient in this layer. At $T=0$ the drag current is equal to

$$j_{\mathrm{dr}}-C_{\mathrm{dr}}\left(\frac{\gamma'}{\gamma}\right)^2\left(\frac{m\gamma}{2\pi\hbar^2}\right)\frac{\hbar}{m}\rho_1\nabla\varphi_2, \tag{35}$$

where

$$C_{\mathrm{dr}}=\int_0^\infty dx\,\frac{x^{1/2}}{\sqrt{x+1}\sqrt{x+\rho_1/\rho_2}(\sqrt{x+1}+\sqrt{x+\rho_1/\rho_2})^3}. \tag{36}$$

The factor C_{dr} is an increasing function of the ratio ρ_2/ρ_1 (at $\rho_2/\rho_1\to 0$ the factor C_{dr} approaches zero, at $\rho_2=\rho_1$ it is

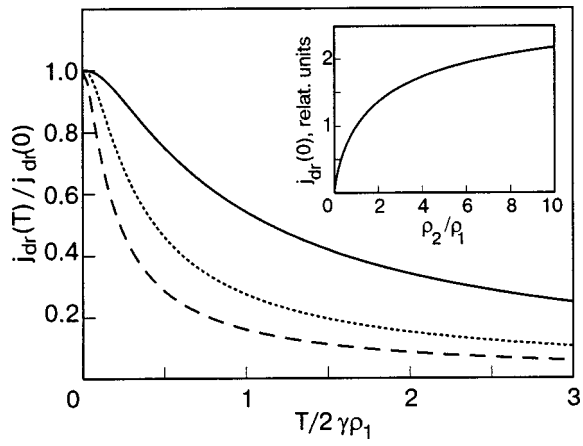

FIG. 1. Dependence of the drag current on the temperature at $\rho_2/\rho_1=5.0$, 1.0, 0.2 (solid, dashed, and dotted curves, respectively) normalized to its value at $T=0$. The dependence of $j_{dr}(0)$ on the ratio ρ_2/ρ_1 normalized to its value at $\rho_2=\rho_1$ is shown in the inset.

equal to 1/12, and it approaches 1/4 at $\rho_2/\rho_1\to\infty$). Thus, the drag current increases with increasing density of particles in the drive layer.

At finite temperatures the drag current decreases. At small T one can use the long-wave approximation for the spectra $E_{1(2)k}$ in the temperature-dependent part of Eq. (32) and evaluate this part analytically. This yields the following relation:

$$j_{dr}(T)=j_{dr}(0)\left[1-\frac{16\zeta(3)}{C_{dr}}\frac{\rho_1}{\rho_2}\left(\frac{T}{2\gamma\rho_1}\right)^3\right]. \tag{37}$$

But, actually, this approximation is valid only at very low temperatures. The results of numerical evaluation of Eq. (32) are shown in Fig. 1. This figure demonstrates that at $T\sim 2\gamma\rho_1$ the temperature decrease of the drag current is much slower. Based on the results presented in Fig. 1, we also conclude that the temperature reduction of the drag current becomes smaller with increasing density of particles in the drive layer.

In a Bose cloud confined in a trap the density is nonuniform. This results in a modification of the spectrum of elementary excitations. One may argue that this modification reveals itself in only minor changes of the value of the drag. It can be shown that the main contribution to the sum in Eq. (32) comes from excitations with wave vectors of the order of or larger than the inverse healing lengths ξ_l^{-1}. In systems with healing lengths much smaller than the linear size of the Bose clouds the spectrum at $q\gtrsim\xi_1^{-1},\xi_2^{-1}$ is well described by the quasi-uniform approximation. Therefore, in such systems the local drag current is given by the same equations (29)–(32) as in the uniform case, with the only modification that the densities ρ_1, ρ_2 in these formulas should be understood as functions of $\mathbf{r}$. In particular, we predict that for two Bose gases confined in harmonic traps having the same Thomas–Fermi radius (and this radius is much larger than the average healing length), the spatial distribution of the superflow in the drag trap at $T=0$ will replicate (with a drag factor) the spatial distribution of the superflow in the drive trap. At finite temperatures one can expect a reduction of the drag factor near the edge of the Bose cloud, where the density is low.

One can ask to what extent the two-dimensionality of the system studied may influence the results obtained. It is known that in 2D systems fluctuations of the phase of the order parameter are large, and at nonzero temperature the off-diagonal one-particle density matrix $\langle\hat{\Psi}^+(\mathbf{r})\hat{\Psi}(0)\rangle$ goes to zero in the limit $|\mathbf{r}|\to\infty$. This implies the absence of long-range order in the systems at $T\neq 0$. But since the asymptotic behavior of the density matrix is described by a power-law dependence on r (not an exponential one), at temperatures lower than the critical (the Kosterlitz–Thouless transition temperature) the superfluid density becomes nonzero. The drag of the superflow between two 2D Bose gases, considered in this paper, is connected with a finite value of the superfluid density, and that is why it decreases with increasing temperature. The density and phase operator approach, used in this paper, is not based on the existence of the Bose–Einstein condensate. Moreover, the power-law asymptotic behavior of the density matrix can be easily derived in this approach with inclusion of thermal excitations described by the Hamiltonian H_2. But at the same level of approximation we do not find any crucial influence of the two-dimensionality on the drag phenomena.

4. THE VALUE OF THE DRAG IN ATOMIC BOSE GASES

Let us present some estimates for the value of the drag in atomic Bose gases. For simplicity we specify the case $\rho_1=\rho_2=\rho$ and $T=0$. It is convenient to introduce the drag factor $f_{dr}=\rho_{dr}/(\rho-\rho_{dr})$, which gives the ratio between the currents in the drag and in the drive traps in the absence of a phase gradient in the drag trap. Taking into account that $\rho_{dr}\ll\rho$, we use the approximate expression $f_{dr}=\rho_{dr}/\rho$ for further analysis.

The value of f_{dr} depends on the interaction parameters γ and γ'. The parameter γ can be expressed in terms of the dimensionless effective "scattering length" $\tilde{a}$:

$$\gamma=\frac{2\sqrt{2\pi}\hbar^2}{m}\tilde{a}. \tag{38}$$

In a quasi-two-dimensional trap the effective scattering length is connected with the 3D scattering length a and the oscillator length in the z direction $l_z=\sqrt{\hbar/m\omega_z}$ by the relation $\tilde{a}=a/l_z$, which is valid for $a\ll l_z$ (Ref. 16). We introduce an interlayer dimensionless effective "scattering length" $\tilde{a}'$ that is connected with the interlayer interaction parameter γ' by the relation

$$\gamma'=\frac{2\sqrt{2\pi}\hbar^2}{m}\tilde{a}'. \tag{39}$$

Substituting Eqs. (38) and (39) into Eq. (34), we obtain the drag factor in the form

$$f_{dr}=\frac{1}{12}\sqrt{\frac{2}{\pi}}\frac{(\tilde{a}')^2}{\tilde{a}}. \tag{40}$$

Equation (40) is valid for $|\tilde{a}'|\ll\tilde{a}$, but one can expect that it is approximately correct at $|\tilde{a}'|\approx\tilde{a}$ (we emphasize that in any case the stability condition requires that the inequality $|\tilde{a}'|<\tilde{a}$ be satisfied).

To estimate the value of $|\tilde{a}'|$ we should specify the mechanism of interlayer interaction. Let us first consider an interaction corresponding to the "tail" of the van der Waals potential:

$$V_{12}^{\mathrm{vdW}}(r) = -\frac{C_6}{(r^2+d^2)^3}. \tag{41}$$

Here C_6 is the van der Waals constant and d is the interlayer distance. The Fourier component of the potential (41) is

$$\mathcal{V}_{12}^{\mathrm{vdW}}(k) = \int d^2 r V_{12}^{\mathrm{vdW}}(r) \mathrm{e}^{i\mathbf{kr}} = -\frac{\pi C_6}{4d^2} k^2 K_2(kd), \tag{42}$$

where $K_2(x)$ is the modified Bessel function of the second kind. Taking into account that the van der Waals interaction is short ranged, we can evaluate γ' as $\gamma' = \mathcal{V}_{12}^{\mathrm{vdW}}(k \to 0) = -\pi C_6/(2d^4)$. This yields $|\tilde{a}'_{\mathrm{vdW}}| \approx \sqrt{\pi/2} C_6 m/(4\hbar^2 d^4)$.

This result can be obtained in a more rigorous way. Our approach is easily generalized to the case of an arbitrary central force interlayer interaction potential. To do this, one should redefine the quantity g_k as

$$g_k = \mathcal{V}_{12}(k) \epsilon_k \sqrt{\frac{\rho_1 \rho_2}{E_{1k} E_{2k}}} \tag{43}$$

and substitute this definition (instead of Eq. (19)) into the formulas for ρ_{sl} and ρ_{dr} obtained in the previous Section. Using Eq. (34), one can present the drag factor (for $T=0$ and $\rho_1 = \rho_2$) in the form

$$f_{\mathrm{dr}} = \frac{1}{16\pi^2} \frac{m^2}{\hbar^4 \tilde{a}} \sqrt{\frac{\pi}{2}} \int_0^\infty dx \frac{x^2 [\mathcal{V}_{12}(q_0 x)]^2}{(x^2+1)^{5/2}} \tag{44}$$

with $q_0 = \sqrt{8\sqrt{2}\pi\rho\tilde{a}}$. Substituting Eq. (42) into Eq. (44), we find

$$f_{\mathrm{dr}} = \frac{1}{12} \left(\frac{C_6 m}{4\hbar^2 d^4} \right)^2 \frac{1}{\tilde{a}} \sqrt{\frac{\pi}{2}} F_{\mathrm{vdW}}(dq_0). \tag{45}$$

Here the function

$$F_{\mathrm{vdW}}(x) = \frac{3x^4}{4} \int_0^\infty dy \frac{y^6}{(1+y^2)^{5/2}} K_2^2(xy) \tag{46}$$

describes the dependence of the drag factor on the density ρ. Comparing Eqs. (46) and (40), we obtain the following expression for the modules of the effective interlayer scattering length:

$$|\tilde{a}'_{\mathrm{vdW}}| = \sqrt{\frac{\pi}{2}} \frac{C_6 m}{4\hbar^2 d^4} \sqrt{F_{\mathrm{vdW}}(dq_0)}. \tag{47}$$

The dependence of the factor $\sqrt{F_{\mathrm{vdW}}}$ on the parameter dq_0 is shown in Fig. 2. One can see from this figure that at $dq_0 \ll 1$ (which corresponds to the low density limit) the factor $\sqrt{F_{\mathrm{vdW}}}$ in Eq. (47) is close to unity, and we arrive at the expression for $|\tilde{a}'_{\mathrm{vdW}}|$ given above.

Due to the short-range nature of the van der Waals interaction the interlayer effective scattering length decreases quickly with increasing d. Therefore, the interlayer distance d should be rather small to achieve an observable value of the drag. Using a typical value of C_6 ($C_6 \approx 3 \times 10^{-57}$ erg·cm^6) and taking $d \approx 10$ nm and $m = 87$ a.u. (Rb), we obtain the estimate $|\tilde{a}'_{\mathrm{vdW}}| \approx 10^{-1}$.

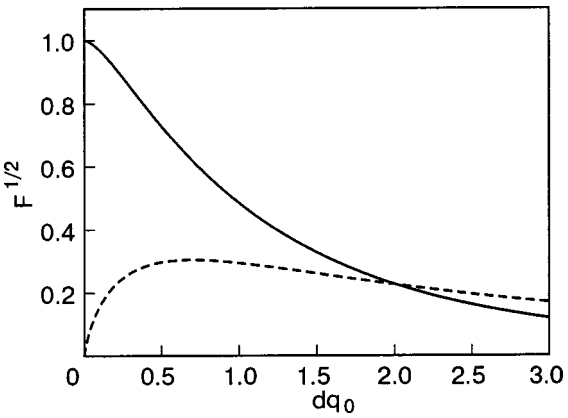

FIG. 2. The density-dependent factors in the effective interlayer scattering length versus the parameter $dq_0 = \sqrt{8\sqrt{2\pi}\rho d^2 \tilde{a}}$. Solid curve—$\sqrt{F_{\mathrm{vdW}}}$ (van der Waals interaction); dashed curve—$\sqrt{F_{d-d}}$ (dipole–dipole interaction).

The quantities l_z and a can be controlled in experiments. The first of these is controlled by changing the profile of the confining potential in the z direction, and the latter, by tuning the magnetic field to the value close to the Feshbach resonance field.[17–19] Near this resonance the scattering length changes sign, and a situation with rather small 3D scattering length a (much smaller than the value of l_z, which, in turn, has to be smaller than $d/2$) can be realized. Using this possibility, one can tune the quantity $\tilde{a}$ close to the value of $|\tilde{a}'_{\mathrm{vdW}}|$ and obtain the drag factor $f_{\mathrm{dr}} \approx 7 \times 10^{-3}$.

Off resonance the typical values of the 3D scattering length lie in the interval 3–5 nm, and for $l_z < d/2$ and $d \approx 10$ nm the estimate $\tilde{a} = a/l_z$ is not applicable. In the ultra-2D limit ($l_z/a \ll 1$) the interaction parameter can be evaluated by using the formula[20]

$$\gamma = \frac{4\pi\hbar^2}{m} \frac{1}{[\ln(\rho a^2)]}.$$

For typical densities $\rho = 10^8 - 10^{10}$ cm^{-2} this yields $\tilde{a} = 0.2 - 0.4$, and the drag factor $f_{\mathrm{dr}} \approx (2-3) \times 10^3$.

At $d \gtrsim 100$ nm the drag caused by the van der Waals interaction becomes negligibly small. But in this last case the dipole–dipole interaction may give an essential contribution to the drag. Let us consider the situation where the dipole moments of the atoms are aligned in the direction perpendicular to the layers. Then the interaction potential has the form

$$V_{12}^{d-d}(r) = D^2 \frac{r^2 - 2d^2}{(r^2+d^2)^{5/2}}, \tag{48}$$

where D is the dipole moment. The Fourier component of the potential (48) reads as

$$\mathcal{V}_{12}^{d-d}(k) = -2\pi D^2 k \mathrm{e}^{-kd}. \tag{49}$$

Substituting Eq. (49) into Eq. (44), we obtain

$$f_{\mathrm{dr}} = \frac{1}{12} \left(\frac{D^2 m}{\hbar^2 d} \right)^2 \frac{1}{\tilde{a}} \sqrt{\frac{\pi}{2}} F_{d-d}(dq_0), \tag{50}$$

where

$$F_{d-d}(x) = 3x^2 \int_0^\infty dy \frac{y^4}{(1+y^2)^{5/2}} \mathrm{e}^{-2xy}. \tag{51}$$

One can see that Eq. (50) is reduced to Eq. (40) under the definition

$$|\tilde{a}'_{d-d}| = \frac{D^2 m}{\hbar^2 d}\sqrt{\frac{\pi}{2}}\sqrt{F_{d-d}(dq_0)}. \quad (52)$$

The dependence $\sqrt{F_{d-d}(dq_0)}$ is also shown in Fig. 2. In contrast to the previous case, the value of $\tilde{a}'_{d-d}$ approaches zero in the low density limit. But at $dq_0 > 0.1$, which corresponds to $\rho > 10^{-2} d^{-2}/(8\sqrt{2\pi}\tilde{a})$, one can neglect the dependence of $f_{\rm dr}$ on the density and put the factor $\sqrt{F_{d-d}} \approx 0.2$. For the estimates given below we assume that the condition $dq_0 > 0.1$ is fulfilled.

For the magnetic dipole–dipole interaction D is the magnetic dipole moment of the atoms. The magnetic dipoles can be aligned in the same direction if a constant magnetic field is applied to the system. Taking $d = 100$ nm, $D = \mu_B$ (the Bohr magneton), and $m = 87$ a.u., we obtain $|\tilde{a}'_{d-d}| \approx 3 \times 10^{-4}$. In the case when $\tilde{a}$ is tuned to the value $|\tilde{a}'_{d-d}|$, one can achieve a drag factor $f_{\rm dr} \approx 2 \times 10^{-5}$.

For Bose atoms with large magnetic dipole moments this value can be much larger. A good candidate atom is Cr ($D = 6\mu_B$). The possibility of realizing a Cr Bose–Einstein condensate is discussed in Ref. 21. For $m = 52$ a.u., $D = 6\mu_B$, and $d = 100$ nm we obtain the value $|\tilde{a}'_{d-d}| \approx 6 \times 10^{-3}$ and, hence, the maximum drag factor $f_{\rm dr} \approx 4 \times 10^{-4}$.

5. THE "DRAG FORCE" AS AN ANALOG OF THE VECTOR POTENTIAL

In Sec. 3 we compute the drag current directly. The same results can be obtained from an analysis of the dependence of the free energy of the system on the phase gradients. The free energy of the system can be found from the common thermodynamic relation

$$F = H_0 + E_{\rm zero} + T\sum_{\lambda=\alpha,\beta}\sum_{\mathbf{k}} \ln\left[1 - \exp\left(-\frac{\mathcal{E}_\lambda(\mathbf{k})}{T}\right)\right]. \quad (53)$$

Here the quantity H_0 given by Eq. (7) is the classical energy of the system, and

$$E_{\rm zero} = \frac{1}{2}\sum_{\lambda=\alpha,\beta}\sum_{\mathbf{k}} [\mathcal{E}_\lambda(\mathbf{k}) - \epsilon_k] \quad (54)$$

is the energy of the zero-point fluctuations.

Substituting the spectra (26), (27) into Eq. (53) and expanding the final expression in powers of the phase gradients, we find the following expression for the free energy:

$$F = F_0 + \int d^2 r \frac{\hbar^2}{2m}[\rho_{s1}(\nabla\varphi_1)^2 + \rho_{s2}(\nabla\varphi_2)^2 - \rho_{\rm dr}(\nabla\varphi_1 - \nabla\varphi_2)^2] + \text{higher order terms}, \quad (55)$$

where F_0 does not depend on the phase gradients, and the quantities ρ_{sl} and $\rho_{\rm dr}$ are determined by expressions (31) and (32). One can see that the answer (29)–(32) obtained in Sec. 3 by another method can also be found from Eq. (55) using the relation

$$\mathbf{j}_l = \frac{1}{\hbar S}\frac{\partial F}{\partial(\nabla\varphi_l)}. \quad (56)$$

Relation (55) is more instructive in the sense that it demonstrates an analogy between the drag effect in superfluids and the exciting of a supercurrent by an external magnetic field in superconductors. To illustrate this analogy let us consider two ring-shaped traps and fix the phase gradient in the drive trap (trap 2 in the notation used below). Then the free energy as a function of the phase gradient in the drag trap (trap 1) can be presented in the form

$$F = \text{const} + \frac{\pi\hbar^2 w}{mR}\tilde{\rho}_{s1}(\Phi + \Phi_{\rm dr})^2, \quad (57)$$

where R is the radius of the ring, w is its width, $\tilde{\rho}_{s1} = \rho_{s1} - \rho_{\rm dr}$,

$$\Phi = \frac{1}{2\pi}\oint_C d\mathbf{l}\nabla\varphi_1 \quad (58)$$

(here C is a contour around the ring) is the winding number for the phase φ_1, and

$$\Phi_{\rm dr} = \frac{\rho_{\rm dr}}{\tilde{\rho}_{s1}}\frac{1}{2\pi}\oint_C d\mathbf{l}\nabla\varphi_2 \quad (59)$$

is the winding number for the phase φ_2 times the drag factor. In deriving (57) we, for simplicity, neglect the dependence of the densities on the coordinate inside the traps.

Since the value of Φ must be an integer, the minimum of the free energy at $|\Phi_{\rm dr}| < 1/2$ is reached for $\Phi = 0$. In this case the phase gradient in the drag trap is equal to zero, and the superfluid current in the drag trap flows in the same direction as in the drive trap. If $|\Phi_{\rm dr}| > 1/2$ the free energy reaches its minimum at nonzero Φ, and a phase gradient is induced in the drag trap. Then, together with the drag current, a counterflow current appears in the drag trap (depending on the value of $\Phi_{\rm dr}$ the total current in this trap can be parallel or antiparallel to the current in the drag trap). Just the same situation takes place in a superconducting ring with nonzero magnetic flux inside the ring. Thus, in two-ring Bose systems the quantity $\Phi_{\rm dr}$ plays the same role as an external magnetic flux (measured in units of flux quanta) in superconducting circuits.

To realize this situation experimentally one should create a circulating superflow in the drive trap. This can be done by elliptic rotating deformation of this trap. The rotation can be switched off when a superflow has been created. The value of the drag current can be found from measurement of the angular momentum of the drag trap. At present a number of methods for measuring this quantity have been realized experimentally.[22–25] The methods are based on the study of the dynamics of collective excitations, on the investigation of interference phenomena under hyperfine state transitions, and on the observation of the dynamics of expansion of the Bose cloud.

To extend the analogy with superconductors, let us consider the case where a drag trap of ring geometry contains a Josephson weak link. Then the free energy as a function of the phase shift $\Delta\varphi$ across the link reads as

$$F = \text{const} - E_J\cos(\Delta\varphi) + \frac{\pi\hbar^2 w}{mR}\tilde{\rho}_{s1}\left(\frac{\Delta\varphi}{2\pi} + \Phi_{\rm dr}\right)^2, \quad (60)$$

where E_J is the Josephson energy. At $E_J > (E_J)_c = \hbar^2 w \tilde{\rho}_{s1}/(2\pi R m)$ and $|\Phi_{dr}| = 1/2, 3/2, \ldots$ the dependence $F(\Delta\varphi)$ has two degenerate minima. If $E_J/(E_J)_c - 1 \ll 1$ these minima are very shallow, and one can expect an observation of a superposition of two quantum states with different phase shifts (and with the superfluid currents flowing in opposite directions). This is the same regime that is required for implementing the superconducting Josephson flux (persistent current) qubit.[26] While in alkali-metal Bose gases the drag factor is rather small, and even under the most favorable conditions the maximum value that can be reached is of order 10^{-2}–10^{-3} (see Sec. 4), the case $|\Phi_{dr}| \approx 1/2$ can be realized in ring-shaped traps of large radius (10^2–10^3 μm).

In closing, we would like to mention another system in which the effects described in this paper may take place, namely, excitonic or electron–hole Bose liquids in electron bilayers. In these systems electron–hole pairs with components belonging to adjacent layers may form a superfluid state. The effect was first predicted in Refs. 27 and 28, and it was recently confirmed experimentally in Ref. 29. The superfluid drag effect may emerge in two parallel bilayers (four-layer system). In the four-layer system the intralayer (in the same bilayer) and interlayer (between bilayers) interactions are of the same order: both of them are determined by the dipole–dipole mechanism. In such a case the dipole moment of the pair is large. Therefore, one can expect that the nondissipative drag in these systems will be rather strong.

This work is supported by INTAS Grant No. 01-2344.

*E-mail: fil@isc.kharkov.ua
†E-mail: shevchenko@ilt.kharkov.ua

[1] A. Rojo, J. Phys.: Condens. Matter **11**, R31 (1999).
[2] S. M. Badalyar and C. S. Kim, cond-mat/0302194.
[3] T. J. Gramila, J. P. Eisenstein, A. H. MacDonald, L. N. Pfeiffer, and K. W. West, Phys. Rev. B **47**, 12957 (1993).
[4] H. C. Tso and P. Vasilopoulos, Phys. Rev. B **45**, 1333 (1992); H. C. Tso, P. Vasilopoulos, and F. M. Peeters, Phys. Rev. Lett. **68**, 2516 (1992); C. Zhang and Y. Takahashi, J. Phys.: Condens. Matter **5**, 5009 (1993).
[5] A. F. Andreev and E. P. Bashkin, Zh. Éksp. Teor. Fiz. **69**, 319 (1975) [Sov. Phys. JETP **42**, 164 (1975)].
[6] J. M. Duan and S. Yip, Phys. Rev. Lett. **70**, 3647 (1993).
[7] B. Tanatar and A. K. Das, Phys. Rev. B **54**, 13827 (1996).
[8] S. V. Terentjev and S. I. Shevchenko, Fiz. Nizk. Temp. **25**, 664 (1999) [Low Temp. Phys. **25**, 493 (1999)].
[9] A. G. Rojo and G. D. Mahan, Phys. Rev. Lett. **68**, 2074 (1992).
[10] J. M Duan, Europhys. Lett. **29**, 489 (1995).
[11] M. H. Anderson, J. R. Ensher, M. R. Matthew, C. E. Wieman, and E. A. Cornell, Science **269**, 198 (1995); C. C. Bradley, C. A. Sackett, J. J. Tollett, and R. G. Hulet, Phys. Rev. Lett. **75**, 1687 (1995); K. B. Davis, M. O. Mewes, M. R. Andrews, N. J. van Druten, D. S. Durfee, D. M. Kurn, and W. Ketterle, Phys. Rev. Lett. **75**, 3969 (1995).
[12] A. Görlitz, J. M. Vogels, A. E. Leanhardt, C. Raman, T. L. Gustavson, J. R. Abo-Shaeer, A. P. Chikkatur, S. Gurta, S. Inouye, T. Rosenband, and W. Ketterle, Phys. Rev. Lett. **87**, 130402 (2001).
[13] S. I. Shevchenko, Fiz. Nizk. Temp. **18**, 328 (1992) [Low Temp. Phys. **18**, 223 (1992)].
[14] D. V. Fil and S. I. Shevchenko, Phys. Rev. A **64**, 013607 (2001).
[15] N. N. Bogolyubov and N. N. Bogolyubov Jr., *Introduction to Quantum Statistical Mechanics*, World Scientific, Singapore (1982).
[16] D. S. Petrov, M. Holzmann, and G. V. Shlyapnikov, Phys. Rev. Lett. **84**, 2551 (2000).
[17] R. A. Duine and H. T. C. Stoof, Phys. Rev. A **68**, 013602 (2003).
[18] K. E. Strecker, G. B. Partridge, and R. G. Hulet, Phys. Rev. Lett. **91**, 080406 (2003).
[19] M. Wouters, J. Tempere, and J. T. Devreese, Phys. Rev. A **68**, 053603 (2003).
[20] M. Schick, Phys. Rev. A **3**, 1067 (1971).
[21] D. H. J. O'Dell, S. Giovanazzi, and C. Eberlein, cond-mat/0308096.
[22] F. Chevy, K. W. Madison, and J. Dalibard, Phys. Rev. Lett. **85**, 2223 (2000).
[23] O. M. Marago, S. A. Hopkins, J. Arlt, E. Hodby, G. Hechenblaikner, and C. J. Foot, Phys. Rev. Lett. **84**, 2056 (2000).
[24] F. Chevy, K. W. Madison, V. Bretin, and J. Dalibard, Phys. Rev. A **64**, 031601 (2001).
[25] G. Hechenblaikner, E. Hodby, S. A. Hopkins, O. M. Marago, and C. J. Foot, Phys. Rev. Lett. **88**, 070406 (2002).
[26] Y. Makhin, G. Schön, and A. Shnirman, Rev. Mod. Phys. **73**, 357 (2001).
[27] Yu. E. Lozovik and V. I. Yudson, Zh. Éksp. Theor. Fiz. **71**, 738 (1976) [Sov. Phys. JETP **44**, 389 (1976)].
[28] S. I. Shevchenko, Fiz. Nizk. Temp. **2**, 505 (1976) [Sov. J. Low Temp. Phys. **2**, 251 (1976)].
[29] I. B. Spielman, J. P. Eisenstein, L. N. Pfeiffer, and K. W. West, Phys. Rev. Lett. **84**, 5808 (2000); M. Kellogg, I. B. Spielman, J. P. Eisenstein, L. N. Pfeiffer, and K. W. West, *ibid.* **88**, 126804 (2002); M. Kellogg, J. P. Eisenstein, L. N. Pfeiffer, and K. W. West, *ibid.* **90**, 246801 (2003); A. A. Dremin, V. B. Timofeev, A. V. Larionov, J. Hvam, and K. Soerensen, JETP Lett. **76**, 450 (2002); L. V. Butov, A. C. Gossard, and D. S. Chemla, Nature (London) **418**, 751 (2002); D. Snoke, S. Denev, Y. Liu, L. Pfeiffer, and K. West, *ibid.* **418**, 754 (2002).

This article was published in English in the original Russian journal. Reproduced here with stylistic changes by AIP.

SUPERCONDUCTIVITY, INCLUDING HIGH-TEMPERATURE SUPERCONDUCTIVITY

Transport of charge carriers in a superconductor–semiconductor contact

G. V. Kuznetsov*

Taras Shevchenko Kiev National University, ul. Vladimirskaya 64, Kiev 01133, Ukraine
(Submitted December 30, 2003; revised April 16, 2004)
Fiz. Nizk. Temp. **30**, 1038–1044 (October 2004)

The changes in the passage of charge carriers through a superconducting metal–semiconductor contact with a tunnel-thin intermediate insulating layer upon the transition of the metal to the superconducting state are analyzed. The transition of the metal to the superconducting state leads to a decrease of the forward current and an increase of the reverse current of thermionic emission in such a contact. For a tunneling mechanism of carrier transport a decrease in thickness of the intermediate insulating layer and in the degree of doping of the semiconductor leads to an increase in the nonlinearity parameter of the current–voltage characteristic. © *2004 American Institute of Physics.* [DOI: 10.1063/1.1808195]

INTRODUCTION

Metal–semiconductor contacts are among the basic elements of modern integrated electronics, and investigation of the influence of superconductivity on the passage of current in such contacts is a topical problem. There is also interest in the possibility of regulating the properties of a potential barrier by changing the degree of doping of the semiconducting material. Electron transport processes in superconductor–semiconductor contact structures are usually analyzed in the framework of a tunneling mechanism, which is dominant under conditions of low temperatures and sufficiently thin potential barriers.[1–3] The current–voltage (I–V) characteristics of such contacts are similar to the corresponding characteristics of metal–insulator–superconductor structures (the role of the normal metal is played by the heavily doped semiconductor and the role of the insulator, by the space-charge region of the semiconductor). The differences are due solely to the shape of the potential barrier of the space-charge region. The advent of materials with a significantly higher temperatures of the critical transition to the superconducting state has led to a greater role of the above-barrier mechanism of passage of the charge carriers, which must be taken into account in determining the total current through the contact.[4,5] Furthermore, in real metal–semiconductor contacts an intermediate insulator layer is typically present at the metal–semiconductor interface, the properties of which are determined by the nature of the materials in contact and the technology used to fabricate the contact.[6] The presence of such an intermediate layer determines the structure of the potential barrier of the contact and can lead to a substantial change in both the value of the current passing through the interface and its dependence on the applied voltage. In the majority of cases the intermediate layer formed in the fabrication of a metal–semiconductor contact is not more than 1–10 nm thick, so that it can be regarded as a tunnel-thin insulating layer.

In this paper we discuss the process of charge carrier transport through a superconductor–semiconductor contact with a tunnel-thin intermediate insulating layer for the case of an isotropic superconductor with a wide energy gap $\Delta \neq 0$ in the density of states. The energy band diagram of such a contact is shown in Fig. 1, where φ_b is the height of the potential barrier, eV_b is the diffusion potential, eV_n is the difference of the energies between the Fermi level and the bottom of the conduction band (for a degenerate semiconductor $eV_n>0$), Δ is the superconductor energy gap parameter, and $V=V_1+V_2$ is the voltage applied to the contact (V_1 and V_2 are the voltage drops across the intermediate layer and across the space-charge region, respectively). The passage of charge carriers is analyzed for an n-type semiconductor in the approximations of diode theory (the energy will be measured from the bottom of the conduction band of the semiconductor, $E_c=0$). Calculations were done for the case of an isotropic superconductor characterized by the presence of an energy gap in the density of states.

If the height of the potential barrier $\varphi_b \gg kT$ and if the passage of current does not disturb the thermodynamic equilibrium in the emission region, then the total current I_t through the contact will be determined by the difference between the fluxes of carriers from the surface to the metal, J_{sm}, and from the metal to the superconductor, J_{ms} (Ref. 7).

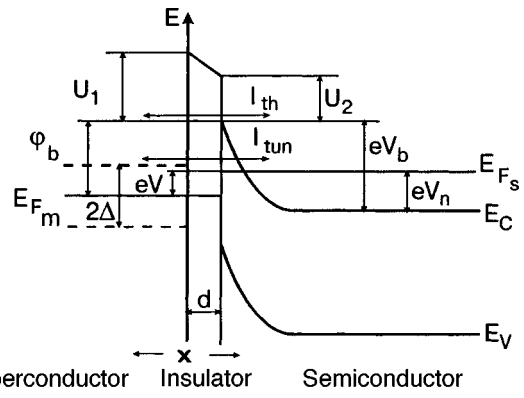

FIG. 1. Energy diagram of a superconductor–semiconductor contact.

The number of electrons passing from the semiconductor into the metal in the energy interval from E to $E+dE$ is proportional to the number of filled states in the semiconductor, $N_s(E)f(E)dE$, the number of unoccupied states in the metal, $N_{ms}(E-eV)[1-f(E-eV)]dE$, and the probability of passage of an electron through the potential barrier, $P_{sm}(E)$:

$$J_{sm}\propto P_{sm}(E)N_s(E)N_{ms}(E-eV)f(E)[1-f(E-eV)]dE. \tag{1}$$

Analogously, one can write for the flux of electrons from the metal into the semiconductor

$$J_{ms}\propto P_{ms}(E)N_s(E)N_{ms}(E-eV)f(E-eV)[1-f(E)]dE. \tag{2}$$

In expressions (1) and (2) we have introduced the following notation: $N_s(E)=[4\pi(2m^*)^{3/2}(E-E_c)^{1/2}]/h^3$ is the density of states in the conduction band of the semiconductor, $N_{ms}(E-eV)=N_m(E-eV)n_s(E-eV)$ is the density of states in the conduction band of the superconducting metal; $N_m(E-eV)=[4\pi(2m^*)^{3/2}(E-E_c+eV)^{1/2}]/h^3$ is the density of states in the normal metal; $n_s(E)=|E-eV_n+eV|[(E-eV_n+eV)^2-\Delta^2]^{-1/2}$ is the superconducting structure of the density of states in the metal; and, $f(E)=[1+\exp(E-eV_n/kT)]^{-1}$ and $f(E-eV)=[1+\exp(E-eV_n+eV/kT)]^{-1}$ are the Fermi distribution functions in the semiconductor and metal, respectively. In calculating the current it is usually assumed that the probability of passage of the charge carriers is independent of their direction of motion: $P_{sm}(E)=P_{ms}(E)=P(E)$, and the density of states in the semiconductor and in the nonsuperconducting metal are slowly varying functions equal to their value at the Fermi surface: $N_s(E)=N_s(0)$ and $N_m(E-eV)=N_m(0)$. The expression for the total current density I_t is obtained after integration over all possible energies:

$$I_t=\frac{G_n}{e}\left\{\int_{eV_n+\Delta-eV}^{\infty}P(E)n_s(E)[(f(E)-f(E-eV)]dE + \int_0^{eV_n-\Delta-eV}P(E)n_s(E)[(f(E)-f(E-eV)]dE\right\}, \tag{3}$$

where $G_n=eAN_n(0)N_m(0)$ is the conductance of the contact in the nonsuperconducting state, and A depends on the geometry of the interface. Equation (3) determines the total number of carriers that are capable of crossing the interface in the superconductor–semiconductor contact at a temperature $T<T_c$.

For determining the energy dependence of the probability of transition of the charge carriers through the potential barrier shown in Fig. 1 we can use the expression obtained for $P(E)$ in the WKB approximation,[6] which in our notation has the form

$$P(E)=P_0\exp\{-\chi[(U_1+eV_b-eV_1-E)^{3/2}-(U_2+eV_b-E)^{3/2}]\}\exp\left\{-\frac{eV_b}{E_{00}}\left(1-\frac{E}{eV_b}\right)^{1/2}-\frac{E}{eV_b}\ln\left[\left(\frac{eV_b}{eV_n}\right)^{1/2}+\left(\frac{eV_b-E}{eV_n}\right)^{1/2}\right]\right\}, \tag{4}$$

where

$$\chi=\frac{8\pi(2m^*)^{1/2}d}{3h(U_1-U_2-eV_1)};\quad E_{00}=\frac{eh}{4\pi}\left(\frac{n_0}{\varepsilon_0\varepsilon_2 m^*}\right)^{1/2};$$

$P_0\sim 1$ is a numerical coefficient.

The first exponential factor in expression (4) determines the transparency of the trapezoidal barrier of the intermediate layer and the second, that of the space-charge region of the semiconductor in the approximation of a uniform impurity distribution.

ABOVE-BARRIER PASSAGE OF CHARGE CARRIERS

Determination of the thermionic component of the current, I_{th}, through a superconductor–semiconductor contact reduces to finding the number of carriers passing above the maximum of the potential barrier: $E\geqslant eV_b=\varphi_b+eV_n-eV_2$.

Voltage interval $eV<\varphi_b$

For $\varphi_b-eV\gg kT$ for the whole range of possible energies of above-barrier electrons $E\geqslant eV_b$ the following relations hold:

$$\exp\left(\frac{E-eV_n}{kT}\right)\gg 1,\quad \exp\left(\frac{E-eV_n+eV}{kT}\right)\gg 1,$$

in which case we have for the difference of the Fermi distribution functions

$$f(E)-f(E-eV)=\left[1-\exp\left(-\frac{eV}{kT}\right)\right]\exp\left(-\frac{E-eV_n}{kT}\right).$$

To determine the influence of the superconducting transition of the metal on the I–V characteristic of the contact we take into account those charge carriers with energies close to the maximum of the potential barrier, which give the main contribution to the thermionic component of the current. Keeping only the first term of the series expansion of the function $n_s(E)$ about the maximum of the potential barrier $eV_b=\varphi_b+eV_n-eV_2$, we obtain

$$n_s(V)\approx\left[1-\left(\frac{\Delta}{\varphi_b+eV_1}\right)^2\right]^{-1/2}.$$

The transparency coefficient for the above-barrier electrons is determined solely by the contribution of the intermediate layer, and, according to (4), in the energy region $E\sim eV_b$ we have

$$P_n(V)=P_0\exp\{-\chi[(U_1-eV_1)^{3/2}-(U_2)^{3/2}]\}. \tag{5}$$

As a rule $\Delta<\varphi_b$, and therefore after integrating (3) from eV_b to ∞ with the values obtained for $P_n(V)$ and $n_s(V)$ taken into account, we find for the thermionic current density

$$I_{\text{th}}=A^*T^2P_n(V)n_s(V)\exp\left(-\frac{\varphi_b}{kT}\right)\left[\exp\left(\frac{eV_2}{kT}\right)-\exp\left(-\frac{eV_1}{kT}\right)\right]. \tag{6}$$

In Eq. (6) we have used the notation $(kT/e)G_n=A^*T^2$, which follows from requirements of consistency of expres-

sion (6) for $\Delta\to 0$, $d\to 0$ with the known expression for the thermionic emission current in an ordinary metal–semiconductor contact:[7]

$$I_{\rm th}=I_s\left[\exp\left(\frac{eV}{kT}\right)-1\right]=A^*T^2\exp\left(-\frac{\varphi_b}{kT}\right)\left[\exp\left(\frac{eV}{kT}\right)-1\right], \tag{7}$$

where $A^*=4\pi em^*k^2/h^3$ is the Richardson constant for thermionic emission.

Voltage interval $eV>\varphi_b$

In this voltage interval the maximum of the potential barrier of the Schottky region $eV_b=\varphi_b+eV_n-eV_2$ is found below the Fermi level eV_n of the semiconductor. For carriers with energy $E\sim eV_b$ we have, for $eV-\varphi_b\gg kT$

$$\exp\left(\frac{E-eV_n}{kT}\right)\ll 1,\quad \exp\left(\frac{E-eV_n+eV}{kT}\right)\gg 1$$

and

$$f(E)-f(E-eV)=1-\exp\left(-\frac{eV}{kT}\right)\approx 1.$$

Using the value of $P(E)$ obtained for $E\sim eV_b$ [Eq. (5)], after evaluation of the integral (3) between the limits eV_b and eV_n we obtain a nearly linear dependence of the current on the applied voltage in the interval $eV>\varphi_b$:

$$I_{\rm th}=A^*T^2P_n(V)\left[1-\exp\left(-\frac{eV}{kT}\right)\right]\times\frac{[(eV)^2-\Delta^2]^{1/2}-[(\varphi_b+eV_1)^2-\Delta^2)]^{1/2}}{kT}. \tag{8}$$

The influence of superconductivity of the metal on the thermionic emission current at a fixed value of the voltage V across the contact can be estimated from the value of the ratio of the current in the superconducting state $I_{\rm th}(S)$ to the current in the normal state $I_{\rm th}(S)/I_{\rm th}(N)$. For "intimate" contact ($d=0$) the ratio $I_{\rm th}(S)/I_{th}(N)$ is determined by the value of Δ/φ_b and is independent of the applied voltage (Fig. 2). In the case $d\neq 0$ the parameters of the I–V characteristic should be determined using the known relations for the redistribution of voltage in a metal–semiconductor contact:[3]

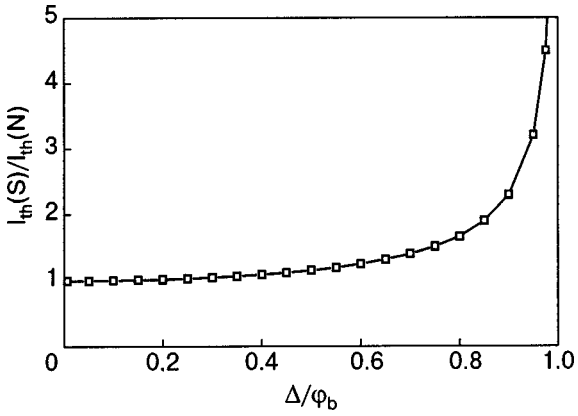

FIG. 2. Dependence of the current ratio $I_{\rm th}(S)/I_{\rm th}(N)$ on the parameter ratio Δ/φ_b ($d=0$).

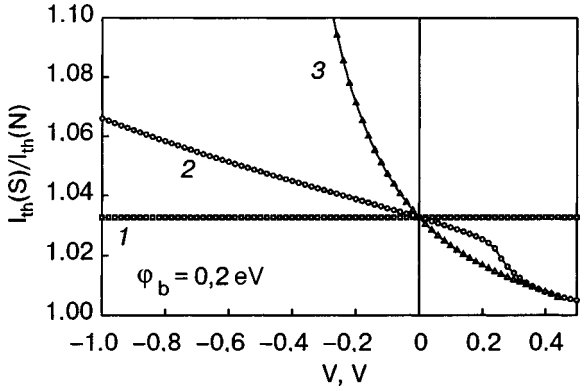

FIG. 3. Dependence of the current ratio $I_{\rm th}(S)/I_{\rm th}(N)$ on the applied voltage ($\Delta/\varphi_b=0.25$) for different values of $\varepsilon_2 d/\varepsilon_1 L_0$: 0 (*1*), 0.1 (*2*), 0.5 (*3*).

$$eV_1=2(\varphi_b+eV_n)\frac{\varepsilon_2 d}{\varepsilon_1 L_0}\times\left\{1+\frac{\varepsilon_2 d}{\varepsilon_1 L_0}-\left[\left(1+\frac{\varepsilon_2 d}{\varepsilon_1 L_0}\right)^2-\frac{eV}{\varphi_b+eV_n}\right]^{1/2}\right\}, \tag{9}$$

where

$$L=\left[\frac{2\varepsilon_0\varepsilon_2(\varphi_b+eV_n-eV_2)}{e^2n_0}\right]^{1/2}$$

is the thickness of the Schottky barrier, L_0 is the value of L at $eV=0$, $eV_n=(3n_0/8\pi)^{2/3}h^2/m^*$ for a degenerate semiconductor, ε_1 and ε_2 are the dielectric constants of the intermediate layer and the semiconductor, respectively, and n_0 and m^* are the density and effective mass of the charge carriers in the semiconductor.

Figure 3 shows the dependence of the ratio $I_{\rm th}(S)/I_{\rm th}(N)$, calculated according to (6)–(9), on the voltage V applied to the contact for different values of $\varepsilon_2 d/\varepsilon_1 L_0$. With increasing thickness d of the intermediate layer the ratio $I_{\rm th}(S)/I_{\rm th}(N)$ decreases for forward voltages and increases for reverse voltages (curves *2* and *3* in Fig. 3). The dependence of $I_{\rm th}(S)/I_{\rm th}(N)$ on V and d derives from the dependence on the applied voltage of the height eV_b of the Schottky potential barrier, which determines the energy of the above-barrier charge carriers. With increasing forward voltage the the value of φ_b+eV_1 increases, the influence of the superconducting structure of the density of states in the metal becomes weaker, and $I_{\rm th}(S)/I_{\rm th}(N)\to 1$.

The difference in the changes of the forward and reverse currents upon the transition of the metal to the superconducting state can even lead to a change in sign of the rectification in the metal–semiconductor contact at large values of the ratio $\varepsilon_2 d/\varepsilon_1 L_0$. Experimentally the change in sign of the rectification in metal–semiconductor contacts has been observed for $YBa_2Cu_3O_{7-x}$–Si structures at a high degree of doping of the silicon (small values of L_0)[8] and for $YBa_2Cu_3O_{7-x}$–$NdGaO_3$–$SrTiO_3$ structures (large values of ε_2).[9]

Nonlinearity parameter of the I–V characteristic

The nonlinearity parameter $\alpha=d\ln I/dV$ characterizes the degree of current growth with increasing applied forward

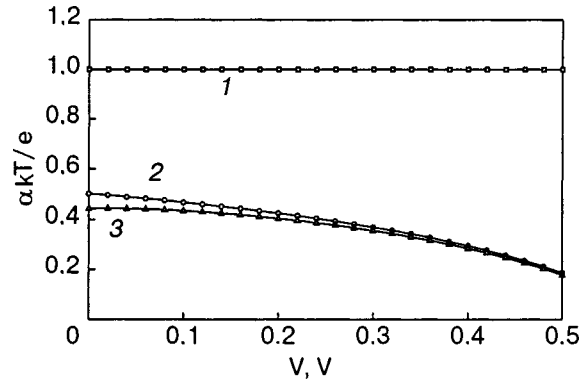

FIG. 4. Influence of the superconductivity of the metal on the nonlinearity parameter α for the thermionic component of the current: *1*—$d=0$; *2*—$\varepsilon_2 d/\varepsilon_1 L_0=1$, $\Delta=0$; *3*—$\varepsilon_2 d/\varepsilon_1 L_0=1$, $\Delta/\varphi_b=0.25$.

voltage and is one of the main parameters of a metal–semiconductor contact. For a metal–semiconductor contact at $eV \gg kT$ we obtain, after differentiation of (6),

$$\alpha=\frac{e}{kT}\frac{dV_2}{dV}+\frac{d\ln P_n(V)}{dV}+\frac{d\ln n_s(V)}{dV}$$
$$=\frac{e}{kT}\left[1-\frac{dV_1}{dV}\left(1-a_t\frac{kT}{e}-a_\Delta\frac{kT}{e}\right)\right], \qquad (10)$$

where

$$\frac{dV_2}{dV}=\left(1+\frac{\varepsilon_2 d}{\varepsilon_1 L}\right)^{-1};\quad \frac{dV_1}{dV}=\frac{\varepsilon_2 d}{\varepsilon_1 L}\left(1+\frac{\varepsilon_2 d}{\varepsilon_1 L}\right)^{-1};$$

$$\frac{d\ln P_n(V)}{dV}=a_t\frac{dV_1}{dV};\quad \frac{d\ln n_s(V)}{dV}=a_\Delta\frac{dV_1}{dV};$$

$$a_t=e\chi\left[\frac{3}{2}(U_1-eV_1)^{1/2}-\frac{(U_1-eV_1)^{3/2}-U_2^{3/2}}{U_1-U_2-eV_1}\right];$$

$$a_\Delta=-e\left\{(\varphi_b+eV_1)\left[\left(\frac{\varphi_b+eV_1}{\Delta}\right)^2-1\right]\right\}^{-1}.$$

Figure 4 shows the dependence of the parameter α on the applied voltage. The calculation was done for the interval of voltages $U_1 \gg eV_1$ at $a_t=0.5$, $\varphi_b=0.2$ eV, $\Delta/\varphi_b=0.25$, $\varepsilon_2 d/\varepsilon_1 L_0=1$. For $d=0$ the transition of the metal to the superconducting state does not lead to changes in the parameter α. With increasing d the influence of the superconductivity grows, causing a slight decrease in the parameter α (curve *3* in Fig. 4).

TUNNELING THROUGH THE POTENTIAL BARRIER REGION

In determining the tunneling component of the current through a superconductor–semiconductor contact it is necessary to take into account in (3) the energy dependence of the probability of transition of a charge carrier through the potential barrier region. For heavily doped semiconductors at sufficiently low temperatures ($E_{00} \gg kT$) the current through the contact is determined by the tunneling of electrons having energies close to the Fermi level (field emission). If the Fermi energy is small compared with the effective barrier height, i.e., if $eV_b \gg eV_n$, then in the region of energies $E \sim eV_n$ we obtain for the transparency coefficient of the barrier (4), after suitable manipulations,

$$P(V)=P_0\exp\{-\chi[(U_1+\varphi_b-eV)^{3/2}-(U_2+\varphi_b-eV_2)^{3/2}]\}\exp\left(-\frac{\varphi_b+eV_n-eV_2}{E_{00}}\right). \qquad (11)$$

Voltage interval $-\Delta \leqslant eV \leqslant \Delta$

By taking the transparency coefficient $P_n(V)$ out from under the integral sign in (3), one can determine the I–V characteristic of the contact for the voltage interval $-\Delta \leqslant eV \leqslant \Delta$, where the influence of the superconducting state on the tunneling current is the most substantial. The calculation is done by making the change of variables $x=E-eV_n-\Delta+eV$ in the first and $x=-E+eV_n-\Delta-eV$ in the second integral of formula (3). For $\Delta \gg kT$ the relation

$$f(E)-f(E-eV)=\exp\left(-\frac{x+\Delta}{kT}\right)\left[\exp\left(\frac{eV}{kT}\right)-1\right]$$

holds for the first and

$$f(E)-f(E-eV)=\exp\left(-\frac{x+\Delta}{kT}\right)\left[1-\exp\left(-\frac{eV}{kT}\right)\right]$$

holds for the second term of (3), and after suitable manipulations we obtain

$$I_{\text{tun}}=\frac{G_n}{e}P(V)\exp\left(-\frac{\Delta}{kT}\right)\left[\exp\left(\frac{eV}{kT}\right)-\exp\left(-\frac{eV}{kT}\right)\right]$$
$$\times\int_0^\infty\frac{x+\Delta}{\sqrt{x(x+2\Delta)}}\exp\left(-\frac{x}{kT}\right)dx. \qquad (12)$$

The integral in (12) can be found in tables of Laplace transforms:[10]

$$\int_0^\infty\frac{(x+\Delta)\exp(-x/kT)}{\sqrt{x(x+2\Delta/kT)}}dx=\Delta\exp\left(\frac{\Delta}{kT}\right)K_1\left(\frac{\Delta}{kT}\right),$$

where $K_1(\Delta/kT)$ is the modified Bessel function of the second kind of order one. For $\Delta \gg kT$ we can use the following asymptotic expression for the Bessel function:

$$K_1\left(\frac{\Delta}{kT}\right)\approx\left(\frac{\pi kT}{2\Delta}\right)^{1/2}\exp\left(-\frac{\Delta}{kT}\right)$$

and, after substitution, obtain for the current density I_{tun}

$$I_{\text{tun}}=A^*T^2P(V)\left(\frac{\pi\Delta}{2kT}\right)^{1/2}\exp\left(-\frac{\Delta}{kT}\right)\left[\exp\left(\frac{eV}{kT}\right)-\exp\left(-\frac{eV}{kT}\right)\right]. \qquad (13)$$

Voltage interval $eV > \Delta$

In the voltage interval $eV > \Delta$ the tunneling current is determined by charge carriers with energy $E \leqslant eV_n$, for which at $\Delta \gg kT$ the following relations hold:

$$\exp\left(\frac{E-eV_n}{kT}\right)\ll 1,\quad \exp\left(\frac{E-eV_n+eV}{kT}\right)\gg 1$$

and

$$f(E)-f(E-eV)=\left[1-\exp\left(-\frac{eV}{kT}\right)\right].$$

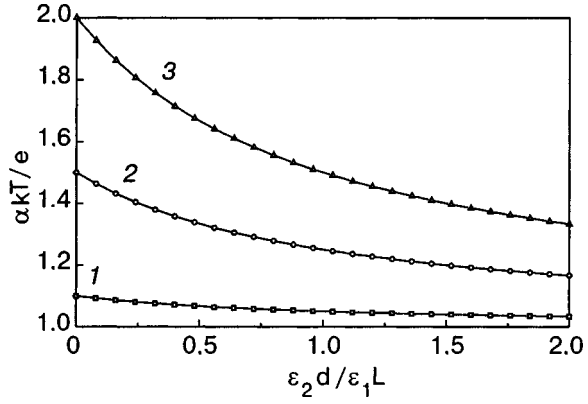

FIG. 5. Curves of the parameter α for a superconductor–semiconductor tunnel contact for different ratios kT/E_{00}: 0.1 (*1*), 0.5 (*2*), 1 (*3*).

After evaluation of the integral (3) between the limits $eV_n+\Delta-eV$ and eV_n we obtain a close to linear dependence of the tunneling component of the current I_{tun} on the applied voltage:

$$I_{\text{tun}}=A^*T^2P(V)\left[1-\exp\left(-\frac{eV}{kT}\right)\right]\frac{[(eV)^2-\Delta^2]^{1/2}}{kT}. \tag{14}$$

The asymmetry of the tunneling I–V characteristic of a superconductor–semiconductor contact is due to the dependence of the transparency coefficient $P(V)$ on the applied voltage. For $\Delta\to 0$, $d\to 0$ relation (14) reduces, up to a preexponential factor, to the well-known expression for the tunneling current in an ordinary metal–semiconductor contact:[7]

$$I_{\text{tun}}=I_{\text{st}}\exp\left(\frac{eV}{E_{00}}\right)\left[1-\exp\left(-\frac{eV}{kT}\right)\right]. \tag{15}$$

Nonlinearity parameter of the I–V characteristic

For the tunneling charge carriers with energy $E\sim eV_n$ in the voltage interval $-\Delta\leqslant eV\leqslant\Delta$ one can neglect the dependence of the transparency coefficient of the insulator layer on the applied voltage. For $eV\geqslant kT$ the nonlinearity parameter $\alpha=d\ln I/dV$ can be written in the form

$$\alpha=\frac{e}{kT}+\frac{d\ln P(V)}{dV}\approx\frac{e}{kT}\left[1+\frac{kT}{E_{00}}\frac{dV_2}{dV}\right]. \tag{16}$$

Figure 5 shows the dependence of the parameter α on the ratio $\varepsilon_2 d/\varepsilon_1 L$ for the tunneling component of the current, calculated according to relation (16). There is a characteristic growth of the values of the parameter α with decreasing thickness d of the intermediate layer, this growth being more substantial at large values of the kT/E_{00}, i.e., at higher temperatures and lower carrier densities in the semiconductor. The dependence of the parameter α described by formula (16) can be compared with the known experimental results of a study of ''super-Schottky'' diodes.[11] It is clear that the presence of the intermediate insulating layer at the superconductor–semiconductor interfaces is one of the main obstacles to achieving maximal values of the nonlinearity parameter of the I–V characteristic in such diodes. At the same time, for superconductor–semiconductor contacts based on cuprate metal oxides the tunneling processes are complicated to a considerable degree by the anisotropy of the properties of the high-temperature superconductor.[12,13]

CONCLUSIONS

We have analyzed the influence of an intermediate insulating layer on the thermionic and tunneling components of the current in a superconductor–semiconductor contact. The transition of the metal to the superconducting state causes a decrease of the forward current and an increase of the reverse current of thermionic emission in a metal–semiconductor contact. In the case of ''intimate'' contact, at intermediate layer thickness $d=0$, the ratio of the above-barrier current in the superconducting and nonsuperconducting states is independent of the applied voltage and increases with increasing ratio Δ/φ_b. In a superconductor–semiconductor tunneling contact the nonlinearity parameter of the I–V characteristic $\alpha=d\ln I/dV$ decreases with increasing relative thickness of the intermediate insulating layer and increasing degree of doping of the semiconductor.

*E-mail: kuznetsov@uninet.kiev.ua

[1] E. L. Wolf, *Principles of Electron Tunneling Spectroscopy*, Oxford Univ. Press, New York (1985), Naukova Dumka, Kiev (1990).
[2] A. W. Kleinsasser, T. N. Jackson, D. McInfurt, F. Rammo, G. D. Pettit, and J. M. Woodall, Appl. Phys. Lett. **57**, 1811 (1990).
[3] B. J. Van Wees, P. de Vries, P. Magnee, and T. M. Klapwijk, Phys. Rev. Lett. **69**, 510 (1992).
[4] R. Kummel, H. Plehn, and U. Schussler, in *Proceedings of the 23rd International Conference on the Physics of Semiconductors, Berlin*, **11.E.2**, 3387 (1996).
[5] G. V. Kuznetsov, JETP Lett. **74**, 495 (2001).
[6] V. I. Strikha, *Contact Phenomena in Semiconductors* [in Russian], Vishcha Shkola, Kiev (1982).
[7] S. M. Sze, *Physics of Semiconductor Devices*, 2nd ed., Wiley, New York (1981), Mir, Moscow (1984).
[8] V. I. Strikha, B. B. Il'chenko, and B. S. Nevolin, *Abstracts of the Second All-Union Conference on High-Temperature Superconductivity* [in Russian], Kiev (1989), p. 214.
[9] H. Takauchi, A. Yoshida, H. Tamura, T. Imamura, and S. Hasuo, Appl. Phys. Lett. **61**, 1462 (1992).
[10] A. Erdéli, it Tables of Integral Transforms (H. Bateman Manuscript Project, Vol. 1, McGraw-Hill, New York (1953), Nauka, Moscow (1969).
[11] R. I. Pedersen and M. McColl, IEEE Trans. Magn. **25**, 286 (1977).
[12] C. Bruder, Phys. Rev. B **41**, 4017 (1990).
[13] F. V. Komissinskiĭ, G. A. Ovsyannikov, and Z. G. Ivanov, Fiz. Tverd. Tela (St. Petersburg) **43**, 769 (2001) [Phys. Solid State **43**, 801 (2001)].

Translated by Steve Torstveit

LOW-TEMPERATURE MAGNETISM

Magnetization of a nonferromagnetic metal spacer sandwiched between two magnetically ordered layers

V. Yu. Gorobets*

Institute of Magnetism of the National Academy of Sciences of Ukraine, 36-b Vernadsky Ave. Kiev 03142, Ukraine

(Submitted January 6, 2004, revised April 1, 2004)
Fiz. Nizk. Temp. **30**, 1045–1052 (October 2004)

The exchange coupling of magnetically ordered layers (MOLs) through a nonmagnetic metallic spacer is calculated. The induced magnetization in the spacer, taking into account the influence of an external magnetic field, is calculated, too. This calculation shows that the energy of coupling of the MOLs through the nonmagnetic metallic spacer is a long-periodic function of the spacer thickness and magnetic field, i.e., the exchange coupling between the layers varies from ferromagnetic to antiferromagnetic and *vice versa* depending on the spacer thickness and magnetic field. Also this calculation shows that in nonferromagnetic spacer the induced magnetization can undergo many complete rotations, depending on distance to the boundaries with the MOLs. Moreover, absolute value of the induced magnetization decays nonmonotonically with distance from the interfaces inside the spacer. It is shown that the character of the decay of the absolute value of the magnetization from the interfaces into the interior of the spacer is influenced by magnetic field.
[DOI: 10.1063/1.1808196]

In the last decade much effort has been dedicated to the study of the magnetic coupling in nanoscale multilayer systems, because ultrathin magnetic films exhibit unusual magnetic configurations and couplings not found in bulk systems.[1,2] In particular, in trilayer systems of the ferromagnet–nonmagnetic spacer–ferromagnet type (e.g., Fe/Cr/Fe, Fe/Cu/Fe, etc.) long-periodic oscillating exchange coupling as a function of spacer thickness has been found.[3–7] This means that the coupling changes from antiferromagnetic to ferromagnetic with spacer thickness. For deeper understanding of indirect exchange coupling through a nonmagnetic spacer one needs to investigate the magnetic properties of a nonmagnetic spacer in a multilayer system. Moreover, investigation of the magnetic properties of a nonmagnetic spacer sandwiched between ferromagnetic layers is very important not only because of oscillating exchange coupling, but also because the contact of a ferromagnetic layer with a nonmagnetic spacer must change the electronic state of the nonmagnetic spacer. Also, many experimental and theoretical works are dedicated to the study of such trilayer systems as antiferromagnet–nonmagnetic spacer–antiferromagnet. Such systems attract much research interest because they can be used in magneto-resistive devices, for example, in magnetic field sensors, magnetic heads in memory devices, etc. In view of the aforementioned problems some studies have been devoted to investigation of the distribution of magnetization induced in a nonmagnetic metal spacer sandwiched between two ferromagnetic layers. Of great interest is the question of the possibility of inducing magnetization in a material which in the normal state is nonmagnetic but which can be polarized if it borders with a magnetically ordered material.[8] Magnetic polarization of a nonmagnetic material by a magnetically ordered material is usually called the proximity effect. The experimental study of the proximity effect is described in some works.[9–11] For example, the magnetic polarization of a nonmagnetic Au spacer in multilayer systems of the ferromagnet–nonmagnetic spacer–ferromagnet type has been measured with the help of Mössbauer spectroscopy using probe atoms in an Au spacer.[12] A small induced magnetic moment in Cu at a Co/Cu interface was detected in Refs. 13 and 14 using circular dichroism and in Ref. 15 using NMR. The oscillating exchange coupling between two ferromagnetic layers separated by a nonmagnetic metal spacer is explained in some theoretical works, usually using RKKY coupling.[16] Moreover, oscillatory exchange coupling between two ferromagnetic layers separated by a nonmagnetic metal spacer layer is associated with oscillation of the magnetic moment in the nonmagnetic spacer layer.[3,17–19] The magnetic moment induced in a nonmagnetic metallic spacer between two ferromagnets with magnetizations turned at an arbitrary angle is calculated theoretically in Ref. 17. As is shown in Ref. 17, the induced magnetization rotates along a complex three-dimensional spiral and can undergo many complete rotations.

In this work we propose a phenomenological method of calculating both the oscillating exchange coupling of magnetically ordered layers through a nonmagnetic metallic spacer and the induced magnetization in a the nonmagnetic spacer using a spin-density model[20] similar to the Ginzburg–Landau model.[21] In comparison with Ref. 17 the approach proposed in our work allows one to calculate the magnetization induced in the spacer and the oscillating exchange cou-

pling taking into account the influence of external magnetic field. The approach can be used whether the magnetically ordered layers are ferromagnetic or antiferromagnetic. To consider the system "magnetically ordered layer–nonmagnetic metallic spacer–magnetically ordered layer" (MOL–NMMS–MOL) in magnetic field, let us consider the case when external magnetic field H is parallel to the z axis and directed perpendicularly to the plane of the spacer. The interface of the spacer with the first MOL is situated in the xy plane, the interface of the spacer with the second MOL is situated in the $z=L$ plane parallel to xy. Following Ref. 20, let us define the order parameter for the spacer as the two-component function

$$\psi=\begin{pmatrix}\Phi_1\\ \Phi_2\end{pmatrix}, \tag{1}$$

in terms of which the magnetic moment density of the spacer is written as

$$\mathbf{M}=\mu_0\psi^+\hat{\boldsymbol{\sigma}}\psi, \tag{2}$$

where μ_0 is a phenomenological parameter and $\hat{\boldsymbol{\sigma}}$ are the Pauli matrices. We suppose in our approach that the state of the MOLs does not depend on the distribution of the order parameter inside the spacer and is characterized only by the directions of homogenous magnetization. Using the approach of Ref. 20 and the functional method of the Ginzburg–Landau type for the order parameter ψ, we write the following Lagrangian function:

$$L=\int\left[\frac{1}{2}i\hbar(\dot{\psi}^+\psi-\psi^+\dot{\psi})-w(\psi)\right]d\mathbf{r}. \tag{3}$$

Here w is the energy density written to forth-order accuracy in powers of the function ψ:

$$w(\psi)=A\nabla\psi^+\nabla\psi+\beta\psi^+\psi+\frac{s}{2}(\psi^+\psi)^2 - \mu_0 H(\psi^+\hat{\sigma}_2\psi), \tag{4}$$

where A, β, and s are phenomenological parameters of the spacer.

From Eq. (3) in a trivial manner we obtain

$$i\hbar\frac{\partial\psi}{\partial t}=A\Delta\psi-\beta\psi-s(\psi^+\psi)\psi+\mu_0 H\hat{\sigma}_z\psi \tag{5}$$

for the order-parameter function, which depends on time and coordinates inside the spacer. The boundary conditions have the form

$$\psi|_{z=0}=\text{const},\quad \psi|_{z=L}=\text{const}, \tag{6}$$

where the points $z=0$ and $z=L$ are the coordinates of the interfaces (see Fig. 1). The solution of Eq. (5) is sought in the form

$$\psi=\begin{pmatrix}\psi_1(\mathbf{r})\exp(i\omega_1 t)\\ \psi_2(\mathbf{r})\exp(i\omega_2 t)\end{pmatrix}. \tag{7}$$

By inserting Eq. (7) into Eq. (3) one obtains the system of nonlinear equations which determines the dependence of ψ_1 and ψ_2 on the space coordinates $\mathbf{r}$:

$$\begin{cases}\Delta\psi_1+a_1\psi_1-b(|\psi_1|^2+|\psi_2|^2)\psi_1+h\psi_1=0\\ \Delta\psi_2+a_2\psi_2-b(|\psi_1|^2+|\psi_2|^2)\psi_2-h\psi_2=0,\end{cases} \tag{8}$$

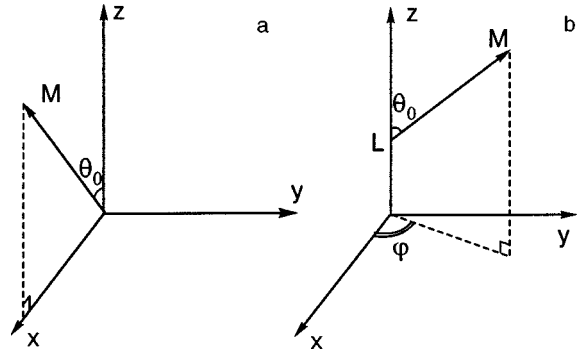

FIG. 1. Direction of magnetization of the spacer at the boundary with the first MOL, $z=0$ (a), and with the boundary with the second MOL, $z=L$ (b).

where $a_i=(\hbar\omega_i-\beta)/A$; $b=s/A$; $h=\mu_0 H/A$.

For simplicity we suppose that the external magnetic field H changes the directions of the magnetizations of the MOLs in the same way, i.e., the polar angle $\theta_0=\theta_0(H)$ for the MOL magnetizations is the same, and the difference in their orientation is described only by change of azimuth angle φ. We choose the constants in the boundary conditions (6) taking into account that the magnetic moment density of the spacer at the interfaces must be parallel or antiparallel, respectively, to the direction of magnetization of the MOLs on variation of the sign of the exchange coupling. Also we suppose that the exchange coupling between the magnetization in the spacer and the magnetizations of the MOLs is appreciable only within the interfacial regions ($a\ll L$), i.e., that MOLs influence the spacer only through the boundary conditions (6). We assume that the magnetization in the spacer at the boundaries with the MOLs is parallel to the magnetization of the MOLs. The case when the orientation is antiparallel can be considered analogously. In accordance with the above-said, one can write the boundary condition using a spherical coordinate system (see Fig. 1) and Pauli matrices, in the form

$$\begin{cases}M_0\sin\theta_0=\mu_0(\Phi_1^*\Phi_2+\Phi_2^*\Phi_1)|_{z=0}\\ 0=-i\mu_0(\Phi_1^*\Phi_2-\Phi_2^*\Phi_1)|_{z=0}\\ M_0\cos\theta_0=\mu_0(\Phi_1^*\Phi_1-\Phi_2^*\Phi_2)|_{z=0}\end{cases}, \tag{9}$$

$$\begin{cases}M_0\sin\theta_0\cos\varphi=\mu_0(\Phi_1^*\Phi_2+\Phi_2^*\Phi_1)|_{z=L}\\ M_0\sin\theta_0\sin\varphi=-i\mu_0(\Phi_1^*\Phi_2-\Phi_2^*\Phi_1)|_{z=L},\\ M_0\cos\theta_0=\mu_0(\Phi_1^*\Phi_1-\Phi_2^*\Phi_2)|_{z=L}\end{cases} \tag{10}$$

where M_0 is the magnitude of the magnetization at the boundaries, which plays the role of a phenomenological parameter of our problem. The magnitude $|\mathbf{M}|$ is chosen the same on both interfaces, equal to $M_0\approx\mu_0/V_0$ (where V_0 is the unit cell volume near the interface of a spacer layer of thickness a, $V_0=L_xL_ya$), taking into account the assumption of the strong polarizing effect of MOLs on the magnetization of the spacer in the immediate neighborhood of the interface.

It's easy to see using direct substitution, that

$$\psi=\begin{pmatrix}B_1e^{i\delta_1}e^{i\kappa_1\rho}e^{-ik_1z}e^{i\omega_1 t}\\ B_2e^{i\delta_2}e^{i\kappa_2\rho}e^{ik_2z}e^{i\omega_2 t}\end{pmatrix}, \tag{11}$$

where κ_i, δ_i, and ω_i are real magnitudes, and $\boldsymbol{\rho}=(x,y)$ satisfies the system of nonlinear equations (8) if the following relations between parameters are fulfilled:

$$\begin{cases} -(\kappa_1^2+k_1^2)+a_1-b(B_1^2+B_2^2)+h=0 \\ -(\kappa_2^2+k_2^2)+a_2-b(B_1^2+B_2^2)-h=0 \end{cases}. \tag{12}$$

To make the solution (11) satisfy the boundary conditions, it is necessary that

$$\begin{cases} \omega_1=\omega_2=\omega \\ \kappa_2=\kappa_1=\kappa, \\ \delta_2-\delta_1=\varphi_0 \end{cases} \quad \begin{cases} B_1=\sqrt{m_0}\cos\dfrac{\theta_0}{2} \\ \\ B_2=\sqrt{m_0}\sin\dfrac{\theta_0}{2} \end{cases}, \tag{13}$$

$$k_1+k_2=\frac{\varphi+2N\pi}{L},$$

where the conditions

$$N=0,\pm1,\ldots, \quad m_0=\frac{M_0}{\mu_0} \tag{14}$$

are fulfilled, too. Then the solution satisfying the system of nonlinear equations (8) and the boundary conditions (9), (10) is transformed to the form

$$\psi=\sqrt{m_0}e^{i\omega t}e^{i(\kappa\rho+\delta)} \times\begin{pmatrix} \cos\dfrac{\theta_0}{2}\exp\left(-i\left\{\dfrac{\varphi+2N\pi}{2L}+\dfrac{\mu_0 HL}{A(\varphi+2N\pi)}\right\}z\right) \\ \sin\dfrac{\theta_0}{2}\exp\left(i\left\{\dfrac{\varphi+2N\pi}{2L}-\dfrac{\mu_0 HL}{A(\varphi+2N\pi)}\right\}z\right) \end{pmatrix},$$

$$\text{if } \varphi\neq0,\ H>0,\ N=0,\ \pm1,\ldots$$

$$\psi=\sqrt{m_0}e^{i\omega t}e^{i(\kappa\rho+\delta)} \times\begin{pmatrix} \cos\dfrac{\theta_0}{2}\exp\left(-i\left\{\dfrac{N\pi}{L}+\dfrac{\mu_0 HL}{2AN\pi}\right\}z\right) \\ \sin\dfrac{\theta_0}{2}\exp\left(i\left\{\dfrac{N\pi}{L}-\dfrac{\mu_0 HL}{2AN\pi}\right\}z\right) \end{pmatrix},$$

$$\text{if } \varphi=0,\ H>0,\ N=\pm1,\ \pm2,\ldots. \tag{15}$$

By inserting the solution (15) into relation (12) one obtains

$$\varepsilon_N=\beta+m_0 s+A\kappa^2+A\left(\frac{\varphi+2N\pi}{2L}\right)^2 +A^{-1}\left(\frac{\mu_0 HL}{\varphi+2N\pi}\right)^2, \tag{16}$$

where $\varepsilon_N=\hbar\omega$. Let us assume that Eq. (15) describes the states of quasiparticles (which we will call magnetized electrons) that behave according to Fermi–Dirac statistics. According to Ref. 22 let us define the total number of magnetized electrons in the spacer magnetically polarized by the MOLs, N_0, as a sum over all possible states of the distribution function. For simplicity we consider the case when $T=0$, because the most interesting magnetoresistive properties of multilayered nanostructured systems appear at low temperatures. Then the Fermi–Dirac distribution function has the form

$$f_0(\varepsilon_N)=\begin{cases} 1, & \varepsilon_N\leqslant\varepsilon_F \\ 0, & \varepsilon_N>\varepsilon_F \end{cases}, \tag{17}$$

where ε_F is the Fermi energy of the magnetized electrons.

According to Eq. (17), the total number of magnetized electrons in the spacer is written in the form

$$N_0=2\frac{L_x L_y}{(2\pi)^2}\sum_N\int_0^{\kappa_N}2\pi\kappa d\kappa, \tag{18}$$

where $L_x\approx L_y\gg L$ are the dimensions of the spacer in the xy plane, and κ_N is the largest possible value of the wave vector κ when N is fixed. κ is calculated as

$$\kappa_N=\sqrt{\frac{\varepsilon_F-\beta-m_0 s}{A}-\left(\frac{\varphi+2N\pi}{2L}\right)^2-\left(\frac{\mu_0 HL}{A(\varphi+2N\pi)}\right)^2}. \tag{19}$$

It is easy to obtain from Eq. (13) that

$$nL=\frac{1}{2\pi}\sum_N\kappa_N^2, \tag{20}$$

where $n=N_0/(L_x L_y L)$ is the density of magnetized electrons in the spacer. The components of the specific magnetization of magnetized electrons in a plane with an arbitrary coordinate z inside the spacer, when Eq. (2) is taken into account, have the form:

$$\begin{cases} M_{xN}=M_0\sin\theta_0\cos\left(\dfrac{\varphi+2N\pi}{L}z\right) \\ \\ M_{yN}=M_0\sin\theta_0\sin\left(\dfrac{\varphi+2N\pi}{L}z\right) \\ \\ M_{zN}=M_0\cos\theta_0 \end{cases}. \tag{21}$$

The average x component of the specific magnetization of the near-interface spacer layer of thickness a equals

$$\langle M_{xN}\rangle=L_x L_y\int_0^a M_0\sin\theta_0\cos\left(\frac{\varphi+2N\pi}{L}z\right)dz=\frac{LL_x L_y M_0\sin\theta_0\sin\left(\dfrac{\varphi+2N\pi}{L}a\right)}{\varphi+2N\pi}. \tag{22}$$

The average y component of the specific magnetization of the near-interface spacer layer of thickness a equals

$$\langle M_{yN}\rangle-L_x L_y\int_0^a M_0\sin\theta_0\sin\left(\frac{\varphi+2N\pi}{L}z\right)dz=-\frac{LL_x L_y M_0\sin\theta_0\cos\left(\dfrac{\varphi+2N\pi}{L}a\right)}{\varphi+2N\pi}. \tag{23}$$

The average z component of the specific magnetization of the near-interface spacer layer of thickness a accordingly equals

$$\langle M_{zN}\rangle=L_x L_y M_0 a\cos\theta_0. \tag{24}$$

In the limiting case when $a\ll L$, the average absolute value of the magnetization of near-interface spacer layer, $\langle M\rangle$

$=\sqrt{\langle M_{xN}\rangle^2+\langle M_{yN}\rangle^2+\langle M_{zN}\rangle^2}$, equals $L_xL_yM_0a$. With the help of Eq. (17) one can find the magnetization of the near-interface spacer layer of thickness a:

$$M=2\frac{L_xL_yM_0}{(2\pi)^2}\sum_N\int_0^{\kappa_N}2\pi\kappa d\kappa. \tag{25}$$

Taking into account Eq. (20), one can find that $M=M_0nL_xL_yL$. Using the ratio $M_0=\mu_0/(L_xL_ya)$, one can write

$$M=\frac{\mu_0nL}{a}, \tag{26}$$

hence:

$$n=\frac{Ma}{\mu_0L}. \tag{27}$$

We denote $n_0=M/\mu_0$ and $n=a_0/L$, where $a_0=Ma/\mu_0$ is a phenomenological constant.

Taking into account Eqs. (19) and (20), we obtain a transcendental algebraic equation for finding the Fermi energy ε_F:

$$nL=\frac{1}{2\pi}\sum_N\left\{\frac{\varepsilon_F-\beta-m_0s}{A}-\left(\frac{\varphi+2N\pi}{2L}\right)^2-\left(\frac{\mu_0HL}{A(\varphi+2N\pi)}\right)^2\right\}, \tag{28}$$

where the allowed values of N are found from the inequality $\kappa_N^2\geqslant 0$. N belongs to

$$N\in\left[-\mathrm{floor}\left\{\frac{\varphi}{2\pi}+\frac{\mu_2}{2\pi}\right\};-\mathrm{ceil}\left\{\frac{\varphi}{2\pi}+\frac{\mu_1}{2\pi}\right\}\right]\cup\left[\mathrm{ceil}\left\{-\frac{\varphi}{2\pi}+\frac{\mu_1}{2\pi}\right\};\mathrm{floor}\left\{-\frac{\varphi}{2\pi}+\frac{\mu_2}{2\pi}\right\}\right], \tag{29}$$

where

$$\mu_1=\sqrt{2}L\sqrt{\frac{\varepsilon_F-\beta-m_0s}{A}-\sqrt{\left(\frac{\varepsilon_F-\beta-m_0s}{A}\right)^2-\left(\frac{\mu_0H}{A}\right)^2}}, \tag{30}$$

$$\mu_2=\sqrt{2}L\sqrt{\frac{\varepsilon_F-\beta-m_0s}{A}+\sqrt{\left(\frac{\varepsilon_F-\beta-m_0s}{A}\right)^2-\left(\frac{\mu_0H}{A}\right)^2}}, \tag{31}$$

ceil is the function that gives the maximal integer closest to a given real number, and floor is the function that gives the minimal integer closest to a given real number. The average energy of the spacer is defined by the standard formula

$$\langle\varepsilon\rangle=2\frac{L_xL_y}{(2\pi)^2}\sum_N\int_0^{\kappa_N}2\pi\kappa\varepsilon_N(\kappa)d\kappa. \tag{32}$$

After simple transformations, Eq. (32) transforms to:

$$\frac{\langle\varepsilon\rangle}{L_xL_y}=(\beta+m_0s)nL+\frac{A}{4\pi}\sum_N\left\{\left(\frac{\varepsilon_F-\beta-m_0s}{A}\right)^2-\left(\frac{\varphi+2N\pi}{2L}\right)^4-\left(\frac{\mu_0HL}{A(\varphi+2N\pi)}\right)^4-\frac{1}{2}\left(\frac{\mu_0H}{A}\right)^2\right\}, \tag{33}$$

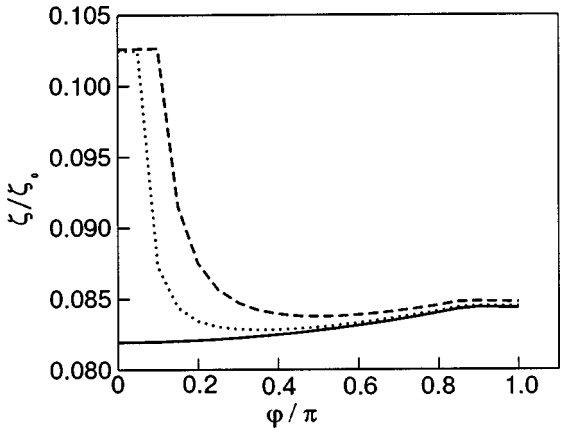

FIG. 2. Dependence of the Fermi energy on the angle φ. Dashed line $H=800$ Oe, dotted line $H=400$ Oe, solid line $H=0$ Oe. $\zeta_0=A(3\pi^2N)^{2/3}$, $\zeta=\varepsilon_F-\beta-m_0s$, $L=23$ Å.

where $\langle\varepsilon\rangle/(L_xL_y)$ is the energy per unit area of the spacer.

By comparing the experimental data for the exchange coupling energy between MOLs and the maximal exchange coupling energy between the layers[23–29] for different types of trilayer systems with the results of numerical calculations using the given model, it was found that if the density of magnetized electrons n equals the tabulated point for the corresponding metal spacer, then the parameter $a\approx 1$ Å and the parameter A may occupy the region 10^{-30} erg·cm$^2<A<10^{-27}$ erg·cm^2. For example, Eq. (28) was solved numerically for the following values of the spacer parameters: $A=0.15\times10^{-30}$ erg·cm^2, $n=5.9\times10^{22}$ cm^{-3}, $\theta_0=\pi/2$, $a=1$ Å. The curves of the Fermi energy as a function of the spacer thickness, magnetic field, and the angle φ, while the remaining parameters are fixed, are shown, are performed in Figs. 2, 3, and 4, respectively. It is obvious from the plots that the Fermi energy has oscillating dependence on the spacer thickness and on magnetic field. These oscillations are a purely dimensional effect analogous to that described Ref. 22.

The results of numerical calculation of $\langle\varepsilon\rangle/(L_xL_y)$ for the parameters of the spacer, taking into account calculated numerically Fermi energy, are shown in Figs. 5 and 6. It is obvious from Figs. 5 and 6 that both $\langle\varepsilon\rangle/(L_xL_y)$ and ε_F also have oscillating behavior depending on the spacer thickness

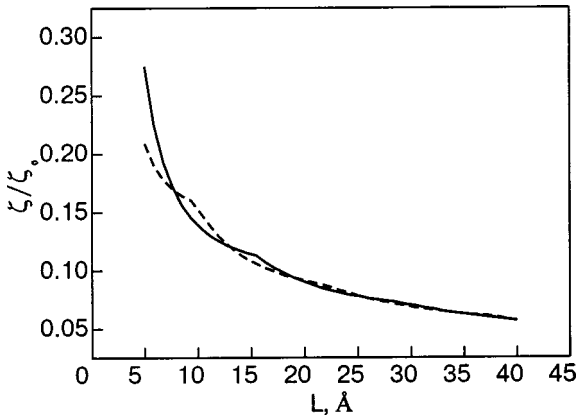

FIG. 3. Dependence of the Fermi energy on the spacer thickness. Solid line $\varphi=0$, dashed line $\varphi=\pi$; $H=0$.

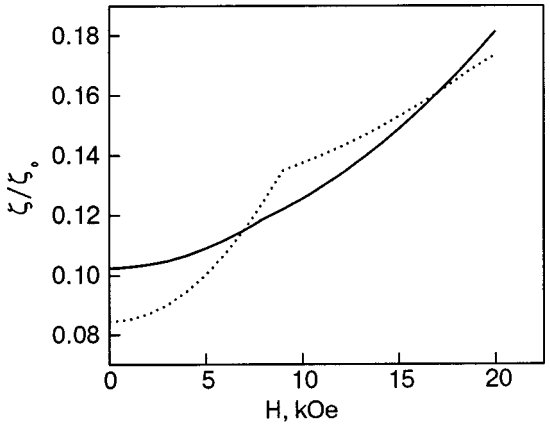

FIG. 4. Dependence of the Fermi energy on magnetic field. Solid line $\varphi=0$, dotted line $\varphi=\pi$, $L=23$ Å.

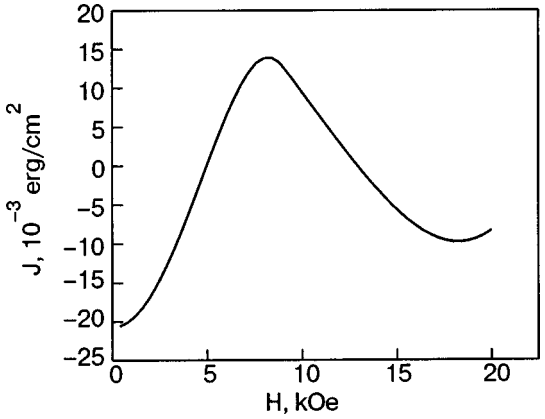

FIG. 6. Dependence of the exchange coupling energy J on magnetic field. $L=23$ Å.

and magnetic field. $\langle\varepsilon\rangle/(L_xL_y)$ and ε_F also have minima when $\varphi=0$ or $\varphi=\pi$, depending on the spacer thickness, magnetic field, and other parameters. That is, the energy-optimal configuration is the parallel or antiparallel mutual orientation of the projections of the magnetizations of the MOLs on the xy plane.

As is seen from Fig. 7, the exchange coupling of the MOLs through the metal spacer has a long-periodic oscillatory dependence on the spacer thickness L, i.e., the exchange coupling changes from antiferromagnetic to ferromagnetic depending on the spacer thickness. As is seen from Fig. 5, the given theoretical calculation shows that $J=\langle\varepsilon\rangle/(L_xL_y)|_{\varphi=\pi}-\langle\varepsilon\rangle/(L_xL_y)|_{\varphi=0}$ descends faster than L^{-2} with increase of L. Moreover, the period of the oscillations of J is not constant but increases with increase of L. Both of these theoretical results agree quantitatively with results of Ref. 29 (see Fig. 5). As is seen from Figs. 8 and 9, the theoretically obtained values of the first three periods of oscillation of the exchange coupling equal 10, 12, and 15 Å, respectively. The experimentally obtained periods of oscillation of the exchange coupling (according to Ref. 29) are equal to 11.0, 13.6, and 15.2 Å with accuracy ±1 Å.

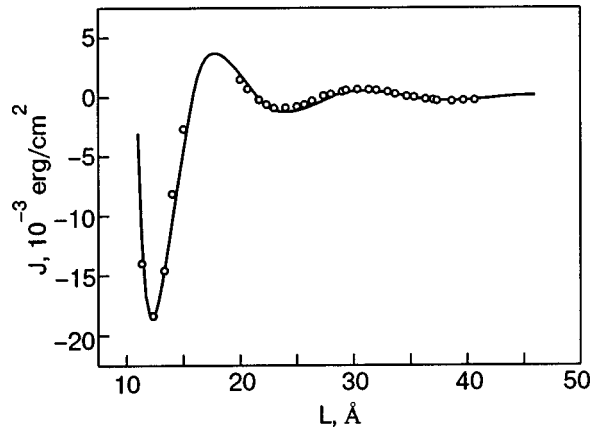

FIG. 5. Dependence of the exchange coupling energy $J=\langle\varepsilon\rangle/(L_xL_y)|_{\varphi=\pi}-\langle\varepsilon\rangle/(L_xL_y)|_{\varphi=0}$ on the spacer thickness. The solid line is the theoretical calculation, "○" the results of the experimental work.[29] It was found by comparing these theoretical and experimental results that they are shifted by 6 Å.

The components of the magnetization at a point with an arbitrary coordinate z inside the spacer have the form (21). Then, taking into account the Fermi–Dirac statistics and the distribution functions (17), the mean value of the magnetization components at an arbitrary point with coordinate z inside the spacer has the form:

$$\begin{cases} \langle M_x\rangle = 2\dfrac{L_xL_y}{(2\pi)^2}\displaystyle\sum_N \int_0^{\kappa_N} 2\pi\kappa d\kappa M_{xN} \\ \langle M_y\rangle = 2\dfrac{L_xL_y}{(2\pi)^2}\displaystyle\sum_N \int_0^{\kappa_N} 2\pi\kappa d\kappa M_{yN}. \\ \langle M_z\rangle = 2\dfrac{L_xL_y}{(2\pi)^2}\displaystyle\sum_N \int_0^{\kappa_N} 2\pi\kappa d\kappa M_{zN} \end{cases} \tag{34}$$

It is simple to transform Eq. (34) to the form:

$$\frac{\langle M_x\rangle}{L_xL_y} = \frac{1}{2\pi}\sum_N M_0\sin\theta_0\cos\left(\frac{\varphi+2N\pi}{L}z\right) \times\left\{\frac{\varepsilon_F-\beta-m_0s}{A}-\left(\frac{\varphi+2N\pi}{2L}\right)^2 -\left(\frac{\mu_0HL}{A(\varphi+2N\pi)}\right)^2\right\}, \tag{35}$$

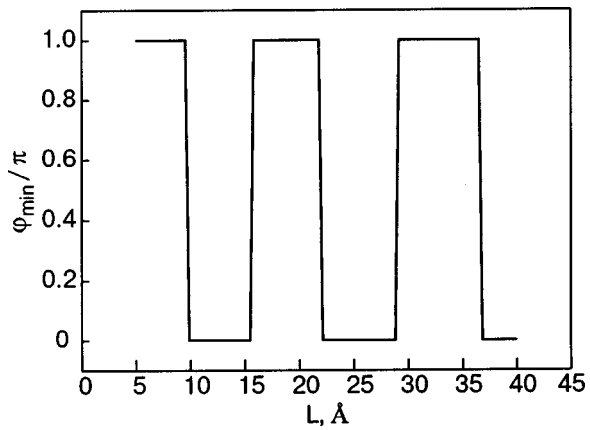

FIG. 7. Dependence of the angle at which the energy of coupling of the MOLs is minimal as a function of the spacer thickness. $H=0$.

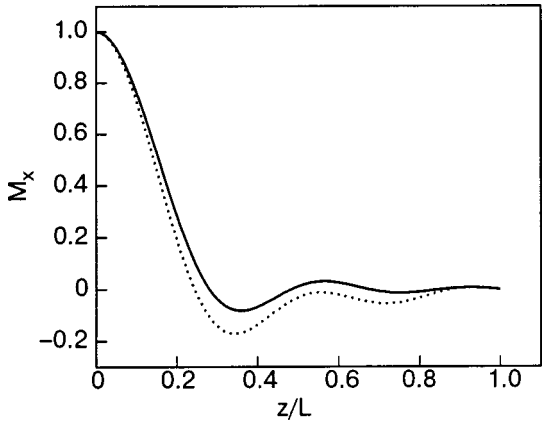

FIG. 8. Magnetization component M_x (divided by the magnetization at the $z=0$ boundary) as a function of z. Solid line $H=0$ Oe; dotted line $H=2000$ Oe. The spacer thickness is 23 Å.

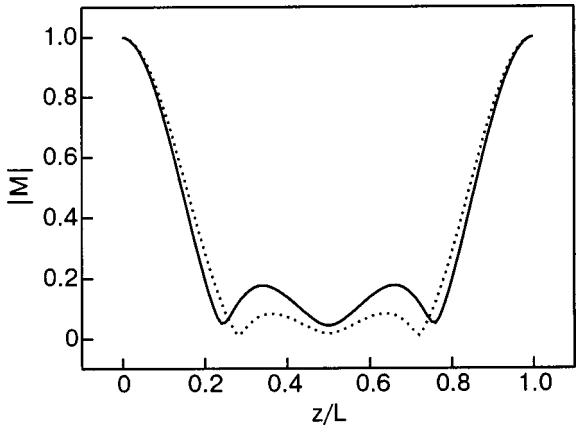

FIG. 10. Absolute value of M (divided by the magnetization at the $z=0$ boundary) as a function of z. Solid line $H=0$ Oe; dotted line $H=2000$ Oe. The spacer thickness is 23 Å.

$$\frac{\langle M_y\rangle}{L_xL_y}=\frac{1}{2\pi}\sum_N M_0\sin\theta_0\sin\left(\frac{\varphi+2N\pi}{L}z\right)\times\left\{\frac{\varepsilon_F-\beta-m_0s}{A}-\left(\frac{\varphi+2N\pi}{2L}\right)^2-\left(\frac{\mu_0HL}{A(\varphi+2N\pi)}\right)^2\right\}, \tag{36}$$

$$\frac{\langle M_z\rangle}{L_xL_y}=M_0\cos\theta_0 nL. \tag{37}$$

The absolute value of the magnetization at a point with coordinate z inside the spacer is calculated as

$$\langle|M|\rangle=\sqrt{\langle M_x\rangle^2+\langle M_y\rangle^2+\langle M_z\rangle^2}. \tag{38}$$

The plots of the dependences of $\langle M_x\rangle$ and $\langle M_y\rangle$ on the coordinate z inside the spacer are performed in Figs. 8 and 9. Here the boundary conditions are chosen so that when $z=0$, the magnetization of the spacer is directed along the x axis, and when $z=L$ the magnetization of the spacer is directed along the y axis. The magnitude $\langle M_z\rangle$, as is seen from Eq. (37), is constant at all spacer thicknesses, according to our model. As is seen from Fig. 10, the average value of $|M|$ is maximal on the spacer's boundaries with the MOLs and decays from the spacer's boundaries inside the spacer symmetrically about of the middle of the spacer.

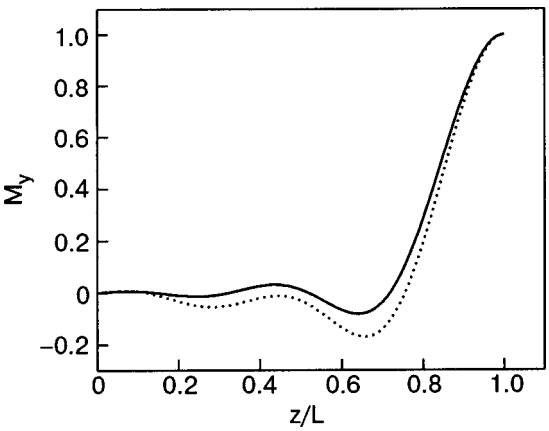

FIG. 9. Magnetization component M_y (divided by the magnetization at the $z=L$ boundary) as a function of z. Solid line $H=0$ Oe; dotted line $H=2000$ Oe. For $H=2000$ Oe the spacer thickness is 23 Å.

DISCUSSION OF RESULTS

In this paper the exchange coupling of magnetically ordered layers through a nonmagnetic metallic spacer was calculated using a spin-density model similar to the Ginzburg–Landau model. The induced magnetization in the spacer, taking into account the influence of an external magnetic field, was calculated, too. This calculation shows that the energy of coupling of the MOLs through the nonmagnetic metallic spacer is an oscillating function of the spacer thickness and magnetic field, i.e., the exchange coupling between the layers varies from ferromagnetic to antiferromagnetic and *vice versa* upon variation of the spacer thickness and magnetic field. Here the magnitude of the exchange coupling decreases with spacer thickness faster than L^{-2}, and the period of oscillation of the exchange coupling is not constant but increaeses with increase of the spacer thickness. These results match with those of Refs. 29–31 which were obtained for Cu and Au spacers and for Co and Fe MOLs. Also, this calculation shows that in a nonferromagnetic spacer the induced magnetization can undergo many complete rotations with variation of the distance to the boundaries with the MOLs. Moreover, the absolute value of the induced magnetization decays nonmonotonically with distance from the interfaces inside the spacer. It is shown that the character of the decay of the absolute value of the magnetization from the interfaces into the interior of the spacer is influenced by magnetic field.

The author is grateful to Prof. V. G. Baryakhtar for fruitful discussion of the results and to Prof. A. V. Svidzinsky for discussion of basic aspects of the model used in this work for calculation of the induced magnetization of the spacer.

*E-mail: gorob@mail.kar.net

[1] S. S. P. Parkin, Phys. Rev. Lett. **71**, 1641 (1993).
[2] P. Bruno, Phys. Rev. B **52**, 411 (1995).
[3] S. S. P. Parkin, N. More, and K. P. Roche, Phys. Rev. Lett. **64**, 2304 (1990).

[4] W. R. Bennett, W. Schwarzacher, and W. F. Egelhoff Jr., Phys. Rev. Lett. **65**, 3169 (1990).
[5] D. H. Mosca, F. Petroff, A. Fert, P. A. Schroeder, W. P. Pratt Jr., and R. Laloee, J. Magn. Magn. Mater. **94**, L1 (1991).
[6] S. S. P. Parkin, R. Bhadra, and K. P. Roche, Phys. Rev. Lett. **66**, 2152 (1991).
[7] S. S. P. Parkin, Phys. Rev. Lett. **67**, 3598 (1991).
[8] L. M. Falicov, Daniel T. Pierce, S. D. Bader, Kristl B. Hathaway, Herbert J. Hopster, David N. Lambeth, S. S. P. Parkin, Gary Prinz, Myron Salamon, Ivan K. Schuller, and R. H. Victora, J. Mater. Res. **5**, 1299 (1990).
[9] P. W. Rooney, A. L. Shapiro, M. Q. Tran, and F. Hellman, Phys. Rev. Lett. **75**, 1843 (1995).
[10] G. P. Felcher, R. O. Hilleke, R. K. Crawford, J. Haumann, R. Kleb, and G. Ostrowsky, Rev. Sci. Instrum. **58**, 609 (1987).
[11] S. Hamada, N. Hosoito, and T. Shinjo, J. Phys. Soc. Jpn. **66**, 30 (1997).
[12] N. Hosoito, T. Emoto, S. Hamada, and T. Shinjo, ICR Annual Report **3**, 167 (1996).
[13] M. G. Samant, J. Stoehr, S. S. P. Parkin, G. A. Held, B. D. Hermsmeier, F. Herman, M. van Schilfgaarde, L. C. Duda, D. C. Mancini, N. Wassdahl, and R. Nakajima, Phys. Rev. Lett. **72**, 1112 (1994).
[14] S. Pizzini, A. Fontaine, C. Giorgetti, E. Dartige, J. F. Bobo, M. Piecuch, and F. Baudelet, Phys. Rev. Lett. **74**, 1470 (1995).
[15] Q. Y. Jin, Y. B. Xu, H. R. Zhai, C. Hu, M. Lu, Q. S. Bie, Y. Zhai, G. L. Dunifer, R. Naik, and M. Ahmad, Phys. Rev. Lett. **72**, 768 (1994).
[16] W. Harrison, Solid State Theory, Mir, Moscow (1972).
[17] J. Mathon, A. Umerski, M. Milleret, R. B. Muñiz, and D. M. Edwards, J. Magn. Magn. Mater. **217**, 188 (2000).
[18] L. Nordstroem and D. J. Singh, J. Appl. Phys. **79**, 4515 (1996).
[19] J. Mathon, A. Umerski, M. Milleret, and R. B. Muñiz, Phys. Rev. B **59**, 6344 (1999).
[20] V. G. Bar'yakhtar and Yu. I. Gorobets, *Bubble Magnetic Domains and Their Lattices* [in Russian], Naukova Dumka, Kiev (1988).
[21] L. D. Landau and E. M. Lifshitz, *Statistical Physics*, 3rd ed. (rev. and enl., by E. M. Lifshitz and L. P. Pitaevskii), Pergamon Press (1980), Nauka, Moscow (1978).
[22] V. Bezak, J. Phys. Chem. Solids **27**, 815 (1966).
[23] P. Bruno, Phys. Rev. B **52**, 411 (1995).
[24] S. O. Demokritov, J. Phys. D **31**, 925 (1998).
[25] P. Grönberg, R. Schreiber, Y. Pang, M. B. Brodsky, and H. Sowers, Phys. Rev. Lett. **57**, 2442 (1986).
[26] C. F. Majkrzak, J. W. Cable, J. Kwo, M. Hong, D. B. Mc Whan, Y. Yafet, J. V. Waszczak, and C. Vettier, Phys. Rev. Lett. **56**, 2700 (1986).
[27] C. F. Majkrzak, J. Kwo, M. Hong, Y. Yafet, Doon Gibbs, C. L. Chien, and J. Bohr, Adv. Phys. **40**, 99 (1991).
[28] S. S. P. Parkin, N. More, and K. P. Roche, Phys. Rev. Lett. **64**, 2304 (1990).
[29] J. J. de Vries, P. J. H. Bloemen, M. T. Johnson, J. van de Stegge, A. Reinders, and W. J. M. de Jonge, J. Magn. Magn. Mater. **129**, L129 (1994).
[30] K. Shintaku, Y. Daitoh, and T. Shinjo, Phys. Rev. B **47**, 14584 (1993).
[31] M. T. Johnson, S. T. Purcell, N. W. E. McGee, R. Coehoorn, J. van de Stegge, and W. Hoving, Phys. Rev. Lett. **68**, 2688 (1992).

This article was published in English in the original Russian journal. Reproduced here with stylistic changes by AIP.

Spectrum of dynamic magnetic susceptibility of a randomized $f-d$ magnet with spin–lattice coupling. II. "Opening" of the spin excitation bands

A. B. Beznosov* and E. S. Orel

B. Verkin Institute for Low Temperature Physics and Engineering, National Academy of Sciences of Ukraine, pr. Lenina 47, Kharkov 61103, Ukraine

(Submitted January 28, 2003; revised February 19, 2004)
Fiz. Nizk. Temp. **30**, 1053–1064 (October 2004)

The transformation of the magnetic absorption spectra of a narrow-band ferromagnetic conductor containing local f and quasilocal d magnetic moments under conditions of weak spin–lattice coupling and spatial randomization of the g factors of the quasilocal and local spin subsystems is investigated. It is shown that randomization of the g factors (e.g., as a result of the introduction of an impurity) leads mainly to the "opening" (i.e., to the appearance in the magnetic absorption spectrum) of acoustic and optical magnon bands formed in the system while not affecting the position and shape of the narrow magnetic resonance lines comprising the spectrum of the impurity-free crystal. The effects of spin–lattice coupling, besides the "opening" of the phonon and magnon bands, lead to a shift and a temperature smearing of the narrow resonance lines. The relative corrections to the effective magnon masses generated by the spin–lattice coupling in a $4f-5d$ metal amount to $\sim 2\times 10^{-4}$ for an acoustic mode and to $\sim 4\times 10^{-4}$ for an optical mode. © *2004 American Institute of Physics.*
[DOI: 10.1063/1.1808197]

1. INTRODUCTION

In Part I of this paper[1] it was shown that the exchange interaction of quasilocal d and local f electrons leads to an effective renormalization of the g factors of both magnetic subsystems, while the spin–lattice coupling at zero temperature alters the shape of the magnon bands and leads to damping of magnons with quasimomenta exceeding some threshold value. At a finite temperature all of the magnons are damped as a result of the absorption of thermal phonons.

The present paper is a continuation of Ref. 1. Here we investigate further the spectrum of the transverse dynamic magnetic susceptibility $\chi^{+-}(\mathbf{Q},\mathbf{Q}',\tilde{\varepsilon})$ of Eq. (I.14)[1)] and analyze the magnetic absorption (the imaginary parts of the coherent $\chi^{+-}_{2\mathrm{coh}}(\mathbf{Q},\varepsilon)$ and incoherent $\chi^{+-}_{2\mathrm{incoh}}(\varepsilon)$ components of the susceptibility $\chi^{+-}(\mathbf{Q},\mathbf{Q}',\tilde{\varepsilon})$ of a narrow-band magnetic $f-d$ conductor in the entire spectral region with allowance for a weak spin–lattice coupling. We shall use the same notation as in Ref. 1.

2. MAGNETIC ABSORPTION

2.1. General formula

The magnetic susceptibility of a system of interacting d and f electrons is determined by the sum of four partial contributions (of the $d-d$, $d-f$, $f-d$, and $f-f$ types) from the four Green's functions (I.16). A technique for calculating such contributions is set forth in Ref. 1 for the example of the Green's function of the $d-d$ type. The result is given by formulas (I.38) and (I.39) for the coherent and incoherent components of the susceptibility, respectively. The contributions from the remaining Green's functions (I.16) differ from (I.38) and (I.39) in the approximation considered, $1/2S \ll 1$, only by numerical factors which depend on the energy interval of the corresponding spin excitations—the acoustic, optical, and Stoner regions of the spectrum (see Ref. 1 and Sec. 2 of the present paper).

The absorption spectrum of the electromagnetic field with wave vector $\mathbf{Q}$ is determined by the imaginary components of the coherent and incoherent spectral components of the total dynamic susceptibility (I.14), (I.36), and (I.37):

$$\chi^{+-}_{2\mathrm{coh}}(\mathbf{Q},\varepsilon) \quad \text{and} \quad \chi^{+-}_{2\mathrm{incoh}}(\varepsilon). \tag{1}$$

Applying the technique used to calculate the $d-d$ contribution (I.38) and (I.39) to the remaining Green's functions (I.16) (of the $d-f$, $f-d$, and $f-f$ types), summing the results, and taking the limit $\alpha\to 0$ in the variable $\tilde{\varepsilon}=\varepsilon+i\alpha$, we obtain the following approximate expressions for the imaginary parts of the functions (1) at zero temperature:

$$\begin{aligned}\chi^{+-}_{2\mathrm{coh}}(\mathbf{Q},\varepsilon)=A\{&\langle g_f S^z-g_d s^z\rangle^2[\,\delta(\varepsilon-\varepsilon_{\mathrm{ac}\xi}(\mathbf{Q}))\\&+\xi^2Q^2L_{\mathrm{ac}}(\mathbf{Q},\varepsilon)N_{\mathrm{ac}\nu}(\varepsilon)]+(g_f+g_d)^2\langle S^z\rangle\\&\times\langle s^z\rangle[\,\delta(\varepsilon-\varepsilon_{\mathrm{op}\xi}(\mathbf{Q}))\\&+\xi^2Q^2L_{\mathrm{op}}(\mathbf{Q},\varepsilon)N_{\mathrm{op}\nu}(\varepsilon)]\}+St_{\mathrm{coh}}(\mathbf{Q},\varepsilon),\end{aligned} \tag{2}$$

$$\begin{aligned}\chi^{+-}_{2\mathrm{incoh}}(\varepsilon)=A\{&(\gamma_f^2\langle S^z\rangle^2+\gamma_d^2\langle s^z\rangle^2)[N_{\mathrm{ac}\xi}(\varepsilon)+\xi^2O_{\mathrm{ac}}(\varepsilon)]\\&+(\gamma_f^2+\gamma_d^2)\langle S^z\rangle\langle s^z\rangle[N_{\mathrm{op}\xi}(\varepsilon)+\xi^2O_{\mathrm{op}}(\varepsilon)]\}\\&+St_{\mathrm{incoh}}(\varepsilon).\end{aligned} \tag{3}$$

Here

$$A=\frac{2\pi\mu_B^2\langle s^z\rangle}{v_a\langle S^z+s^z\rangle} \tag{4}$$

is the amplitude constant of the magnetic susceptibility, v_a is the atomic volume,

$$N_{\mathrm{ac(op)}\xi}(\varepsilon)=\frac{1}{N}\sum_{\mathbf{q}}\ \delta(\varepsilon-\varepsilon_{\mathrm{ac(op)}\xi}(\mathbf{q})) \tag{5}$$

is the density of states of the acoustic (ac) and optical (op) magnons, normalized per lattice site,

$$N_{\mathrm{ac(op)}\nu}(\varepsilon)=\frac{1}{N}\sum_{\mathbf{p}}\ \delta(\varepsilon-\varepsilon_{\mathrm{ac(op)}+}(0,\mathbf{p})) \tag{6}$$

is the combined atomic density of states of magnons and phonons (we are neglecting the wave vector $\mathbf{Q}$ of the electromagnetic wave in comparison with the most probable values of the phonon quasimomenta $\mathbf{p}$, so that we use $\varepsilon_{\mathrm{ac(op)}+}(0,\mathbf{p})$ instead of $\varepsilon_{\mathrm{ac(op)}+}(\mathbf{Q},\mathbf{p})$; $O_{\mathrm{ac(op)}}(\varepsilon)$ is a function whose maximum values do not exceed the values of the function (6) or, at least, are of the same order of magnitude as that function;

$$L_{\mathrm{ac(op)}}(\mathbf{Q},\varepsilon)=\left[\frac{a\langle s^z\rangle S_{\mathrm{ac(op)}}}{\langle S^z+s^z\rangle}\right]^2\{[\varepsilon-\varepsilon_{\mathrm{ac(op)}0}(\mathbf{Q})-M'_{\mathrm{ac(op)}}(Q,\varepsilon)]^2+[M''_{\mathrm{ac(op)}}(Q,\varepsilon)]^2\}^{-1} \tag{7}$$

is the form-factor function of the acoustic (optical) absorption band, where

$$M'_{\mathrm{ac(op)}}(Q,\varepsilon)=\left[\frac{\xi Qa\langle s^z\rangle S_{\mathrm{ac(op)}}}{\langle S^z+s^z\rangle}\right]^2\mathcal{P}\int\frac{N_{\mathrm{ac(op)}\nu}(E)dE}{\varepsilon-E}, \tag{8}$$

$$M''_{\mathrm{ac(op)}}(Q,\varepsilon)=\pi\left[\frac{\xi Qa\langle s^z\rangle S_{\mathrm{ac(op)}}}{\langle S^z+s^z\rangle}\right]^2 N_{\mathrm{ac(op)}\nu}(\varepsilon), \tag{9}$$

$\mathcal{P}$ denotes the principal value of the integral; $S_{\mathrm{ac}}=\langle s^z\rangle$, $S_{\mathrm{op}}=\langle S^z\rangle$; a is the crystal lattice constant (for simplicity we are considering a simple cubic lattice);

$$St_{\mathrm{coh}}(\mathbf{Q},\varepsilon)\approx\frac{\pi\mu_B^2}{v_a}(g_f+g_d)^2\left\{\frac{\tilde{N}(Q,\varepsilon)}{1+[\pi(U-J)\tilde{N}(Q,\varepsilon)]^2}+\xi^2Q^2O_{\mathrm{sec}}(\mathbf{Q},\varepsilon)\right\}, \tag{10}$$

where

$$\tilde{N}(Q,\varepsilon)=\frac{1}{N}\sum_{\mathbf{k}}\ \delta(\varepsilon-\Delta-2QaT\sin(ka))n_{\mathbf{k}\uparrow}, \tag{11}$$

$$St_{\mathrm{incoh}}(\varepsilon)\approx\frac{\pi\mu_B^2}{v_a}(\gamma_d^2+\gamma_f^2)\times\left[\int\frac{N(E)N(E-\Delta+\varepsilon)n_\uparrow(E)}{1+[\pi(U-J)N(E)n_\uparrow(E)]^2}dE+\xi^2O_{\mathrm{sei}}(\varepsilon)\right] \tag{12}$$

are the absorption bands in the region of the Stoner (single-particle) excitations (T is the electron hopping integral, $n_\uparrow(E)$ is the Fermi distribution);

$$N(E)=\frac{1}{N}\sum_{\mathbf{k}}\ \delta(E-E(\mathbf{k})) \tag{13}$$

is the electron density of states per spin-atom, $E(\mathbf{k})$ is the electron energy (I.31); $O_{\mathrm{sec}}(\mathbf{Q},\varepsilon)$ and $O_{\mathrm{sei}}(\varepsilon)$ are functions whose maximum values (with the corresponding normalization (20), (29)) do not exceed the values of the function (13) or, at least, are of the same order of magnitude as that function; and, it is assumed that the condition $\langle s^z\rangle(U-J)\geqslant zT$ holds (z is the coordination number of the crystal lattice).

Since the wave vector $\mathbf{Q}$ of the electromagnetic wave is quite small ($Q\ll\pi/a$) and since the largest contribution in the summation over phonon quasimomenta is given by values of $\mathbf{p}$ close to p_B, the function $|\Xi_{\mathbf{Q},\mathbf{p}}|^2$ in the corresponding sums in (2), (8), (9), and (10) is replaced by a constant [see Eq. (A8)]:

$$|\Xi_{\mathbf{Q},\mathbf{p}}|^2\approx\frac{Q^2a^2}{4}\left|\sin\frac{pa}{2}\right|^3\approx\frac{Q^2a^2}{4}. \tag{14}$$

The origin of the contributions to the magnetic absorption in different spectral regions and the main details of the derivation of expressions (2) and (3) are discussed below.

2.2. Narrow absorption peaks

Taking relations (I.51)–(I.54) into account, we can write the expression for $\chi^{+-}_{\mathrm{coh}}(\mathbf{Q},\tilde{\varepsilon})$ in the regions of the acoustic and optical magnon branches in the form

$$\chi^{+-}_{\mathrm{coh}}(\mathbf{Q},\tilde{\varepsilon})=\mathrm{const}_{\mathrm{ac(op)}}\frac{1}{\tilde{\varepsilon}-\varepsilon_{\mathrm{ac(op)}\xi}(\mathbf{Q},\tilde{\varepsilon})} \tag{15}$$

and determine the position of the poles from the zeros of the denominator of the function in (15):

$$D(\mathbf{Q},\varepsilon)=\varepsilon-\varepsilon_{\mathrm{ac(op)}0}(\mathbf{Q})-\frac{2\langle s^z\rangle S_{\mathrm{ac(op)}}}{\langle S^z+s^z\rangle}M(\mathbf{Q},\varepsilon). \tag{16}$$

Then for the poles of the susceptibility $\chi^{+-}_{\mathrm{coh}}(0,\tilde{\varepsilon})$ which lie outside the region of the poles of the mass operator $M(\mathbf{Q},\tilde{\varepsilon})$ [see Eqs. (I.53) and (I.54)] we obtain, with allowance for the relation $(x+i\alpha)^{-1}=\mathcal{P}(x^{-1})-i\pi\delta(x)$, the corresponding spectral contributions to (2) in the form

$$\chi^{+-}_{2\mathrm{coh}}(\mathbf{Q},\varepsilon)=\mathrm{const}_{\mathrm{ac(op)}}\delta(\varepsilon-\varepsilon_{\mathrm{ac(op)}\xi}(\mathbf{Q})). \tag{17}$$

2.3. Magnon–phonon bands

In the region of the poles (I.46) of the mass operator (I.32) the imaginary part of the susceptibility (15) is generated by the imaginary parts of the mass operator (I.49). Using relations (6) and (14), it is easy to see that the real (I.48) and imaginary (I.49) components of the mass operator can be written in the form (8), (9), so that, to leading order in $1/S$, we obtain the imaginary part of the susceptibility in the form

$$\chi^{+-}_{2\mathrm{coh}}(\mathbf{Q},\varepsilon)=\mathrm{const}_{\mathrm{ac(op)}}\xi^2Q^2L_{\mathrm{ac(op)}}(\mathbf{Q},\varepsilon)N_{\mathrm{ac(op)}\nu}(\varepsilon), \tag{18}$$

where $L_{\mathrm{ac(op)}}(\mathbf{Q},\varepsilon)$ is given by expression (7). As follows from (6)–(9), the function (18) has a peak of height $\sim 1/M''_{\mathrm{ac(op)}}(Q,\varepsilon_{\mathrm{ac(op)}\xi}(\mathbf{Q}))$ in a narrow energy interval $\sim M''_{\mathrm{ac(op)}}(Q,\varepsilon_{\mathrm{ac(op)}\xi}(\mathbf{Q}))$ centered at the point $\varepsilon_{\mathrm{ac(op)}\xi}(\mathbf{Q})$ and an extended region of relatively slow variation at the level $\sim M''_{\mathrm{ac(op)}}(Q,\varepsilon)/(\theta_{\mathrm{ac(op)}}+\theta_D)^2$ in the remaining domain of definition of the function $M''_{\mathrm{ac(op)}}(Q,\varepsilon)$. Here and below $\theta_{\mathrm{ac}}=\theta_C$, $\theta_{\mathrm{op}}=\theta'_C$.

2.4. Single-particle excitations

In the Stoner spectral region ($\varepsilon \sim \Delta$) the susceptibility $\chi^{+-}_{\mathrm{coh}}(\mathbf{Q},\tilde{\varepsilon})$ can be written approximately in the following form with allowance for relations (I.29)–(I.35), (I.38), and (I.43):

$$\chi^{+-}_{\mathrm{coh}}(\mathbf{Q},\tilde{\varepsilon}) \approx \frac{\mu_B^2}{v_a}(g_f+g_d)^2 \times \frac{\chi_0(\mathbf{Q},\tilde{\varepsilon})}{1-[U-J-M(\mathbf{Q},\tilde{\varepsilon})]\chi_0(\mathbf{Q},\tilde{\varepsilon})}. \quad (19)$$

Separating the real and imaginary parts of $\chi_0(\mathbf{Q},\tilde{\varepsilon})$ and $M(\mathbf{Q},\tilde{\varepsilon})$, neglecting the component $\chi_0'(\mathbf{Q},\varepsilon)$ in the absorption region (the real part of the susceptibility vanishes at the resonance frequency), we obtain, with accuracy up to the term

$$\sim(\pi/v_a)[\mu_B(g_f+g_d)\xi Qa/E_F]^2 \times \int N(E)N_{\mathrm{ph}}(E-\Delta+\varepsilon)n_{\uparrow}(E)dE,$$

$$\chi^{+-}_{2\mathrm{coh}}(\mathbf{Q},\varepsilon) \approx \frac{\mu_B^2}{v_a}(g_f+g_d)^2 \frac{\chi_0''(\mathbf{Q},\varepsilon)}{1+[(U-J)\chi_0''(\mathbf{Q},\varepsilon)]^2}, \quad (20)$$

where $\chi_0''(\mathbf{Q},\varepsilon) \approx \pi\tilde{N}(Q,\varepsilon)$, and $\tilde{N}(Q,\varepsilon)$ and $N(E)$ are determined by relations (11) and (13); $N_{\mathrm{ph}}(\varepsilon) = 1/N\,\Sigma_{\mathbf{p}}\delta(\varepsilon - \nu_{\mathbf{p}})$ is the phonon density of states; E_F is the Fermi energy measured from the bottom of the band of states $\mathbf{k}\uparrow$. The correction to (20) due to the spin–lattice coupling is nonzero in an energy interval of length $E_F+\theta_D$, which is a broader interval than that for the function (20).

2.5. Incoherent component in the region of the collective modes

According to (I.39), (I.51), and (I.52), in the region of the magnon branches one has

$$\chi^{+-}_{\mathrm{incoh}}(\tilde{\varepsilon}) = \mathrm{const}_{\mathrm{ac(op)}} \sum_{\mathbf{q}} \frac{1}{\tilde{\varepsilon} - \varepsilon_{\mathrm{ac(op)}\xi}(\mathbf{q})} \quad (21)$$

and the poles of the susceptibility outside the poles of the mass operator are determined by the zeros of the function

$$D(\mathbf{q},\varepsilon) = \varepsilon - \varepsilon_{\mathrm{ac(op)}0}(\mathbf{q}) - \frac{2\langle s^z\rangle S_{\mathrm{ac(op)}}}{\langle S^z+s^z\rangle} M(\mathbf{q},\varepsilon) \quad (22)$$

[cf. with (15), (16)]. In the region of the poles of $M(\mathbf{q},\tilde{\varepsilon})$ the imaginary part of the susceptibility is determined by the imaginary part of the mass operator (I.49):

$$\chi^{+-}_{2\mathrm{incoh}}(\varepsilon) = \mathrm{const}_{\mathrm{ac(op)}} \times \sum_{\mathbf{q}} \frac{\tilde{M}''_{\mathrm{ac(op)}}(\mathbf{q},\varepsilon)}{[\varepsilon - \varepsilon_{\mathrm{ac(op)}0}(\mathbf{q}) - \tilde{M}'_{\mathrm{ac(op)}}(\mathbf{q},\varepsilon)]^2 + [\tilde{M}''_{\mathrm{ac(op)}}(\mathbf{q},\varepsilon)]^2}, \quad (23)$$

where

$$\tilde{M}'_{\mathrm{ac(op)}}(\mathbf{q},\varepsilon) = 0.35\left[\frac{2\xi\Xi^2_{\mathbf{q}}\langle s^z\rangle S_{\mathrm{ac(op)}}}{\langle S^z+s^z\rangle}\right]^2 \times \mathcal{P}\int \frac{N_{\mathrm{ac(op)}\nu}(\mathbf{q},E)dE}{\varepsilon - E}, \quad (24)$$

$$\tilde{M}''_{\mathrm{ac(op)}}(\mathbf{q},\varepsilon) = 0.35\pi\left[\frac{2\xi\Xi^2_{\mathbf{q}}\langle s^z\rangle S_{\mathrm{ac(op)}}}{\langle S^z+s^z\rangle}\right]^2 N_{\mathrm{ac(op)}\nu}(\mathbf{q},\varepsilon),$$

$$N_{\mathrm{ac(op)}\nu}(\mathbf{q},\varepsilon) = \frac{1}{N}\sum_{\mathbf{p}} \delta(\varepsilon - \varepsilon_{\mathrm{ac(op)}+}(\mathbf{q},\mathbf{p})), \quad (25)$$

$$\Xi^2_{\mathbf{q}} = \frac{1}{N}\sum_{\mathbf{p}} |\Xi_{\mathbf{q},\mathbf{p}}|^2. \quad (26)$$

It follows from (21)–(26) that the terms of the sum over $\mathbf{q}$ in (23) as functions of energy have the form of smeared resonance peaks of height $\sim 1/\tilde{M}''_{\mathrm{ac(op)}}(\mathbf{q},\varepsilon_{\mathrm{ac(op)}\xi}(\mathbf{q}))$ and width $\sim \tilde{M}''_{\mathrm{ac(op)}}(\mathbf{q},\varepsilon_{\mathrm{ac(op)}\xi}(\mathbf{q}))$, centered on the curve $\varepsilon_{\mathrm{ac(op)}\xi}(\mathbf{q})$, and relatively slowly varying functions $\sim \tilde{M}''_{\mathrm{ac(op)}}(\mathbf{q},\varepsilon)/(\theta_{\mathrm{ac(op)}}+\theta_D)^2$ in the rest of the domain of definition of $\tilde{M}''_{\mathrm{ac(op)}}(\mathbf{q},\varepsilon)$ (in the region where magnon–phonon pairs are generated in the system by the external field). To obtain a simplified expression for $\chi^{+-}_{2\mathrm{incoh}}(\varepsilon)$ with the use of the magnon and phonon distribution functions, we replace the terms of the sum (21) by functions of the form

$$\delta(\varepsilon - \varepsilon_{\mathrm{ac(op)}\xi}(\mathbf{q})) + \frac{\tilde{M}''_{\mathrm{ac(op)}}(\mathbf{q},\varepsilon)}{(\theta_{\mathrm{ac(op)}}+\xi_D)^2};$$

we replace $N_{\mathrm{ac(op)}\nu}(\mathbf{q},\varepsilon)$ in formula (24) by the sums $1/N\,\Sigma_{\mathbf{p}}\delta(\varepsilon - \varepsilon_{\mathrm{ac(op)}0}(\mathbf{q}) - \nu_{\mathbf{p}})$, and we replace $\Xi^2_{\mathbf{q}}$ by its mean value $1/N\,\Sigma_{\mathbf{q}}\Xi^2_{\mathbf{q}} \approx 0.14$. Then we finally obtain

$$\chi^{+-}_{2\mathrm{incoh}}(\varepsilon) = \mathrm{const}_{\mathrm{ac(op)}}[N_{\mathrm{ac(op)}\xi}(\varepsilon) + \xi^2 O_{\mathrm{ac(op)}}(\varepsilon)],$$

where

$$O_{\mathrm{ac(op)}}(\varepsilon) = 0{,}14\pi\left[\frac{2\langle s^z\rangle S_{\mathrm{ac(op)}}}{\langle S^z+s^z\rangle(\theta_{\mathrm{ac(op)}}+\theta_D)}\right]^2 \times \int N_{\mathrm{ac(op)}}(E)N_{\mathrm{ph}}(\varepsilon - E)dE,$$

$$N_{\mathrm{ac(op)}}(\varepsilon) = \frac{1}{N}\sum_{\mathbf{q}} \delta(\varepsilon - \varepsilon_{\mathrm{ac(op)}0}(\mathbf{q}))$$

is the density of "unperturbed" magnon states, which differs little from $N_{\mathrm{ac(op)}\xi}(\varepsilon)$ in the main region of values in view of the smallness of the differences between $\varepsilon_{\mathrm{ac(op)}\xi}(\mathbf{q})$ and $\varepsilon_{\mathrm{ac(op)}0}(\mathbf{q})$.

2.6. Incoherent component in the Stoner region

Taking the condition ($\varepsilon \sim \Delta$) into account, we can write an approximate expression for (I.39) in the form [cf. (19)]

$$\chi^{+}_{\mathrm{incoh}}(\tilde{\varepsilon}) \approx \frac{\pi\mu_B^2}{v_a}(\gamma_f^2+\gamma_d^2) \times \sum_{\mathbf{q}} \frac{\chi_0(\mathbf{q},\tilde{\varepsilon})}{1-[U-J-M(\mathbf{q},\tilde{\varepsilon})]\chi_0(\mathbf{q},\tilde{\varepsilon})}. \quad (27)$$

Using the approach taken in Sec. 2.4, we obtain the imaginary part of the susceptibility (27) in the form [cf. (20)]

$$\chi^{+-}_{2\text{incoh}}(\varepsilon)\approx\frac{\pi\mu_B^2}{v_a}(\gamma_f^2+\gamma_d^2)\sum_{\mathbf{q}}\frac{\chi_0''(\mathbf{q},\varepsilon)}{1+[(U-J)\chi_0''(\mathbf{q},\varepsilon)]^2}. \tag{28}$$

The further transformation of expression (28) can be simplified substantially if the electron quasimomentum takes on only small values, i.e., if $k_F \ll k_B$. In that case the energy of the Stoner excitations (I.30) can be written approximately in the form $\Delta(\mathbf{k},\mathbf{q})\approx\Delta+E(\mathbf{q})-E(\mathbf{k})$ [see (I.31) and (I.43)]. We then obtain [see (I.35)]

$$\chi_0''(\mathbf{q},\varepsilon)=\pi N(\Delta+E_{\mathbf{q}}-\varepsilon)n_\uparrow(\Delta+E_{\mathbf{q}}-\varepsilon),$$

$$\chi^{+}_{2\text{incoh}}(\varepsilon)\approx\frac{\pi\mu_B^2}{v_a}(\gamma_f^2+\gamma_d^2)\times\int\frac{N(E)N(E-\Delta+\varepsilon)n_\uparrow(E)dE}{1+[\pi(U-J)N(E)n_\uparrow(E)]^2}, \tag{29}$$

and $N(E)$ is given by expression (13). The correction to (29) due to the spin–lattice coupling can be expressed approximately as

$$\frac{\pi\mu_B^2}{v_aN}(\gamma_f^2+\gamma_d^2)\times\sum_{\mathbf{q}}\frac{M''(\mathbf{q},\varepsilon)[\chi_0'(\mathbf{q},\varepsilon)]^2}{[1-(U-J)\chi_0'(\mathbf{q},\varepsilon)]^2+[(U-J)\chi_0''(\mathbf{q},\varepsilon)]^2}.$$

This correction is of order of magnitude $\sim\pi\mu_B^2(\gamma_f^2+\gamma_d^2)\xi^2/v_aE_F^2(E_F+\theta_D)$ and is nonzero in an interval of length $E_F+\theta_D$, which is broader than that for the function (29).

3. ABSOLUTE VALUES OF THE EFFECTS

3.1. Spin–lattice coupling constant

The abundance of contributions to the magnetic absorption spectrum which can in principle compete with each other requires making numerical estimates of their magnitudes. A key question here is the force constant ξ of the spin–lattice interaction due to the relation between the magnon stiffness coefficient and the interatomic distance. In the narrow-band magnet model under consideration the contribution $E_{m\text{ph}}$ (I.5) to the magnon energy due to the longitudinal displacement of the lattice sites is determined by the gradient of the hopping integral, ∇T. To estimate it we write the hopping integral in the form[2]

$$T=T(r)=T_0\exp(-r/a), \tag{30}$$

where T_0 is the hopping integral in the equilibrium position of the lattice sites, a is the lattice constant (for simplicity the lattice is assumed to be simple cubic), and $r=|\eta'-\eta|$ is the modulus of the longitudinal displacement of the ion which is the nearest neighbor of site λ from its equilibrium position $\lambda+\eta$. We then have $\nabla T(\mathbf{r})=(\partial T/\partial r)\mathbf{e}_\mathbf{r}$ ($\mathbf{e}_\mathbf{r}$ is a unit vector in the direction of the displacement $\mathbf{r}$), and the modulus of the gradient of expression (30) is equal to $|\partial T/\partial r|=T/a$.

In the equilibrium state at zero temperature the displacement r can be expressed in terms of the rms amplitude A_0 of the zero-point vibrations of the atoms with a cutoff frequency ν_0 (we assume for simplicity that the phonon dispersion relation is isotropic):[3]

$$A_0=\frac{\hbar}{\sqrt{2M_a\nu_0}}, \tag{31}$$

where M_a is the mass of the atom. For numerical estimates we use the characteristics of gadolinium, the central $4f-5d$ metal. Substituting into (31) the values $M_a=157$ a.m.e. and $\nu_0\approx\theta_D=184$ K (here ν_0 and θ_D are expressed in kelvin), we obtain $A_0=2.9\times10^{-2}$ Å. Now the spin–lattice coupling constant ξ can be calculated using the relation between the magnon stiffness and the hopping integral T on the acoustic branch [see (I.44)] and the requirement that the renormalization of the magnon spectrum in the long-wavelength region be independent of the microscopic model used for the interactions, in which case the phenomenological approach is valid. The calculation (see Appendix A) gives

$$\xi=\frac{zTA_0}{a}\frac{x^{2/3}\sin(k_Fa)}{2\pi\langle s^z\rangle^2}. \tag{32}$$

It is of interest first to estimate the influence of the spin–lattice coupling on the intrinsic characteristics of the spin system—the renormalization of the effective masses and the magnon damping.

3.2. Renormalization of the effective masses

The magnon stiffness in the acoustic band can be expressed in terms of the Curie temperature θ_C. Taking into account the relation between the hopping integral and the Curie temperature [see Eq. (B.14)], we can write expression (32) in the form

$$\xi\approx\frac{\theta_CA_0}{a}\frac{C(S+\langle s^z\rangle)}{0.591(S+1/2)\langle s^z\rangle^2}, \tag{33}$$

where C is a structure constant.

For gadolinium $\theta_C=293$ K, $a=2.98$ Å, $A_0=2.9\times10^{-2}$ Å, $\langle S^z\rangle=3.5$, $\langle s^z\rangle\approx0.05\langle S^z\rangle$, and expression (33) gives $\xi=297$ K. Then the relative corrections to the magnon effective masses in the acoustic and optical bands on account of the spin–lattice interaction, which for a simple cubic lattice have the form

$$\frac{\Delta m^*_{\text{ac}}}{m^*_{\text{ac}}}=\frac{2\pi}{x^{2/3}\sin(k_Fa)}\frac{\langle s^z\rangle^4}{\langle S^z+s^z\rangle}\frac{\xi^2}{T(\theta_C+\theta_D)},$$

$$\frac{\Delta m^*_{\text{op}}}{m^*_{\text{op}}}=\frac{2\pi}{x^{2/3}\sin(k_Fa)}\frac{\langle S^z\rangle\langle s^z\rangle^3}{\langle S^z+s^z\rangle}\frac{\xi^2}{T(\theta_C'+\theta_D)} \tag{34}$$

(here $\theta_C'\approx\theta_C\langle S^z\rangle/\langle s^z\rangle$), take the values

$$\frac{\Delta m^*_{\text{ac}}}{m^*_{\text{ac}}}=\frac{\xi^2}{\theta_C(\theta_C+\theta_D)}\frac{0.591z\langle s^z\rangle^4(S+1/2)}{C\langle S^z+s^z\rangle(S+\langle s^z\rangle)}\approx2.2\cdot10^{-4},$$

$$\frac{\Delta m^*_{\text{op}}}{m^*_{\text{op}}}=\frac{\xi^2}{\theta_C(\theta_C'+\theta_D)}\frac{0.591z\langle S^z\rangle\langle s^z\rangle^3(S+1/2)}{C\langle S^z+s^z\rangle(S+\langle s^z\rangle)}$$

$$\approx3.6\cdot10^{-4}. \tag{35}$$

In absolute terms the effective masses and the corrections to them have the values

$$m^*_{\text{ac}}=\frac{\hbar^2}{a^2T}\frac{\pi\langle S^z+s^z\rangle}{x^{2/3}\sin(k_Fa)}\approx155m_e,$$

$$\Delta m^*_{\rm ac}\approx 3.47\cdot 10^{-2} m_e\,,$$

$$m^*_{\rm op}=\frac{\hbar^2}{a^2 T}\frac{\pi\langle S^z+s^z\rangle}{x^{2/3}\sin(k_F a)}\frac{\langle s^z\rangle}{\langle S^z\rangle}\approx 6.6 m_e\,,$$

$$\Delta m^*_{\rm op}\approx 2.36\cdot 10^{-3} m_e\,. \qquad (36)$$

3.3. Magnon damping

The characteristic magnon damping time is given by the expression

$$\tau_{\mathbf{q}}=\frac{\hbar}{2\,{\rm Im}\,\varepsilon(\mathbf{q})}, \qquad (37)$$

where $\hbar$ is Planck's constant, and ${\rm Im}\,\varepsilon(\mathbf{q})$ is the imaginary part of the magnon energy.[3] The latter, according to (I.39), (I.51), and (I.52), is equal to

$${\rm Im}\,\varepsilon_{{\rm ac(op)}\xi}(\mathbf{q})=\frac{2\langle s^z\rangle S_{\rm ac(op)}}{\langle S^z+s^z\rangle}M''(\mathbf{q},\varepsilon_{{\rm ac(op)}\xi}(\mathbf{q})). \qquad (38)$$

Magnons with quasimomenta not exceeding a critical value $q_{0\,{\rm ac(op)}}$, are not damped,[1] and therefore one is interested in an estimate of (38) near the edge of the magnon band, where $q\approx q_B$. The maximum value of the function $|\Xi_{q_B,p}|^2 = |\sin(pa/2)|\cos^2(pa/2)$ is approximately ~ 0.35 [see Eq. (A.8)]. Using the definition (I.49), one can conclude that the imaginary part of the mass operator in (38) does not exceed the value [cf. Eq. (9)]

$$M''_{\rm ac(op)max}=\frac{0.7\pi\xi^2\langle s^z\rangle S_{\rm ac(op)}}{\langle S^z+s^z\rangle}N_{{\rm ac(op)}\nu\,\max}, \qquad (39)$$

where $N_{{\rm ac(op)}\nu\,\max}$ is the maximum value of the function in (25), which is achieved in the three-dimensional case at a value of the magnon quasimomentum $q_{\max}\sim q_B$. The interval of nonzero values of $N_{{\rm ac(op)}\nu}(\mathbf{q},\varepsilon)$ is equal to the sum of the widths of the magnon and phonon bands. Using the normalization $\int N_{{\rm ac(op)}\nu}(\mathbf{q},\varepsilon)d\varepsilon=1$, we estimate $N_{{\rm ac(op)}\nu}(\mathbf{q},\varepsilon)$ by the quantity $(\theta_C+\theta_D)^{-1}$ for the acoustic band and $(\theta'_C+\theta_D)^{-1}$ for the optical band. Using Eq. (39) and the characteristics of gadolinium (see Sec. 3.2), we obtain from (37) and (38) the following estimate for the magnons with Brillouin quasimomentum q_B:

$${\rm Im}\,\varepsilon_{\rm ac}(q_{\max})=10^{-4}\theta_C,\quad \tau_{\rm ac}\approx 10^{-10}\ \text{s},$$

$${\rm Im}\,\varepsilon_{\rm op}(q_B)=2\cdot 10^{-4}\theta'_C,\quad \tau_{\rm op}=3\cdot 10^{-12}\ \text{s}.$$

3.4. Magnon absorption by collective modes

To determine the relative importance of the effects appearing in the magnetic absorption as a result of the spin–lattice coupling and as a result of randomization of the system, let us estimate the absolute values of the magnetic absorption. For the coherent component the corresponding contribution is contained in (2). Using the normalization $\int N_{{\rm ac(op)}\nu}(\varepsilon)d\varepsilon=1$, the values of the constants (32), and the characteristics of gadolinium, including its atomic volume $v_a=33$ Å^3 and g factors $g_f=g_d=2$, we obtain a value $A\approx 10^{-2}$ K for the amplitude constant (4) and the following estimates for the contributions to (2):

$$Q\sim\frac{\theta_C}{\hbar\tilde{c}},$$

$$L_{\rm ac}(\mathbf{Q},\varepsilon)N_{{\rm ac}\nu}(\varepsilon)\approx\left[\frac{2a\langle s^z\rangle^2}{\langle S^z+s^z\rangle\theta_C}\right]^2\frac{1}{\theta_C+\theta_D},$$

$$A(g_f S^z-g_d s^z)^2\xi^2 Q^2 L_{\rm ac}(\mathbf{Q},\varepsilon)N_{{\rm ac}\nu}(\varepsilon)\approx 2\cdot 10^{-16} \qquad (40)$$

for the acoustic region, and

$$Q\sim\frac{\Delta}{\hbar\tilde{c}},$$

$$L_{\rm op}(\mathbf{Q},\varepsilon)N_{{\rm op}\nu}(\varepsilon)\approx\left[\frac{2a\langle S^z\rangle\langle s^z\rangle}{\langle S^z+s^z\rangle\theta'_C}\right]^2\frac{1}{\theta'_C+\theta_D},$$

$$A(g_f+g_d)^2\langle S^z\rangle\langle s^z\rangle\xi^2 Q^2 L_{\rm op}(\mathbf{Q},\varepsilon)N_{{\rm op}\nu}(\varepsilon)\approx 2\cdot 10^{-15} \qquad (41)$$

for the optical region; here $\tilde{c}$ is the speed of light.

The maximum values of the magnetic absorption attained under excitation of the system by a field with wave vector $Q\sim q_B$ amounts to $\sim 1.5\times 10^{-7}$ for the acoustic magnon branch and $\sim 10^{-8}$ for the optical magnon branch.

The contribution to the incoherent component in the region of the collective modes is contained in Eq. (3). Assuming $\gamma_f=\gamma_d=\gamma$, we obtain

$$N_{{\rm ac}\xi}(\varepsilon)\approx(\theta_C+\theta_D)^{-1},$$

$$A(\gamma_f^2\langle S^z\rangle^2+\gamma_d^2\langle s^z\rangle^2)N_{{\rm ac}\xi}(\varepsilon)\approx 4.6\cdot 10^{-4}\gamma^2 \qquad (42)$$

for the acoustic region and

$$N_{{\rm op}\xi}(\varepsilon)\approx(\theta'_C+\theta_D)^{-1},$$

$$A(\gamma_f^2+\gamma_d^2)\langle S^z\rangle\langle s^z\rangle N_{{\rm op}\xi}(\varepsilon)\approx 9\cdot 10^{-6}\gamma^2 \qquad (43)$$

for the optical.

Considering a crystal with a nonmagnetic substitutional impurity with concentration c and assuming $g_f=g_d=2$, we obtain $\gamma^2=4c(1-c)$. In such a case the maximum values of the magnetic absorption in the region of the magnon bands owing to the incoherent component (42), (43) and to the spin–lattice coupling (40), (41) become equal at $c\approx 8\times 10^{-3}\%$ in the first case and at $c\approx 3\times 10^{-2}\%$ in the second.

3.5. Absorption of single-particle excitations

The contribution to $\chi^{+-}_{2\rm coh}(\mathbf{Q},\varepsilon)$ and $\chi^{+-}_{2\rm incoh}(\varepsilon)$ in the region of the single-particle Stoner excitations is given by expressions (20) and (29). The function $\tilde{N}(Q,\varepsilon)$ can be estimated as follows:

$$\tilde{N}(Q,\varepsilon)=\frac{x}{4QaT\sin(k_F a)}\ \text{ for }\ \Delta_-\leqslant\varepsilon\leqslant\Delta_+$$

and

$$\tilde{N}(Q,\varepsilon)=0\ \text{ for }\ \varepsilon<\Delta_-\ \text{ or }\ \varepsilon>\Delta_+\,,$$

where

$$\Delta_\pm=\Delta\left(1\pm\frac{2aT\sin(k_F a)}{\hbar\tilde{c}}\right).$$

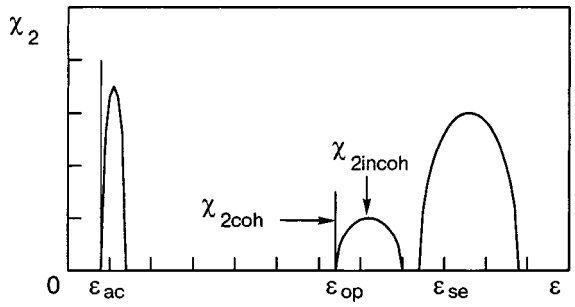

FIG. 1. Diagram of the spectrum of the imaginary part $\chi_2(0,\varepsilon)$ of the dynamic magnetic susceptibility of the model under consideration for a uniform high-frequency field: ε_{ac} and ε_{op} are the positions of the δ-function peaks of the coherent component of the susceptibility $\chi_{2coh}(0,\varepsilon)$; $\chi_{2incoh}(\varepsilon)$ is the incoherent component, which is proportional to the density of states of acoustic N_{ac} and optical N_{op} magnons in the regions corresponding to the frequencies ε_{ac} and ε_{op}; ε_{se} is the band of single-particle (Stoner) excitations with a spin flip and arbitrary quasimomentum.

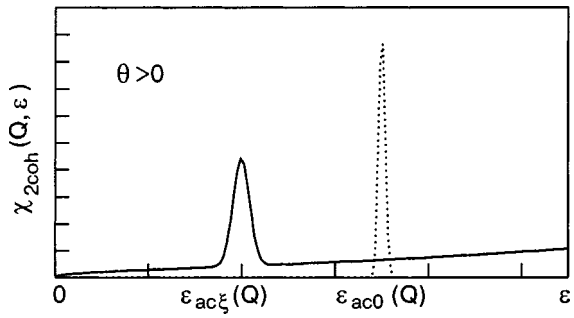

FIG. 3. Diagram of the spectra of the imaginary part $\chi_{2coh}(Q,\varepsilon)$ of the coherent component of the dynamic magnetic susceptibility of the model in the region of the inhomogeneous magnetic resonance (near the bottom of the acoustic magnon branch) at finite absolute temperature; $\varepsilon_{ac\xi}(Q)$ and $\varepsilon_{ac0}(Q)$ are the positions of the susceptibility peaks with (solid curve) and without (dotted curve) the spin–lattice coupling. The temperature and wave vector of the field satisfy the inequalities $0<\theta\ll\theta_C$ and $0<Q<q_{0ac}$.

Assuming that $x\sim 0.3$, $k_F a\sim 0.3$, $E_F/2zT\approx 0.1$, $2zT\approx 10^3$ K,[4] $U-J=zT/\langle s^z\rangle$, $\Delta\sim 10^4$ K, and a value of the integral in (29) equal to

$$\sim \frac{1}{2zT+E_F}\,\frac{1}{1+[(U-J)/E_F]^2},$$

we obtain $St_{coh\nu}(\mathbf{Q},\varepsilon)\approx 9\times 10^{-9}$, $St_{incho\nu}(\varepsilon)\approx 9\times 10^{-9}\gamma^2$. Equality of the magnetic absorption in the coherent and incoherent Stoner spectral regions is reached at $c\approx 0.3\%$.

4. GRAPHIC REPRESENTATION OF THE MAGNETIC ABSORPTION SPECTRUM

The magnetic absorption spectra obtained above [Eqs. (2), (3)] are shown schematically in Figs. 1–3. Figure 1 shows the overall picture of all the absorption bands on a large energy scale. Figure 2 shows the narrow coherent bands of the inhomogeneous resonance in the optical region of the spectrum with and without the spin–lattice interaction. Also shown are the ''phonon wing,'' which arises on account of the spin–lattice coupling, and the absorption band due to single-electron transitions with nonzero quasimomentum transfer. Figure 3 shows the inhomogeneous magnetic resonance lines in the acoustic region of the spectrum (near the bottom of the acoustic magnon band) at nonzero temperature both with and without the spin–lattice coupling (in the former case the resonance line is smeared). This contribution is subsumed in the total coherent contribution, which is allowed thanks to the spin-lattice coupling—the absorption of magnons by thermal phonons (above and below $\varepsilon_{ac0}(Q)$) and the emission of phonons by both thermal magnons and magnons excited by the electromagnetic field (above $\varepsilon_{ac0}(Q)$).

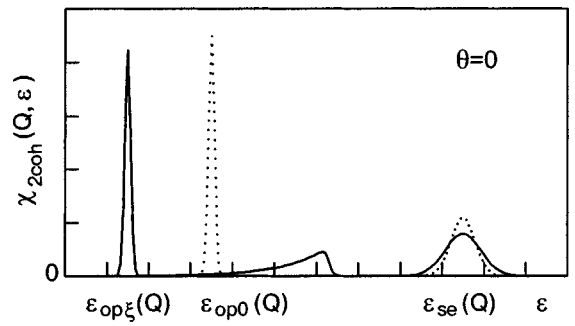

FIG. 2. Diagram of the spectra of the imaginary part $\chi_{2coh}(Q,\varepsilon)$ of the coherent component of the dynamic magnetic susceptibility of the model in the region of the $d-f$ exchange resonance and single-electron spin (Stoner) excitations at zero absolute temperature with (solid curve) and without (dotted curve) the spin–lattice coupling; $\varepsilon_{op\xi}(Q)$, $\varepsilon_{op0}(Q)$, and $\varepsilon_{se}(Q)$ are the positions of the susceptibility peaks (a weak ''magnon–phonon wing'' lies to the right of the main peak with energy $\varepsilon_{op\xi}(Q)$, starting at the point $\varepsilon_{op0}(Q)$); the wave vector of the field satisfies the inequality $0<Q<q_{0op}$.

5. DISCUSSION

The results obtained give a quantitative estimate of the spin–lattice coupling effects in the magnon system and permit one to compare the degrees to which the spectra of electron excitations with a spin flip is influenced by a weak spin–lattice coupling and by randomization of the g factors of the d and f subsystems. The latter leads mainly to ''opening'' (i.e., appearance in the magnetic absorption spectrum) of bands of acoustic and optical magnons that are being formed in the system, but it does not alter the position and shape of the characteristic magnetic resonance lines of the defect-free crystal. As is seen from formulas (2) and (3) and Figs. 1 and 2, a weak spin–lattice coupling at zero temperature does not affect the shape of the narrow magnetic absorption lines if the modulus of the wave vector Q of the field is less than the Cherenkov value $q_{0ac(op)}$, as is usually the case in $4f-5d$ metals. The main effects of weak spin–lattice coupling reduce to the following.

1. Weak spin–lattice coupling leads to opening of the phonon and magnon bands in the coherent component of the absorption (i.e., even in a perfect crystal).

2. The real part of the mass operator (I.48) leads to a shift of the magnon frequencies: the narrow lines (16) of the inhomogeneous ferromagnetic and exchange resonances in the perfect crystal at zero temperature are split off from the continuous bands arising as a result of the ''opening'' of the phonon and magnon bands (Fig. 2).

3. The imaginary component of the mass operator (I.49) causes smearing of the δ-function resonance lines if those resonances fall in the region of nonzero values of $M''(\varepsilon)$

(Fig. 3). The latter occurs at nonzero temperature for $Q < q_{0\mathrm{ac(op)}}$ and at any temperature for $Q > q_{0\mathrm{ac(op)}}$.

4. The relative corrections to the magnon effective masses from allowance for the spin–lattice coupling in a $4f-5d$ metal have values $\sim 2\times 10^{-4}$ for an acoustic mode and $\sim 4\times 10^{-4}$ for an optical mode.

5. The value of the maximum magnetic absorption due to the influence of the spin–lattice coupling on the coherent component of the magnetic susceptibility of an $f-d$ metal at zero temperature is comparable in order of magnitude with the influence of randomly distributed defects on the incoherent component in a crystal with a concentration of $\sim 0.03\%$ for an acoustic mode and $\sim 0.3\%$ for an optical mode.

6. The characteristic lifetime of magnons near the edge of the band in a narrow-band $d-f$ magnet is limited by the spin–lattice coupling to $\sim 10^{-10}$ s for the acoustic branch and $\sim 3\times 10^{-12}$ s for the optical branch.

The authors thank V. V. Eremenko and N. F. Kharchenko for interest and support and A. A. Loginov for helpful discussions and important critical comments.

APPENDIX A

Calculation of the coupling amplitude $\xi_{\mathbf{p},\mathbf{q}}$ in (I.5) for the model under discussion constitutes a separate problem. At the same time, it is clear that a not oversimplified microscopic model in the long-wavelength limit should give a magnon–phonon coupling amplitude for the acoustic magnon branch in agreement with the result of the calculations in the framework of the well-known[5] phenomenological approach. Let us therefore obtain a qualitative representation of the behavior of the coupling amplitude in the whole Brillouin zone using a better-studied path—the model of a Heisenberg ferromagnet.[3,5,6] In such a model the dispersion of magnons in a band of width W is determined by an expression of the same form as that obtained in the present paper for acoustic magnons:

$$\varepsilon_{\mathbf{q}}=\frac{W}{2}(1-\gamma_{\mathbf{q}}),\quad \gamma_{\mathbf{q}}=\frac{1}{z}\sum_{\boldsymbol{\eta}}\exp(i\mathbf{q}\cdot\boldsymbol{\eta}), \tag{A1}$$

and the Hamiltonian of the spin–lattice interaction has the form[6]

$$\mathcal{H}_{\mathrm{sp-lat}}=-\sum_{\boldsymbol{\lambda},\boldsymbol{\eta}}\nabla^{\alpha}_{\boldsymbol{\lambda}\boldsymbol{\eta}}I(\boldsymbol{\lambda},\boldsymbol{\eta})u^{\alpha}_{\boldsymbol{\lambda}\boldsymbol{\eta}}(\mathbf{S}_{\boldsymbol{\lambda}}\cdot\mathbf{S}_{\boldsymbol{\lambda}+\boldsymbol{\eta}}), \tag{A2}$$

where $I(\boldsymbol{\lambda},\boldsymbol{\eta})$ is the intersite exchange integral, and $\mathbf{u}_{\boldsymbol{\lambda}\boldsymbol{\eta}}=\mathbf{u}_{\boldsymbol{\eta}}-\mathbf{u}_{\boldsymbol{\lambda}}$ is the relative displacement of the atoms.

Assuming that the exchange integral is nonzero only for pairs of atoms within the first coordination sphere, we write its coordinate dependence in a form analogous to (28):

$$I(\boldsymbol{\lambda},\boldsymbol{\eta}')=I(r)=I_0\exp(-r/a), \tag{A3}$$

where $r=|\boldsymbol{\eta}'-\boldsymbol{\eta}|$ is the value of the longitudinal displacement of the ion that is the nearest neighbor of site $\boldsymbol{\lambda}$ from its equilibrium position $\boldsymbol{\lambda}+\boldsymbol{\eta}$, and I_0 is the exchange integral in the equilibrium position of the lattice sites. Using the standard form for the acoustic phonon frequencies[3]

$$\nu_p=\nu_0|\sin(pa/2)|, \tag{A4}$$

we express the cutoff angular frequency ν_0 in terms of the rms amplitude A_0 of the zero-point vibrations of the atoms with that frequency (see Eq. (31)):

$$\nu_0=\frac{\hbar^2}{2M_aA_0^2}. \tag{A5}$$

Using relations (A2)–(A5), expressing $\mathbf{u}_{\boldsymbol{\lambda}\boldsymbol{\eta}}$ and $\mathbf{S}_{\boldsymbol{\lambda}}$ in terms of the phonon and magnon operators, and neglecting the magnon anharmonicity, we obtain from (A2) the following magnon–phonon coupling operator, which agrees in form with (I.5):

$$\mathcal{H}_{m\mathrm{ph}}=\frac{1}{\sqrt{N}}\sum_{\mathbf{q},\mathbf{p}}\xi_{\mathbf{q},\mathbf{p}}a^{+}_{\mathbf{q}+\mathbf{p}}a_{\mathbf{q}}(b_{\mathbf{p}}+b^{+}_{-\mathbf{p}}). \tag{A6}$$

The magnon–phonon coupling amplitude in (A6),

$$\xi_{\mathbf{q},\mathbf{p}}=\xi\Xi_{\mathbf{q},\mathbf{p}} \tag{A7}$$

decomposes into a product of the reduced dimensionless amplitude

$$\Xi_{\mathbf{q},\mathbf{p}}=i\frac{\sin\dfrac{pa}{2}\sin\dfrac{qa}{2}\sin\dfrac{(q+p)a}{2}}{\sqrt{\left|\sin\dfrac{pa}{2}\right|}} \tag{A8}$$

and the force constant

$$\xi=W\frac{A_0}{a}, \tag{A9}$$

in which, in turn, we have separated out the magnon bandwidth[3]

$$W=4I_0Sz. \tag{A10}$$

The magnon energy $\varepsilon_{\xi}(\mathbf{q})$ renormalized by coupling (A6) is calculated by the standard method and is expressed in terms of the bare energy $\varepsilon_0(\mathbf{q})$ and the real part of the magnon mass operator:[3]

$$\varepsilon_{\xi}(\mathbf{q})=\varepsilon_0(\mathbf{q})+M'(\mathbf{q},\varepsilon_{\xi}(\mathbf{q})), \tag{A11}$$

$$M'(\mathbf{q},\varepsilon)=\frac{\xi^2}{N}\mathcal{P}\sum_{\mathbf{p}}|\Xi_{\mathbf{q},\mathbf{p}}|^2\left[\frac{1+n'_{\mathbf{p}}}{\varepsilon-\varepsilon_{+}(\mathbf{q},\mathbf{p})}+\frac{n'_{\mathbf{p}}}{\varepsilon-\varepsilon_{-}(\mathbf{q},\mathbf{p})}\right], \tag{A12}$$

$$\varepsilon_{\pm}(\mathbf{q},\mathbf{p})=\varepsilon_0(\mathbf{q}+\mathbf{p})\pm\nu_{\mathbf{p}}. \tag{A13}$$

The notation in (A11)–(A13) is analogous to that used in (I.51), (I.48), and (I.46).

The width of the acoustic magnon band calculated for a simple cubic lattice ($\gamma_{\mathbf{q}}=(1/3)[\cos(q_xa)+\cos(q_ya)+\cos(q_za)]$) in the $f-d$ magnet model under consideration with the Fermi surface approximated by the surface of a cube of side $k_F=\pi x^{1/3}/a$ is given, in distinction to (A10), by

$$W_{\mathrm{ac}}=\frac{Tzx^{2/3}\sin(k_Fa)}{\pi\langle S^z+s^z\rangle}. \tag{A14}$$

We note that for the value of the electron concentration chosen by us for numerical estimates, $x=0.3$, the Fermi quasimomentum is close to the Brillouin one, $k_F\approx 0.7k_B$, which

justifies the approximation adopted above for the shape of the Fermi surface. Comparing (A11)–(A13) with (I.51), (I.48), and (I.46), using (A14), and, for clarity, explicitly separating off the electron bandwidth [see (I.31)],

$$W_e = 2Tz, \tag{A15}$$

we obtain the desired expression for the magnon–phonon coupling amplitude in Eq. (I.5) in the form of (A7), (A8) with the force constant

$$\xi = W_e \frac{A_0}{a} \frac{x^{2/3}\sin(k_F a)}{4\pi\langle s^z\rangle^2}. \tag{A16}$$

The use of the form (A15) here emphasizes, in comparison with (A9), the difference of (A16) from the simple electron–phonon coupling.

APPENDIX B

The relation between the Curie temperature and the parameters of Hamiltonian (I.2) is of great interest, but its calculation in the model under consideration is the subject of a separate study. At the same time, it is not hard to obtain an estimate of θ_C with acceptable accuracy for the purposes of the present study, as a comparison with the Heisenberg model shows. We note that the published value of θ_C for systems with double exchange, calculated numerically in the dynamic molecular field model,[7] cannot be used in our case, since the calculation in Ref. 7 was done for $3 \leqslant J/W_e < \infty$, while in this paper $J/W_e \approx 0.1$.

Following Refs. 8 and 9, we consider the occupation of the magnon states in the temperature region $\theta \sim \theta_C$. The relative magnetization

$$\sigma(\theta) = 1 - \frac{n(\theta)}{S} \tag{B1}$$

is determined by the number of all spin deviations divided by the number of crystal lattice sites (for simplicity we are assuming that the same spin S is found in each of them):

$$n(\theta) = \frac{1}{N}\sum_{\mathbf{q}} n_{\mathbf{q}}, \tag{B2}$$

where $n_{\mathbf{q}}$ is the magnon distribution function

$$n_{\mathbf{q}} = [\exp(\varepsilon_{\mathbf{q}}/\theta) - 1]^{-1}, \tag{B3}$$

and $\varepsilon_{\mathbf{q}}$ is the magnon energy [see (A1)].

For $\theta > \varepsilon_{\mathbf{q}}$ the number of magnons with quasimomentum $\mathbf{q}$ can be written approximately in the form

$$n_{\mathbf{q}} = \frac{\theta}{\varepsilon_{\mathbf{q}}} - \frac{1}{2}. \tag{B4}$$

If relation (B4) is fulfilled for the majority of the magnons, then the reduced magnetization can be represented using (B1–B3) approximately in the form

$$\sigma(\theta) = 1 + \frac{1}{2S} - \frac{2\theta}{WS}\frac{1}{N}\sum_{\mathbf{q}} \frac{1}{1-\gamma_{\mathbf{q}}}. \tag{B5}$$

The value of the sum in (A5)

$$C = \frac{1}{N}\sum_{\mathbf{q}} \frac{1}{1-\gamma_{\mathbf{q}}} \tag{B6}$$

depends on the type of magnetic lattice and is equal to 1.5164 for the simple cubic structure, to 1.393 for the bcc structure, and to 1.345 for the fcc structure.[6,8]

In the high-temperature region, where the number of spin deviations is large and the magnon–magnon coupling becomes important, the corresponding effects of nonlinearity in the magnon spectrum can be taken into account to a first approximation by the following renormalization of the magnon bandwidth:[8–10]

$$\tilde{W} = W\left(1 - \frac{1}{SN}\sum_{\mathbf{q}} (1-\gamma_{\mathbf{q}}) n_{\mathbf{q}}\right). \tag{B7}$$

At the Curie point the relative magnetization goes to zero, and from (B5) and (B6) we obtain

$$\theta_C = \frac{W(S+1/2)}{2C}. \tag{B8}$$

Magnon anharmonicity lowers this value. Substitution of (B8) into (B7) gives the following coefficient in the first step of the iteration scheme for a simple cubic lattice:[9]

$$1 - \frac{1}{SN}\sum_{\mathbf{q}} (1-\gamma_{\mathbf{q}}) n_{\mathbf{q}} \approx 0.591. \tag{B9}$$

We consider a Heisenberg ferromagnet [$W = 4I_0 zS$; see (A10)] with the simple cubic lattice ($z = 6$) and spin $S = 7/2$, and we compare the values of the Curie temperature obtained by the different methods. The lowest value, which we adopt as the base, is given by the spin-wave model in the Bogolyubov–Tyablikov approximation[5,6,11]

$$\theta_C = \frac{W(S+1)}{6C}. \tag{B10}$$

A somewhat larger value is given by the Rushbrooke–Wood formula,[8,9,12] obtained by the method of high-temperature expansions of the magnetic susceptibility:

$$\theta_C = \frac{5}{96} I_0 (z-1)[11S(S+1) - 1]. \tag{B11}$$

The molecular field model leads to a value higher than the "true" value [(B10) or (B11)] by approximately a factor of 1.5:

$$\theta_C = \frac{W(S+1)}{6}. \tag{B12}$$

The value in (B8) exceeds that in (B10) by approximately a factor of three, but if the renormalization (B9) is taken into account, we obtain the value

$$\theta_C = 0.591 \frac{W(S+1/2)}{2C}, \tag{B13}$$

which is higher than the "true" value approximately by a factor of 1.5.

Thus the accuracy of determination of the Curie temperature with the use of expression (B13) is approximately the same as with the use of the molecular field model (B12). Substituting into (B13) the acoustic magnon bandwidth (A14), we obtain for an $f-d$ magnet

$$\theta_C = 0.591 \frac{zTx^{2/3}\sin(k_F a)(S+1/2)}{2\pi C(S+\langle s^z\rangle)}. \quad \text{(B14)}$$

If we take into consideration the result of Ref. 13, which implies that the magnon stiffness in the system with double exchange[14] (and, accordingly, in an $f-d$ magnet) near the Curie point is higher than in a Heisenberg ferromagnet, then we would expect that the ''true'' value of θ_C will be higher than is predicted by (B10). In such a case the difference between the value in (B14), in which this increase of the magnon stiffness is not taken into account, and the true value of θ_C should be diminished in comparison with that mentioned above.

The foregoing analysis has shown that the accuracy of determination of the Curie temperature with the use of expression (B14) is completely comparable to the accuracy of determination of θ_C for a Heisenberg ferromagnet with the use of the molecular field model. It should also be noted that formula (B14) gives a maximum of θ_C at $x=0.35$, which is in much better agreement with expression ($x=0.33$)[14] than the value obtained by a numerical method in the dynamic molecular field model,[7] which gives a maximum of θ_C at $x=0.5$.

*E-mail: beznosov@ilt.kharkov.ua

[1)]References to Part I of this study[1] will be denoted using the Roman numeral I.

[1] A. B. Beznosov and E. S. Orel, Fiz. Nizk. Temp. **30**, 958 (2004) [Low Temp. Phys. **30**, 721 (2004)].
[2] N. F. Mott and E. A. Davis, *Electronic Processes in Non-Crystalline Materials*, Clarendon Press, Oxford (1979), Mir, Moscow (1982).
[3] A. S. Davydov, *Theory of the Solid State* [in Russian], Nauka, Moscow (1976).
[4] A. B. Beznosov, V. P. Gnezdilov, and V. V. Eremenko, JETP Lett. **38**, 587 (1983).
[5] A. I. Akhiezer, V. G. Bar'yakhtar, and S. V. Peletminskii, *Spin Waves*, North-Holland, Amsterdam (1968), Nauka, Moscow (1967).
[6] S. V. Tyablikov, *Methods in the Quantum Theory of Magnetism*, transl. of 1st ed., Plenum Press, New York (1967), 2nd ed., Nauka, Moscow (1975).
[7] N. Furukawa, in *Physics of Manganites*, T. A. Kaplan and S. D. Mahanti (eds.), Kluwer Academic, New York (1999), p. 1.
[8] D. C. Mattis, *Theory of Magnetism*, Harper and Row, New York (1965), Mir, Moscow (1967).
[9] É. L. Nagaev, *Physics of Magnetic Semiconductors*, Mir, Moscow (1983), Nauka, Moscow (1979).
[10] C. Kittel, *Quantum Theory of Solids*, Wiley, New York (1963), Nauka, Moscow (1967).
[11] V. G. Bar'yakhtar, V. N. Krivoruchko, and D. A. Yablonskiĭ, *Green's Functions in the Theory of Magnetism* [in Russian], Naukova Dumka, Kiev (1984).
[12] G. S. Rushbrooke and P. J. Wood, Mol. Phys. **1**, 257 (1958).
[13] C. W. Searle and S. T. Wang, Can. J. Phys. **48**, 2023 (1970).
[14] J. M. D. Coey, M. Viret, and S. von Molnar, Adv. Phys. **48**, 167 (1999).

Translated by Steve Torstveit

Single-pulse and secondary echoes in systems with a large inhomogeneous broadening of NMR lines

J. G. Chigvinadze, G. I. Mamniashvili, and Yu. G. Sharimanov

*E. Andronikashvili Institute of Physics of the Georgian Academy of Sciences, 6 Tamarashvili St., Tbilisi 380077, Georgia**

(Submitted February 11, 2003, revised February 10, 2004)
Fiz. Nizk. Temp. **30**, 1065–1070 (October 2004)

The equations for the nuclear magnetizations which describe the dynamics of nuclear spin-systems with strong Larmor and Rabi inhomogeneous broadenings of the NMR line under conditions of their nonequilibrium are obtained in the framework of the Mims transformation matrix method; these equations have been obtained previously by the statistical tensors method. As an example, the properties of the proton single-pulse echo and its secondary signals in a test material (silicone oil) coated on the surface of high-T_c superconducting-oxide powders and in metallic hydride are presented. © *2004 American Institute of Physics.*
[DOI: 10.1063/1.1808198]

The single-pulse echo (SPE) is a resonance response of the inhomogeneously broadened nuclear spin system to the application of a solitary radio-frequency (rf) pulse arising at a time approximately equal to the pulse duration τ after its termination. Though SPE was discovered by Bloom in 1955 for protons in water placed in an inhomogeneous magnetic field, the mechanism of SPE formation is not yet so clear-cut as for the classical Hahn two-pulse echo (TPE) and it continues to attract research attention.[1]

The point is that the theoretical models based exclusively on strong Larmor inhomogeneous broadening (LIB) do not agree with the experimentally observed signals but instead result in the formation of oscillatory free-induction decays (OFIDs).[1]

SPE formation mechanisms could be conditionally subdivided into two classes: the first class comprises the so-called edge-type mechanisms, wherein the rf pulse edges act like the rf pulses in the TPE method; these include the distortion mechanism[1] and the mechanism connected with the consideration of spectral densities of sufficiently steep rf pulse edges.[2] The second class includes mechanisms of an internal nature due to particular nonlinearities in the dynamics of spin systems, for example, connected with a strong dynamic frequency shift of the NMR frequency or with a nonlinear dynamics of nuclear spins due to the simulteneous presence of large Larmor and Rabi inhomogeneous broadenings of the NMR line.[1]

In this work we consider in more detail the so-called multipulse mechanism of SPE formation, presented in Ref. 1, for systems with both types of frequency inhomogeneities of NMR lines. An important example of such a system is that of nuclei arranged in the domain walls of multidomain magnets, both in the normal metals, due to the metallic skin effect, and in the normal cores of Abrikosov vortices in type-II superconductors. Earlier in Ref. 3 we have investigated the properties of the SPE formation in lithium ferrite. It was established that its properties differ sharply from the SPE properties in hexagonal cobalt, where it is formed by the distortion mechanism. It was therefore concluded that the SPE internal mechanism of formation could be effective in lithium ferrite, but its concrete mechanism was not finally established.

Later on, the effectiveness of the multipulse mechanism of SPE formation was experimentally established in this magnet.[4] Moreover, the secondary echo signals of SPE and the two-pulse echo were also formed by this mechanism.

It was shown in Ref. 1 that the multipulse mechanism of SPE formation is effective in some multidomain ferromagnets like Fe and FeV. From this point of view further theoretical and experimental investigations of SPE multipulse mechanism formation in systems with large Larmor and Rabi inhomogeneous broadenings of NMR lines are of practical interest. In Ref. 1, using the formalism of statistical tensors, a theoretical investigation of the SPE and its secondary echo-signal formation mechanism was carried out, allowing for both large Larmor and Rabi inhomogeneous broadenings of the NMR line when the repetition period of the rf pulses T obeys the inequality $T_3 \ll T_2 < T < T_1$, where T_1 is the spin-lattice relaxation time, T_2 is the transverse irreversible relaxation time, and T_3 characterizes the transverse reversible relaxation time ($T_3 \sim 1/\Delta$, where Δ is the half width at half maximum of the inhomogeneously broadened line); therefore, the spin system was in a nonequilibrium state before the application of the exciting rf pulse, and only the longitudinal component of the nuclear magnetization was important before the rf pulse. It was shown that a dephasing of the nuclear spin system was accumulated during n-time pulse excitations and restored within a time interval elapsing from the trailing edge of the last "counting" $[(n+1)\text{th}]$ pulse in the multipulse train. This resulted in the SPE formation and also its secondary signals at times which were multiples of the rf pulse duration after termination of the "counting" rf pulse.

Let us show further a simple classical derivation of the equations describing the nuclear spin-system dynamics in the investigated case, in the framework of the usual classical approach, by solving Bloch equations or by the equivalent Mim's transformation matrix method.[5] We will use the latter

as it is more visual from the experimental point of view.

Let us consider the case when a local static field H_n is directed along the Z axis, and a rf field is along the X axis of the rotating coordinate system (RCS).[5,6] The modulus of $\mathbf{H}_{\text{eff}}$ in the RCS could be expressed by:

$$H_{\text{eff}}=\frac{1}{\gamma_n}\sqrt{\Delta\omega_j^2+\omega_1^2}=\frac{\overline{\omega_1}}{\gamma_n}\sqrt{a^2+x^2}. \tag{1}$$

Here $x=\Delta\omega_j/\overline{\omega_1}$, where $\Delta\omega_j=\omega_j-\omega_0$ is an isochromate frequency; $a=\eta/\overline{\eta}$ (or $a=\omega_1/\overline{\omega_1}$), where η is the rf field gain factor and $\overline{\eta}$ its mean value; $\overline{\omega_1}=\overline{\eta}\omega_1^{APPL}$ is the mean value of the rf amplitude in frequency units; $\omega_1=\eta\omega_1^{APPL}$ is the Rabi frequency of the applied rf field; and, γ_n is the nuclear gyromagnetic ratio. In addition, let us introduce the following designations[1] for the mean value of the pulse area $y=\overline{\omega_1}\Delta t$, where Δt is the rf pulse duration, $b=\overline{\omega_1}\tau$ is a characteristic of the time interval following a pulsed excitation and is measured from the trailing edge of the rf pulse; ω_0 designates the center of the resonance line, and ω_j is the frequency of the jth isochromate. The transformation matrix describing the rotation of the magnetization vector around $\mathbf{H}_{\text{eff}}$ is:[6] $\overline{m}=(\overline{m}_x;\overline{m}_y;\overline{m}_z)$

$$(R)=\begin{bmatrix} S_\psi^2+C_\psi^2C_\theta & -C_\psi S_\theta & S_\psi C_\psi(1-C_\theta) \\ C_\psi S_\theta & C_\theta & -S_\psi S_\theta \\ S_\psi C_\psi(1-C_\theta) & S_\psi S_\theta & C_\psi^2+S_\psi^2C_\theta \end{bmatrix}, \tag{2}$$

C_ψ, S_ψ, C_θ, and S_θ stand for $\cos\psi$, $\sin\psi$, $\cos\theta$, and $\sin\theta$, and $\Psi=\tan^{-1}(\omega_1/\Delta\omega_j)$ is the angle between the effective field $\mathbf{H}_{\text{eff}}$ and the Z axis; θ is the angle by which the magnetization turns about the effective field $\mathbf{H}_{\text{eff}}$ during the pulse time Δt: $\theta=\gamma_n H_{\text{eff}}t$, where $\mathbf{H}_{\text{eff}}$ is given by (1).

Let us consider first the case of single-pulse excitation. Let

$$X_j=m_{xj}/m;\quad Y_j=m_{yj}/m;\quad Z_j=m_{zj}/m,$$

$$\text{and}\quad \overline{\mu}=(X_j;Y_j;Z_j),$$

where m is the equilibrium nuclear magnetization, and at equilibrium $\overline{\mu}_{\text{eq}}=(0;0;1)$.

If before the excitation by the rf pulse the nuclear spin system was at equilibrium conditions, and therefore $\overline{\mu}_{\text{eq}}=(0;0;1)$, then the result of the rf pulse action is given by $\overline{\mu}=(R)\overline{\mu}_{\text{eq}}$. At the termination of the rf pulse the isochromates precess freely around the Z axis; this is described by the matrix

$$R_\varphi=\begin{pmatrix} C_\varphi & -S_\varphi & 0 \\ S_\varphi & C_\varphi & 0 \\ 0 & 0 & 1 \end{pmatrix},$$

where $\varphi=\Delta\omega_j\tau$ is the angle of rotation of the isochromate around the Z axis, and τ is the time elapsing from the trailing edge of a pulse. Therefore, we have finally:

$$\overline{\mu}_1=(R_\varphi)(R)\overline{\mu}_{\text{eq}}=\begin{pmatrix} C_\varphi S_\psi C_\psi(1-C_\theta)+S_\varphi S_\psi S_\theta \\ S_\varphi S_\psi C_\psi(1-C_\theta)-C_\varphi S_\psi S_\theta \\ C_\psi^2+S_\psi^2C_\theta \end{pmatrix}, \tag{3}$$

or in the adopted designations:

$$\frac{m_x}{m}=\cos bx\frac{ax}{a^2+x^2}(1-\cos y\sqrt{a^2+x^2})+\sin bx\frac{a}{\sqrt{a^2+x^2}}\sin y\sqrt{a^2+x^2},$$

$$\frac{m_y}{m}=\sin bx\frac{ax}{a^2+x^2}(1-\cos y\sqrt{a^2+x^2})-\cos bx\frac{a}{\sqrt{a^2+x^2}}\sin y\sqrt{a^2+x^2}, \tag{4}$$

$$\frac{m_z}{m}=1-\frac{a^2}{a^2+x^2}(1-\cos y\sqrt{a^2+x^2}).$$

Expressions (4) coincide with the corresponding ones obtained in Ref. 1 for the case of single-pulse excitation, and with similar expressions[7] obtained by solving the system of Bloch equations for inhomogeneously broadened Hahn systems.

Let us now find the effect of n-time rf excitation in the model of Ref. 1, when before the next rf pulse of a train only the longitudinal component of the nuclear magnetization remains. It is not difficult to prove by successive matrix multiplication that the expression for the nuclear magnetization before the final ''counting'' $(n+1)$th pulse is:

$$\overline{\mu}_n=(C_\psi^2+S_\psi^2C_\theta)^n\overline{\mu}_{\text{eq}},$$

where $\overline{\mu}_{\text{eq}}=(0;0;1)$.

Then the result of excitation by the ''counting'' pulse and subsequent free precession of the magnetization is described by the expression

$$\overline{\mu}_{n+1}=(R_\varphi)(R)\overline{\mu}_n=(C_\psi^2+S_\psi^2C_\theta)^n\begin{pmatrix} C_\varphi S_\psi C_\psi(1-C_\theta)+S_\varphi S_\psi S_\theta \\ S_\varphi S_\psi C_\psi(1-C_\theta)-C_\varphi S_\psi S_\theta \\ C_\psi^2+S_\psi^2C_\theta \end{pmatrix}, \tag{5}$$

which is similar to the one for single-pulse excitation but allows for a new initial condition.

It follows from the previous expressions (5) that in terms of the adopted designations

$$\frac{m_x}{m}=\left(1-\frac{a^2}{a^2+x^2}[1-\cos y\sqrt{a^2+x^2}]\right)^n\times\left[\cos bx\frac{ax}{a^2+x^2}(1-\cos y\sqrt{a^2+x^2})+\sin bx\frac{a}{\sqrt{a^2+x^2}}\sin y\sqrt{a^2+x^2}\right], \tag{6}$$

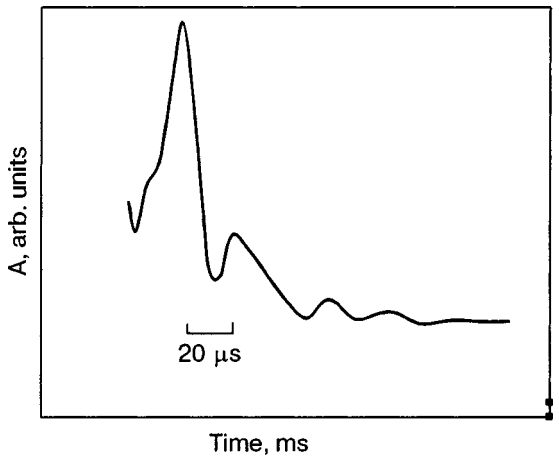

FIG. 1. Single-pulse echo and its secondary signals in a liquid solution of $MnCl_2$ at room temperature. $\tau=20$ μs, $T=4$ ms, $T_1=86$ ms, $T_2=72$ ms.

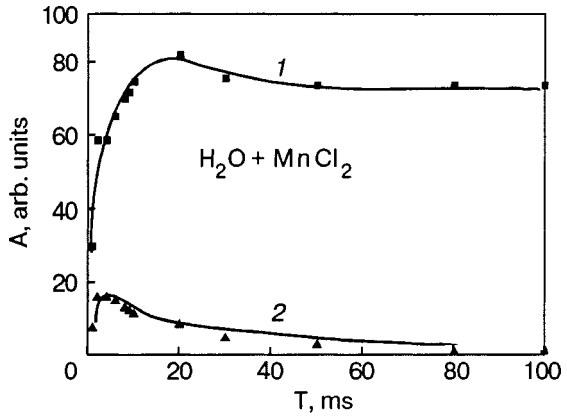

FIG. 2. Dependence of the SPE (*1*) and its secondary echo signal's peak intensities (*2*) on the rf pulse repetition period T at room temperatures in a liquid solution of $MnCl_2$.

$$\frac{m_y}{m}-\left(1-\frac{a^2}{a^2+x^2}[1-\cos y\sqrt{a^2+x^2}]\right)^n \times\left[\sin bx\,\frac{ax}{a^2+x^2}(1-\cos y\sqrt{a^2+x^2}) + \cos bx\,\frac{a}{\sqrt{a^2+x^2}}\sin y\sqrt{a^2+x^2}\right].$$

These expressions coincide with those obtained in Ref. 1 using the formalism of statistical tensors. The nth degree multiplier has the simple physical meaning of the longitudinal nuclear magnetization created by the n previous pulses of a multipulse train, reflecting the spin system's memory of the excitation. The expressions for the SPE and its secondary echo signal amplitudes were already obtained in Ref. 1 using similar expressions for the nuclear magnetization vectors. It is easy to prove that the approach considered above could be immediately applied to the case of periodic two-pulse excitation, which is of interest for the description of secondary echo signals in the investigated systems.

Suppose we also know[1] that the effect of SPE and its secondary echo signals formation is present for a large LIB in isolation but is stronger in the simultaneous presence of both frequency inhomogeneities, as in the case of multidomain ferromagnets and type II superconductors.

Let us illustrate some of the above-mentioned dependences on concrete examples of practical interest.

Experimental results were obtained on a Bruker Minispec p20 NMR spectrometer provided with a Kawasaki Electronica digital signal averager at room and liquid nitrogen temperatures.

Figure 1 shows the averager record of SPE and its secondary signals from protons in a liquid solution of $MnCl_2$ (water was doped by Mn^{++} paramagnetic impurities by adding a paramagnetic solution of $MnCl_2$ in order to obtain a suitable length of the spin–lattice relaxation time T_1 for the data collection) under periodic excitation by a pulse train with a period $T=4$ ms. The longitudinal and transverse relaxation times are, respectively, $T_1=86$ ms and $T_2=72$ ms at room temperature ($T=300$ K). The standard inversion-recovery and spin-echo train pulse sequences were employed in this work for the T_1 and T_2 determinations, respectively.

The dependence of the peak intensities (curve *2*) of the SPE (curve *1*) and its secondary echo signal on the rf pulse repetition period T at room temperatures in a liquid solution of $MnCl_2$ are presented in Fig. 2. The optimal inhomogeneous width of the NMR line for the observation of echo signals was achieved by using an additional iron plate placed in the magnet's clearance, as in Ref. 8.

Let us consider in more detail the SPE signal formation for the example of protons in a test material (silicone oil (SO), Silicon KF96) coated on the surface of a powdered sample of the high-T_c superconductor (HTSC) YBCO-(SO + YBCO), which is an object similar the one used in Ref. 8 to study the effect of inhomogeneous broadening of NMR lines due to the formation of an Abrikosov vortex lattice in a HTSC.

Figure 3 shows the SPE record of the investigated sample (SO+YBCO) at room temperature, and in Fig. 4 the dependence of its peak intensity on the rf pulse period T at room temperature (a) and at liquid nitrogen temperature ($T=77$ K) (b).

We note that at the given maximal rf pulse length of the spectrometer (20 μs) for the observation of the SPE signal

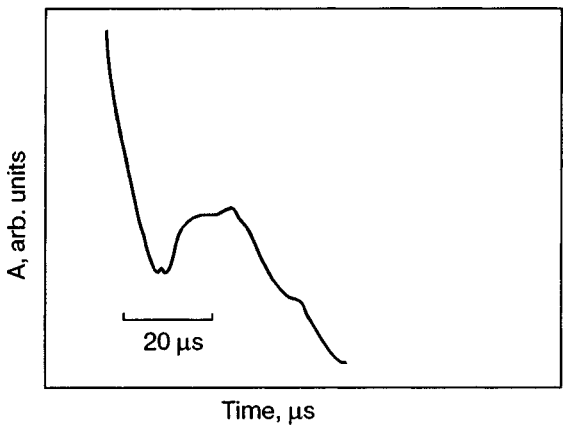

FIG. 3. SPE in silicone oil (SO) mixed with YBCO powder (SO + YBCO) at room temperature. $T=500$ ms, $T_2=150$ ms, $T_1=350$ ms.

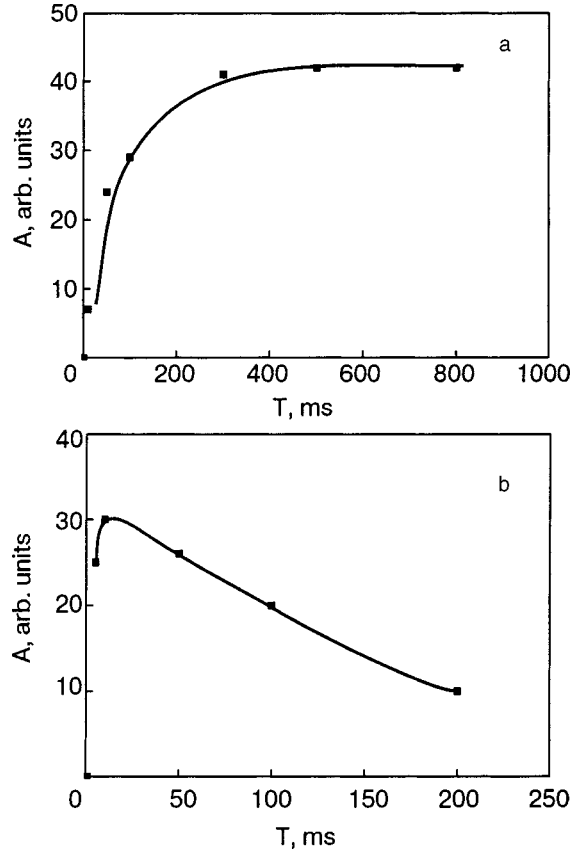

FIG. 4. Dependence of SPE peak intensities on the period T of the single-pulse train at room temperature (a) and at liquid nitrogen temperature (b) in SO+YBCO.

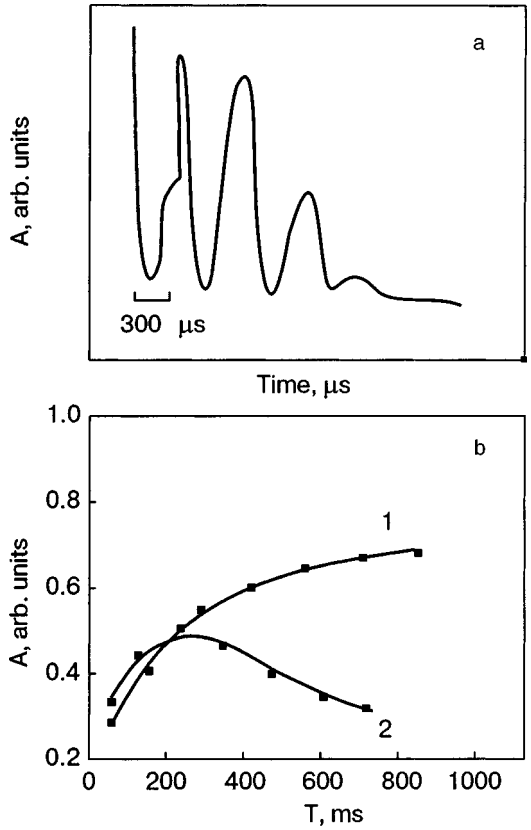

FIG. 5. Two-pulse echo (TPE) and its secondary signals in SO+YBCO (a). Dependences of TPE (*1*) and its secondary signal peak intensities (*2*) on the period T of the two-pulse train (b). The marks show the time position of the rf pulses for $T=300$ K.

one should introduce an artificial external magnetic field inhomogeneity (with the help of an additional iron plate[8]) to allow for condition (1)). At the same time at $T=77$ K (b), the SPE signal is observed in an homogeneous magnetic field, but the inhomogeneity of the NMR line is caused by the effect of the Abrikosov vortex lattice (AVL) formation.

The character of the dependence on the repetition period T points to a comparatively large role of the multipulse mechanism in the SPE formation at low temperatures.

The SO concentration in the sample under investigation was chosen as small as possible for enhancement of the vortex lattice effect.[9]

For comparision, Fig. 5a shows a record of the TPE and its secondary echo signals for an SO+YBCO sample with a larger concentration of coating material for obtaining more intense signals, while Fig. 4b shows the peak intensity dependences of the TPE (curve *1*) and its secondary signal (curve *2*) on the period T of the two-pulse train at room temperature.

It is seen that dependences of the SPE and secondary TPE signals on T have a similar character, reflecting the significant contribution of the multipulse mechanism in the SPE intensity. It is known that secondary TPE signals are formed by the multipulse mechanism in proton-containing systems.[10]

Vanadium hydride ($VH_{0.68}$) could be considered as one more example of a system possessing both types of inhomogeneities. In this case the inhomogeneities are the result of the metallic skin effect. Figure 6 shows the dependence of the SPE signal peak intensity on T at room temperature. In this case its intensity is practically unchanged with increase of T, showing that the contribution of the distortion mechanism is significant in this material, as it is in some metallic ferromagnets.[1]

Analysis of the results obtained shows that the SPE could be useful not only for a simple determination of the characteristic relaxation parameters of inhomogeneously broadened spin systems, but could provide an interesting approach to the study of AVL dynamics using the SPE signal

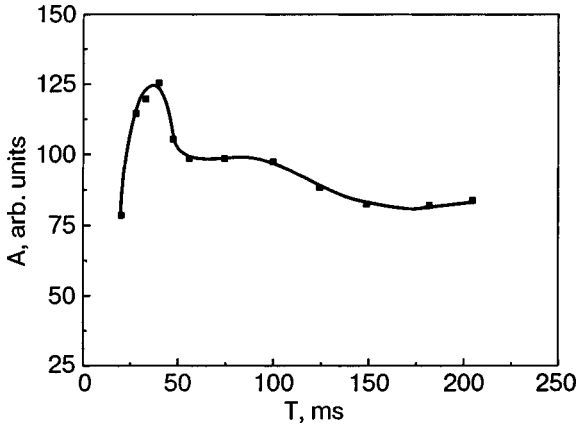

FIG. 6. The dependence of the SPE peak intensity on the period T of the single-pulse train in vanadium hydride $VH_{0.68}$. $\tau=20$ μs, $T=300$ K.

due to the effect of magnetic field inhomogeneity caused by the AVL formation.

This allows one to use the SPE effect for the study of AVL stimulated dynamics using pulsed and low-frequency magnetic fields.[11]

In conclusion, in the framework of a simple classical approach using Mim's transformation matrix method, the equations for the nuclear magnetizations are obtained which describe the dynamics of nuclear spin systems with strong Larmor and Rabi inhomogeneous broadenings of NMR lines under conditions of their nonequilibrium.

Properties of the proton single-pulse echo and its secondary signals in a test material (silicone oil) coated on the surface of high-T_c superconducting-oxide powders and in metallic hydride are presented.

In addition, it is shown experimentally that the single-pulse echo effect gives an opportunity to obtain valuable information on the inhomogeneous NMR broadening, reflecting the character of the microscopic distribution of magnetic field in such systems as superconductors, hydrides of metals, and so on.

This work was supported by the International Science and Technology Center through Project G-389.

*E-mail: jaba@physics.iberiapac.ge

[1] L. N. Shakhmuratova and D. K. Fowler, Phys. Rev. A **55**, 2955 (1997).
[2] B. P. Smolyakov and E. P. Khaĭimovich, Zh. Éksp. Teor. Fiz. **76**, 1303 (1979) [Sov. Phys. JETP **49**, 661 (1979)].
[3] A. M. Akhalkatsi and G. I. Mamniashvili, Fiz. Met. Metalloved. **81**, 79 (1996).
[4] A. M. Akhalkatsi and G. I. Mamniashvili, Phys. Lett. A **291**, 34 (2001).
[5] T. O. Gegechkori and G. I. Mamniashvili, Proc. TSU. **38**, 11 (2001).
[6] W. B. Mims, K. Nassau, and J. D. McGee, Phys. Rev. **123**, 2059 (1961).
[7] V. P. Chekmarev, M. I. Kurkin, and S. I. Goloshchapov, Zh. 'Éksp. Teor. Fiz. **76**, 1675 (1979) [Sov. Phys. JETP **49**, 851 (1979)].
[8] Y. Maniwa, T. Mituhashi *et al.*, Physica C **175**, 401 (1991).
[9] M. Kumimoto, T. Endo *et al.*, Phys. Rev. A **25**, 2235 (1982).
[10] B. F. Alekseev and V. D. Gadaev, JETP Lett. **22**, 169 (1975).
[11] J. G. Chigvinadze and G. I. Mamniashvili, Fiz. Nizk. Temp. **24**, 946 (1998) [Low Temp. Phys. **24**, 712 (1998)].

This article was published in English in the original Russian journal. Reproduced here with stylistic changes by AIP.

On the theory of the formation of equilibrium domain structure in antiferromagnets

E. V. Gomonay*

National Technical University of Ukraine "Kiev Polytechnic Institute," pr. Peremogi 37, Kiev 03056, Ukraine

V. M. Loktev†

N. N. Bogolyubov Institute of Theoretical Physics, National Academy of Sciences of Ukraine, ul. Metrologicheskaya 14-b, Kiev 03143, Ukraine

(Submitted February 12, 2004)
Fiz. Nizk. Temp. **30**, 1071–1085 (October 2004)

A model is proposed which describes the formation and reversible rearrangement of the equilibrium domain structure in bulk antiferromagnets with a rather strong magnetoelastic coupling. The model is based on the assumed existence of a microscopic ordering of a tensor nature—the microstress tensor that arises due to magnetoelastic coupling during the formation of the magnetic moment. It is necessary to take such a parameter into account for adequate description not only of the macroscopic internal stresses and the spontaneous strains corresponding to them but also of the microstructure of the crystal (e.g., the domain structure). The microstresses arising locally in each unit cell are equivalent, from a formal standpoint, to elastic dipoles, and they create long-range fields whose contribution to the free energy of the crystal is analogous to that of the magnetostatic energy in ferromagnets and favors a decrease in the macroscopic strain of the sample through the formation of an equilibrium domain structure. The corresponding contribution is given the name ''destressing energy'' by the authors. It is shown that taking this energy into account in antiferromagnetic crystals allows one not only to explain the cause of the formation of the domain structure but also to trace its dependence on the shape of the crystal and the external fields. [DOI: 10.1063/1.1808199]

1. INTRODUCTION

The possibility of the formation and reversible rearrangement of a domain structure in antiferromagnetic crystals was predicted by Néel more than a half century ago.[1] Although its presence is indicated by experiment, the causes that lead to the formation of domain structure at phase transitions in crystals that do not possess a macroscopic magnetic moment but are characterized by appreciable spontaneous strains have still not been clarified.

As a rule, the cause of a nonuniform distribution of antiferromagnetic vectors and the accompanying spontaneous lattice strains are assumed to be initial nonuniformity of the sample (technological defects), the existence of boundary conditions of a definite type (e.g., rigid coupling between the sample and a nonmagnetic substrate), or, finally, the entropy factor. Unfortunately, the models based on these assumptions cannot explain a number of experimental facts (see, e.g., Refs. 2–7) connected with the reversible rearrangement of the domain structure in antiferromagnetic crystals in the presence of external influences (e.g., a magnetic field or mechanical stresses). Furthermore, in the description of the phase transition itself the spontaneous strains accompanying the transition are considered to be exactly like the macroscopic strains arising when the sample is subjected to external loads, without any analysis of their microscopic causes.

The authors have previously[8–10] made attempts to explain the causes of the formation of domain structure in antiferromagnets by their internal properties and, in particular, by the presence of anisotropic surface energy,[8] the importance of the taking of which into account was first pointed out in Ref. 11, and also by the incompatibility of the spontaneous strains on the surface and in the bulk of the sample.[9,10] However, such an approach is applicable only under rather strong restrictions on the properties of the surface (for example, its properties must differ substantially from those of the bulk) and, furthermore, it does not explain the microscopic nature of the phenomenon.

In Refs. 12 and 13, *apropos* the formation of domain structure in ferromagnets with rather strong (in comparison with the magnetic anisotropy energy) magnetoelastic coupling, the idea was first set forth that internal stresses analogous to the stresses produced by defects (e.g., dislocations or inclusions) arise at transitions of this kind, but nothing was said about the microscopic nature of those stresses. And even though today the microscopic character of the spontaneous strains caused by magnetoelasticity is not in doubt, the influence of the internal stresses causing these strains on the thermoelastic[1)] phase transitions in antiferromagnets and other substances and on the formation of macroscopic (in particular, domain) structure in them remains an open question.

Let us discuss in general terms the process wherein magnetic order arises in a so-called Heisenberg magnet. According to the established ideas, at the critical temperature at each lattice site, i.e., locally, magnetic moments spontaneously form, their mutual directions agreeing as a result of the ex-

change interaction. It is perfectly clear that in the presence of magnetoelastic coupling (including interactions of a spin–orbit nature) the appearance of spontaneous moments should lead to a change in the value of the interaction potential between an atom on which a spin moment has arisen, and its nearest neighbors, i.e., to the formation of *local* stresses that can be characterized by a certain parameter $\hat{\sigma}^{\mathrm{mag}}$ of a tensor nature. In the simplest case (when only pair interactions are taken into account) this is a second-rank tensor whose symmetry should correspond to the local symmetry of the crystal lattice, lowered because of the onset of the spin ordering. Thus, in besides the ''main'' microscopic order parameter, which in this case is conventionally taken as the antiferromagnetic vector for the given unit cell, one can introduce an ''additional'' (but which nevertheless has completely equal standing) microscopic order parameter characterizing the local stresses (concentrated forces) and which, in the terminology of Kléman,[12,13] corresponds to quasi-defects.

It should be emphasized that the local microstresses introduced here and the global macrostrains employed in the theory of elasticity, which characterizes the state of the crystal as a whole, are completely different physical quantities. They are related only in that both of these quantities characterize the change of the elastic state of the crystal, and the microstrains created by them can be regarded as some ''degrees of freedom'' of the crystal which take part in the magnetic phase transitions and influence the magnetocrystalline structures that form as a result of those transitions. Taking these degrees of freedom into account is justified when doing so leads to nontrivial results, in particular, when describing phase transitions in ferro- and antiferromagnetic crystals with a degenerate direction of the axis of easy magnetization.

In this paper we propose a model that makes it possible to describe in a consistent way the formation and reversible rearrangement of the equilibrium domain structure in bulk antiferromagnets with a sufficiently strong magnetoelastic coupling by starting from ideas about the aforementioned microstresses and utilizing the formalism for description of the fields of elastic dipoles which is well known in the theory of elasticity.[14]

The structure of this paper is as follows. In Sec. 2 we analyze from the standpoint of the theory of continuous media the interaction of two regions lying far apart (in comparison with the size of the regions) in which antiferromagnetic order has spontaneously arisen and show that under certain conditions it is energetically favorable to have states with different (noncollinear) orientations of the antiferromagnetic vectors in each of the regions. In Sec. 3 we consider a microscopic mechanism based on the assumption that internal microstresses arise due to the magnetoelastic coupling, and we obtain a general expression describing the contribution of the long-range elastic fields to the free energy of the crystal—the so-called ''destressing'' energy. In Sec. 4 we consider examples of the calculation of the destressing energy for samples in the form of thin slabs with different crystallographic symmetry. In Sec. 5 the model developed is applied for analysis of the process of formation and rearrangement of the domain structure in antiferromagnetic crystals of different types. Finally, in the Conclusion we summarize the main results and conclusions of this study.

2. INTERNAL STRESSES AND THE INTERACTION OF TWO "MAGNETOELASTIC DIPOLES"

Let us consider a phase transition to an antiferromagnetic state with allowance for the magnetoelastic coupling in the crystal. We shall assume that in a uniform crystal found in the paramagnetic state at temperature $T \geqslant T_N$, antiferromagnetic order is established, owing to fluctuations, in a region of physically small volume ΔV centered at a point $\mathbf{r}_0$; this order is characterized by the so-called antiferromagnetic vector $\mathbf{L}(\mathbf{r}) = \mathbf{L}_0 \delta(\mathbf{r} - \mathbf{r}_0)$, where in the limit $\Delta V \to 0$ the form function $\delta(\mathbf{r} - \mathbf{r}_0)$ is the Dirac delta function.

It is known that the presence of magnetoelastic coupling leads to a change in the interatomic interaction potential in the region ΔV, which in turn gives rise to local internal stresses that can be described by a tensor $\hat{\sigma}^{\mathrm{mag}}(\mathbf{r})$ that depends on the coordinate $\mathbf{r}$ and is related to the magnetic order parameter by the relations

$$\hat{\sigma}^{\mathrm{mag}}(\mathbf{r}) = \hat{\Lambda}\mathbf{L}_0 \otimes \mathbf{L}_0 \delta(\mathbf{r} - \mathbf{r}_0) \to \sigma_{jk}^{\mathrm{mag}}(\mathbf{r}) = \Lambda_{jklm}\mathbf{L}_{0l}\mathbf{L}_{0m}\delta(\mathbf{r} - \mathbf{r}_0), \tag{1}$$

where the 4th-rank tensor $\hat{\Lambda}$ characterizes the magnetoelastic coupling and reflects the magnetocrystalline symmetry of the lattice. In Eq. (1) and below, as always, summation over repeated indices is assumed.

According to the theory of elasticity,[14,15] at distances substantially greater than the linear dimensions of the region ΔV the internal stresses (1) concentrated at the point $\mathbf{r}_0$ create a displacement field

$$u_j(\mathbf{r}) = \frac{\partial}{\partial \mathbf{r}_k} \int_{\Delta V} G_{jl}(\mathbf{r} - \mathbf{r}')\sigma_{kl}^{\mathrm{mag}}(\mathbf{r}')d\mathbf{r}' = \Lambda_{klmn}L_m L_n \frac{\partial}{\partial r_k} G_{jl}(\mathbf{r} - \mathbf{r}_0), \tag{2}$$

where the Green's function $G_{jk}(\mathbf{r})$ of an infinite elastic medium satisfies the equation

$$\frac{\partial}{\partial r_k} c_{jklm} \frac{\partial}{\partial r_l} G_{nm}(\mathbf{r}) + \delta_{jn}\delta(\mathbf{r}) = 0, \tag{3}$$

in which c_{jklm} is the tensor of elastic constants.

In complete analogy with ferromagnets one can say that the tensor $\hat{\sigma}^{\mathrm{mag}}(\mathbf{r})$ characterizes a ''dipole'' moment of the medium, while the displacement vector $\mathbf{u}(\mathbf{r})$ characterizes the potential of the elastic field created by those dipoles at sufficiently large distances.

We now assume that antiferromagnetic order has arisen in two regions ΔV_1 and ΔV_2 which are the neighborhoods of points $\mathbf{r}_1$ and $\mathbf{r}_2$, respectively, the distance between which is also much greater than the size of these regions of spontaneous ordering. The elastic stress fields (1) and the displacement fields (2) induced in the strained regions by the magnetoelastic transition interact with each other. The corresponding contribution Φ_{dd} to the Gibbs thermodynamic potential can be calculated as the energy of interaction of two elastic dipoles:[14,15]

$$\Phi_{dd} = \frac{1}{2} \frac{\partial^2}{\partial r_{1j}\partial r_{1k}} G_{ml}(\mathbf{r}_1 - \mathbf{r}_2)\sigma_{jl}^{\mathrm{mag}}(\mathbf{r}_1)\sigma_{km}^{\mathrm{mag}}(\mathbf{r}_2). \tag{4}$$

We note that independently of the directions of the antiferromagnetic vectors at the points $\mathbf{r}_1$ and $\mathbf{r}_2$ the traces of the two tensors $\hat{\sigma}^{\text{mag}}(\mathbf{r}_1)$ and $\hat{\sigma}^{\text{mag}}(\mathbf{r}_2)$, which determine the spontaneous dilatation (volume expansion), are equal:

$$\text{Tr}\,\hat{\sigma}^{\text{mag}}(\mathbf{r}_1)=\text{Tr}\,\hat{\sigma}^{\text{mag}}(\mathbf{r}_2)=\text{Tr}\,\hat{\sigma}^{\text{mag}}.$$

The interaction energy acquires a nontrivial contribution, which depends on the mutual orientation of the elastic dipoles and, hence, the local directions of the antiferromagnetic vectors, from the shear (deviator) part of the stress tensor, which we denote as

$$\hat{\sigma}^{(\alpha)}\equiv\hat{\sigma}^{\text{mag}}(\mathbf{r}_\alpha)-\frac{\hat{\mathbf{1}}}{3}\text{Tr}\,\hat{\sigma}^{\text{mag}},\quad \alpha=1,2,$$

where $\hat{\mathbf{1}}$ the unit matrix. Substituting into expression (4) the Green's function for an isotropic medium[14]

$$G_{jk}(\mathbf{r})=\frac{1}{16\pi\mu(1-\nu)r}\left[(3-4\nu)\delta_{jk}+\frac{r_j r_k}{r^2}\right] \tag{5}$$

(where $\mu\equiv c_{44}$ and ν are the shear modulus and Poisson's ratio, respectively) and assuming without loss of generality that $\mathbf{r}_1=\mathbf{r}$, $\mathbf{r}_2=0$, and $\mathbf{e}=\mathbf{r}/r$, we find that

$$\Phi_{dd}=-\frac{1}{16\pi\mu(1-\nu)r^3}\left[(1-2\nu)\text{Tr}(\hat{\sigma}^{(1)}\hat{\sigma}^{(2)})+6\nu(\mathbf{e}\hat{\sigma}^{(1)},\hat{\sigma}^{(2)}\mathbf{e})-\frac{15}{2}(\mathbf{e}\hat{\sigma}^{(1)}\mathbf{e})(\mathbf{e}\hat{\sigma}^{(2)}\mathbf{e})+\text{Tr}\,\hat{\sigma}^{\text{mag}}(\mathbf{e}(\hat{\sigma}^{(1)}+\hat{\sigma}^{(2)})\mathbf{e})\right]. \tag{6}$$

In the case of a medium that is isotropic in both the elastic and magnetoelastic respects (here and below for symmetric 4th-rank tensors we adopt the Voight notation) ($\Lambda_{11}-\Lambda_{12}=2\Lambda_{44}$)

$$\text{Tr}\,\hat{\sigma}^{\text{mag}}=(\Lambda_{11}+2\Lambda_{12})\mathbf{L}^2$$

and the shear part of the stress tensor is expressed extremely simply in terms of the components of the antiferromagnetic vector:

$$\hat{\sigma}^{(\alpha)}=2\Lambda_{44}\left[\mathbf{L}^{(\alpha)}\otimes\mathbf{L}^{(\alpha)}-\frac{\hat{\mathbf{1}}}{3}\mathbf{L}^2\right]\to\sigma_{jk}^{(\alpha)}=2\Lambda_{44}\left[L_j^{(\alpha)}L_k^{(\alpha)}-\frac{\delta_{jk}}{3}\mathbf{L}^2\right]. \tag{7}$$

Substituting (7) into (6), we find that the interaction energy of two antiferromagnetically ordered regions (''antiferromagnetic dipoles'') consists of three contributions:

$$\Phi_{dd}=\Phi_{\text{is}}+\Phi_{\text{an}}+\Phi_{\text{afm}}. \tag{8}$$

The first term in (8) describes an energy that does not depend on the orientation of the magnetic moments and therefore does not play any role in the establishment of the equilibrium direction of the antiferromagnetic vectors:

$$\Phi_{\text{is}}=\frac{\Lambda_{44}\mathbf{L}^4}{12\pi\mu(1-\nu)r^3}[\Lambda_{44}(1-4\nu)+\Lambda_{11}+2\Lambda_{12}]. \tag{9}$$

The second term in (8) is determined by the orientation of each of the vectors $\mathbf{L}^{(\alpha)}$ with respect to the vector $\mathbf{e}$:

$$\Phi_{\text{an}}=\frac{\Lambda_{44}^2}{8\pi\mu(1-\nu)r^3}\left\{15(\mathbf{L}^{(1)},\mathbf{e})^2,(\mathbf{L}^{(2)},\mathbf{e})^2-\mathbf{L}^2\left[5-4\nu+\frac{\Lambda_{11}+2\Lambda_{12}}{\Lambda_{44}}\right][(\mathbf{L}^{(1)},\mathbf{e})^2+(\mathbf{L}^{(2)},\mathbf{e})^2]\right\}. \tag{10}$$

This contribution can be regarded as the anisotropy energy, which influences the equilibrium direction of the antiferromagnetic vectors.

Finally, the last term contains the scalar products of the antiferromagnetic vectors on different sites and thus determines their mutual orientation, which is brought about by an indirect interaction via the elastic subsystem:

$$\Phi_{\text{afm}}=-\frac{\Lambda_{44}^2}{4\pi\mu(1-\nu)r^3}[(1-2\nu)(\mathbf{L}^{(1)},\mathbf{L}^{(2)})^2+6\nu(\mathbf{L}^{(1)},\mathbf{L}^{(2)})(\mathbf{L}^{(1)},\mathbf{e})(\mathbf{L}^{(2)},\mathbf{e})]. \tag{11}$$

It is seen from expressions (9)–(11) that the ''dipole–dipole'' energy (8) remains unchanged, as it should, when the sign of any of the vectors is changed, $\mathbf{L}^{(\alpha)}\to-\mathbf{L}^{(\alpha)}$, and, hence, unlike ferromagnets, is indifferent to antiphase domains.[2)] At the same time, at phase transitions accompanied by a lowering of the spatial symmetry, the vector $\mathbf{L}$ and, accordingly, the tensor $\hat{\sigma}^{\text{mag}}$ can have several equilibrium orientations differing by a rotation of 60°, 90°, or 120°.

Suppose, for example, that the equilibrium orientations $\mathbf{L}^{(1)}$ and $\mathbf{L}^{(2)}$ can differ by 90° (as, for example, in the case of the antiferromagnetic insulators $KNiF_3$, $KCoF_3$, K_2NiF_4 and in the underdoped high-T_c superconductors Y–Ba–Cu–O and La–Sr–Cu–O). Analysis of the terms of expression (8) shows that for certain orientations of the vector $\mathbf{e}$ the configuration with a parallel direction of the vectors $\mathbf{L}^{(1)}\|\mathbf{L}^{(2)}$ will have a lower interaction energy, while for others the configuration with mutually perpendicular ordering, $\mathbf{L}^{(1)}\perp\mathbf{L}^{(2)}$, will have.

Indeed, if the vector $\mathbf{e}$ is parallel to one of the ''easy'' directions for the vector $\mathbf{L}$, i.e., $\mathbf{e}\|\mathbf{L}^{(1)}$, then the difference of the energies of the parallel ($\|$) and perpendicular ($\perp$) orderings

$$\Phi_{dd}^{\|}-\Phi_{dd}^{\perp}=\frac{\Lambda_{44}^2\mathbf{L}^4(2-\nu)}{2\pi\mu(1-\nu)\mathbf{r}^3}>0, \tag{12}$$

and, as a result, the mutually perpendicular orientation of the magnetoelastic dipoles will be more favorable. This corresponds to Le Chatelier's principle: if the appearance of antiferromagnetic order in the region ΔV_1 leads to elongation of the lattice along $\mathbf{L}^{(1)}$, then the stresses created in the remote region ΔV_2 will also be tensile in the same direction and can be diminished by compressive stresses in the case when the vector $\mathbf{L}^{(2)}$ ''turns sideways.'' In the other limiting case the vector $\mathbf{e}$ is directed at the same angle to both antiferromagnetic vectors $(\mathbf{e},\mathbf{L}^{(1)})=(\mathbf{e},\mathbf{L}^{(2)})$, which corresponds to the ''hard'' direction of $\mathbf{L}$. Then

$$\Phi_{dd}^{\|}-\Phi_{dd}^{\perp}=-\frac{\Lambda_{44}^2\mathbf{L}^4(1+\nu)}{4\pi\mu(1-\nu)r^3}<0, \tag{13}$$

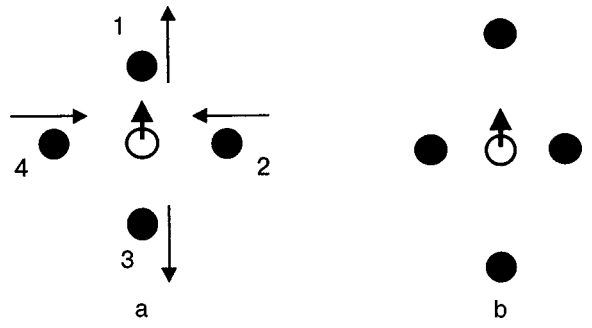

FIG. 1. Displacements of the atoms of a square lattice under the influence of local stresses due to the appearance of spin at the atom of species A (unfilled circle): the undeformed (a) and the deformed (b) states. The arrows indicate the direction of displacements of the atoms of species B (filled circles) from the initial state to the deformed state.

i.e., the parallel orientation of these vectors at different points of the crystal will have the lower energy (generally speaking, this does not rule out the formation of antiphase domains).

Thus, as in the case of ferromagnetic dipoles, in magnetoelastic crystals with antiferromagnetic ordering there exist certain directions in which it is energetically favorable for dipoles of different types to appear, corresponding to equivalent but noncollinear orientations of the spontaneously strained regions. An important difference from the case of ferromagnetic dipoles lies in the choice of this orientation. For dipoles of a vector nature (magnetic, electric) the greatest differences arise in the directions parallel to and perpendicular to the axis of the dipole, while for elastic and, accordingly, antiferromagnetic dipoles, which are characterized by a 2nd-rank tensor, they arise along the ''easy'' and ''hard'' axes of the antiferromagnetic vector, the angle between which can, in particular, be 45°.

3. DESTRESSING ENERGY IN AN ANTIFERROMAGNET

In the previous Section the interaction of two magnetoelastic dipoles was actually reduced (in the continuous medium approximation) to the interaction of two spatially separated inclusions of a strained antiferromagnetic phase in a paramagnetic matrix. That approach is applicable if the temperature of the paramagnetic state is only slightly above the critical temperature. In this Section we explore the question of how the formalism used can be generalized to the case when the antiferromagnetic vector and the directions corresponding to it arise in every unit cell of the crystal.

Let us begin with the simplest example of a two-dimensional square lattice in which magnetic ions of species A ($\mathbf{r}_0$) are surrounded by nonmagnetic nearest neighbors of species B ($\mathbf{r}_n=\mathbf{r}_0+\boldsymbol{\rho}_n$, $n=1,2,3,4$; see Fig. 1). Such a structure exists in the cuprate layers of high-T_c superconductors, for example, where the paramagnetic copper ions Cu^{2+} ($S=1/2$) are surrounded by the nonmagnetic ligands O^{2-}. The appearance of a spontaneous moment directed along the Ox axis at site A leads to the displacement of atoms 1 and 3 along the same axis ($u_x(\mathbf{r}_1)=-u_x(\mathbf{r}_3)=u_0$) and of atoms 2 and 4 along the perpendicular direction ($u_y(\mathbf{r}_2)=-u_y(\mathbf{r}_4)=u_0$). The total change of the configuration of the B atoms, leading to a shear strain, can be characterized by the quantity

$$\varepsilon(\mathbf{r}_0)=\frac{1}{4}[u_x(\mathbf{r}_1)-u_y(\mathbf{r}_2)-u_x(\mathbf{r}_3)+u_y(\mathbf{r}_4)], \tag{14}$$

which transforms according to the same irreducible representation of the local symmetry group[3)] as does a linear combination of components of the 2nd-rank tensor $\varepsilon_{xx}-\varepsilon_{yy}$. In the general case this quantity can be written as

$$\hat{\varepsilon}(\mathbf{r}_0)=\frac{1}{z}\sum_{n=1}^{z}\mathbf{u}(\mathbf{r}_0+\rho_n)\otimes\boldsymbol{\rho}_n, \tag{15}$$

where the vectors $\boldsymbol{\rho}_n$ characterize the position of the z ($=4$) nearest neighbors. The tensor conjugate to this quantity determines the change of V^{mag}, the interatomic interaction potential caused by the magnetic ordering, and can be regarded as the microstress tensor in the neighborhood of a specified site:

$$\sigma_{jk}^{\mathrm{micro}}(\mathbf{r}_0)=\frac{\partial V^{\mathrm{mag}}(\mathbf{r}_0)}{\partial\varepsilon_{jk}}. \tag{16}$$

For an antiferromagnet the nontrivial components of the tensor $\hat{\sigma}^{\mathrm{micro}}$ are related to the orientation of the spin moments by a relation of the type (1), where the components of the 4th-rank tensor Λ_{jk} are invariant with respect to transformations of the local symmetry group. In the general case the change of the local environment of the magnetic atom can be determined by tensors of higher ranks (when next-nearest neighbors are taken into account).

We recall that the local stress and strain tensors introduced above are essentially different from the corresponding macroscopic quantities that are used for describing the state of the crystal in the theory of elasticity. For example, the quantities specified by expression (15) depend on the correlation functions of the distribution at the neighboring sites and actually assign a tensor characteristic to every point of the medium. At the same time, the strains in the standard theory of elasticity are determined as gradients of the mean displacement vectors, i.e., they depend on the first and not the second moments of the distribution functions. Furthermore, the strains corresponding to the local stresses $\hat{\sigma}^{\mathrm{micro}}$ can in some sense be considered quasi-plastic (in the terminology of Ref. 13), since they arise in the absence of external loads and can be removed only through a change of the whole thermodynamic state of the sample (for example, by raising the temperature of the crystal). In other words, for the microstress tensor one can adopt the same assumptions as for the magnetic moments (Ampère ''microcurrents'') in magnetic media—once formed at the point of the phase transition, both the magnetic moment and the microstress tensor retain their value; the action of external forces can lead only to their reorientation with respect to the axes of the crystal. And just as the existence of a magnetic moment does not lead to the onset of macroscopic conduction currents, the existence of the microstress tensor does not lead to plastic flows of the sample as a whole.

For a phenomenological description of the elastic state that arises at the phase transition, we turn from the microscopic stresses (16) to the stresses averaged over macroscopic but physically small volumes of the crystal. Then for the case of a magnetic transition [cf. Eq. (1)]

$$\sum_{\mathbf{r}_l} \hat{\sigma}^{\text{micro}}(\mathbf{r}_l)\,\delta(\mathbf{r}-\mathbf{r}_l) \to \hat{\sigma}^{\text{mag}}(\mathbf{r}) = \frac{1}{v_0}\langle \hat{\sigma}^{\text{micro}} \rangle, \qquad (17)$$

where v_0 is the unit cell volume and the angle brackets denote averaging.

Expression (17) together with (1) actually *postulates* the existence at magnetoelastic phase transitions of two primary[4] order parameters of microscopic origin: a magnetic one, which in the present case is the antiferromagnetic vector **L**, and a (magneto)elastic order parameter, characterized by the tensor $\hat{\sigma}^{\text{mag}}(\mathbf{r})$. In contrast to this, in the conventional description of transitions of this type only the magnetic vectors are considered to be primary order parameters, while the spontaneous strains and the stresses that have caused them are considered secondary, macroscopic quantities.

The contribution to the free energy of the crystal which depends on the stresses (17) contains terms of different natures. The most important for the formation of the ordered state are the local interactions, which in the vicinity of the phase transition are well approximated by a bilinear form, in terms of the components of the tensor $\hat{\sigma}^{\text{mag}}(\mathbf{r})$, which is invariant with respect to the symmetry point group of the crystal:

$$\Phi_{\text{afm}} = \int dV \left[\frac{1}{2}\sigma_{jk}^{\text{mag}} s_{jklm} \sigma_{lm}^{\text{mag}} - \lambda_{jklm}\sigma_{jk}^{\text{mag}} L_l L_m \right]. \qquad (18)$$

The first term in (18) models the energy of formation of an elastic dipole (with a strength coefficient $\hat{s}$) while the second models the magnetoelastic coupling, which is what gives rise to $\hat{\sigma}^{\text{mag}}(\mathbf{r})$ on magnetic ordering [see expression (1), where $\hat{\Lambda} = \hat{s}^{-1}\hat{\lambda}$]. Coupling of the type (18) together with the exchange interaction of a purely magnetic nature leads to ''parallel'' (uniform) ordering of the elastic dipoles and can therefore, by analogy with magnetism, be treated as ''exchange.''

A weaker, but nevertheless important, contribution is that due to the coupling of elastic dipoles, which is described on the microscopic level by expression (4). Upon integration over the whole crystal we note that at small (of the order of interatomic) distances the interactions between elastic dipoles are of a substantially nonlinear character and a detailed description of them requires taking into account the interatomic potentials, electronic structure of the crystal, etc. However, it is clear from physical considerations that in the presence of long-range magnetic order these interactions are responsible for orientation of the elastic dipoles with respect to the axes of the crystal and the magnetic moments at a given point, i.e., in essence they determine the elastic anisotropy. Phenomenologically the local orientation of the elastic dipoles is described by expression (18) under the condition that the coefficients λ_{jklm} depend not only on the mutual orientation of the antiferromagnetic vectors **L** but also on their orientation with respect to the crystallographic directions, or the magnetic anisotropy.

In view of what we have said, the macroscopic energy of the elastic dipole coupling can be written in the form of an integral,

$$\Phi_{dd} = \frac{1}{2}\int_{|\mathbf{r}-\mathbf{r}'|>\rho} d\mathbf{r} \int d\mathbf{r}'\, \sigma_{jk}^{\text{mag}}(\mathbf{r})\sigma_{lm}^{\text{mag}}(\mathbf{r}') \times \frac{\partial^2}{\partial r_j \partial r_l} G_{km}(\mathbf{r}-\mathbf{r}'), \qquad (19)$$

where the Green's function is defined by Eq. (3) and the physically small macroscopic length ρ is much greater than the interatomic distances a (at which the contribution (18) is dominant) but much less than the linear dimension d_D of the elastic (and magnetic)[5] domains: $a \ll \rho \ll d_D$.

Expression (19) has an important feature that permits reducing the problem of domain formation at a thermoelastic phase transition to the analogous problem of the formation of domains with the opposite direction of the magnetization vector in ferromagnetic crystals.[19] For example, it is known that the Green's function appearing in expression (19) decays asymptotically as $G_{km}(\mathbf{r}) \approx 1/r$ independently of the symmetry of the crystal, thus ensuring the long-range character of the dipole forces.[6] This leads to two important consequences: first, in a system of elastic dipoles the interactions have a nonlocal character and, hence, it is possible for inhomogeneous (domain) structures to arise; second, as will be seen below [see formula (22)], the quantity Φ_{dd} is proportional to the volume of the crystal and, consequently, its contribution to the free energy of the crystal is comparable to the change of its chemical potential due to a phase transformation.

We now use expression (19) to describe the elastic state arising in a crystal at a thermoelastic phase transition and show that (by analogy with ferromagnetism) that taking the dipole interactions into account does in fact allow one to explain the breaking up of an antiferromagnetic crystal of finite size into magnetoelastic domains with different orientations of the elastic dipoles.

We start by introducing the quantity that determines the macroscopic strain created by concentrated ''forces'' $\hat{\sigma}^{\text{mag}}$:

$$u_{jk}(\mathbf{r}) = -\frac{1}{2}\int_V \left[\frac{\partial}{\partial r_k} G_{jl}(\mathbf{r}-\mathbf{r}') + \frac{\partial}{\partial r_j} \times G_{kl}(\mathbf{r}-\mathbf{r}') \right] \frac{\partial \sigma_{ml}^{\text{mag}}(\mathbf{r}')}{\partial r_m'} d\mathbf{r}', \qquad (20)$$

where the integration is over the entire crystal volume V. It is easy to see that if the Green's function $G(\mathbf{r})$ is given by expression (3), then the tensor $u_{jk}(\mathbf{r})$ (20) satisfies the equation

$$\frac{\partial}{\partial r_k} c_{jklm} u_{lm}(\mathbf{r}) = \frac{\partial}{\partial r_k}\sigma_{jk}^{\text{mag}}(\mathbf{r}). \qquad (21)$$

Thus the tensor $\hat{\sigma}^{\text{mag}}$ has the meaning of the macroscopic stresses, while the symmetric tensor $\hat{u}$ introduced in Eq. (20) has the meaning of the corresponding spontaneous strains arising at the phase transition. We emphasize that in contrast to the standard theory of elasticity, $\hat{\sigma}^{\text{mag}}$ is the result of exclusively internal changes in the crystal and not of an external load applied to it. In some sense the expressions obtained resemble the expressions for the stress and strain fields created by point defects, but, unlike the latter, the internal stresses $\hat{\sigma}^{\text{mag}}$ considered here arise spontaneously and

exist at all points of the medium and not at isolated individual points in it that form a set of measure zero.

In the case when the tensor $\hat{\sigma}^{\mathrm{mag}}$ is independent of $\mathbf{r}$, in a sample of infinite size the spontaneous strain $\hat{u}$ is also uniform and is given by the formula

$$\hat{u}=\hat{c}^{-1}\hat{\sigma}^{\mathrm{mag}}.$$

For a sample of finite size the integrals in (19) and (20) depend on its shape. Then the distribution of the internal stresses that brings about the minimum free energy must be determined from the solution of a self-consistent problem taking into account the ''exchange'' and anisotropic couplings (18), the dipole interactions (19), and the contribution of the spin subsystem. In the simplest case, that of a sample in the form a thin slab, the internal stress field is uniform on scales exceeding the size of the individual domains but less than the thickness of the slab, $d \gg d_D$. In this case the global strain of the sample

$$u_{jk}^{\mathrm{macro}}=\aleph_{jklm}\langle\sigma_{lm}^{\mathrm{mag}}\rangle \tag{22}$$

is determined by the averaged tensor over the different types of domains

$$\langle\hat{\sigma}^{\mathrm{mag}}\rangle\equiv\frac{1}{V}\int_V\hat{\sigma}^{\mathrm{mag}}(\mathbf{r})d\mathbf{r}$$

and the coordinate-independent 4th-rank tensor

$$\aleph_{jklm}\equiv\frac{\partial^2}{\partial r_k\partial r_m}\int_V G_{jl}(\mathbf{r}-\mathbf{r}')d\mathbf{r}', \tag{23}$$

which by analogy with magnetism can be called the tensor of ''destressing'' coefficients.[7)]

In this case the energy of the dipole interaction takes the rather simple form

$$\Phi_{dd}=\frac{V}{2}\langle\sigma_{jk}^{\mathrm{mag}}\rangle\aleph_{jklm}\langle\sigma_{lm}^{\mathrm{mag}}\rangle. \tag{24}$$

The averaged internal stress tensor $\langle\hat{\sigma}^{\mathrm{mag}}\rangle$ describes a certain effective (''molecular'' or self-consistent) field that is created by the phase transition and leads to spontaneous strains (22). It is extraordinarily important that, both in the particular case under discussion and in the general case, the dipole interaction energy (24) is proportional to the volume of the sample, which is what leads to the possibility of lowering the free energy of the crystal through the formation of an inhomogeneous structure, i.e., magnetoelastic domains, despite a certain increase in energy owing to the unavoidable formation of domain walls.

In the foregoing analysis of the elastic state arising in a crystal at a phase transition with spontaneous strains, it was implicitly assumed that no external stresses were present in the sample (the boundary conditions correspond to a free surface of the crystal). However, the result obtained is easily generalized to the case when the crystal is subjected to external loads (e.g., mechanical stress or magnetic field) or to displacements somehow externally fixed on the surface of the sample (the crystal is glued, has a coherent interphase/intergrain boundary, the surface has enhanced stiffness, etc.), i.e., the boundary conditions have a more general character. For example, in the presence of external stresses $\hat{\sigma}^{\mathrm{ext}}$ the effective field inside the crystal will contain a contribution both from the destressing fields $\langle\hat{\sigma}^{\mathrm{mag}}\rangle$ and from the external fields:

$$\hat{\sigma}^{\mathrm{eff}}=\langle\hat{\sigma}^{\mathrm{mag}}\rangle+\hat{\sigma}^{\mathrm{ext}}.$$

Fixed displacements at the boundary of the sample can be taken into account by the introduction of additional strains $\hat{u}^{\mathrm{add}}$ ensuring satisfaction of the boundary conditions and the compatibility conditions. In this case the total strain of the sample is given by

$$u_{jk}^{\mathrm{tot}}(\mathbf{r})=u_{jk}(\mathbf{r})+u_{jk}^{\mathrm{add}}(\mathbf{r}), \tag{25}$$

where the first term is given by formula (20) and the second is an additional strain which satisfies the standard equations of the theory of elasticity, including the compatibility conditions. The requirement of compatibility of the total strains at the boundary of a sample of arbitrary shape leads to the equation

$$\mathrm{curl}(\mathrm{curl}\,\hat{u}^{\mathrm{add}}(\mathbf{r}))^T=\hat{e}_{\mathrm{el}}(\mathbf{r}), \tag{26}$$

$$\hat{e}_{\mathrm{el}}(\mathbf{r})=-\mathbf{n}\times\hat{u}(\mathbf{r}_S)\times\mathbf{n}\delta'[\mathbf{n}(\mathbf{r}-\mathbf{r}_S)], \tag{27}$$

where δ' is the derivative of the Dirac delta function with respect to the argument, $\mathbf{n}(\mathbf{r}_S)$ is the normal to the surface of the sample at the point $\mathbf{r}_S$, and the tensor $\hat{e}_{\mathrm{el}}$ plays the role of the ''incompatibility charges'' arising as a result of the incompatibility of the elastic strains in the bulk and on the surface of the sample. The particular solution of Eq. (26) has the form

$$\hat{u}^{\mathrm{add}}(\mathbf{r})=\frac{1}{4\pi}\int_V d\mathbf{r}_1\frac{\hat{e}_{\mathrm{el}}(\mathbf{r}_1)-\hat{\mathbf{1}}\mathrm{Tr}\,\hat{e}_{\mathrm{el}}(\mathbf{r}_1)}{|\mathbf{r}-\mathbf{r}_1|}. \tag{28}$$

Substitution of (28) into (24) allows one to express the dipole energy in terms of the spontaneous strains (rather than stresses). In the particular case discussed above, that of a thin slab, this leads to an expression that was obtained previously by the authors in the model of a sample with a rigid surface[9,10] [cf. Eq. (24)]

$$\Phi_{dd}=\frac{V}{2}\langle\hat{u}\rangle\aleph^{-1}\langle\hat{u}\rangle, \tag{29}$$

where the ''destressing'' tensor is given by the expression

$$\hat{\aleph}^{-1}=\hat{c}+\mathbf{n}\otimes\mathbf{n}\mathrm{Tr}\,c-\mathbf{n}\otimes(\hat{c}\mathbf{n})-(\hat{c}\mathbf{n})\otimes\mathbf{n}, \tag{30}$$

or

$$\aleph_{jklm}^{-1}=c_{jklm}+n_jn_kc_{lmpp}-n_jc_{klmp}n_p-n_pc_{jpkl}n_m,$$

and the domain structure is determined by the average value of the strain tensor over the sample, $\langle\hat{u}\rangle$.

4. TENSOR OF "DESTRESSING" COEFFICIENTS AND THE "DESTRESSING" ENERGY IN THE CASE OF A THIN SLAB WITH A FREE SURFACE

Calculation of the dipole–dipole interaction energy (19) in a sample of arbitrary shape relies on knowledge of the Green's function, the calculation of which is not a simple problem in itself. An exception once again is the case of a thin slab, for which the tensor of destressing coefficients, $\aleph$, introduced by expression (23) can be calculated in explicit form.

We suppose that the normal to the plane of the slab is specified by the vector **n**, the coordinates of which are determined with respect to the crystallographic axes. Then the destressing tensor is expressed in terms of the components of the so-called dynamical matrix $D_{jk}^{-1}\equiv c_{ijkl}n_in_l$ (see, e.g., Refs. 14 and 20) as

$$\aleph_{jklm}=D_{jl}n_kn_m. \tag{31}$$

The destressing energy, accordingly, takes the form

$$\Phi_{dd}=\frac{V}{2}\langle \mathbf{n}\hat{\sigma}^{\mathrm{mag}}\rangle\hat{D}\langle\hat{\sigma}^{\mathrm{mag}}\mathbf{n}\rangle. \tag{32}$$

Importantly, the contribution to the free energy of the crystal due to the dipole–dipole interaction (32) is always a positive-definite quadratic form with respect to the components of the vector $\langle\hat{\sigma}^{\mathrm{mag}}\mathbf{n}\rangle$. This follows from the positive definiteness of the dynamical matrix D_{jk}^{-1}, which determines the spectrum of the long-wavelength acoustic modes. Furthermore, this contribution is proportional to the volume of the crystal and therefore, as we have said, can compete with the contribution due to the phase transition itself for any size of the sample.

As an example let us consider an elastically isotropic medium. It follows from symmetry considerations that in this case the matrix D_{jk} (the explicit form of which can be found in Ref. 20) has one eigenvector in the direction of the normal **n** to the surface of the slab, which corresponds to an eigenvalue $1/c_{11}$, and two mutually perpendicular vectors ($\mathbf{e}_1$ and $\mathbf{e}_2$) lying in the plane of the slab and corresponding to an eigenvalue $1/c_{44}$. Taking into account the aforementioned relation between the matrix D_{jk} and the dynamical matrix, we can say that the eigenvectors of this matrix determine the polarization of three acoustic modes—one longitudinal and two transverse, propagating in the direction of the normal. In view of what we have said, the expression for the dipole energy (32) becomes

$$\Phi_{dd}=\frac{V}{2}\left[\frac{1}{c_{11}}\langle\mathbf{n}\hat{\sigma}^{\mathrm{mag}}\mathbf{n}\rangle^2+\frac{1}{c_{44}}(\langle\mathbf{e}_1\hat{\sigma}^{\mathrm{mag}}\mathbf{n}\rangle^2+\langle\mathbf{e}_2\hat{\sigma}^{\mathrm{mag}}\mathbf{n}\rangle^2)\right]. \tag{33}$$

This contribution to the energy is clearly non-negative and, consequently, as in the case of a ferromagnet, in the absence of external fields it can be decreased only when the corresponding averaged components of the tensor $\hat{\sigma}^{\mathrm{mag}}$ vanish. We emphasize that, in contrast to the case of a ferromagnet, the destressing tensor depends not only on the shape of the sample (in the present case, on the orientation of the vector **n**) but also on the value of the elastic constants. Consequently, the directions of **n** for which the shape effect will be most strongly manifested depend not only on the geometry of the sample but also on its material constants.

In the general case expression (32) can be written in a form analogous to (33) provided that the normal to the plane of the slab is directed in one of the so-called ''pure'' directions of the crystal, i.e., if **n** is an eigenvector of the matrix $\hat{D}$. Expressing the eigenvalues of the matrix $\hat{D}$ in terms of the effective elastic constants corresponding to the longitudinal c_l and two transverse $c_{t1,2}$ polarizations, we find that

$$\Phi_{dd}=\frac{V}{2}\left[\frac{1}{c_l}\langle\mathbf{n}\hat{\sigma}^{\mathrm{mag}}\mathbf{n}\rangle^2+\frac{1}{c_{t1}}\langle\mathbf{e}_1\hat{\sigma}^{\mathrm{mag}}\mathbf{e}_1\rangle^2+\frac{1}{c_{t2}}\langle\mathbf{e}_2\hat{\sigma}^{\mathrm{mag}}\mathbf{e}_2\rangle^2\right]. \tag{34}$$

Expressions (33) and (34) allow one to draw some rather general conclusions about the relative scale of the dipole–dipole energy as it depends on the sample shape. Since in many crystals the elastic constants corresponding to transverse modes are considerably smaller than in the case of longitudinal modes, $c_t<c_l$, the last two terms in (33) and (34) can be much greater than the first. Thus in order to achieve the maximum destressing effect the sample should be cut so that the condition $\hat{\sigma}^{\mathrm{mag}}\mathbf{n}=0$ is satisfied in all of the domains. Otherwise, when $\hat{\sigma}^{\mathrm{mag}}\mathbf{e}_{1,2}=0$ the destressing energy is small, and, as will be shown in the next Section, the sample can easily be brought to a single-domain state (''monodomainized'') by external influences.

5. DOMAIN STRUCTURE OF ANTIFERROMAGNETS

Let us now apply the expressions (32)–(34) obtained in the last Section to elucidate the conditions of formation and reversible rearrangement of the equilibrium domain structure at thermoelastic phase transitions.

As the first example we consider an antiferromagnetic crystal whose symmetry group belongs to the tetragonal class (e.g., underdoped Y–Ba–Cu–O or La–Sr–Cu–O compounds). For simplicity we shall assume that the crystal is isotropic in the plane of symmetry ($c_{11}-c_{12}=2c_{66}$). In the case of an infinite crystal there are two equivalent equilibrium directions of the vector **L**, lying in the symmetry (basal) plane of the crystal: $\mathbf{L}\|Ox$ (X domain) and $\mathbf{L}\|Oy$ (Y domain). These directions are determined from the conditions that the part of the free energy that is of purely magnetic origin be minimum, and in our treatment they are assumed to be specified. The equivalence of the domains in the absence of external fields means that in the region of uniform ordering, the specific thermodynamic (chemical) potentials of the two domains are identical: $\mu_X=\mu_Y$. In the presence of a magnetic field **H** lying in the symmetry plane the domains become inequivalent, and their chemical potentials differ by an amount determined by the Zeeman energy:

$$\mu_X-\mu_Y=\frac{1}{2}\chi(H_x^2-H_y^2), \tag{35}$$

where χ is the magnetic susceptibility of the antiferromagnetic phase in the direction perpendicular to the easy axis of the crystal.

In an infinite sample containing domains of both types with volume fractions ξ and $(1-\xi)$ the thermodynamic potential is a linear function of ξ:

$$\Phi_\infty=V[\xi\mu_X+(1-\xi)\mu_Y]=\Phi_0+\frac{V}{2}\left(\xi-\frac{1}{2}\right)\chi(H_y^2-H_x^2), \tag{36}$$

where Φ_0 is a constant that is unimportant for the given problem.

Clearly in the absence of external field ($\mathbf{H}=0$) the energy of the crystal does not depend on the ratio of the fractions of domains of each type and the formation of a domain structure is thermodynamically unfavorable, since it involves energy costs for the formation of the domain walls. The imposition of a field leads to stabilization of the more favorable of the two single-domain states, i.e., the one for which the potential (36) will be minimal [domain X ($\xi=1$) if $\mathbf{H}\|Oy$ and domain Y ($\xi=0$) if $\mathbf{H}\|Ox$].

In a sample of finite size the thermodynamic potential should include the dipole–dipole energy (32) in addition to the term (36). For calculating that energy we determine the internal stress tensor averaged over the volume:

$$\langle \sigma_{xx}^{\mathrm{mag}}\rangle = \mathbf{L}^2\left[\frac{\Lambda_{11}+\Lambda_{12}}{2}+\Lambda'(1-2\xi)\right],$$

$$\langle \sigma_{yy}^{\mathrm{mag}}\rangle = \mathbf{L}^2\left[\frac{\Lambda_{11}+\Lambda_{12}}{2}-\Lambda'(1-2\xi)\right],$$

$$\langle \sigma_{zz}^{\mathrm{mag}}\rangle = \Lambda_{13}\mathbf{L}^2, \quad 2\Lambda' \equiv \Lambda_{11}-\Lambda_{12}. \tag{37}$$

Clearly if the normal to the plane of the sample is directed along the Oz axis (the symmetry group of the sample coincides with the point group of the high-symmetry phase), then the quantity

$$\langle \hat{\sigma}^{\mathrm{mag}}\rangle \mathbf{n} = \Lambda_{13}\mathbf{L}^2\mathbf{n}$$

will be identical in all the domains. This means that the dipole–dipole interaction energy (32) in a sample free of external stresses will not depend on the domain fraction at all, i.e., it will not lead to destressing.[8)]

However, if the normal to the plane of the slab is perpendicular to the Oz axis (the symmetry group of the sample can be lower than the point group of the high-symmetry phase), then the main contribution to the dipole–dipole interaction energy depends quadratically on the relative fraction ξ of the domains:

$$\Phi_{dd} = \frac{1}{2}\Lambda'^2\mathbf{L}^4 V\left(\xi-\frac{1}{2}\right)^2\left[\frac{(n_x^2-n_y^2)^2}{4c_{11}}+\frac{n_x^2 n_y^2}{c_{66}}\right]. \tag{38}$$

As is seen from Eq. (38), the destressing energy depends substantially on the orientation of the slab with respect to the crystallographic axes. Since the shear modulus c_{66} here is usually smaller than c_{11} by a factor of 3–10 (see, e.g., Ref. 20), the value of the destressing energy will be maximum in the case when the plane of the slab coincides with a twinning plane (i.e., with the plane of a domain boundary, $\mathbf{n}\|[110]$). A substantially lower value of the energy Φ_{dd} is obtained when the slab is cut perpendicular to one of the easy axes for the antiferromagnetic vector ($\mathbf{n}\|Ox$ or Oy).

The equilibrium domain fraction ξ is determined from the condition that the total thermodynamic potential, $\Phi=\Phi_\infty+\Phi_{dd}$, be minimum, and it is equal to

$$\xi = \frac{1}{2}+\frac{\chi(H_x^2-H_y^2)}{\Lambda'^2\mathbf{L}^4}\left[\frac{(n_x^2-n_y^2)^2}{4c_{11}}+\frac{n_x^2 n_y^2}{c_{66}}\right]^{-1}. \tag{39}$$

It follows from (39) that for any orientation of $\mathbf{n}$ a change of the relative fraction of one domain or the other can lead to a lowering of the thermodynamic potential of the system, and so the multidomain state is thermodynamically favorable. From expression (39) we also arrive at the conclusion that a certain characteristic ''monodomainization'' field exists,

$$H_{MD} = \frac{\Lambda'}{\sqrt{\chi}}\mathbf{L}^2\sqrt{\frac{(n_x^2-n_y^2)^2}{4c_{11}}+\frac{n_x^2 n_y^2}{c_{66}}}, \tag{40}$$

at which the ''unfavorable'' domain disappears completely from the sample. Remarkably, the value of that field depends on how the sample is cut and can vary over wide limits, from zero to a value comparable to the magnetostriction field.

The relation between the shape of the sample and its domain structure was used on an empirical level in the experiments of Refs. 5–7. In particular, for studying the shape memory effect in the antiferromagnet La–Sr–Cu–O, which involves the displacement of the domain walls, a sample in the form of a thin slab was cut out in such a way that its face was perpendicular to the easy axes, i.e., $\mathbf{n}\|Ox$ or Oy. Then, after several on–off cycles of the field the sample became practically single-domain, when the domain structure was no longer restored. At the same time, for any other orientation of the slab, as was mentioned in Refs. 5 and 6, the memory effect was not observed (it must be assumed that the applied fields were insufficient for monodomainization of the sample). In experiments where it was required to maintain equal fractions of the domains even in the presence of a field, the slab was cut in such a way that its faces were parallel to the hard directions, i.e., $n_x=n_y$, and that, in the opinion of the authors of Ref. 7, prevented motion of the domain walls (but, as we see, this simply lowered the ''susceptibility'' of the magnetoelastic domain structure to an external magnetic field).

Expression (40) allows one to estimate an experimentally observable quantity: the monodomainization field. Let us consider, as an example, an underdoped high-T_c superconductor La–Sr–Cu–O in the antiferromagnetic state, the domains in which have a nonmagnetic nature but are rigidly coupled to the magnetic properties of the sample and can be rearranged under the influence of an external field. Substituting into (40) the value $\sigma_0 \equiv \Lambda'\mathbf{L}^2 \approx 30$ MPa (defined as the saturation stress, at which, according to Ref. 21, the sample becomes single-domain), the elastic constants $c_{11}=213$ GPa (Ref. 22) and $\chi=5\times10^{-7}$ c.g.s.m.s.u./cm^3 (Ref. 21), we obtain the value of the monodomainization field $H_{MD}=15$ T for a slab cut in the direction of the easy axis ($\mathbf{n}\|Ox$), which practically coincides with the experimentally observed[5,6] value of 14 T. Importantly, for the other orientation of the slab (at a 45° angle to the easy axis), the value of the monodomainization field calculated according to formula (40) with $c_{66}=54$ GPa increases to 60 T. In this case, up to external field values of 10–15 T, according to formula (39), the fraction of the favorable domain can change by not more than 10%, i.e., the domain structure is practically insensitive to the external field. The corresponding curves of the fraction of the domain versus the strength of the external field for the two $\mathbf{n}$ orientations mentioned are shown in Fig. 2. Figure 3 shows the angle diagram for the dependence of the of the monodomainization field on the direction of $\mathbf{n}$ in the basal plane of the crystal. We note that a relation between the value of the monodomainization field and the shape of the sample has also been observed in ferromagnets, but in anti-

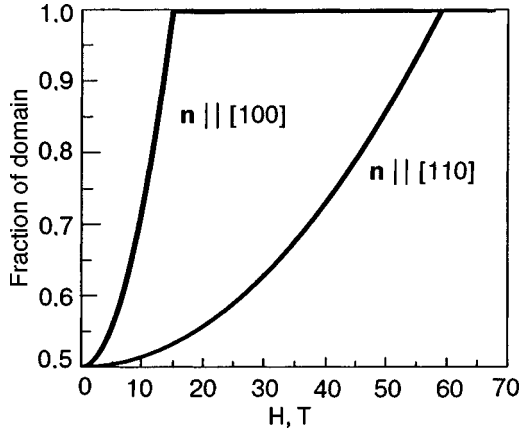

FIG. 2. Relative fraction of the "favorable" domain as a function of the external magnetic field; calculation according to formula (39) for the La–Sr–Cu–O crystal for different directions of the normal to the surface of the sample: $\mathbf{n} \parallel [100]$ (curve *1*) and $\mathbf{n} \parallel [110]$ (curve *2*).

ferromagnets the equivalent orientations of the sample will differ by 90° rather than 180°.

As a second example let us consider the formation of domains in a crystal in which the high-temperature (high-symmetry) phase has cubic symmetry while the low-temperature (ordered) phase has tetragonal symmetry. Such a situation arises, e.g., in antiferromagnetic ordering of the crystals $KNiF_3$ and $KCoF_3$ and also at thermoelastic transitions of the martensitic type. In the last case the cause of the internal stresses is ordering not of the spin but of the charge subsystem, although the behavior of the elastic subsystem is completely analogous.

The elastic characteristics of a crystal of cubic symmetry are isotropic and to a first approximation can be approximated by the expressions (5) and (23). The low-symmetry (antiferromagnetic or martensitic) phase can be realized in the form of three equivalent domains of tetragonal symmetry with principal axes along Ox, Oy, and Oz, respectively. Suppose that only two types of domains, X and Y, are present in the slab, with volume fractions ξ and $1-\xi$, respectively. The internal stress tensor in each of the domains has the form

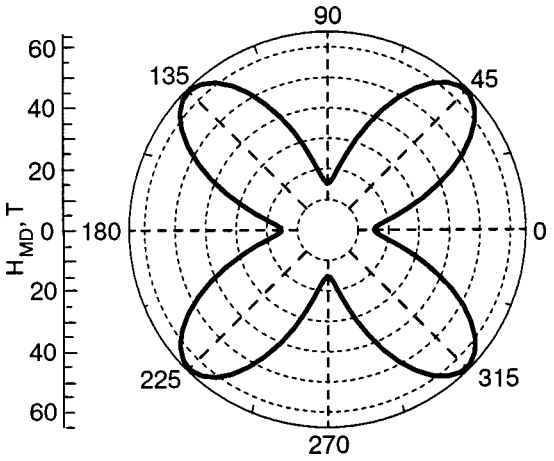

FIG. 3. Angle diagram of the dependence of the monodomainization field on the direction of **n** in the basal plane of the La–Sr–Cu–O crystal; calculation according to formula (40).

$$\hat{\sigma}_X = \begin{pmatrix} -2\sigma_0 & 0 & 0 \\ 0 & \sigma_0 & 0 \\ 0 & 0 & \sigma_0 \end{pmatrix}, \quad \hat{\sigma}_Y = \begin{pmatrix} \sigma_0 & 0 & 0 \\ 0 & -2\sigma_0 & 0 \\ 0 & 0 & \sigma_0 \end{pmatrix}. \tag{41}$$

Then with (41) taken into account, the destressing energy (33) takes the form[9)]

$$\Phi_{dd} - \frac{9}{2} V \sigma_0^2 \left\{ \frac{1}{c_{11}} \left[\xi(n_y^2 - n_x^2) + \frac{1}{3} - n_y^2 \right]^2 + \frac{1}{c_{44}} (2\xi - 1)^2 n_x^2 n_y^2 + \frac{1}{c_{44}} n_z^2 [\xi(n_x^2 - n_y^2) + n_y^2]^2 \right\}. \tag{42}$$

Analysis of expression (42) shows directly that if the normal to the plane of the slab coincides with an easy direction of one of the domains ($\mathbf{n} \parallel Ox$ or Oy), then the main contribution to the destressing energy comes from the first term. Here in the absence of external fields the state in which the domain fractions are in a ratio of 2:1 ($\xi = 1/3$ or $2/3$) are energetically favorable. In the other limiting case, when the plane of the sample coincides with the interface between X and Y domains [$\mathbf{n} \perp (110)$], the second term, which favors a structure with equal fractions of domains of the two types ($\xi = 1/2$), is nontrivial. Finally, if the plane of the slab coincides with a habit plane [$\mathbf{n} \perp (011)$], then the fraction of one of the domains is determined by the ratio c_{44}/c_{11} and can be much less than unity. We emphasize that such a ratio of the equilibrium domain fractions can be observed only under the condition that the surface of the sample is free.

In the opposite case of a transition with a coherent interphase boundary one should use expression (29) for the destressing energy; analysis of that expression leads to a result that is well known in the physics of martensitic phase transformations—the equilibrium fractions of the domains of the two types stand in a ratio of 2:1 provided that the interphase boundary is parallel to a habit plane (see above). We note that in contrast to the crystallographic approach adopted in the theory of the martensitic transformations and based on the requirement of coherent matching of the lattices of the two phases, martensitic and austenitic, the model of "elastic dipoles" enables one to predict the possibility of formation of a domain structure and to calculate the fraction of the domains of the different types for different boundary conditions, particularly in the presence of external mechanical stresses or in the case when the interphase boundary at the transition is absent altogether (e.g., for a second-order transition).

6. CONCLUSION

The elastic dipole model proposed above is based on physical assumptions that can be stated as follows.

1. At a thermoelastic phase transition, concentrated forces–elastic dipoles—arise at every point of the medium; the origin of these elastic dipoles is due to the change in character of the interatomic bonds. Having arisen, these dipoles do not vanish, but they can change their orientation under the influence of external forces of different natures.

2. The orientation of the elastic dipoles is determined mainly by the magnitude and orientation of the primary (here, magnetic) order parameter.

3. At large distances the elastic dipoles create strain fields that can be described in the framework of the standard theory of elasticity.

The model developed here can give a consistent explanation of the causes for the appearance and the conditions for the formation of a domain structure in substances in which the primary order parameter [the (antiferro)magnetic moment or electron density] does not create the long-range fields necessary for the formation of a macroscopically inhomogeneous structure. Such substances include, for example, the collinear (compensated) antiferromagnets considered in this paper, and crystals undergoing a thermoelastic martensitic transformation. Furthermore, the formalism developed here can also be applied for the description of the domain structure in ferromagnetic crystals with strong magnetoelastic interactions and a degenerate orientation of the magnetization vector. A special case in light of what we have said above may be weak ferromagnets and ferromagnetic martensites, where a competition between the purely magnetic (ferromagnetic) and magnetoelastic factors giving rise to the domain structure is not ruled out.

The expressions (19) obtained for the energy of the magnetoelastic dipole–dipole interaction are formally analogous to the expressions for the dipole–dipole energy of an ordered ferromagnet. This analogy is based on the identical character of the spatial dependence of the Green's function of the elastic medium, which determines the destressing tensor, and of the Green's function of the Laplacian operator, which appears in the expression for the components of the demagnetization tensor. Such an analogy, even without calculations, allows one to extend the basic results pertaining to the conditions of formation of the domain structure in ferromagnets to antiferromagnetic and martensitic crystals. For example, in both cases the dipole–dipole energy contains two contributions: one that depends on the order parameters (e.g., the magnetic moments) averaged over the sample and is proportional to the volume of the crystal, and another that is due to the nonuniform distribution of the order parameter over distances of the order of the period of the domain structure. The first contribution, which is discussed in the present paper, brings about a lowering of the total energy of the crystal on account of its breaking up into domains and the decrease of the average quantities. The second contribution influences the size of the domains and in the case when the size of the sample is much greater than the size of a domain it is negligibly small compared with the first contribution. Both in ferro- and in antiferromagnets there should exist a certain limiting size of the sample (thickness of the slab) below which the formation of domain structure becomes energetically unfavorable for any ratio of the domain fractions.[10)]

The differences between the dipole interactions in ferromagnets and antiferromagnets is due primarily to the tensor (rather than vector) character of the internal stresses, which are the order parameter at thermoelastic transitions. As a result, in the case of thermoelastic crystals the calculation of the domain structure becomes a much more complicated problem, but a greater diversity of possible domain structures arises. For example, the structure of the destressing tensor, unlike the demagnetizing tensor, depends in the general case on the ratio between the different elastic constants, and in the final analysis that leads to substantial scatter in the monodomainization fields in relation to the orientation and shape of the sample.

The expressions obtained in this study for the relation between the domain fraction and the value and orientation of the external magnetic field permit one to calculate the field dependence of the macroscopic parameters of antiferromagnetic crystals, i.e., such as the elongation or magnetoresistance. The dependence of the monodomainization field of a sample on its shape (in the simplest case, the orientation of the plane of the slab in respect to the crystallographic axes) in turn opens up the possibility of an experimental check of the hypothesis of microscopic elastic dipoles.

Finally, let us mention another circumstance in connection with the value of the internal stress tensor $\hat{\sigma}^{\mathrm{mag}}$. As experiments show, the value of the mechanical stress at which monodomainization of the sample occurs in elastic and magnetoelastic materials (see, e.g., Refs. 5, 18, and 23) is ≈ 30 MPa, while at the same time the value of the microstresses estimated from the value of the spontaneous strain and the shear modulus equals ≈ 300 MPa. A difference of an order of magnitude can be explained from the standpoint of the model proposed above if the quantity s_{jklm} appearing in expression (18) is treated as an anisotropy constant related to the possibility of ''rotation'' of the elastic dipole but not to the creation (ordering) of it.

This study was supported in part by the Ministry of Education and Science of Ukraine (Grant NF7/514-2001) and in part under the directed research plan of the National Technical University of Ukraine ''Kiev Polytechnic Institute'' (State Registration No. 0103U000303). The authors thank Acad. V. G. Bar'yakhtar for interest and active discussion of the results of this study and Prof. V. I. Marchenko and S. M Ryabchenko for fruitful discussions and critical comments that served as a stimulus for addressing this problem. E.V.G. thanks A. A. Malyshenko for financial and technical support during the performance of this study.

*E-mail: malyshen@ukrpack.net
†E-mail: vloktev@bitp.kiev.ua

1) Thermoelastic phase transitions are those at which the internal stresses caused by the transition are so small that they can be treated as elastic, i.e., they do not lead to macroscopic plastic deformation of the crystal. As a rule such conditions are realized at phase transitions in magnets (ferromagnets and antiferromagnets) and in many cases at martensitic phase transitions, e.g., in In–Tl, Co–Pt, etc. crystals.

2) Antiphase domains are those in which the order parameters (in the case of antiferromagnets–the antiferromagnetic vector) are transformed into each other by a translation (by time reversal, by spare rotations; see, e.g., Ref. 16). Formally they are analogous to collinear domains in ferromagnets, which go over into each other under the operation of time reversal. Furthermore, in both ferro- and antiferromagnets there can exist domains that go over into each other under spatial rotations—these are orientational domains. Both types are observed experimentally, but in this paper we consider only the orientational domains.

3) It is easy to see this if it is noted that upon a rotation of the crystallographic axes by 90° around the Oz axis one has $x \to y$, $y \to -x$, and $\boldsymbol{\rho}_1 \to \boldsymbol{\rho}_2 \to \boldsymbol{\rho}_3 \to \boldsymbol{\rho}_4$.

4) Following the terminology introduced in Ref. 16, the primary or true order parameter is one that arises at the transition point and has transformation properties that completely describe the observable change of symmetry at the phase transition and the anomalies of the physical properties.

5) In the majority of experimentally observable cases the elastic domains in ferro- and antiferromagnets coincide with the magnetic domains, as, e.g., in the crystals NiO (Ref. 17) and Ni_2GaMn (Ref. 18).

6) Continuing the analogy with ferromagnetism, we should say that the

Green's function of the Laplacian operator, which appears in the expression for the energy of magnetic dipoles, behaves in the same way.[19]

[7)]The proposed term ''destressing'' tensor and ''destressing'' energy reflect the role of the corresponding contribution to the free energy in the formation of the microstructure of the sample. For example, the influence of the long-range fields (22) leads to a decrease of the macroscopic strain of the sample owing to the formation of domains of different orientation, despite the fact that the local values of the strain tensor in the domains remain unchanged. The term ''detwinning'' which we introduced previously in Ref. 10 is, from this standpoint, unfortunate, since it presupposes exactly the opposite process—the vanishing of the domain structure.

[8)]An analogous situation takes place in the case of the demagnetization of a ferromagnetic crystal, e.g., if the sample is in the form of a thin slab cut parallel to the plane of easy magnetization.

[9)]It is assumed that the surface of the sample is free, and effects due to the presence of coherent interphase boundaries in the sample are not taken into account.

[10)]A detailed analysis of the optimal period of the domain structure arising at a magnetoelastic phase transition and of the critical size of the sample is given in Ref. 10.

[1] L. Néel, *Proceedings of the International Conference on Theoretical Physics, Kyoto and Tokyo, September, 1953*, publ. Science Council of Japan, Tokyo (1954), p. 701.
[2] M. Safa and B. K. Tanner, Philos. Mag. B **37**, 739 (1978).
[3] E. V. Amitin, A. G. Baĭkalov, A. G. Blinov, L. A. Boyarskiĭ, V. Ya. Dikovskiĭ, K. R. Zhdanov, M. Yu. Kameneva, L. P. Kozeeva, and A. P. Shelkovnikov, JETP Lett. **70**, 352 (1999).
[4] V. M. Kalita, A. F. Lozenko, and S. M. Ryabchenko, Fiz. Nizk. Temp. **26**, 671 (2000) [Low Temp. Phys. **26**, 489 (2000)].
[5] A. N. Lavrov, S. Komiya, and Y. Ando, Preprint cond-mat/0208013 (2002).
[6] A. N. Lavrov, S. Komiya, and Y. Ando, Nature (London) **418**, 385 (2002).
[7] Y. Ando, A. N. Lavrov, and S. Komiya, Phys. Rev. Lett. **90**, 247003 (2003).
[8] E. V. Gomonaj and V. M. Loktev, Fiz. Nizk. Temp. **25**, 699 (1999) [Low Temp. Phys. **25**, 520 (1999)].
[9] E. V. Gomonaj and V. M. Loktev, Phys. Rev. **64**, 064406 (2001).
[10] H. Gomonay and V. M. Loktev, J. Phys.: Condens. Matter **14**, 3959 (2002).
[11] V. I. Marchenko and A. Ya. Parshin, Zh. Éksp. Teor. Fiz. **79**, 257 (1980) [Sov. Phys. JETP **52**, 129 (1980)].
[12] M. Kléman and M. Schlenker, J. Appl. Phys. **43**, 3184 (1972).
[13] M. Kléman, J. Appl. Phys. **45**, 1377 (1974).
[14] C. Teodosiu, *Elastic Models of Crystal Defects*, Springer-Verlag, Berlin (1982), Mir, Moscow (1985).
[15] L. D. Landau and E. M. Lifshitz, *Theory of Elasticity*, 3rd Eng. ed., Pergamon Press, Oxford (1986), Fizmatgiz, Moscow (1987).
[16] Yu. A. Izyumov and V. N. Syromyatnikov, *Phase Transitions and Symmetry of Crystals* [in Russian], Nauka, Moscow (1984).
[17] N. B. Weber, H. Ohldag, H. Gomonaj *et al.*, Phys. Rev. Lett. **91**, 237205 (2003).
[18] K. Ullakko, J. K. Huang, C. Kantner *et al.*, Appl. Phys. Lett. **69**, 1966 (1996).
[19] A. I. Akhiezer, V. G. Bar'yakhtar, and S. V. Peletminskiĭ, *Spin Waves*, North-Holland, Amsterdam (1968), Nauka, Moscow (1967).
[20] A. G. Khachaturyan, *Theory of Phase Transformations and the Structure of Solid Solutions* [in Russian], Nauka, Moscow (1974).
[21] A. N. Lavrov, Y. Ando, S. Komiya, and I. Tsukada, Phys. Rev. Lett. **87**, 017007 (2001).
[22] M. Nohara, T. Suzuki, Y. Maeno, and T. Fujita, Phys. Rev. B **52**, 570 (1995).
[23] A. N. Vasil'ev, D. Buchel'nikov, V. T. Takagi, V. V. Khovaĭlo, and É. I. Yastrin, Usp. Fiz. Nauk **173**, 577 (2003).

Translated by Steve Torstveit

LOW-DIMENSIONAL AND DISORDERED SYSTEM

Fractal character of the spectrum in the vicinity of a local mode in linear chains with isotopic impurities

M. A. Ivanov,* V. S. Molodid, and Yu. V. Skripnik

G. V. Kurdyumov Institute of Metal Physics, National Academy of Sciences of Ukraine, pr. Vernadskogo 36, Kiev 03142, Ukraine

(Submitted February 13, 2004)
Fiz. Nizk. Temp. **30**, 1086–1091 (October 2004)

The vibrational spectrum of a one-dimensional disordered chain of atoms with light isotopic substitutional impurities is calculated numerically for frequencies near a local mode of an isolated impurity atom. It is shown that in the entire frequency region accessible to the calculation, the spectrum does indeed have the characteristic features of a fractal. Series of lines clustered around the lines of an isolated impurity atom or of two and three impurity atoms are examined. It is shown that in these cases a self-similar structure is preserved at arbitrary reductions of the scale both outside and inside the concentration broadening region. © *2004 American Institute of Physics.* [DOI: 10.1063/1.1808200]

1. INTRODUCTION

In Ref. 1 we reported numerical calculations of the vibrational spectrum of a one-dimensional disordered chain of atoms with light isotopic substitutional impurities. The results of the numerical simulation were compared with simple analytical estimates for the spectral distribution of frequencies in the vicinity of a local mode of an isolated impurity atom, and it was shown that the smoothed density of states in this region can be found to a sufficient degree of accuracy from considerations based on separating out clusters of two impurity atoms separated by different distances. The analytical expressions obtained are in satisfactory agreement with the numerical calculations both outside and inside the region of concentration broadening of the local mode.

The complex hierarchical structure of the vibrational spectrum in the vicinity of a local mode outside the concentration broadening region was first analyzed in detail by I. M. Lifshits.[2,3] At the time it was assumed that the density of states inside the concentration broadening region is a rather smooth function.[4–7] However, in Ref. 1 we pointed out that for one-dimensional systems the hierarchical structure of the spectrum was completely preserved even inside the concentration broadening region. In addition, the spectrum in the vicinity of a local mode is self-similar with respect to a change of scale, i.e., it has a fractal character.

The present paper is devoted mainly to a more detailed analysis of the fine structure of the vibrational spectrum in the concentration broadening region. Using numerical calculations based on the Dean method,[8,9] we show that all the way to the limit of accessability for the method of solution used the spectrum does in fact have the characteristic features of a fractal. For example, at the vibrational frequency of an isolated impurity atom the main peak consists of lines corresponding to two, three, four, and more-complex combinations of interacting impurities, each of which, in turn, is also self-similar. The fine structure of the spectrum of the main peak and the peaks corresponding to two and three impurity atoms is investigated over as wide a change of scale as possible.

2. SELF-SIMILARITY OF THE SPECTRUM OF PAIR IMPURITY MODES IN THE VICINITY OF A LOCAL MODE FREQUENCY

According to Ref. 3, the vibrational spectrum near a local mode at low impurity concentrations consists of series of discrete lines, the more-intense lines of the spectrum being points of clustering of less-intense lines. There, as was shown in Ref. 10, those lines that are split off from the local mode by a rather wide frequency interval owing to the interaction of defects can be successfully associated to practically isolated vibrations of impurity clusters of small size. The main series of these lines, clustered at the frequency of the local mode, corresponds to vibrations of pairs of impurities. It is clear that, the closer the impurity atoms to each other, the larger the interval by which the two pairs of modes are separated from the main peak. For the model considered here, that of an isotopic substitutional impurity, the small deviations Δ of the square frequencies ω_R^2 of these pair modes from the square frequency ω_L^2 of an isolated impurity are described approximately by the expression[11,12]

$$\omega_R^2=\omega_L^2\pm\Delta(R),\quad \Delta(R)\approx A^R\frac{2\varepsilon^2}{(1-\varepsilon^2)^2},$$

$$A=\frac{1-\varepsilon}{1+\varepsilon},\quad \Delta(R)\ll\omega_L^2-1, \tag{1}$$

where $\varepsilon=(m_0-m_d)/m_0$, m_0 and m_d are the masses of the host and impurity atoms, respectively, and the maximum frequency of the acoustic band is taken as unity, so that $\omega_L^2=1/(1-\varepsilon^2)$. For a light substitutional impurity $m_d<m_0$, and therefore $0<\varepsilon<1$ and $0<A<1$. From Eq. (1) we obtain

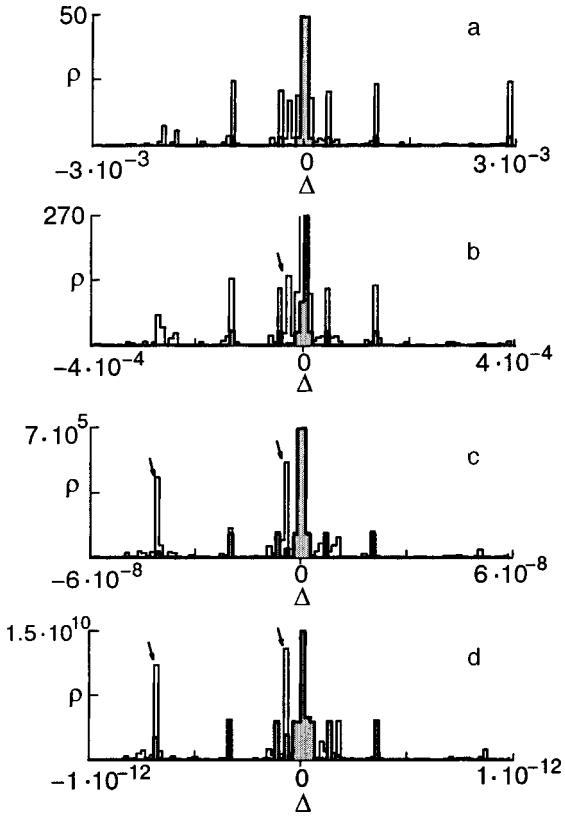

FIG. 1. Fine structure of the vibrational spectrum of a disordered chain of atoms near a local mode frequency for $\varepsilon=0.5$ and concentrations $c=0.1$ and $c=0.02$ (shaded region). The density of states, normalized to unity, is plotted along the vertical axis, and the distance from the frequency of an isolated impurity (the difference of the squares of the frequencies) is plotted along the horizontal.

$$\Delta(R+1)=A\Delta(R). \tag{2}$$

Since $A<1$ it follows from Eq. (2) that as the local mode is approached, the frequency intervals between successive pair modes decreases. Furthermore, under the condition of constant intensity of the corresponding lines of the spectrum the overall picture of their distribution does not change when the scale is changed by a factor of A. Thus on the basis of Eq. (2) one can say that the spectrum of pair modes has the property of self-similarity.

Figure 1 shows the results of a numerical calculation of the fine structure of the vibrational spectrum of a disordered chain for $\varepsilon=0.5$ and concentrations $c=0.1$ and $c=0.02$ (shaded region). Here and below the results are obtained by numerical simulation of chains with a length of 10^8 atoms. The so-called region of concentration broadening of the local mode is specified by the value of the splitting of the pair impurity modes that corresponds to the mean distance between impurities in the chain and was previously determined to be $\Delta_c=\Delta(1/2c)$. [The coefficient 2 in this formula comes from the fact that the integral density of states for all the pair modes for which the distance between impurity atoms is less than a certain value is equal to $2c^2R_1$. Therefore, this quantity becomes of the order of the total number of impurity levels c precisely for $R_1\approx1/(2c)$.] In the case $c=0.02$ all of the graphs except the last one correspond to the region outside the concentration broadening (for $c=0.02$ the concentration broadening region $\Delta_c\approx10^{-12}$). As can be seen in the figure, the spectrum consists mainly of pair modes, and the first three histograms are practically identical in structure despite the scale change by a factor of 2×10^5. For a concentration $c=0.1$ the concentration broadening is significantly larger: $\Delta_c\approx4\times10^{-3}$. Therefore the self-similarity is observed not too deep inside the concentration broadening region (Fig. 1a,b). Deep inside the region of width Δ_c (Fig. 1c,d) the spectrum also retains the property of self-similarity, but it has a different appearance from the previous ones. In all parts of the spectrum at the given concentration one can clearly see several modes corresponding to more-complex combinations of impurity atoms in addition to the pair modes. A few of the most noticeable of these modes, corresponding to clusters of three interacting impurities, are indicated by arrows. The relative intensity of such modes increases as ω_L is approached, so that deep inside the region of width Δ_c the density of states consists almost completely of peaks corresponding to combinations of three and more impurity atoms.

We note that the calculations were also carried out for other values of the system parameters, e.g., for $\varepsilon=0.1$, and all the qualitative conclusions reached above remain valid for them as well.

3. VIBRATIONAL SPECTRUM OF A THREE-PARTICLE IMPURITY CLUSTER

Let us consider the spectrum of vibrations of an isolated group of atoms consisting of three impurity centers. The positions of the lines of this spectrum outside the initial acoustic band ω_3^2 can be found as the solutions of a cubic equation obtained on the basis of the results of Ref. 13:

$$(\omega_3^2-\omega_L^2)^3-(\omega_3^2-\omega_L^2)[\Delta(R_{01})+\Delta(R_{02})+\Delta(R_{12})] -2\Delta(R_{01})\Delta(R_{02})\Delta(R_{12})=0, \tag{3}$$

where $\Delta(R)$ is defined in Eq. (1), and R_{01}, R_{02}, and R_{12} are the distances between atoms 0, 1, and 2 in the given cluster of impurity atoms.

Let us take two impurity atoms (0 and 1) separated by a fixed distance R_{01} and bring a third impurity atom toward this pair (for the sake of definiteness, from the side of atom 1). Clearly, for $R_{12}\gg R_{01}$ there will exist two modes slightly shifted relative to the frequencies corresponding to the isolated pair of impurities, and a vibration with a frequency approximately equal to ω_L. Such a structure of the spectrum at $R_{01}=8$ is shown in Fig. 2 (the case $R_{01}=9$ is also shown in Fig. 2c), where the quantity on the abscissa is the deviation (i.e., the difference Δ of the squares of the frequencies) of the vibrational frequency from that of the local mode, and the distance R_{12} is plotted along the ordinate. The circlets show the frequencies obtained as a result of the numerical calculations for discrete values of R_{12}, and the solid curve is the solution of equation (3) for a continuous variation of R_{12}.

As is seen in Fig. 2a, in the case when R_{12} is noticeably larger than the distance between impurities in the pair (in the given case, for $R_{12}\geqslant10$) one indeed obtains the spectral structure described above [the vertical dashed lines in this figure show the values of the frequencies of the pair modes

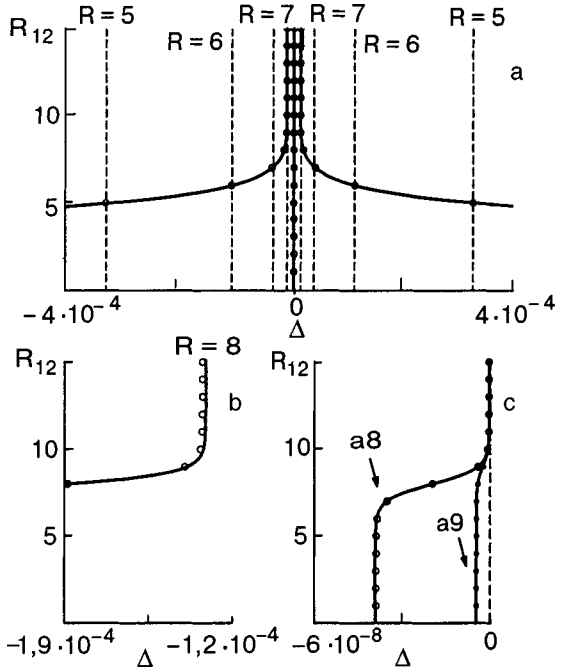

FIG. 2. Change in the position of the spectral lines as a third impurity atom approaches a pair of impurities separated by a distance R_{01}. The position of the spectral lines in the scale Δ is plotted along the horizontal axis, and the distance R_{12} along the vertical. The circles show the calculated positions of the lines, and the solid curves show the solution of the equation for a continuous variation of R_{12}; $R_{01}=8$. The vertical dashed lines show the frequencies of pair levels with the corresponding values of the distance R. The curves labeled a8 and a9 show the shift of the central lines in the triples for $R_{01}=8$ and $R_{01}=9$.

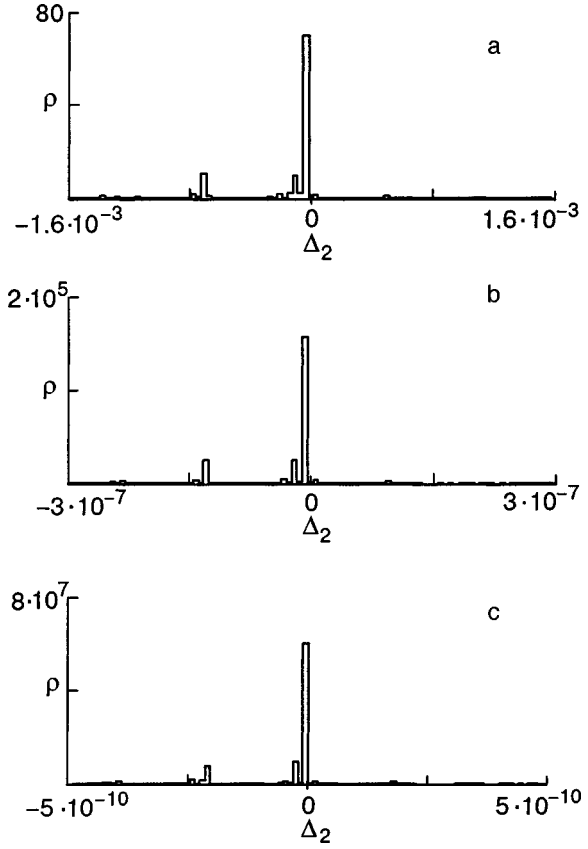

FIG. 4. Fine structure of the pair mode corresponding to $R=4$ and located on the main-band side of the frequency of an isolated impurity ($\varepsilon=0.5$, $c=0.1, \omega_L^2=4/3$). The quantity plotted along the horizontal is $\Delta_2=\omega^2-\omega_R^2$, where $\omega_R^2=1.3217394506$.

corresponding to different values of R in Eq. (1)]. The shift of the left and central lines with decreasing R_{12} is shown in more detail in Fig. 2,b,c.

As a third impurity approaches the original pair, when $R_{12}<R_{01}$ the structure of the spectrum does not change substantially: the two extreme modes are located almost symmetrically about ω_L^2 at frequencies corresponding to the closest pair, with the separation R_{12}, while the third is shifted slightly relative to the local mode frequency. Upon further decrease of R_{12} the value of the shift of the central level goes to some constant for a number of R_{12} values. One can therefore assume that the intensity of such a mode corresponding to three impurities will be anomalously high. For a given configuration ($R_{01}=8$) the position of this mode is indicated in Fig. 3 as a8, and it is located between the frequencies of the pair vibrations corresponding to $R=15$ and $R=16$ (the $R=15$ line is not seen in Fig. 3, as it lies to the left of the ordinate interval shown). Here, for a concentration $c=0.1$, its intensity is considerably higher than that of the neighboring pair modes. For the initial configuration $R_{01}=9$ the position of the corresponding central mode in the triple (a9) is found between levels $R=17$ and $R=18$ (Fig. 3). We note that the lines a8 and a9 are shifted relative to the local level in the direction of the initial band.

The small shifts of the levels of a pair when a third impurity approaches it at distances $R_{12}\gg R_{01}$ is in fact one of the causes of the appearance of fine structure of the pair levels.

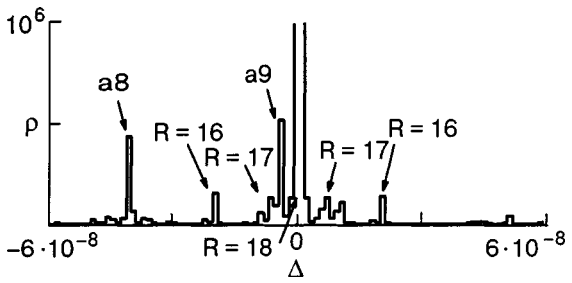

FIG. 3. Part of the spectrum in the vicinity of a local level ($\varepsilon=0.5, c=0.1$). The arrows denote the pair levels corresponding to $R=17$ and $R=18$. The frequencies of the shifted central lines corresponding to three impurity atoms for $R_{01}=8$ and $R_{01}=9$ are labeled a8 and a9.

4. FRACTAL PROPERTIES OF THE FINE STRUCTURE OF MODES CORRESPONDING TO TWO AND THREE IMPURITY CENTERS

Let us discuss in more detail the behavior of the spectrum near individual pair modes. Figure 4 shows the fine structure of a pair mode which corresponds to $R=4$ and lies between the main band and the local mode, for the case $c=0.1$. At such a distance between impurities in the pair and at the chosen concentration, the frequency of this mode lies outside the concentration broadening region of the local mode ($\Delta_c\approx4\times10^{-3}$). However, as the scale is enlarged, as is seen in Fig. 4c, one can examine a neighborhood of the

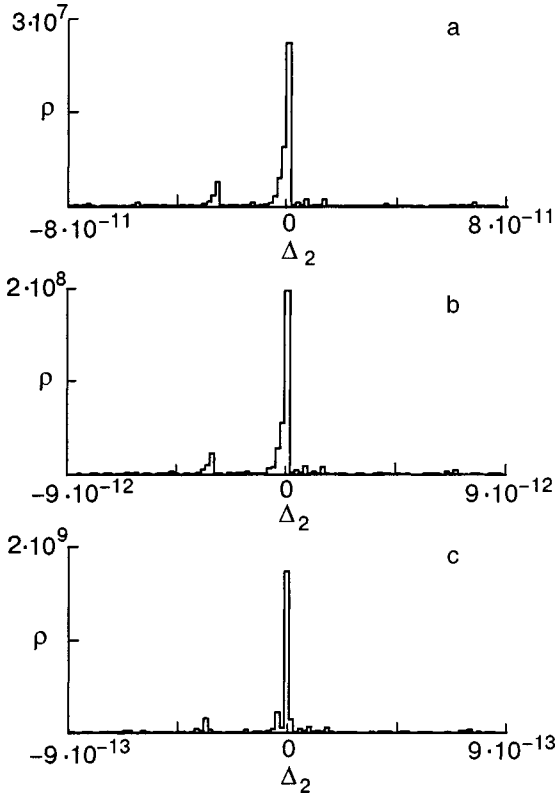

FIG. 5. Structure of the pair level inside the concentration broadening region. $R=20$ (the region opposite from the main band). $\omega_R^2 = 1.3333333335883$. The remaining parameters and notation are the same as in Fig. 4.

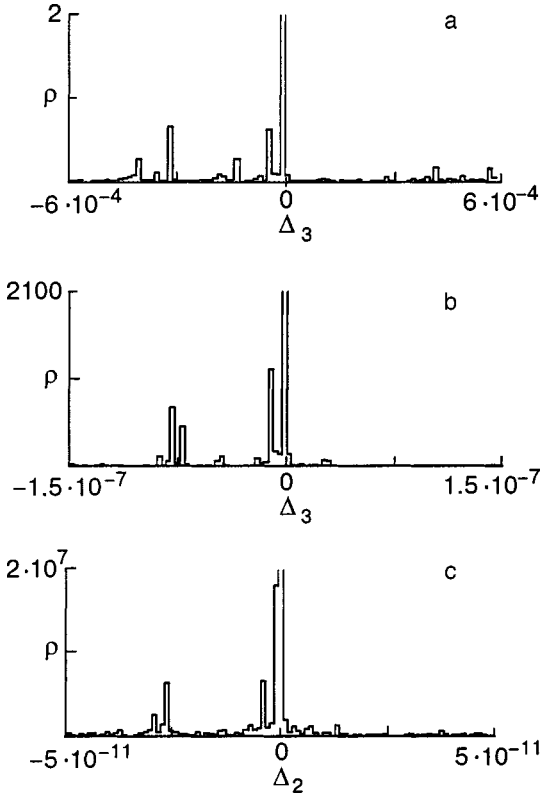

FIG. 6. Fine structure of a level corresponding to three impurity atoms lying at distances $R_{01}=3$, $R_{12}=4$ (the level closest to the band with frequency $\omega_3^2=1.29466407$). The quantity plotted along the horizontal is $\Delta_3=\omega^2=-\omega_3^2$. (a,b). The part of the spectrum shown in Fig. 5a but replotted in a different scale (c).

pair level which is much smaller than the indicated value of the concentration broadening. However, the self-similarity property of the vibrational spectrum nevertheless continues to hold. The fine structure of the spectrum of the pair mode lying inside the concentration broadening region is also of a fractal character. This can be seen for the sample shown in Fig. 5, which displays the spectrum in the neighborhood of a pair mode whose frequency is higher than the vibrational frequency and which corresponds to $R=20$ for a chain with the same parameters.

It is of interest to examine the fine structure of the modes corresponding to clusters of a greater number of impurity atoms. For example, Fig. 6a,b shows the spectrum near a mode corresponding to three impurity centers lying at distances $R_{01}=3$ and $R_{12}=4$, for $c=0.1$ and $\varepsilon=0.5$. As we see from this figure, even the fine structure of the modes of three impurity atoms is characterized by a high degree of self-similarity upon a change of scale. For comparison, the part of the spectrum shown in Fig. 5a, corresponding to lines clustered around a pair mode, is replotted in another scale in Fig. 6c. It is seen that even the parts of the spectrum corresponding to different hierarchical levels exhibit a considerable degree of self-similarity. This fact, together with the self-similarity within a single hierarchical structure, is indicative of a fractal character of the whole spectrum of vibrational modes of a disordered linear chain near a local mode.

It is not possible to examine the modes corresponding to isolated vibrations of an even greater number of impurity centers, since the chains that must be generated for doing that are too long.

5. CONCLUSION

We have calculated the vibrational spectra of disordered linear chains of atoms near an initial local mode. We have shown that the spectrum in this region has a clear hierarchy and has the self-similarity property that is characteristic of a fractal. We have considered the fine structure of the modes corresponding to an isolated impurity and to two and three impurity centers. In all the range of scale variations accessible in this study the overall form of the spectrum near these modes remains unchanged—a central mode with lines of lower intensity clustered around it. Here it turns out that the interval between closest frequencies of the fine structure is proportional to the size of the interval between these frequencies and the central peak.

Finally, if one considers the thermodynamic quantities (heat capacity, neutron scattering), then the broadening of the lines of the local modes[14–17] will be much larger than the fine structure considered in this paper. However, for kinetic processes such as the passage of sound through a chain, the fine structure can have a extremely important influence. It is therefore also of interest to consider analogous effects for the electronic spectrum of a chain.

The authors thank A. M. Kosevich for a helpful discussion.

*E-mail: ivanov@imp.kiev.ua

[1] M. A. Ivanov, Yu. V. Skripnik, and V. S. Molodid, Fiz. Nizk. Temp. **30**, 217 (2004) [Low Temp. Phys. **30**, 159 (2004)].
[2] I. M. Lifshits, Zh. Éksp. Teor. Fiz. **44**, 1723 (1963) [Sov. Phys. JETP **17**, 1159 (1963)].
[3] I. M. Lifshits, Usp. Fiz. Nauk **83**, 617 (1964) [Sov. Phys. Usp. **7**, 549 (1965)].
[4] M. N. Botvinko, M. A. Ivanov, and Yu. G. Pogorelov, Zh. Éksp. Teor. Fiz. **70**, 610 (1976) [Sov. Phys. JETP **43**, 317 (1976)].
[5] I. M. Lifshits, S. A. Gredeskul, and L. A. Pastur, *Introduction to the Theory of Disordered Systems*, Wiley, New York (1988), Nauka, Moscow (1982).
[6] M. A. Ivanov and Yu. V. Skripnik, Fiz. Tverd. Tela (Leningrad) **32**, 2965 (1990) [Sov. Phys. Solid State **32**, 1722 (1990)].
[7] M. A. Ivanov and Yu. V. Skripnik, Fiz. Tverd. Tela (St. Petersburg) **34**, 351 (1992) [Sov. Phys. Solid State **34**, 342 (1992)].
[8] P. Dean, Proc. R. Soc. London, Ser. A **254**, 507 (1960).
[9] P. Dean, Proc. R. Soc. London, Ser. A **260**, 263 (1961).
[10] P. Dean, Rev. Mod. Phys. **44**, 127 (1972).
[11] A. A. Maradudin, E. W. Montroll, and G. H. Weiss, *Theory of Lattice Dynamics in the Harmonic Approximation*, Academic Press (1963).
[12] E. W. Montroll, A. A. Maradudin, and G. H. Weiss, *Proceedings of the Stevens Institute Many Body Conference*, Interscience (1964).
[13] M. A. Ivanov, Fiz. Tverd. Tela (Leningrad) **12**, 1895 (1970) [Phys. Solid State **12**, 1508 (1970)].
[14] M. A. Krivoglaz, Zh. Éksp. Teor. Fiz. **40**, 567 (1961) [Sov. Phys. JETP **13**, 397 (1961)].
[15] M. A. Ivanov, L. B. Kvashnina, and M. A. Krivoglaz, Fiz. Tverd. Tela (Leningrad) **7**, 2047 (1965) [Sov. Phys. Solid State **7**, 1652 (1965)].
[16] M. A. Ivanov, M. A. Krivoglaz, D. N. Mirlin, and I. I. Reshina, Fiz. Tverd. Tela (Leningrad) **8**, 192 (1966) [Sov. Phys. Solid State **8**, 150 (1966)].
[17] A. A. Maradudin, *Theoretical and Experimental Aspects of the Effects of Point Defects and Disorder on the Vibrations of Crystals*, Academic Press (1966).

Translated by Steve Torstveit

SHORT NOTES

Low-temperature ESR spectrum in a powder sample of $Cu(C_{10}H_8N_2)(H_2O)_2SO_4$

O. Kravchyna* and A. Kaplienko

B. Verkin Institute for Low Temperature Physics and Engineering, National Academy of Sciences of Ukraine, pr. Lenina 47, Kharkov 61103, Ukraine

M. Kajnakova†

Department of Experimental Physics Faculty of Sciences, P. J. Safarik University, 9 Park Angelinum, Kosice 04154, Slovakia

(Submitted April 19, 2004; revised May 11, 2004)
Fiz. Nizk. Temp. **30**, 1092–1094 (October 2004)

The ESR spectrum of a powder sample of the metal-organic complex $Cu(C_{10}H_8N_2)(H_2O)_2SO_4$ is investigated in the temperature interval 2–30 K. It is found that the orbital ground level of the Cu^{2+} ion in this compound is the Kramers doublet $|x^2-y^2\rangle$. The temperature dependences of the effective g-factor components and of the resonance linewidth ΔH of individual powder particles are obtained. Low-temperature broadening of the resonance line connected with short-range magnetic order in the system is observed. An estimate of the value of the exchange coupling in the magnetic system is made. © *2004 American Institute of Physics.*
[DOI: 10.1063/1.1808201]

Metal-oxide compounds, being magnetically concentrated systems, often exhibit properties of low-dimensional magnets because of the features of the spatial surroundings of the magnetic ion, which formed directed interionic bonds. Information about the ground state of the magnetic ion in a compound by which one can largely predict its magnetic properties can be obtained from the electron spin resonance (ESR) spectrum. In the case of single-crystal objects, studies by the resonance method are extremely informative. For powder and polycrystalline samples, which are usually obtained in the synthesis of metal-organic compounds, the possibilities of this method are essentially limited. As a rule, it is used only for complexes with a magnetic ion of spin $S=1/2$, the spectrum of which does not have fine structure and so permits unambiguous interpretation of the results.

The goal of the present study is to determine both the ground state of the Cu^{2+} ion ($S=1/2$) in a polycrystalline bipyridine metal-organic complex $Cu(C_{10}H_8N_2)(H_2O)_2SO_4$ [henceforth called $Cu(bpy)(H_2O)_2SO_4$] and the exchange interactions in its magnetic subsystem.

The crystal structure of this compound is characterized by the monoclinic space group $C2/c$; the cell contains four molecules and is specified by the parameters $a=15.136$ Å, $b=12.464$ Å, $c=6.999$ Å, $\beta=105.97°$ (Ref. 1). This structure is similar to that of compounds which have investigated previously.[2] They are characterized by the presence of chains of axially distorted octahedra, which are the local environment of the divalent copper ions and lie in the c direction of the cell. The octahedra are joined to each other through apical oxygen atoms belonging to SO_4 groups. The basal plane of the octahedra, formed by two oxygen ions belonging to water molecules and two nitrogen ions of the organic complex, is almost perfectly square.

The resonance spectra were measured in the $\lambda=4$ mm wavelength region, making it possible to obtain higher resolution of the spectra with respect to the value of the g factor. The low-temperature properties of the complex were studied in the temperature interval 4.2–30 K. The precision of the temperature stabilization and the measurement accuracy were 0.1 K in the interval 4.2–15 K and 0.5 K at $T>15$ K.

The compound was synthesized in the form of a fine powder. The ESR spectrum of the sample is a superposition of the spectra of small single-crystal particles randomly oriented with respect to the direction of the external magnetic field and represents an absorption band spanning a rather wide range of fields. In the case of axial symmetry of the local environment of a paramagnetic ion the axis of symmetry of most of the powder particles is oriented perpendicular to the external field, $\mathbf{H}\perp\mathbf{c}$. This gives a rather narrow peak at the high-field edge of the absorption band, as is shown in Fig. 1. Particles with the $\mathbf{H}\|\mathbf{c}$ orientation of the local axes contribute to the intensity of the opposite edge of the absorption band.

In these extremal orientations of the particles the values of the resonance fields $H_\|$ and $H_\perp$ are determined by the values of the effective g factor $g_\|$ and $g_\perp$, and in the case of a Lorentzian line shape for the individual powder particles the shape of the absorption band takes the form[3]

$$I(H)\sim\int_{H_\|}^{H_\perp}\frac{H(1+H_\|^{-2}H'^2)dH'}{[(H-H')^2+\Delta H^2]H'^2(H_\perp^2-H'^2)^{1/2}}. \quad (1)$$

Here $H_{\|,\perp}=h\nu/g_{\|,\perp}\mu_B$, ν is the working frequency, μ_B is the Bohr magneton, and h is Planck's constant.

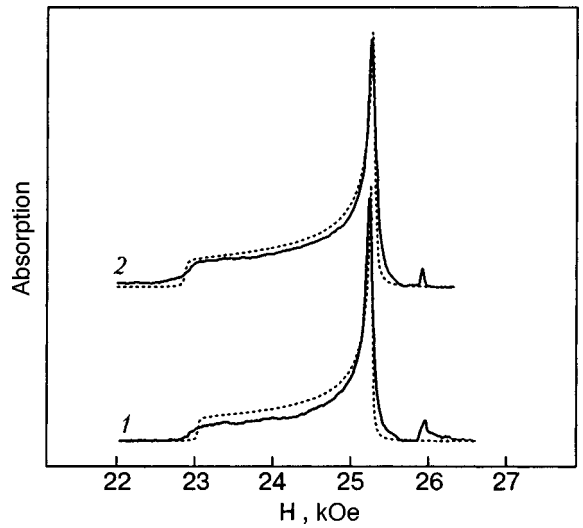

FIG. 1. ESR absorption band in a powder sample of $Cu(bpy)(H_2O)_2SO_4$ at a frequency $\nu=72.81$ Hz for T [K]: 15 (*1*), 8 (*2*). The dotted curves are calculated according to Eq. (1) for the parameter values: $g_\parallel=2.26$, $g_\perp=2.057$, $\Delta H=13.1$ Oe (*1*); $g_\parallel=2.27$, $g_\perp=2.055$, $\Delta H=19.1$ Oe (*2*). The weak absorption peak at $H=26$ kOe is the ESR signal of a standard sample.

This expression was used for computer modeling of the experimentally observed absorption band. The fitting was done by the least-squares method over the whole width of the band; the fitting parameters were $g_\parallel$, $g_\perp$, and ΔH, the linewidth of the individual particles of the powder.

Temperature variations of the shape of the absorption band made it possible to track the temperature dependence of these parameters, which are shown in Fig. 2. We see that the values of $g_\parallel$ and $g_\perp$ are almost independent of temperature, while the ΔH plot shows appreciable temperature broadening of the line, which can be connected with short-range magnetic order in the magnetic system.

On the high-temperature part of the investigated temperature range the values of the g factor are $g_\parallel=2.26$ and $g_\perp=2.05$. According to Ref. 4, satisfaction of the relations $g_\parallel>g_\perp$ and $(g_\parallel-2)/(g_\perp-2)\approx 4$ means that the local environment of the copper ion in this compound is an octahedron elongated along the fourfold axis and that the lowest orbital state is the Kramers doublet $|x^2-y^2\rangle$. Thus the results of the x-ray studies[1] of the structure of the local environment of the Cu^{2+} ion are confirmed. Since the angular distribution of the electron density that is characteristic for the $|x^2-y^2\rangle$ state should lie in the basal plane of the octahedron, it follows that the exchange interactions along the chains formed by these octahedra will be absent or at least substantially attenuated.

At the same time, the signs of possible magnetic ordering manifested in the low-temperature broadening of the resonance line attest to the presence of an exchange interaction in the system, which must be realized predominantly in the interchain directions. A calculation of the exchange integral is difficult because of the complexity of the ligand structure, but it can be estimated from the expression relating the exchange field $H_e=zJ$ with the second moment M_2 of the line and the linewidth:[5]

$$H_e=2M_2/\Delta H, \tag{2}$$

where z is the number of magnetic nearest neighbors of the given ion.

The second moment of the line for a powder sample with a small anisotropy of the g factor can be calculated numerically[6] proceeding from the interionic distance in the lattice. For $Cu(bpy)(H_2O)_2SO_4$ it is found by direct summation of the contribution of 10^6 sites that $M_2=1.105\times10^4$ Oe^2. With a linewidth $\Delta H=15.7$ Oe, the value obtained in our experiment for the high-temperature part of the $\Delta H(T)$ curve, the exchange field $H_e=1.404\times10^3$ Oe, corresponding to a critical temperature for magnetic ordering of 0.094 K. Such a weak exchange interaction can be realized with the participation of the hydrogen bonds present in the interchain directions in the structure of this compound.

Thus the orbital ground state of the copper ionj $|x^2-y^2\rangle$ in the compound $Cu(bpy)(H_2O)_2SO_4$ should form a quasi-two-dimensional magnetic structure with exchange interactions in the a and b directions of the cell. The extremely wide range of critical broadening of the resonance line may also attest to the low-dimensional character of the magnetic structure of this compound.

The authors thank Prof. A. G. Anders for interest in this study and helpful discussions.

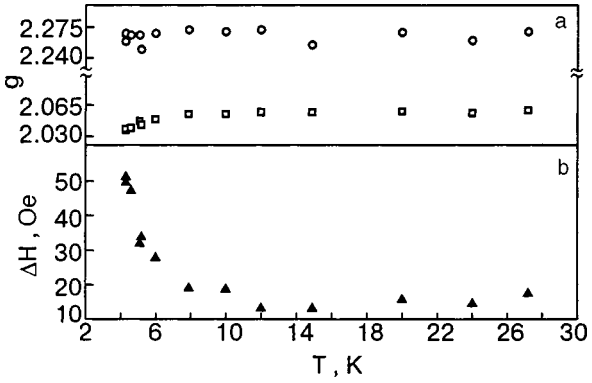

FIG. 2. Temperature dependence of the extremal values of the g factor: $g_\parallel$ (○); $g_\perp$ (□) (a) and the resonance linewidth ΔH (▲) (b).

*E-mail: kravchina@ilt.kharkov.ua
†E-mail: feher@kosice.upjs.sk

[1] J. C. Tedenac and E. Philippot, J. Inorg. Nucl. Chem. **37**, 846 (1975).
[2] O. V. Kravchyna, A. I. Kaplienko, A. G. Anders, M. Orendáč, A. Orendáčova, M. Kajňakova, and A. Feher, Fiz. Nizk. Temp. **30**, 198 (2004) [Low Temp. Phys. **30**, 144 (2004)].
[3] James A. Ibers and J. D. Swalen, Phys. Rev. **127**, 1914 (1962); T. S. Al'tshuler, Zh. Éksp. Teor. Fiz. **55**, 1821 (1968) [Sov. Phys. JETP **28**, 962 (1969)].
[4] A. Abragam and B. Bleaney, *Electron Paramagnetic Resonance of Transition Ions*, Clarendon Press, Oxford (1970), Mir, Moscow (1973).
[5] P. W. Anderson and P. R. Weiss, Rev. Mod. Phys. **25**, 269 (1953).
[6] J. H. Van Vleck, Phys. Rev. **73**, 1249 (1948).

Translated by Steve Torstveit

LETTER TO THE EDITOR

Magnetic ordering caused by a disorder in quasi-one-dimensional spin systems and non-Fermi-liquid systems

A. A. Zvyagin*

B. Verkin Institute for Low Temperature Physics and Engineering of the National Akademy of Sciences of Ukraine, 47 Lenin Ave., Kharkov 61103, Ukraine

A. V. Makarova

Kharkov State Economic University, 9a Lenin Ave., Kharkov 61001, Ukraine; B. Verkin Institute for Low Temperature Physics and Engineering of the National Akademy of Sciences of Ukraine, 47 Lenin Ave., Kharkov 61103, Ukraine

(Submitted July 5, 2004)
Fiz. Nizk. Temp. **30**, 1095–1097 (October 2004)

It is shown that a strong disorder in the distribution of exchange couplings between magnetic impurities and hosts in quantum spin chains and non-Fermi-liquid rare-earth and actinide compounds can be the cause of magnetic orderings in these systems at low temperatures. © *2004 American Institute of Physics.* [DOI: 10.1063/1.1808202]

Low-dimensional quantum spin systems and heavy-fermion systems are of great interest for physicists because in those systems an interaction between quantum particles plays an important role. Such an interaction manifests itself in many characteristics of those systems. It is important to point out that in heavy-fermion systems, as well as in many compounds with the properties of quantum spin chains, quantum spin fluctuations often determine their low-energy properties.

For low-dimensional spin systems quantum spin fluctuations are enhanced. According to the Mermin–Wagner theorem,[1] isotropic Heisenberg magnets have no magnetic order in one and two space dimensions at any nonzero temperature. In rare-earth and actinide compounds exhibiting properties of heavy fermions[2] and so-called non-Fermi-liquids[3] a hybridization of rare-earth or actinide localized electrons of $4f$ or $5f$ states with conduction electron band(s) usually produces the Kondo effect,[4] i.e., the screening of the spin of a localized electron (magnetic impurity) by spins of conduction electrons. In heavy-fermion compounds it also gives rise to spin fluctuations of localized spin moments, which are completely screened below some characteristic energy (the Kondo temperature, T_K), i.e., the ground state is a singlet with a finite magnetic susceptibility. Because of this effect the effective masses of the carriers are enhanced compared to normal metals. It manifests itself in large values of the low-temperature magnetic susceptibility, of the Sommerfeld coefficient of the linear temperature dependence of the electron specific heat, and of the low-temperature coefficient of the resistivity. Such behavior can be described in the framework of the standard Fermi liquid theory[5] with a heavy effective electron mass. On the other hand, for non-Fermi-liquid compounds the magnetic susceptibility and the Sommerfeld coefficient of the specific heat are usually divergent at low temperatures. It turns out that there is often no magnetic ordering in heavy-fermion systems (they are metals with zero order parameter). However, very often, by tuning some parameters such as the concentration of impurities, such systems undergo phase transitions to ordered magnetic or superconducting states.[2,3] Sometimes such phase transitions happen only at zero temperature, i.e., they are quantum critical transitions. In both of these two classes magnetic impurities play an important role. For example, according to two known scenarios the non-Fermi-liquid behavior in rare-earth and actinide compounds is caused either by the so-called multichannel Kondo effect (the spin of the magnetic impurity is overscreened by spins of electrons from several channels) or by disorder in the distribution of Kondo temperatures of magnetic impurities.[1)]

The idea of (nonscreened) magnetic moments existing in disordered metallic systems and quantum spin chains has been formulated in Refs. 6–8. It was proposed that the change in interactions between the impurity sites and the host spins can be considered as a modification of the Kondo temperature. The same characteristic, i.e., T_K, can be introduced for the description of the behavior of magnetic impurities in quantum spin chains.[8–10]

The random distribution of magnetic characteristics of impurities renormalizes the single universal parameter, T_K, which characterizes the state of each magnetic impurity.

Later it was pointed out that the problem of the behavior of magnetic impurities with random distributions of their Kondo temperatures in metals can be solved exactly with the help of the Bethe ansatz.[8–10] It was also shown[9–12] that distributions of effective Kondo temperatures for each magnetic impurity can cause divergences of the magnetic susceptibility and the Sommerfeld coefficient of the specific heat for quasi-one-dimensional organic conductors and quantum spin chains, where such behavior has been observed experimentally.[13–16] To explain power-law divergences of the magnetic susceptibilities and Sommerfeld coefficients of rare-earth and actinide compounds, as well as quasi-one-dimensional organic conductors and quantum spin chains, it was necessary to use a distribution of Kondo temperatures

(the strong disorder distribution, for which the ''tails'' were large enough) which starts with the term $P(T_K) \propto G^{-\lambda}(T_K)^{\lambda-1}$ ($\lambda<1$), valid till some energy scale G for the lowest values of T_K.[9,10,12] Such a distribution was recently derived from first principles in Ref. 17.

Let us consider a number of quantum spin chains, weakly coupled with each other (quasi-one-dimensional system). Then the magnetic susceptibility of the three-dimensional set of one-dimensional spin chains is determined by Dyson's formula

$$\chi_{\text{set}}(T)=\frac{\chi_1(T)}{1-zJ'\chi_1(T)}, \tag{1}$$

where J' is the constant of the interaction between spin chains, z is the number of nearest-neighbor chains, and χ_1 is the magnetic susceptibility of a chain. In a similar way one can calculate the magnetic susceptibility of an ensemble of weakly intercoupled magnetic impurities in a metal (in such a case χ_1 describes the magnetic susceptibility of magnetic impurities in a metal with no interaction between them, and J' specifies the interaction between impurtities). Notice that the interaction between each impurity and the host (a quantum spin chain, or a metal for non-Fermi-liquid systems) is considered exactly in our approach; it determines χ_1. Obviously, the denominator in Eq. (1) becomes zero at the point of the phase transition to a magnetically ordered state, and the critical temperature is determined from the condition $\chi_1(T_c)zJ'=1$.

We know[18] that for a set of homogeneous quantum spin chains the magnetic susceptibility χ_1 as a function of temperature has a maximum with the value $\sim 0.14/|J|$ (we are considering units in which the g factors and the Bohr magneton are equal to 1), where J is the exchange constant along the quantum spin chain. Hence, for weak enough interactions $J'<|J|/0.14z$ the quasi-one-dimensional spin system never undergoes a phase transition to the ordered state. The same is true for spin chains with single impurities and for spin chains with a weak disorder in the distribution of their Kondo temperatures: In those cases the ground state is a singlet, and the magnetic susceptibility of those spin chains is finite at low temperatures. Thus, for small enough values of the interchain couplings ($J'<\text{const}\, T_K$) the denominator in Eq. (1) never becomes zero, and there is no phase transition to a magnetically ordered state. On the other hand, for a strong disorder in the distribution of Kondo temperatures of magnetic impurities in quantum spin chains the magnetic susceptibility of each chain is divergent at low temperatures, and any, even infinitely weak interchain interaction has to produce a phase transition to a magnetically ordered state. For example, for the distribution of Kondo temperatures derived in Ref. 17 the magnetic susceptibility of a spin chain with disordered magnetic impurities is $\chi_1 \propto T^{\lambda-1}$. Hence, the critical temperature of the magnetic transition can be estimated as $T_c \sim (zJ')^{1/(1-\lambda)}$. For the special case $\lambda=1$ one has $\chi_1 \propto -\ln T$, and the critical temperature is approximately $T_c \sim \exp(-1/zJ')$. Obviously, we can reach similar conclusions about the possibility of phase transitions to magnetically ordered states for rare-earth or actinide compounds, which exhibit non-Fermi-liquid behavior: Any, even infinitely weak interaction between magnetic impurities with strong disorder in the distribution of their Kondo temperatures has to produce a phase transition to a magnetically ordered state. On the other hand, for heavy-fermion systems and for metals with single Kondo impurities and impurities with a weak disorder in the distribution of their Kondo temperatures there exist critical values of the impurity–impurity couplings J'. In those cases, if the coupling J' is smaller than a critical value, the total system cannot undergo a phase transition to a magnetically ordered phase. The weak interchain or impurity–impurity couplings may be due to the magnetic dipole–dipole interaction, present in any magnetic system; it is weak and long-ranged. Notice that the presence of a phase transition at low temperatures $T_c \neq 0$ for rare-earth or actinide systems with non-Fermi-liquid behavior obviously calls into question the applicability of the ''quantum critical point'' scenario in those cases.

Summarizing, in this Communication we have shown that due to a strong disorder in the distribution of characteristics of magnetic impurities (Kondo temperatures) in quantum spin chains and non-Fermi-liquid rare-earth and actinide compounds, any weak interaction between spin chains or between magnetic impurities in non-Fermi-liquid systems can produce a phase transition to a magnetically ordered state. On the other hand, for homogeneous spin chains or spin chains and heavy-fermion systems with a weak disoder of the distribution of Kondo temperatures there exists a critical value of the coupling, below which there is no such phase transition.

*E-mail: zvyagin@ilt.kharkov.ua

[1)]Another possible cause of the non-Fermi-liquid behavior is the presence of a quantum critical point: Fluctuations of an order parameter interact with itinerant electrons and can cause low-temperature divergences of thermodynamic characteristics.[2,3]

[1] N. D. Mermin and H. Wagner, Phys. Rev. Lett. **17**, 1133 (1966).
[2] F. Steglich, J. Magn. Magn. Mater. **226**, 1 (2001).
[3] G. R. Stewart, Rev. Mod. Phys. **73**, 797 (2001).
[4] J. Kondo, in *Solid State Physics: Advances in Research and Applications*, Vol. 23, F. Seitz, D. Turnbull, and H. Ehrenreich (eds.), Academic, New York (1969), p. 184.
[5] D. Pines and P. Noziéres, *The Theory of Quantum Liquids*, Addison-Wesley, Redwood City (1989).
[6] R. N. Bhatt and D. S. Fisher, Phys. Rev. Lett. **68**, 3072 (1992).
[7] V. Dobrosavljević, T. R. Kirkpatrick, and G. Kotliar, Phys. Rev. Lett. **69**, 1113 (1992).
[8] A. Klümper and A. A. Zvyagin, Phys. Rev. Lett. **81**, 4975 (1998).
[9] A. A. Zvyagin, Phys. Rev. B **62**, R6069 (2000).
[10] A. A. Zvyagin, Fiz. Nizk. Temp. **28**, 1274 (2002) [Low Temp. Phys. **28**, 907 (2002)].
[11] A. Klümper and A. A. Zvyagin, J. Phys.: Condens. Matter **12**, 8705 (2000).
[12] A. A. Zvyagin, Phys. Rev. B **63**, 033101 (2001).
[13] L. N. Bulaevsky, A. V. Zvarykina, Yu. S. Karimov, R. B. Lyubosky, and I. F. Shchegolev, Zh. Eksp. Teor. Fiz. **62**, 725 (1972) [JETP **35**, 384 (1972)].
[14] K. Ikegami, S. Kuroda, M. Saito, K. Saito, M. Sugi, T. Nakamura, M. Matsumoto, and Y. Kawabata, Phys. Rev. B **35**, 3667 (1987).
[15] K. Mukai, K. Suzuki, K. Ohara, J. B. Jamali, and N. Achiwa, J. Phys. Soc. Jpn. **68**, 3078 (1999).
[16] S. V. Demishev, R. V. Bunting, L. I. Leonyuk, E. D. Obraztsova, A. A. Pronin, N. E. Sluchanko, N. A. Samarin, and S. V. Terekhov, JETP Lett. **73**, 31 (2001).
[17] A. A. Zvyagin and A. V. Makarova, Fiz. Nizk. Temp. **30**, 639 (2004) [Low Temp. Phys. **30**, 479 (2004)].
[18] J. C. Bonner and M. E. Fisher, Phys. Rev. **135**, A640 (1964).

This article was published in English in the original Russian journal. Reproduced here with stylistic changes by AIP.